



Radium at Needle's Eye, Scotland, UK

By

Dimitrios Kosmidis

Doctoral Thesis

**Submitted in partial fulfilment for the award of
Doctor of Philosophy of Loughborough University**

Supervisors: Professor Sandie Dann and Professor Peter Warwick

© Dimitrios Kosmidis 2019

Acknowledgments

Every PhD research project is a marathon that usually involves extreme situations at the level of achieving scientific tasks and goals fast and efficiently, as well as, experiencing challenging interpersonal characters and attitudes. The present research project started as a research marathon and transformed to a Golgotha during the journey, mainly because of external factors and people.

It would have been impossible to complete this project without the assistance of my supervisors, Professor Sandie Dann and Professor Peter Warwick. I would like to express my sincere gratitude to them for their continuous support of my PhD study and related research, for their patience, motivation and guidance.

I would like to express my sincere gratitude to Dr Nick Evans for his supervision during the first two years of my PhD study and for providing me with the opportunity to conduct a PhD project and allow me to work as part of Lo-RISE consortium. Our relationship benefited as well from a similar taste of football and other sports.

I would like to thank Dr Oliver Preedy. Without his continuous support this project and thesis would not have been in this state today.

Coming to England in June 2014 I didn't know a single person but the radiochemistry group has contributed the most to make my life better and comfortable in all aspects, therefore, I would like to sincerely thank Mrs Julie Gosden - Turner (Strategic Scientific Development Officer, Lead on Chemical, Radiological or Biological Safety, Radioactive Waste Advisor/Biosafety Consultant), Ms Joan Sutherland (Laboratory Technician), Dr Joel Garner and Mr Phil Davis, Dr Joanna Kulaszewska, Dr Hayley Gillings, Dr James Holt and Dr Manuel Alonso for his support. Thanks also to Dr Monica Felipe-Sotelo, Dr Matt Issacs, Dr Caroline Kirk and Dr John Hinchliff. I would like to thank Dr Manuel Alonso as well for his support.

I wish to express my sincere gratitude to Professor Francis Livens and principal investigator of the Lo-RISE consortium for his support during the first two years of my PhD. Many thanks as well to Dr Margaret Graham for her help and support in organising and getting the required

permission, on my behalf to conduct the sampling fieldworks at Needle's Eye site. Finally, I would like to thank Dr Anthony Milodowski at BGS (British Geological Survey) who advised me and helped me during the second sampling visit at Needle's Eye site, his input was essential for my research. I would like to thank as well the Vice Chancellor and President of Loughborough University Professor Robert (Bob) Allison.

To my dear and friends Mr Vasileios Bagiatis, Mr Konstantinos Kourantidis, Mrs Paraskevi Vatougiou, Ms Elli Nikolaidou, Dr Athanasios Goulas, Ms Andria Hadjithekli, Mr Spyridon Akritidis, Mr Iordanis Kerasiotis, Dr Christos Katrakazas, Dr Eleni Nyktaki, Mr Georgi Babalev and Mr Praveen Elango. Our friendship benefited from a similar taste of humour and gastronomic tastes. Special thanks to my dear friends from back home, Mr Nikolaos Katapidis, Mr Andreas Nikolopoulos, to Mr Christos Kofidis and his family, to Mr Antonios Markozanis and his family, to Mr Panagiotis Kalogouris, Ms Karolina Rakitzi, and to Mr Panagiotis Menemenoglou and his family. I would like to thank as well, my dear Lo-RISE friends, Dr Daisy Ray, Dr Helena Susan Davies, Dr Kieran Tierney and Dr Peter Leary for the unforgettable moments we had during our consortium meetings and workshops. I would like to thank my previous supervisors and mentors as well, Professors Ioannis Arvanitoyannis and Konstantinos Voudouris.

The biggest thanks are to my parents. It would not have been able to attempt and complete this difficult challenge I faced so far in my life without the help of my family, my mother Eleni and my father Vasilis. I will never forget how much they sacrificed and how hard they worked in order to provide me with proper education, morals and ethics and always helped me to make my dreams come true.

Θα ήθελα να ευχαριστήσω από καρδιάς τους γονείς μου, Ελένη και Βασίλη, για όλα αυτά που μου πρόσφεραν όλα αυτά τα χρόνια. Κατάφεραν μέσα από πολλές δυσκολίες, οικονομικές κυρίως, να με εφοδιάσουν με αγάπη, αρχές, ιδανικά και μόρφωση. Προσπάθησα να σταθώ αντάξιος των προσδοκιών και φρονώ πως τώρα που έφτασα στο ανώτατο σημείο προσωπικής και επαγγελματικής καταξίωσης, να τους κοιτάξω στα μάτια και να τους πω ότι τα κατάφερα.

Finally, I would like to thank my life partner Dr Maria Karapli who helped me throughout this challenge. We have lived thousand miles apart the last 3 years. She has always been there for

me in all aspects. I think that the main thing that I have to thank her is that she gives me is that she genuinely makes me happy as she is my inexhaustible source of positive energy.

Philotimo (also spelled *filotimo*; Greek: φιλότιμο),
is a Greek noun translating to "love of honor".
It is almost impossible to translate sufficiently
as it describes a complex array of virtues

Abstract

Samples of soil have been taken from five different locations in Needle's Eye Scotland to establish the processes and conditions which govern the possible movement of radium through the natural environment at the site. The samples were analysed using gamma spectroscopy, powder X-ray diffraction (PXRD), loss on ignition, X-ray fluorescence (XRF), UV/visible spectroscopy, scanning electron microscopy (SEM), and ICP MS - OES to determine the quantity of radium at different areas in the site and examine whether the levels were associated with any particular organic and inorganic phase.

Initial gamma spectroscopy measurements on samples taken from Needle's Eye highlighted some key challenges with the determination of radium by inference by using the measurement of the uranium series progenies, bismuth and lead. Equilibrium between ^{226}Ra and the two progenies (^{214}Bi and ^{214}Pb) was not reached, despite long collection times due to loss of radon gas from the experimental container. Various containers including plastic and aluminium cans sealed with different substances (wax, tape and plastic encapsulation) were then trialled to eliminate radon loss and hence accurately determine the radium content as evidenced by equilibrium being reached. It was proven that aluminium canisters (sealed with wax, Teflon tape on the threads, Scotch tape and vacuum sealed plastic bags) produced the most reliable results since they minimised the radon loss when measuring radium indirectly. A method for measuring radium directly, including the determination of errors, which takes into account the overlap between uranium and radium emission lines in gamma spectroscopy, has been developed.

The activity concentrations for the different samples collected from Needle's Eye (NE1 – NE5) varied significantly; ^{226}Ra varied from $0.67 \times 10^2 \pm 0.05 \times 10^2$ to $26.67 \times 10^2 \pm 6.40 \times 10^2$ Bq kg⁻¹, ^{214}Pb varied from $0.25 \times 10^2 \pm 0.03 \times 10^2$ to $17.70 \times 10^2 \pm 2.00 \times 10^2$ Bq kg⁻¹ and ^{214}Bi varied from $1.63 \times 10^2 \pm 0.12 \times 10^2$ to $17.30 \times 10^2 \pm 0.70 \times 10^2$ Bq kg⁻¹. The average activity ratios of Ra/Pb and Ra/Bi were found to be 1.48 ± 0.15 and 1.84 ± 0.34 respectively and showed significant variance from the ratio expected at equilibrium without radon loss. Loss on ignition treatment (500 and 1000 °C) was performed at the five sites and varied significantly (3.2 – 39.1 %). UV - Vis analysis of samples generated by creating equilibrated water from the samples and altering the pH, suggests that the natural organic matter present in the Needle's Eye soil samples is dominated by humin, followed by lesser amounts of fulvic and humic acids.

Further investigation of the soil from Needle's Eye was conducted by characterisation of topsoil (NE4_T) from the organic rich location of the site. Significant amounts of radium were found to be present in topsoil ($\sim 30 \times 10^3 \text{ Bq kg}^{-1}$). Loss on ignition treatment (500 and 1000 °C) on the topsoil recorded mass a loss of $\sim 86 \%$, and further CHN analysis reported a strong presence of carbon ($\sim 41 \%$) suggesting that about half of the mass lost during loss on ignition experiments is associated with organic carbon and the rest is from carbonate and the breakdown of hydrated minerals. The relative high percentages for carbon, in topsoil, are not surprising when taking into account the natural origin of the samples and the background geology of the site which is dominated by the presence of limestone (CaCO_3), hornblende ($\text{Ca}_2(\text{Mg,Fe,Al})_5(\text{Al, Si})_8\text{O}_{22}(\text{OH})_2$), and granodiorite (rich in calcium).

Sequential extractions were performed on topsoil and deeper soil from the organic rich locality and showed that radium at Needle's Eye is not associated with a single fraction. Approximately 80 % (combined) of the radium was split between 4 fractions with the carbonate fraction (i.e. calcite (CaCO_3) and dolomite ($\text{CaMg}(\text{CO}_3)_2$)), with iron and manganese oxides (i.e. ferrihydrite ($(\text{Fe}^{3+})_2\text{O}_3 \cdot 0.5\text{H}_2\text{O}$), goethite ($\text{FeO}(\text{OH})$), and hematite (Fe_2O_3)), with the organic fraction (i.e. humin), and with the residual fraction (i.e. silicates, feldspars, and sulfates).

PXRD analysis of the bulk soil phases was only successful in identifying quartz (SiO_2), muscovite ($\text{KAl}_2(\text{AlSi}_3\text{O}_{10})(\text{F,OH})_2$) and chlorite ($(\text{Mg,Al})_6(\text{Si,Al})_4\text{O}_{10}(\text{OH})_8$) phases as well as poorly crystalline feldspar phases as inorganic components of the soil samples taken from Needle's Eye due to the large proportion of organic matter in the soil. Using Loss on Ignition at 500°C to remove the organic phases but retain the inorganics showed the presence of carbonate mineral phases, such as, calcite (CaCO_3) and sulfate containing phases such as anhydrite (CaSO_4); as expected since limestone is present in the geology of Needle's eye site together with gypsum ($\text{CaSO}_4 \cdot 2\text{H}_2\text{O}$) and baryte (BaSO_4). Furthermore, PXRD analysis of the topsoil sample after heating at 1000°C to crystallise out the poorly crystalline iron phases evidenced by sequential extraction indicated prominent phases are anhydrite, gehlenite ($\text{CaSi}_2\text{Al}_2\text{O}_7$), quartz (SiO_2) and magnesioferrite (MgFe_2O_4). PXRD analysis supported by XRF elemental analysis, which showed elevated concentrations for calcium, may also suggest the presence of anhydrite (CaSO_4), as well as calcite (CaCO_3) after the sequential extraction of the carbonate fraction.

The sorption experiments that were performed using topsoil under three different conditions for the binary experiments (i.e. radium spiked equilibrated water with topsoil, radium spiked demineralised water with topsoil, and radium spiked demineralised water with prewashed topsoil). The distribution ratios for radium were reported to vary between 158.3- and 180.1- mL g⁻¹ suggesting that radium is not mobile under these conditions.

Radium mobility was conducted by using column experiments in an effort to duplicate the environmental conditions of the Needle's Eye site. Therefore, topsoil was used in a column and radium spiked equilibrated water was passed through the column. In the analysis of the effluent fractions coming out of the column, radium was not detected and therefore it was concluded that radium is not mobile under these conditions.

Table of Contents

Acknowledgments.....	5
Abstract.....	9
Abbreviations.....	15
Chapter 1. Introduction	18
1.1 The Lo-RISE Project	18
1.2 Radium.....	18
1.2.1 Radium Chemistry.....	19
1.2.2 Radium Isotopes	19
1.2.3 Radium in the Environment	21
1.2.4 Radium Aqueous Speciation	39
1.2.5 Radium Absorption - Desorption	40
1.3 The measurement of radium by gamma spectrometry	41
1.3.1 Gamma Spectrometry Instrumentation	42
1.3.2 Use of gamma spectrometry to measure radium in environmental samples ..	44
1.3.3 The use of gamma spectrometry to measure known activities of a ²²⁶ Ra standard.....	46
1.4 The Needle's Eye Site	46
1.4.1 Geology of study area.....	47
1.5 Aims and Objectives.....	56
Chapter 2. Experimental work	58
2.1 Research Planning	58
2.2 Sampling.....	58
2.2.1 First sampling visit	58
2.2.2 Second and third sampling visits.....	60
2.3 Soil Sample Preparation	63
2.4 Analyses of the soil samples.....	65
2.4.1 Gamma spectrometry	65
2.4.2 pH Determination	82
2.4.3 X-Ray Diffraction.....	82
2.4.4 Elemental Analyses	86
2.5 Loss on Ignition (LoI).....	93

2.6 Soil Texture Analysis	95
2.7 Scanning Electron Microscopy / Energy Dispersive X-ray spectroscopy (SEM/EDX)	99
2.8 Liquid Scintillation Counting (LSC)	102
2.9 UV/visible spectroscopy – Absorbance spectroscopy	102
2.9.1 General information	102
2.9.2 Calibration of UV/visible spectrophotometer	104
2.10 Binary Experiments	107
2.10.1 ²²⁶ Ra spiked equilibrated water (eqH ₂ O) - NE4 _T	107
2.10.2 ²²⁶ Ra spiked demineralised water (dH ₂ O) - NE4 _T	108
2.10.3 ²²⁶ Ra spiked demineralised water (dH ₂ O) - NE4 _T	109
2.11 Column Experiments	110
2.12 Sequential Extractions	111
2.12.1 Sequential extraction introduction.....	111
2.12.2 Methodology	113
2.12.2.1 F1 – Exchangeable Fraction	113
2.12.2.2 F2 – Bound to Carbonates Fraction.....	113
2.12.2.3 F3 - Bound to Iron and Manganese Oxides Fraction	113
2.12.2.4 F4 - Bound to Organic Matter Fraction.....	114
2.12.2.5 F5 – Residual.....	114
2.13 Non – sequential extraction	114
2.14 Topsoil	115
2.14.1 Introduction – Why study topsoil?	115
2.14.2 Needle’s Eye topsoil.....	117
2.14.3 NOM characterisation of NE4 _T	117
2.15.4 Preparation of NE4 _T bulk sample.....	118
Chapter 3. Results and Discussion.....	120
3.1 Results of the analyses of the samples from the first visit to Needle’s Eye	120
3.1.1 Soil Particle Size and Physicochemical Characterisation	120
3.1.2 Gamma Spectrometry Analysis.....	121
3.2 Results from the Second Visit on the Site	124
3.2.1 Gamma Spectrometry Analysis.....	124
3.2.2 Elemental Composition	126

3.2.3 Physicochemical Characterisation.....	126
3.2.4 Mineralogical Analyses.....	128
3.3 Results from the Third Visit on the Site.....	134
3.3.1 Gamma Spectrometry Analysis.....	134
3.3.2 Physicochemical Characterisation.....	136
3.3.3 Elemental Analysis.....	137
3.3.4 Mineralogical Analyses.....	139
3.3.5 Results for Needle’s Eye NE4 topsoil (NE4 _T).....	140
3.3.5.1 Initial γ spectrometry analyses.....	140
3.3.5.2 γ spectrometry and LoI analysis of NE4 _T samples.....	140
3.3.5.3 Non – sequential extractions.....	142
3.3.5.3.1 0.1M NaOH extractions.....	142
3.3.5.3.2 0.1M HNO ₃ extractions.....	143
3.3.5.3.3 dH ₂ O extractions.....	145
3.3.5.4 Sequential extraction analysis on NE4 _T and NE4-b1.....	148
3.3.5.4.1 Sequential Extractions on deeper soil (NE4-b1).....	161
3.3.5.5 Elemental and mineralogical analysis of topsoil and deeper soil.....	169
3.3.5.5.2 Mineralogical Analysis.....	172
3.3.5.6.1 Sorption Experiments.....	183
3.3.5.6.2 ²²⁶ Ra mobility through top soil in column experiments.....	189
Chapter 4. Conclusions.....	194
Chapter 5. Further Work.....	197
5.1 ²³⁸ U/ ²²⁶ Ra Equilibrium – Disequilibrium.....	197
5.2 Binary – Ternary systems.....	197
Bibliography.....	198

Abbreviations

α	Alpha
β	Beta
γ	Gamma
μ	Micro-
σ	Standard Deviation
AC	Available Carbon
AOD	Above Ordnance Datum
AMD	Acid Mine Drainage
ARD	Acid Rock Drainage
BGS	British Geological Survey
Bq	Becquerel
BSEM	Back Scattered Electron Microscopy
$^{\circ}\text{C}$	Celsius Degrees
CE	Counting Efficiency
CoRWM	Committee on Radioactive Waste Management
eV	Electron volt
FA	Fulvic Acid
FWHM	Full Width Half Maximum
G	Grams
H	Hours
HA	Humic Acid
HPGe	High Purity Germanium
HV	High Voltage
IAEA	International Atomic Energy Agency
ICDD	International Centre for Diffraction Data
ICP - MS	Inductively Coupled Plasma Mass Spectrometry
ICP - OES	Inductively Coupled Plasma Optical Emission Spectroscopy

GDF	Geological Disposal Facilities
GPS	Global Positioning System
k	Kilo-
L	Litre
LOD	Limit of Detection
LoI	Loss on Ignition
Lo-RISE	long-lived radionuclides in the surface environment
m	Meter or Milli-
M	Mega- or Molar
MCA	Multi – Channel Analyser
MDA	Minimum Detectable Activity
n	Nano-
NDA	Nuclear Decommissioning Authorities
NOM	Natural Organic Matter
NORM	Naturally Occurring Radioactive Material
pH	Potential of Hydrogen
PZC	Point of Zero Charge
RATE	Radioisotopes and the Environment
REE	Rare – Earth Element
s	Seconds
SEM	Scanning Electron Microscopy
SGD	Submarine Groundwater Discharge
SOP	Standard Operating Procedure
TOC	Total Organic Carbon
UK	United Kingdom
UN	United Nations
XRD	X-ray diffraction
Y	Years

Chapter One: Introduction

Chapter 1. Introduction

1.1 The Lo-RISE Project

The research described in this thesis was funded by Loughborough University and was conducted as part of a wider project called Lo-RISE (Long - lived Radionuclides in the Surface Environment). The Lo-RISE project forms part of the Radioactivity in the Environment (RATE) research program sponsored by Natural Environment Research Council (NERC).

The principal focus of the Lo-RISE research program is to outline the key chemical, biological and physical processes that govern radionuclide mobility through the environment (from soil and sediment to biota) at three natural analogue sites (South Terras, Needle's Eye and Ravenglass). The research reported in this thesis concentrates on radium movement at Needle's Eye only.

1.2 Radium

One of the first elements discovered by means of its radioactive properties was radium, and thus it is strongly associated with the discovery of radioactivity. Henri Becquerel found that uranium salts continuously emit photons that are not the same as ordinary light, subsequent to the discovery of X - rays by Wilhelm Conrad Rontgen (1895). This property of matter consisting of the emission of rays was named radioactivity. Furthermore, the research of Marie and Pierre Curie showed that both uranium and thorium are highly radioactive².

Many minerals were found to have greater radioactivity levels than the oxides of thorium and uranium, suggesting that these materials may contain a new element with an activity concentration (radioactivity per mass) greater than that of uranium and thorium. The discovery of polonium and radium extracted from a pitchblende ore in 1898 verified this statement².

1.2.1 Radium Chemistry

Radium is an alkaline earth metal and has an atomic number of 88 ($Z = 88$). Radium has similar chemical characteristics to those of the other alkaline – earths and all elements from this group are present in nature as divalent cations².

There are various trends observed when descending the alkaline earth group including increasing ionic radius with atomic number. The behaviour of radium is assumed to be similar to that of barium due to their similar ionic radii (radium: 1.48 – 1.7 and barium: 1.35 – 1.61)². Therefore, where radium data are not available, barium has often been used as a chemical analogue for predicting radium behaviour.

1.2.2 Radium Isotopes

Radium has no stable isotopes. In the environment, there are four naturally occurring radioactive isotopes of radium (Table 1) and they are formed from the decay series of primordial radionuclides as is shown in Figure 1².

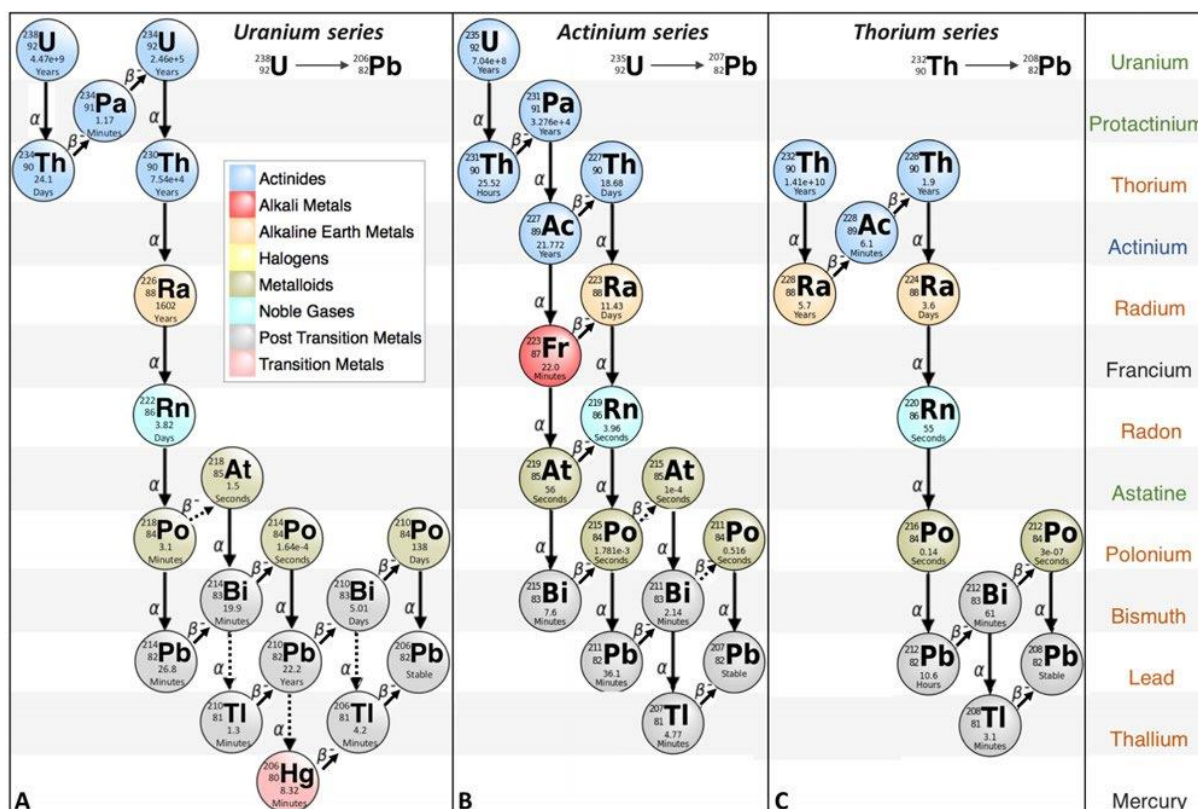


Figure 1. Radionuclides decay series³

^{226}Ra is part of the ^{238}U series, ^{223}Ra is part of the ^{235}U series and ^{224}Ra and ^{228}Ra are part of the ^{232}Th series. The only anthropogenic isotope of radium that has a significant half-life ($t_{1/2}$) is ^{225}Ra ($t_{1/2} = 14.9$ days) part of the ^{237}Np series, where the direct parent is ^{229}Th ($t_{1/2} = 7880$ years). ^{225}Ra has been used as a yield tracer for the study of radium chemistry and as the subject of nuclear physics studies⁴.

Table 1. Radium Isotopes and their half – lives²

Isotope	Half-Life	Decay Constant	Activity concentration (Bq kg ⁻¹)
^{223}Ra	11.43 days	22.15 years	1.896×10^{15}
^{224}Ra	3.632 days	69.7 years	5.92×10^{15}
^{226}Ra	1600 years	4.33×10^{-4} years	3.66
^{228}Ra	5.75 years	0.12 years	1.0×10^{13}

The concentration of each isotope in a decay series is controlled by the concentration of the parent, in addition to the time since fractionation between the isotope and its parent. In the case of sealed samples over long timescales, if the activity of each isotope (the decay rate) is negligible in comparison to that of its parent, the quantity of a radioactive isotope remains constant because its production rate (e.g. due to decay of a parent isotope) is equal to its decay rate when secular equilibrium is achieved².

Secular equilibrium is achieved when the half-life of the parent is much greater than that of the daughter and this behaviour is described by Equation 1:

$$\frac{N_A}{N_B} = \frac{\lambda_B}{\lambda_A} \quad \text{Equation 1}$$

Where,

N_A = number of atoms of the parent,

N_B = number of atoms of the daughter,

λ_A = decay constant of the parent,

λ_B = decay constant of the daughter,

Each radium isotope produces a chain of short-lived daughters that contribute to the overall activity. For ^{223}Ra and ^{224}Ra , the daughter isotopes all have short half - lives, and so will rapidly grow into secular equilibrium with the parent Ra isotope (Figure 2)⁵.

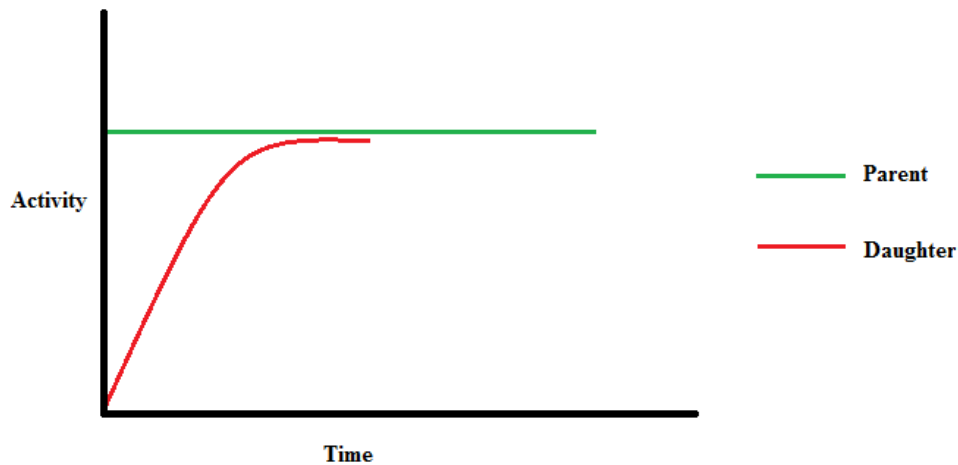


Figure 2. Secular equilibrium¹

For ^{226}Ra , the immediate decay product is the noble gas ^{222}Rn (Figure 1), which may be readily lost prior to its decay from non - retentive materials. Radon may not escape before its decay, usually when trapped in minerals or large organisms, and thus, will generate a chain of short - lived daughter nuclides. In conclusion, the impact of the ^{226}Ra and ^{228}Ra and their daughters may depend upon the retention of ^{222}Rn and the time of separation from ^{210}Pb and ^{210}Po ^{4,6}.

1.2.3 Radium in the Environment

The Earth's crust consists of a variety of igneous (e.g. granodiorite, granite), sedimentary, and metamorphic rocks, 95 % migmatites (which is a rock composed of two combined but distinguishable components, typically a granitic rock within a metamorphic host rock (Figure 3)².



Figure 3. Ordinary granite: K-feldspar (pink), quartz (grey), and biotite (black)⁷

Concentrations of naturally occurring radionuclides in igneous rocks were found to be higher compared to sedimentary rocks, with the exceptions of shale, deep - sea sediments and phosphate rocks, while metamorphic rocks have concentrations similar to those of the rocks from which they were derived. Uranium concentrations were found to be relatively higher in igneous rocks rich in silica (e.g. granodiorite from Needle's Eye site), compared to low silica igneous rocks (e.g. basalt)^{2,8}.

The activity concentration of ^{238}U in the continental crust is 32.9 Bq kg^{-1} , and by assuming secular equilibrium of $^{238}\text{U}/^{226}\text{Ra}$, then the ^{226}Ra activity in crystals is expected to be of an equivalent order. It is expected that radium isotopes are present in equilibrium order, with their precursors, in most igneous rocks. The ratios of ^{226}Ra or ^{228}Ra and their precursors, i.e. ^{230}Th and ^{232}Th , may be changed due to the impact factors, such as weathering, which may result to their different mobility². These phenomena and distribution of radium in different environments is discussed in *Sections 1.3.3.1 and 1.3.3.5*.

1.2.3.1 Radium in Soils

Soil properties, including concentrations of naturally occurring radionuclides in the soil, depend on properties of the parent rock. Rocks are continuously affected by environmental factors that contribute to soil formation, such as changes in temperature, water, flora and fauna. The ion exchange capacity of different soil types varies considerably with absolute composition

such as mineral phases which has a considerable influence on the distribution of radium in soil by interaction with either organic or mineral phases. Quantities of radium by concentration and activity for different types of soil are given in Table 2².

Table 2 shows ²²⁶Ra concentrations in soil in normal areas (i.e. not areas of high natural background) vary from 3.7 to 126 Bq kg⁻¹. The largest values were found to be in light brown desert soil. The lowest value was found in lime (3.7 Bq kg⁻¹), while intermediate values vary within a narrow range (20 - 40 Bq kg⁻¹) with the soil composition/texture (by means of soil particle size).

Table 2. ²²⁶Ra Concentrations in soils²

Landscape	Texture of Soil	Location	²²⁶ Ra (Bq kg ⁻¹)
Tundra	Not available	Russia	140 ± 20
Taiga	Loam	Russia	280 ± 70
Mixed forest	Loam	Russia	30 ± 3.7
Mixed forest	Loam	Russia	28.1 ± 0.7
Mixed forest	Clay	Russia	37 ± 4
Deciduous forest	Loam	Russia	17 - 33
Meadows steppe	Clay, heavy loam	Russia	30.7 ± 2.5
Wet subtropics	Clay	Florida, USA	7.4
Desert	Not available	USSR	70.3 – 126
Atlantic maritime	Sandy loam	Canada	30
Mixed wood plants	Sandy loam	Canada	20
Boreal shield	Sandy loam	Canada	20
Mixed wood plants	Sandy loam	Canada	30
Boreal shield	Clay loam	Canada	30

The average global value for ²²⁶Ra in soil is 32 Bq kg⁻¹ based on values from the United Nations (UN). There are some areas in the world where average concentration of naturally occurring radionuclides in soils or waters exceeds this average value by a considerable amount. These

areas include the well - known sites of Kerala and Tamil Nadu in southern India, with sands containing monazite with a high thorium content, and Ramsar in the Islamic republic of Iran (Iran) where high levels of ^{226}Ra in water have been identified^{2,9-11}.

1.2.3.2 Radium sorption in soils

Sorption is defined as a physical and chemical phenomenon by which one substance becomes attached to another through several different processes including ion exchange and surface physisorption. Radium can interact with both clays and mineral oxides present in soils in this way, especially at near neutral and alkaline pH conditions. For most natural waters, radium will be present primarily as the un-complexed Ra^{2+} cation. Sorption studies generally confirm the adsorption behaviour expected for Ra^{2+} as a function of pH, with negligible adsorption at very acidic pH values and increasing adsorption with increasing pH. The pH range at which adsorption of cations begins to increase on mineral surfaces depends on the values of the point of zero charge (PZC) for each type of mineral, when the electrical charge density on a surface is zero. In general, at pH values of less than the PZC, the mineral surface has a net positive charge and strongly adsorbs anions. At pH values, greater than the PZC, the surface strongly adsorbs dissolved cations. Radium competes with the other alkaline earth cations for ion exchange sites. In comparison to other alkaline earth elements, the relative affinity of this group of elements for ion exchange is in theory: $\text{Ra}^{2+} < \text{Ba}^{2+} < \text{Sr}^{2+} < \text{Ca}^{2+} < \text{Mg}^{2+}$. It should be noted that ion exchange and sorption do not describe the same phenomenon. Ion exchange depends on size of site into which an ion is placed, whereas sorption is the process in which one substance takes up or holds onto another (adsorption or absorption). While absorption is the process in which a fluid is dissolved by a liquid or a solid, adsorption describes the process where atoms, ions or molecules from a substance (i.e. gas, liquid or dissolved solid) adhere to a surface of the adsorbent. The adsorption of radium has been shown to be strongly dependent on ionic strength and concentrations of other competing ions with adsorption of radium decreasing with increasing ionic strength^{2,12}.

The processes of advection and diffusion are opposed by a number of retardation processes. While ligands can aid the dissolution and solubility of radionuclides, it is also possible for the ligated radionuclides that are mobile in the environment to interact with the charged surface of minerals or soils. This, therefore, could result in the retention of the complex at the surface and

a reduction in migratory radionuclides. Sorption at a mineral interface will be strongly affected by the geochemical conditions in a given environment. Ionic strength and pH can both affect how much radionuclide the mineral surface can retard. Also, the presence of various organic and inorganic ligands can also have an effect on sorption^{2,13}.

Adsorption constants vary strongly with the composition of the solution (e.g. pH and other cations), temperature, surface characteristics and degree of alteration. The examples of mineral phases and NOM (natural organic matter), as discussed below, are of interest when considering radium behaviour in the environment. Moreover, site specific values can be accurately determined with the consideration of mineralogy, the water chemistry and competing ions, the surface chemistry, the availability of active surfaces and variations in site conditions².

Ion exchange can be described as a reversible interchange of one kind of ion present in an insoluble solid with another of like charge present in a solution surrounding the solid.¹⁴ Materials capable of ion exchange are used for softening or demineralising water, the purification of chemicals and the separation of substances. This process is important when considering radionuclide retention in a given environment. Ion exchange is highly dependent on the ionic strength of the surface water, and to a lesser extent on pH.²

The cation exchange capacity (CEC) of a mineral describes the ability of a material to exchange cations with the surface water (surrounding solution) and this property varies considerably between minerals. These reactions are usually fast, reversible, stoichiometric (in terms of charge) and usually favour one ion over another depending on the size, charge of the ion and its level of hydration.² Some examples of minerals that undergo ion exchange are, in order of likelihood: montmorillonite $((\text{Na,Ca})_{0.33}(\text{Al,Mg})_2(\text{Si}_4\text{O}_{10})(\text{OH})_2 \cdot n\text{H}_2\text{O})$ and illite $((\text{K,H}_3\text{O})(\text{Al,Mg,Fe})_2(\text{Si,Al})_4\text{O}_{10}[(\text{OH})_2,(\text{H}_2\text{O})])$. Materials with no exchangeable cations such as pyrophyllite $(\text{Al}_2\text{Si}_4\text{O}_{10}(\text{OH})_2)$ and kaolinite $(\text{Al}_2\text{Si}_2\text{O}_5(\text{OH})_4)$, etc. (Figure 4) cannot facilitate ion exchange and interactions with ions in solution is through weak electrostatic interactions/surface absorption^{2,15,16}.

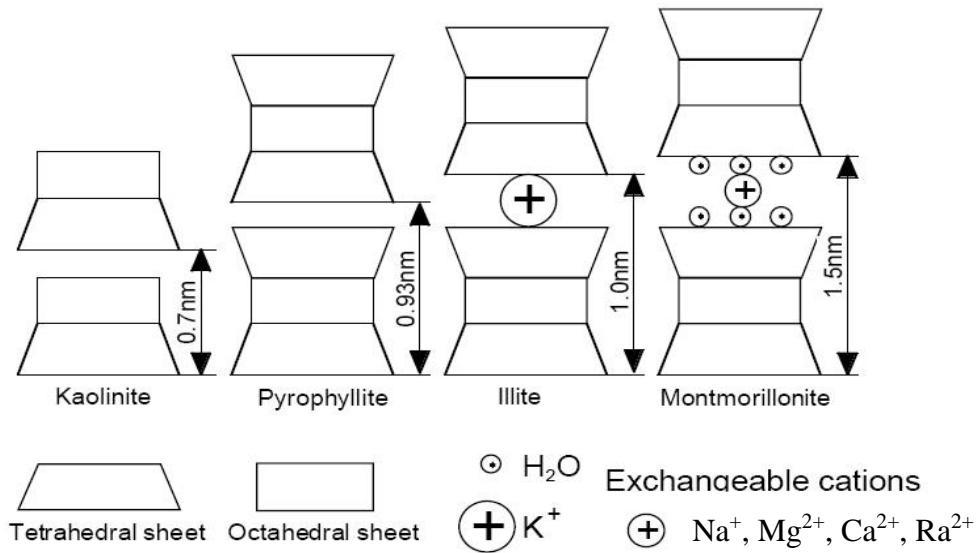


Figure 4. Examples of minerals with/without exchangeable cations

Muscovite is a phyllosilicate mineral of aluminium and potassium with general formula $(KAl_2(AlSi_3O_{10})(F,OH)_2)$ (Figure 5). It can be found in igneous rocks (e.g. granite) and is one of the most common micas. Muscovite can be found in nature as crystalline material or in flaky grains in rocks. Ames¹³ et al., reported sorption of uranium and radium on muscovite, from Stoneham (USA).

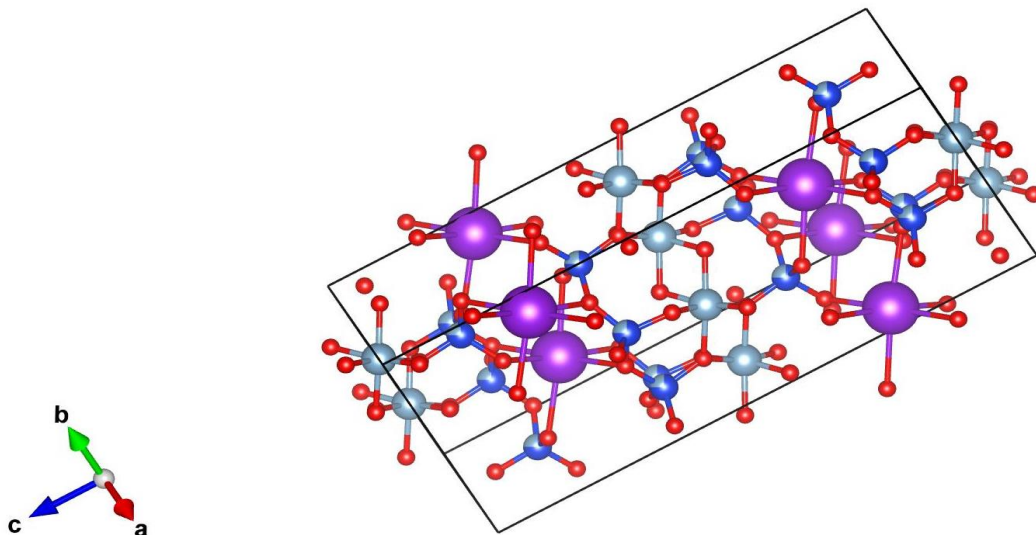


Figure 5. Muscovite structure with general formula $(KAl_2(AlSi_3O_{10})(F,OH)_2)$, potassium (purple spheres), aluminium (grey spheres), silicon (blue spheres), and oxygen (red spheres)¹⁷

Montmorillonite is a mineral from a very soft group of phyllosilicates (from the Greek φύλλο *phyllo* meaning leaf or sheet) which consist of parallel sheets of silicate tetrahedra with the formula Si_2O_5 . These materials have the general formula $(\text{M}_1, \text{M}_2)_{0.33}(\text{Al}, \text{Mg})_2(\text{Si}_4\text{O}_{10})(\text{OH})_2 \cdot n(\text{H}_2\text{O})$, where M_1 is a monovalent and M_2 is a divalent cation, which form from the weathering of silicate rocks (e.g. chlorite) (Figure 6).^{18,19} The structure of montmorillonite consists of aluminosilicate layers with exchangeable cations between the layers. In 2009, Shao^{2,20} et al., investigated the competitive effect of radium transport in the near - field of a low and intermediate level nuclear waste repository in the presence of different species. A geochemical model of numerical simulations showed that radium can not only substitute for both barium and strontium in the corresponding simple sulfates (BaSO_4 , SrSO_4) but also the exchangeable cations between the layers in montmorillonite².

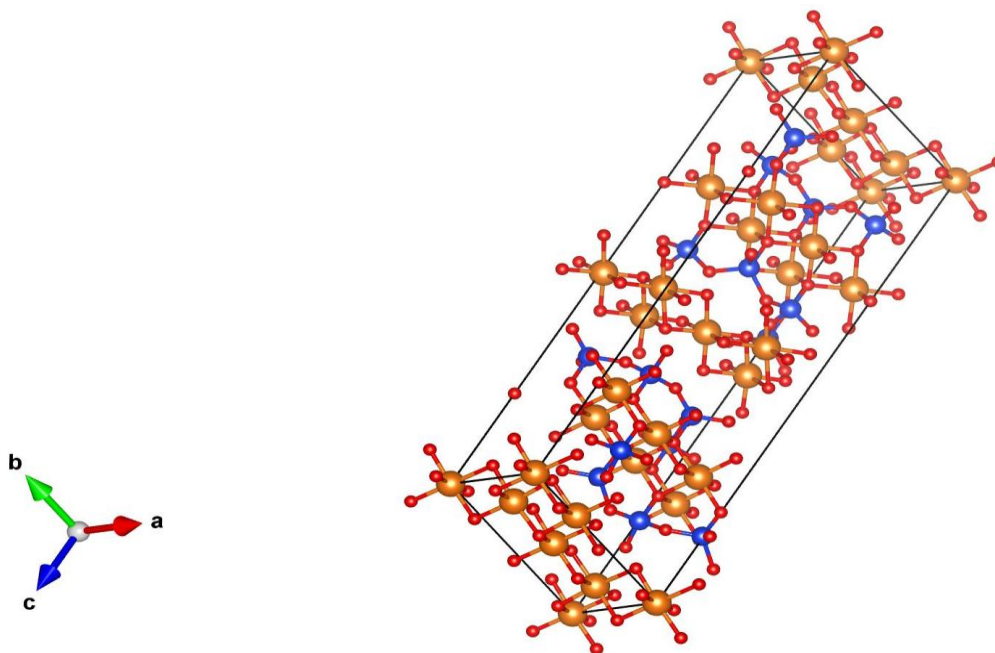


Figure 6. The chlorite structure with general formula $(\text{Mg}, \text{Fe})_3(\text{Si}, \text{Al})_4\text{O}_{10}$, blue spheres represent Si/Al tetrahedral and octahedral Fe/Mg species shown as orange spheres²¹

Biotite belongs to the mica group and is a common phyllosilicate mineral (Figure 7). It can be found in nature usually in black colour and is a decay product of igneous (i.e. granodiorite) and metamorphic (i.e. gneiss) rocks. Biotite has a general chemical formula $\text{K}(\text{Mg}, \text{Fe})_{2-3}\text{Al}_2\text{Si}_2\text{O}_{10}(\text{OH}, \text{F})_2$, where magnesium, oxygen, hydrogen, iron, aluminium and silicon weakly bounded sheets together with potassium ions^{22,23}. Finally, biotite has weak resistance to weathering and it can be transformed into clay minerals. Radium was found to be associated

with biotite in Finnish granites, and furthermore, the total amount of radium increases as the volume of biotite increases in the granitic rock²⁴.

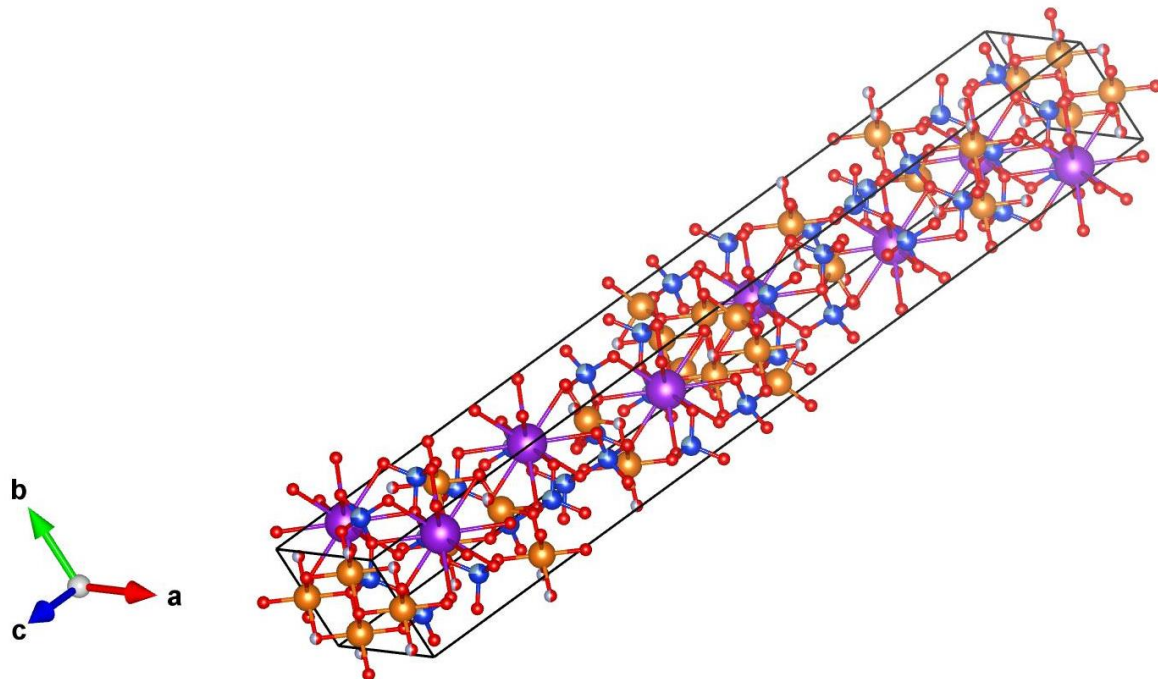


Figure 7. The biotite structure with formula $K(Mg,Fe)_{2-3}Al_2Si_2O_{10}(OH,F)_2$, purple spheres represent potassium, orange spheres represent magnesium, dark blue spheres represent silicon, light blue spheres represent aluminium, red spheres represent oxygen, and grey spheres represent fluorine²⁵

Feldspar is defined as an abundant rock - forming mineral typically occurring as colourless or pale with general chemical formula $M(SiAl)_4O_8$ (Figure 8) and can be found in the group of rock forming tectosilicate minerals (or “framework minerals” that have a three – dimensional framework of silicate tetrahedra with SiO_2 or 1:2 ratio) that make up about 41% of the Earths’ continental crust by weight^{26,27}. Feldspars are a result of magma crystallisation and veins that can be found in both intrusive and extrusive igneous rocks. Feldspar can also be present in metamorphic and sedimentary rocks in all parts of the world. Common feldspars include: orthoclase ($KAlSi_3O_8$), albite ($NaAlSi_3O_8$), anorthite ($CaAl_2Si_2O_8$), amazonite $K(AlSi_3O_8)$, andesine ($(Na,Ca)[Al(Si,Al)Si_2O_8]$), as a result of Al – Si ratio variation. Feldspars can be divided into two compositional series: the alkali feldspars and the plagioclase feldspars. The alkali feldspars have chemical compositions that form a solid solution mainly between the two end member compositions orthoclase ($KAlSi_3O_8$) and albite ($NaAlSi_3O_8$). The plagioclase feldspars have chemical compositions that form a solid solution mainly between the two end member compositions albite ($NaAlSi_3O_8$) and anorthite ($CaAl_2Si_2O_8$). Most natural feldspars

have been reported to contain negligible amounts of other components. The major third component for alkali feldspars is anorthite ($\text{CaAl}_2\text{Si}_2\text{O}_8$) and for plagioclase feldspars is orthoclase (KAlSi_3O_8)^{28,29}.

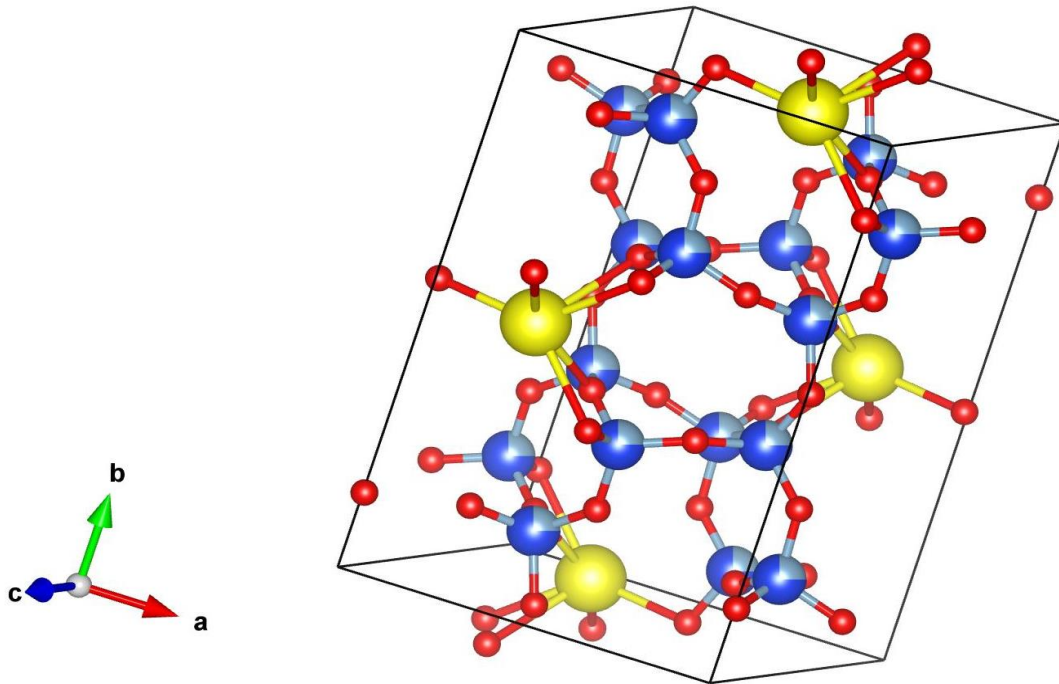


Figure 8. Albite structure containing sodium (dark grey), aluminium (light grey), silicon (blue), oxygen (red)³⁰

Quartz is a mineral composed of silicon and oxygen atoms in a continuous framework of silicon oxygen tetrahedra, and each oxygen is being shared between two tetrahedra, giving an overall chemical formula of SiO_2 (Figure 9)³¹. Crystals of quartz are chiral and exist in two forms: the normal α -quartz and the high-temperature β -quartz. Transformation from alpha to beta quartz takes place at 573 °C.^{31,32} This transformation results in a significant change of volume. Quartz is the second most abundant mineral in Earth's continental crust after feldspar. Benes¹⁶ et al., reported experiments on radium absorption on quartz, which was easily adsorbed at pH 7.37 and the distribution coefficient (K_d) reported about $2 \times 10^3 \text{ mL g}^{-1}$.

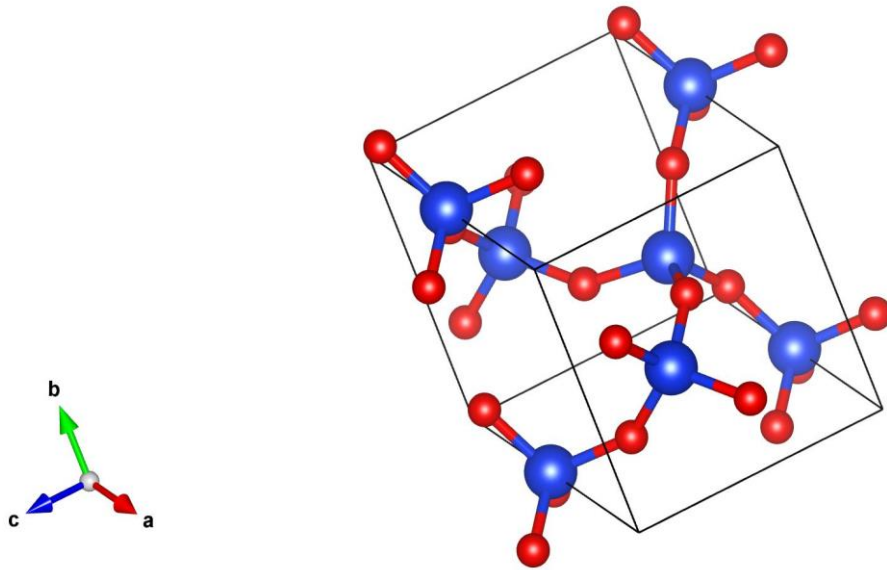


Figure 9. α -Quartz structure containing silicon (blue) and oxygen (red)³³

It was reported that the effect of pH (< 7) along with concentrations of suspended sediments less than 100 mg L^{-1} quartz and ferric hydroxide have no effect on radium migration. Furthermore, when radium adsorbs on quartz it can be desorbed using dilute solutions of sodium chloride (NaCl) or hydrochloric acid (HCl)³¹.

Natural Organic Matter (NOM), consists of carbon containing compounds which can be found in natural and manmade terrestrial and aquatic environments (Figure 10)³⁴⁻³⁶. NOM is composed of organic compounds that are derived from the remains of plants, animals and their waste products in the environment³⁴⁻³⁶. Chemical reactions that do not involve life can also produce organic molecules. Basic NOM structures can be created from cellulose, tannin, cutin and lignin along with other various proteins, lipids and carbohydrates.³⁴⁻³⁶ Only a few studies have been conducted on the adsorption of radium on natural organic matter.² Nathwani and Phillips³⁷ investigated the absorption of ^{226}Ra by using batch equilibration experiments to different soils by means of their physicochemical characteristics. The absorption of ^{226}Ra was investigated by batch experiments of varying activities of ^{226}Ra ($40 \times 10^3 - 2 \times 10^6 \text{ Bq kg}^{-1}$), by the use of the Freundlich adsorption isotherms. The soil was characterised by a strong presence of clay minerals, as well as, organic matter which contributed to the adsorption of ^{226}Ra ⁴². Ion exchange capacity may affect the adsorption affinity of the organic matter and clays. Finally, by the use of selective chemical extraction separations radium was found in significant concentrations in the organic (humic) matter fraction³⁸.

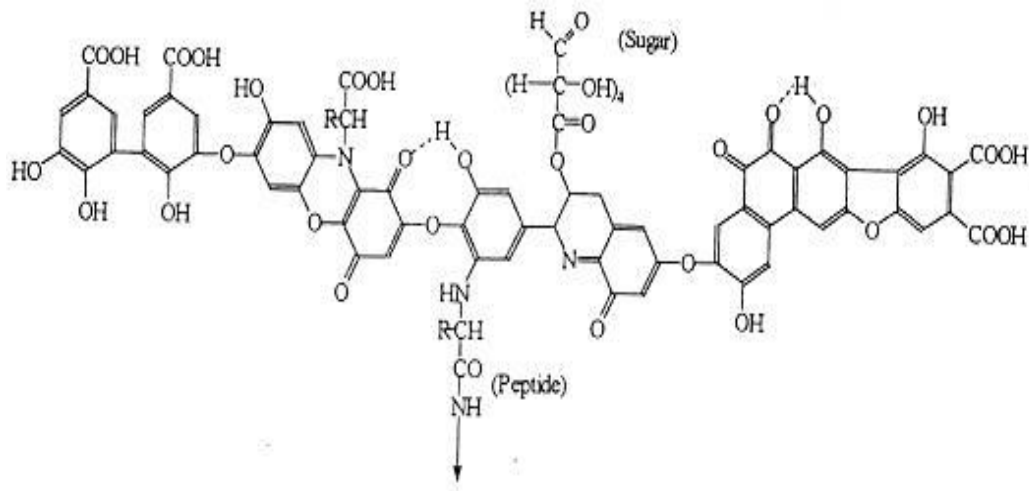


Figure 10. Proposed structure of humic acid³⁹

Radium can be removed from waters by co-precipitation of phases in which radium can form a solid solution. In natural waters, barium is present in molar concentrations which can be 100 times greater compared to those of radium. When moderate amounts of sulfate and barium concentrations are present radium can be controlled by the precipitation of barite, BaSO₄, since typical barium concentrations are near saturation levels. Radium can be incorporated in solid solution by barite, as (Ba, Ra)SO₄. This radium incorporation can be described by a partition coefficient (λ' , Equation 2) which can be defined as the ratio of radium over barium in the solution and can be compared to that measured in the surface of minerals in contact with the solution²:

$$\lambda' = \frac{\left(\frac{[Ra]}{[Ba]}\right)_{surface}}{\left(\frac{[Ra]}{[Ba]}\right)_{solution}} \quad \text{Equation 2}$$

Values for λ' from 1.21 to 1.8 have been reported by Doerner and Hoskins⁴⁰ showed that radium is potentially immobile. Kinetic effects may be responsible when this empirical relationship is affected and may deviate from a thermodynamic equilibrium constant which is calculated from free ion activities. Bosbach⁴¹ et al. investigated experimentally the incorporation of radium by barite from solution through recrystallisation. It was reported that the solubility of radium, in a range of natural waters, may be controlled by the precipitation of

(Ba, Ra)SO₄. Langmuir and Melchior⁴² reported that radium may be controlled by the coprecipitation of trace amounts of radium in celestite (SrSO₄), as well as, in barite (BaSO₄) in some deep brines from north Texas.

Partition coefficient (λ') values of 0.32 ± 0.15 were measured for radium in gypsum (CaSO₄·2H₂O), which were significantly lower than for radium in barite (BaSO₄). The lower solubility reflects the much greater difference between radium / calcium, and radium / barium in terms of the size of their ionic radii⁴³.

Andrews⁴⁴ et al., suggested that carbonate minerals control radium activity in groundwaters circulating within the Stripa granite. The Stripa mine, located in south-central Sweden, is an inactive iron mine which drew its ore from hematite (Fe₂O₃)-rich zones in leptite, an obsolete term for a fine-grained gneissose to granulose metamorphic rock of sedimentary origin mainly composed of feldspar and quartz with subordinate mafic minerals^{45,46}. This leptite was intruded by a medium-grained granite in which a considerable part of the mine accessways are located, and the granitic rock intruded by monzonite (an igneous rock, rich in plagioclases and alkali feldspars). The carbonate mineral saturations and the observed correlation between ²²⁶Ra and calcium were investigated by Schmidt and Cochran⁴⁷ for the suitability of radium and radium daughters in the dating of carbonates. Freshly precipitated carbonates uniformly showed excesses of ²²⁶Ra relative to its parent ²³⁰Th, and ²²⁶Ra decay can provide ages of carbonates over Holocene time scales. Dissolved radium (0.1 – 1 nM), as well as its chemical analogue barium, were reported to exchange with calcite (CaCO₃), dolomite (Ca,Mg(CaCO₃)₂), strontianite (SrCO₃), rhodochrosite (MnCO₃), ankerite (Ca(Fe,Mg,Mn)(CO₃)₂) and witherite (BaCO₃). Uptake has shown to increase with increasing radium concentration in these materials suggesting a coprecipitation reaction. However, in siderite (FeCO₃), magnesite (MgCO₃), and ankerite (Ca(Fe,Mg,Mn)(CO₃)₂) behaviour was observed which suggested simple sorption (with decreasing uptake as radium concentration increases, or with no dependence on radium concentration)⁴⁸.

High concentrations of iron sulfate, low calcium concentrations and low ionic forces in solution reduce the mobility of radium and favour its absorption in soils. Radium forms water soluble chloride, bromide, and nitrate salts.⁴⁹ The phosphate (PO₄³⁻), carbonate (CO₃²⁻), selenate (SeO₄²⁻), fluoride (F⁻), and oxalate (C₂O₄²⁻) salts of radium are sparingly soluble in water and radium sulfate is described as insoluble in water. The solubility product for RaSO₄, the

presumed chemical form of radium in sulfuric acid-leached tailings, corresponds to a radium concentration of $1.5 \times 10^{-3} \text{ g L}^{-1}$ of pure water, and of $4.6 \times 10^{-6} \text{ g L}^{-1}$ of water containing 200 ppm sulfate. The hydrated ion of radium is the smallest in the alkaline earth series and therefore, it would tend to be retained by the ion exchange series. In alkaline solutions, anionic complexes of radium with organic ligands, such as EDTA (ethylenediamine tetraacetic acid) and citric acid, are known to occur. Radium compounds have low solubility in organic solvents and can coprecipitate with calcium carbonate (CaCO_3), hydrous ferric oxides (i.e. goethite $\text{FeO}(\text{OH})$), anhydrite (CaSO_4), barite (BaSO_4), celestite (SrSO_4), anglesite (PbSO_4), calcium phosphate ($\text{Ca}_3(\text{PO}_4)_2$) and aluminium phosphate (AlPO_4)⁴⁹.

Brady⁵⁰ et al., investigated the fraction of contaminants that were irreversibly sorbed by minerals. Ferrihydrite, a poorly crystalline iron oxide similar to hematite (Fe_2O_3), is a natural sink for sorbed contaminants. Contaminants may be sorbed/occluded as ferrihydrite ($(\text{Fe}^{3+})_2\text{O}_3 \cdot 0.5\text{H}_2\text{O}$) precipitates in natural waters or as it ages and transforms to more crystalline iron oxides such as goethite ($\text{FeO}(\text{OH})$) or hematite (Fe_2O_3). It was reported that barium and radium in or near the alkaline pore waters of a cement waste form or repository would be significantly retained by the transformation of ferrihydrite ($(\text{Fe}^{3+})_2\text{O}_3 \cdot 0.5\text{H}_2\text{O}$) to goethite ($\text{FeO}(\text{OH})$), though this would depend on the amount of iron present in the pore waters, its oxidation state and the presence of other sorbents⁵⁰. Benes⁵¹ et al., calculated that at pH values higher than 7, a ferric hydroxide ($\text{Fe}(\text{OH})_3$) concentration $> 6 \text{ mg L}^{-1}$ would be required to have a significant effect on radium mobility in natural waters. At alkaline pH, a smaller ferrihydrite concentration should be effective at retaining barium or radium. Radium sorption on ferric hydroxide ($\text{Fe}(\text{OH})_3$) at pH 6 and 7 was found to be reversible, while data showed that at least 75% of the added barium was occluded during ferrihydrite ($(\text{Fe}^{3+})_2\text{O}_3 \cdot 0.5\text{H}_2\text{O}$) transformation to goethite ($\text{FeO}(\text{OH})$) at pH 12. Irreversible sorption of strontium at pH 8 was not as effective as sorption at pH 12, but at least 15 % of the added strontium remained occluded after ferrihydrite ($(\text{Fe}^{3+})_2\text{O}_3 \cdot 0.5\text{H}_2\text{O}$) aging^{52,53}.

Several studies on the leachability of radium from uranium ores and mill tailings showed that radium present in uranium ore is slightly soluble in sulfuric acid (H_2SO_4), but highly soluble in hydrochloric acid (HCl) and nitric acid (HNO_3), presumably because of the higher solubility of radium chloride (RaCl_2) and radium nitrate ($\text{Ra}(\text{NO}_3)_2$) when compared to radium sulfate (RaSO_4)⁵⁴.

The dependence on pH of radium sorption to ferrihydrite ($(\text{Fe}^{3+})_2\text{O}_3 \cdot 0.5\text{H}_2\text{O}$) and goethite ($\text{FeO}(\text{OH})$) was investigated by Chen and Kocar⁵⁵. For pH values from 3 to 9, ferrihydrite ($(\text{Fe}^{3+})_2\text{O}_3 \cdot 0.5\text{H}_2\text{O}$) showed greater sorption compared to goethite ($\text{FeO}(\text{OH})$) and the extent of sorption increased with increasing pH for both iron (hydr-)oxides. Differences in the extent of radium sorption between goethite ($\text{FeO}(\text{OH})$) and ferrihydrite ($(\text{Fe}^{3+})_2\text{O}_3 \cdot 0.5\text{H}_2\text{O}$) may be explained by disparate surface areas, with ferrihydrite ($(\text{Fe}^{3+})_2\text{O}_3 \cdot 0.5\text{H}_2\text{O}$) having nearly twice the surface area of goethite ($\text{FeO}(\text{OH})$)⁵⁵.

Oxides and oxyhydroxides are responsible for about 70 % of the radium immobilisation in a uranium mill tailing environment. About half of these oxides and hydroxides can be associated with amorphous materials (mostly iron and manganese oxides and oxyhydroxides). As a function of time, the crystallisation of the amorphous material can occur, which may result in the redistribution of radium between solid and solution phases. Increased mobility of radium may affect significantly the impact of these tailings in the environment. The determination of the amount of radium released in solution during the crystallisation process of hydrous ferric oxyhydroxide, containing radium, showed that about 20 % of the initial radium present in solution is associated with amorphous hydrous ferric oxyhydroxide^{56,57}.

Radium sorption by a mixture of iron and manganese oxides in the solid phase was investigated by batch experiments. These batch experiments showed a potential for treating drinking waters with radium contamination. The capacities of the iron and manganese oxide mixture showed that radium sorption depends on parameters such as: the composition of the solid phase, the pH of the aqueous solution, and the presence of competing cations. Radium influent concentrations were reported to drop from approximately 3.7 Bq L^{-1} to $0.074 - 0.333 \text{ Bq L}^{-1}$ after the removal of radium – oxide complexes contained in the aqueous suspension with the use of green manganese sand as a filter medium⁵⁸.

Landa⁵⁹ et al., investigated ^{226}Ra release by Fe(III)-rich microbial (*Alteromonas putrefaciens*) reduction in uranium mill tailings. A direct correlation between the accumulation of dissolved ^{226}Ra and Fe(III) reduction was reported, which suggests that dissolved ^{226}Ra may be released, from mill tailings, as a result Fe(III) microbial reduction under anaerobic conditions.

1.2.3.3 Radium in Groundwater

^{226}Ra and ^{238}U concentrations may vary by three to five orders of magnitude in groundwater and depend on the availability and solubility of these radionuclides, rock permeability, and the acidity of the environment².

Human activities, including mining and exploitation, may be responsible for releasing radium and other naturally occurring radionuclides into the environment². More specifically, during *in situ* mining, well patterns are used to create a well-controlled hydro dynamical flow regime for the lixiviant (a liquid medium used in hydrometallurgy to selectively extract the desired metal from the ore or mineral)^{60,61}, thus minimising dispersion losses and the contamination of surrounding aquifers². Leaching processes, *in situ*, may result in the development of contaminated water plumes which may extend beyond the boundary of producing well fields. These phenomena have been reported in the copper and uranium mining industries. Uranium, radium, selenium, molybdenum, manganese, arsenic, nitrate and sulfate contaminants may be found in groundwater in exceeding value limits for drinking waters^{62,63}.

Radium can be found in groundwaters as a result of geothermal energy production and geothermal springs. Co-precipitation of radium with barium and calcium salts (typically carbonates and sulfates) may occur as scale during oil and gas production, usually located in the surface of drilling and production equipment⁶⁴.

1.2.3.4 Radium in non-saline water

Radium may be contained in freshwaters (non - saline waters) as a result of natural sources such as groundwater inflow, sediment resuspension, re-solubilisation of sediment bound radionuclides and from air through precipitation and particle deposition. The activity concentrations of ^{226}Ra and ^{228}Ra were reported to have a wide range, for groundwaters, due to their dependence upon the characteristics of the source in the study area, as well as the ionic strength of the groundwater. In surface waters, the activities of ^{226}Ra and ^{228}Ra were found to be low^{2,65-69}.

Activity concentrations of ^{226}Ra were found to vary mainly from 0.5×10^{-3} to $20 \times 10^{-3} \text{ Bq kg}^{-1}$ in river waters, though a few sporadic enhanced activity concentrations (of up to 0.3 Bq kg^{-1}) were reported also⁷⁰. The range of ^{228}Ra is similar to that for ^{226}Ra for river waters but generally the data are rare^{2,70}. In surface waters, such as lakes, the activity concentration of ^{226}Ra was reported to be also within a wide range of 0.5×10^{-3} to $15 \times 10^{-3} \text{ Bq kg}^{-1}$, which is similar to the concentrations reported for river waters⁷⁰. Several studies reported the distribution of ^{226}Ra in surface waters in nearby regions of containing uranium deposits. Concentrations of ^{226}Ra were reported in river waters, at the Pocos de Caldas (Brazil) uranium mining area. The activity concentrations varied within the range of 7.4×10^{-3} to 0.222 Bq kg^{-1} during the baseline study that was conducted in 1977 - 1978. The levels of ^{226}Ra were reported to be generally below $37 \times 10^{-3} \text{ Bq kg}^{-1}$ for most river-water samples, with an exception of an activity concentration of 1.1 Bq L^{-1} located within the exploratory region of small streams^{2,71}.

A recent area of concern is the use of a mixture of water, sand, and chemicals used at high pressures to release natural gas as a result of the fracture of rock formations, a procedure known as hydro-fracking. During this process, a significant volume of water is inserted into each well and then resurfaces during a few weeks of the hydro-fracking process commencing. Within this volume of water high activity concentrations of ^{226}Ra may be present (up to 620 Bq kg^{-1})⁷². Unfortunately, the poor and inadequate management of the wastewater may result in the contamination of the environment (surface and deeper) during the process of waste deposition.

Sulphides, when exposed to the open air, can be oxidised to sulphuric acid (H_2SO_4). These acidic conditions may be responsible for the acceleration of the weathering of the mining debris, as well as the dissolution and leaching process of mineral constituents, which may include radionuclides, owing to their higher solubility at lower pH values. This process is known as acid mine drainage (AMD) or acid rock drainage (ARD) and is a major global problem which has been the subject of significant scientific importance. High activity concentrations of radionuclides have been reported often during AMD/ARD. More specific, during the ARD of the uranium mining at the milling facilities of Poços de Caldas in Brazil, the concentrations of ^{238}U and ^{226}Ra were found to be 175 and 0.29 Bq kg^{-1} , respectively^{2,71}.

Furthermore, human activity can also enhance the radium movement cycle from groundwater through surface water and into sediments. Wastewater from coalmines has contributed to the release of significant amounts of ^{226}Ra into the environment. During this process, the

wastewater located within the mine, or after it is being transferred to the surface environment, may contain Ra^{2+} and Ba^{2+} mixed with natural water which contains SO_4^{2-} ions, and thus radium may co-precipitate as RaSO_4 or BaSO_4 , as well as the solid solution which contains both species (see *Section 1.3.5*). The activity of RaSO_4 and BaSO_4 was reported to be significantly high (i.e. $10 \times 10^5 \text{ Bq kg}^{-1}$). This type of sediment can be found inside mines and on the benthos of the deposition banks and ponds and their outlet canals^{2,71}.

The release of naturally occurring radioactive material (NORM) to the environment can also be affected by mineral and metal processing activities. NORM may be released during the separation of valuable mineral bearing radionuclides from sands and sediments, with the use of large volumes of water, through physical separation in the tin slag process. Although the process may be used effectively during the separation, the waste water deposited in ponds may contain NORM that accumulates thereby affecting the surrounding environment of the processing industry^{2,73}.

1.2.3.5 Radium in Seawater

In the oceanic waters, the main processes that affect the distribution of the long - lived radium isotopes include the supply from continents, the removal by radioactive decay and, the particle scavenging. ^{226}Ra can be distributed throughout the water column. Significant variations in radium concentrations may occur within the oceans (Table 3)⁵⁶.

Significant amounts of radium can be found in estuaries and coastal waters because of contributions from rivers, sediments and submarine groundwater discharges (SGD). The locations where SGD reaches the oceanic body are of significant importance due to the high marine concentrations that are reported. In general, ^{226}Ra in estuaries is enriched by over an order of magnitude relative to the surface ocean; the other isotopes are generally enriched even more^{2,74,82,83,75,75-81}.

Table 3. ^{226}Ra distribution in the oceans

Water body	^{226}Ra (Bq kg ⁻¹)
Atlantic Ocean*	$0.135 \times 10^{-3} \pm 0.014 \times 10^{-3}$
Indian Ocean*	$0.147 \times 10^{-3} \pm 0.029 \times 10^{-3}$
Pacific Ocean*	$0.122 \times 10^{-3} \pm 0.024 \times 10^{-3}$
Antarctic Ocean*	$0.258 \times 10^{-3} \pm 0.05 \times 10^{-3}$
N Atlantic Ocean**	$0.253 \times 10^{-3} \pm 0.045 \times 10^{-3}$
S Atlantic Ocean**	$0.33 \times 10^{-3} \pm 0.056 \times 10^{-3}$
Antarctic Ocean**	$0.365 \times 10^{-3} \pm 0.015 \times 10^{-3}$
S Indian Ocean**	$0.459 \times 10^{-3} \pm 0.053 \times 10^{-3}$
N Indian Ocean**	$0.476 \times 10^{-3} \pm 0.098 \times 10^{-3}$
S Pacific Ocean**	$0.431 \times 10^{-3} \pm 0.063 \times 10^{-3}$
N Pacific Ocean**	$0.592 \times 10^{-3} \pm 0.079 \times 10^{-3}$

* = surface water, ** = deep water

Table 4 shows the distribution of radium isotopes in estuaries during the past two decades. These estimates are essential to establish information about oceanic fluxes not only of radium, but also of nutrients, carbon and metals. Radionuclide discharges from the phosphate industry may contribute significantly to the radium cycle in the marine environment in addition to the natural processes. More specifically, the production of phosphoric acid, while it is being used to break down apatite $\text{Ca}_5(\text{PO}_4)_3\text{X}$; (X = OH, Cl) can be found in the discharges of fertiliser production and may be a main source of contribution. Phosphogypsum residues, which are contained in ores, may be a source of various radionuclides from the uranium series that can be discharged into surface waters, stockpiled on land or sold as a by-product. Phosphogypsum, is simply gypsum (hydrated calcium sulfate formed as a by-product of the production of fertiliser from phosphate rock) but also contains nearly all of the ^{226}Ra , ^{210}Pb and ^{210}Po present in the ore and smaller quantities of uranium and thorium isotopes^{2,84}.

Table 4. Activities of radium isotopes in estuaries worldwide

Region	²²⁶ Ra (Bq kg ⁻¹)	²²⁸ Ra (Bq kg ⁻¹)	²²⁴ Ra (Bq kg ⁻¹)	²²³ Ra (Bq kg ⁻¹)
North Inlet (USA)	0.16x10 ⁻² - 1.00x10 ⁻²	15x10 ² - 150x10 ²	0.22 - 6.33	0.03 - 0.83
Port Royal Sound (USA)	0.5x10 ⁻² - 1.33x10 ⁻²	60x10 ² - 120x10 ²	0.5 - 2.17	0.15 - 0.35
St. Johns Estuary (USA)	0.25x10 ⁻² - 1.17x10 ⁻²	20x10 ² - 40x10 ²	0.05 - 0.13	0.01 - 0.08
Satila Estuary (USA)	0.06x10 ⁻² - 0.67x10 ⁻²	5x10 ² - 80x10 ²	0.1 - 1.17	0.07 - 0.10
Savannah Estuary (USA)	0.12x10 ⁻² - 0.5x10 ⁻²	9x10 ² - 70x10 ²	0.08 - 0.83	0.01 - 0.12
Charleston Harbor (USA)	0.17x10 ⁻² - 0.67x10 ⁻²	8x10 ² - 70x10 ²	0.06 - 0.92	0.01 - 0.22
Winyah Bay (USA)	0.1x10 ⁻² - 0.5x10 ⁻²	6x10 ² - 40x10 ²	0.06 - 0.83	0.01 - 0.08
Tampa Bay (USA)	0 - 4.67x10 ⁻²	45x10 ² - 175x10 ²	0.33 - 3.0	0.25 - 2.57
Loxahatchee Estuary (USA)	0.25x10 ⁻² - 1.25x10 ⁻²	7x10 ² - 24x10 ²	0.15 - 0.58	0.03 - 0.22
Jamaica Bay (USA)	1.00x10 ⁻² - 1.67x10 ⁻²	160x10 ² - 23x10 ³	6.33 - 10.83	0.12 - 0.5
Great South Bay (USA)	0.12x10 ⁻² - 0.32x10 ⁻²	12x10 ² - 32x10 ²	0.26 - 0.65	0.01 - 0.02
Elkhorn Slouth (USA)	2.17x10 ⁻² - 4.25x10 ⁻²	60x10 ² - 560x10 ²	3.0 - 18.3	0.2 - 2.92

1.2.4 Radium Aqueous Speciation

Dickson⁸⁵ studied the aqueous speciation of radium in natural waters. Values for the equilibrium constant (Log *K*) for the formation of the primary radium complexes in most natural waters are shown in Table 5.

Table 5. Aqueous (aq) radium complexes

Complex	Log K^{42}
$\text{Ra}^{2+} + \text{OH}^- = \text{RaOH}^+$	0.5
$\text{Ra}^{2+} + \text{Cl}^- = \text{RaCl}^+$	- 0.1
$\text{Ra}^{2+} + \text{CO}_3^{2-} = \text{RaCO}_3 \text{ (aq)}$	2.5
$\text{Ra}^{2+} + \text{SO}_4^{2-} = \text{RaSO}_4 \text{ (aq)}$	2.75
$\text{Ra}^{2+} + \text{HCO}_3^- = \text{RaHCO}_3^+$	*

* = no available data

Langmuir⁴² et al., reported radium complexes by calculating thermodynamic data based on data used for the other alkaline earths. In waters with high sulfate concentrations, a significant fraction of Ra^{2+} would be in the sulfate form; for a sulfate concentration of 70 mg L^{-1} , half of the radium would be found as RaSO_4 . In contrast, in water with a chloride concentration as high as 4 mg L^{-1} , only 10% would be in the form of RaCl^+ . A significant fraction of radium would be complexed as RaCO_3 only at high pH (> 10.25) and high carbonate concentrations ($> 60 \text{ mg L}^{-1}$)^{16,86-90}.

1.2.5 Radium Absorption - Desorption

Radium mobility and concentrations in waters, can be controlled by interaction with surfaces by adsorption through ion exchange. The degree of sorption resulting from this process can be described by a partition coefficient (K_d , Equation 3), which is defined as^{2,91}:

$$K_d = \frac{\text{Concentration in solid phase}}{\text{Concentration in solution}} \quad \text{Equation 3}$$

The concentration in the solid phase can be expressed as the amount of adsorbent in a total mass of solid (e.g. moles kg^{-1}), whereas the concentration in solution phase can be expressed in moles L^{-1} . Therefore, the unit of K_d is in terms of volume of solution to mass of solids (e.g. L kg^{-1})⁹¹.

K_d is a thermodynamic function and laboratory measurement of sorption depend on experimental conditions. Therefore, the function measured in the laboratory is R_d . To obtain meaningful values of R_d , the following experimental conditions must be adhered to: a) check that simple precipitation of radium is absent by carrying out relevant control experiments i.e. in the absence of solid, b) check that the batch experiments have reached equilibrium by carrying out suitable kinetic experiments, and c) consideration of the solid/solution ratio to ensure that the surface of the solid has not been saturated⁹¹.

1.3 The measurement of radium by gamma spectrometry

In this research, radium was measured by the use of gamma spectrometry which is a non-destructive technique that allows the simultaneous determination of radionuclides, both quantitatively and qualitatively. Gamma spectrometry does not require complicated and time-consuming radiochemical separations as is required for alpha spectrometry. It is known that each individual radionuclide can have one or more characteristic gamma rays that can be detected over a certain period of time and recorded in counts. These counts can be converted to activity concentration (Bq kg^{-1})^{6,92}.

The use of gamma spectrometry analysis may be challenging for various reasons including the poor efficiency of the High Purity Germanium (HPGe) detectors over a wide range of energies, the fact that many emission lines have weak emission probabilities, the difficulty of calibrating the detector with precision, and the need for the evaluation of self-absorption effects^{5,6}.

The gamma spectrometry method depends strongly on the generation of an electronic pulse which is proportional in magnitude to the gamma ray energy produced from the radioactive decay of the radioactive material being measured. The magnitude of the electronic pulse is used to identify a radionuclide. In addition, the number of electronic pulses recorded per unit time is proportional to the amount of the radionuclide in the sample being measured. Thus, gamma spectrometry is both quantitative and qualitative^{5,6}.

Generally, gamma spectrometry systems can be divided into two categories. In the first category they depend on either the generation of a light pulse in a scintillating inorganic or organic material, following the collection of the generated photon by the help a photomultiplier

tube or photodiode, and secondly, they depend on a semi – conducting material which generates electrical pulses directly proportional to the energy of the gamma photons striking the detector element. Sodium iodide (NaI) doped with thallium has been used extensively up until now as the standard scintillation gamma spectrometer, but they suffer from poor spectral resolution. Recently, modern materials that include caesium iodide (CsI), bismuth germanate (BGO), lanthanum bromide (LaBr), and a number of organic scintillators have been developed to provide significantly improved robustness, resolution and efficiency compared to the older NaI detectors^{92,93}.

1.3.1 Gamma Spectrometry Instrumentation

A schematic diagram of equipment used for gamma spectrometry analysis is shown in Figure 11. Each measurable radionuclide emits one or more characteristic gamma rays which are detected by a suitable detector which converts the energy of the gamma photon into an electrical pulse which is then recorded by a multi - channel analyser (MCA)^{6,92,93}.

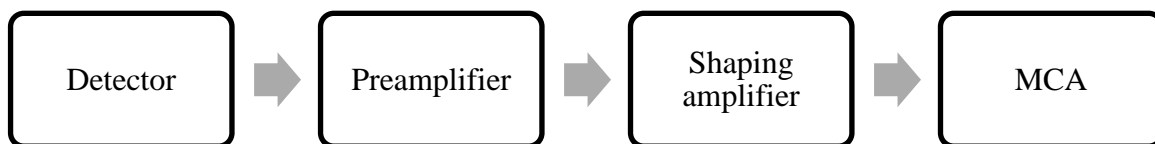


Figure 11. Schematic diagram of equipment used in gamma spectrometry

Two important relationships exist in gamma spectroscopy. Firstly, the magnitude of the electrical pulse produced is proportional to the energy of the gamma photon interacting with the detector material. The MCA shows the electrical pulses as “peaks” in a “pulse height spectrum” (Figure 12). This allows the identification of gamma emitting radionuclides that may be present in a sample. Secondly, the number of counts in a peak is proportional to the activity of the gamma emitting radionuclide in a sample. A suitable mixed radionuclide gamma emitting standard can be used to determine the counting efficiency of gamma photons as a

function of gamma photon energy and the counting efficiency (CE) can then be used to convert the peak counts divided by the counting time (cps) into absolute activity (Bq) and activity concentration (e.g. Bq Kg⁻¹ or Bq cm⁻³) present in the sample. Suitable computer software (e.g. Genie, see later) can be used to model counting efficiency, and to calculate and report the activity concentration present in a sample^{6,92,93}.

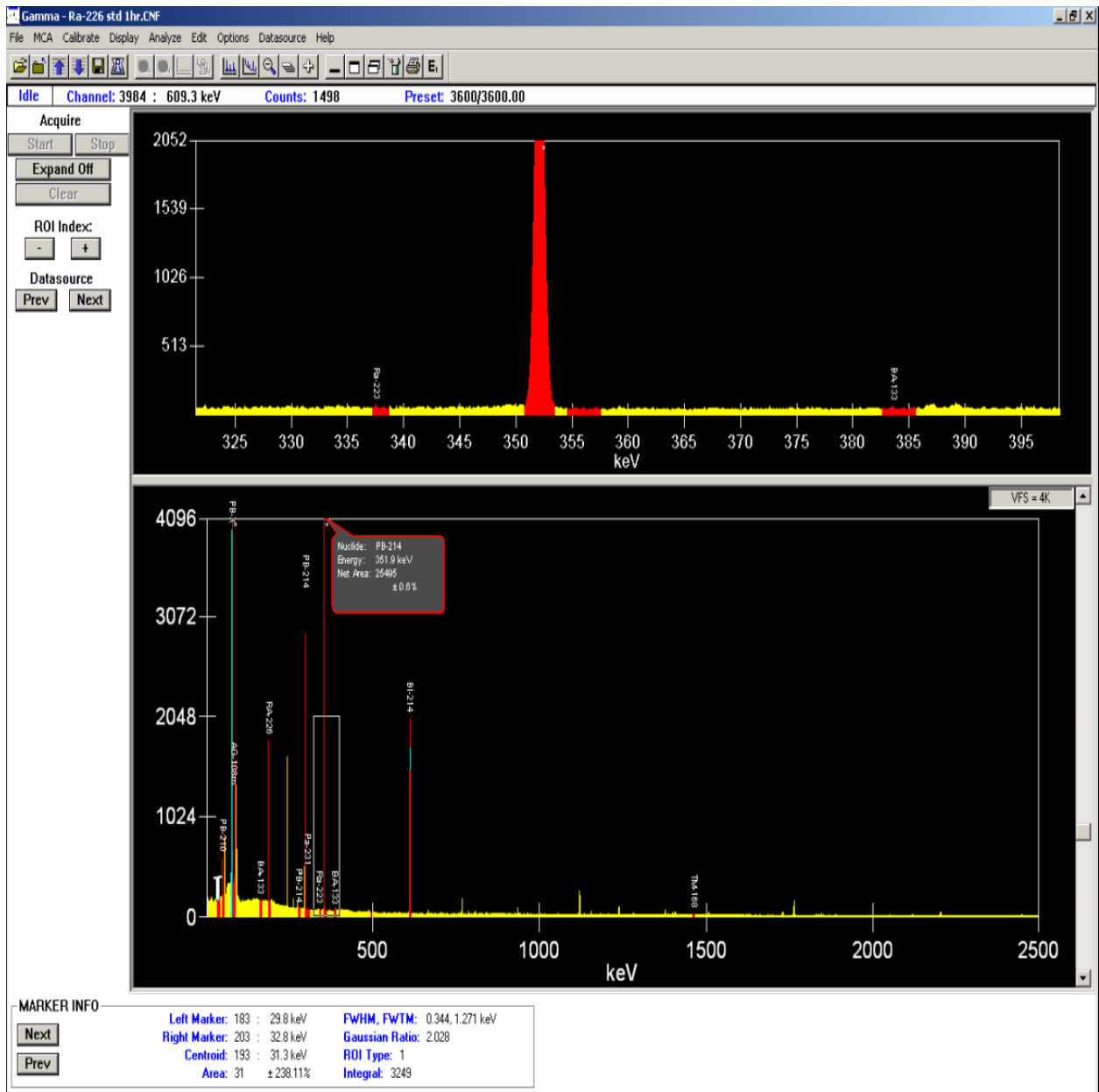


Figure 12. Pulse height spectrum as shown on the multi - channel analyser

1.3.2 Use of gamma spectrometry to measure radium in environmental samples

Radium can be measured using gamma spectrometry by either measuring ^{226}Ra directly or by measuring either ^{214}Pb and/or ^{214}Bi , provided that they are in secular equilibrium with ^{226}Ra . These three radionuclides are in the natural decay chain shown in Figure 13^{6,92}.

Without chemical separation, or a suitable computer software (e.g. Genie), it is not possible to measure radium in soil by measuring ^{226}Ra directly because of the presence of ^{235}U which has a similar gamma photon energy (185.7 keV) to that of ^{226}Ra (186 keV). ^{235}U therefore interferes with the direct measurement of ^{226}Ra ^{6,92}.

^{238}U is 99.3 % of natural uranium and is the head of the chain which contains ^{226}Ra . ^{235}U is 0.7 % of natural uranium and will be present in all-natural samples (e.g. soil samples), which contain ^{238}U and, therefore, radium. Many papers and reports have described the measurement of ^{214}Pb and/or ^{214}Bi and related their activities to that of ^{226}Ra . Reports of the direct measurement of ^{226}Ra , without further details on how they eliminated the ^{235}U interference problem, make any comparison between the results reported in the literature difficult^{6,92}.

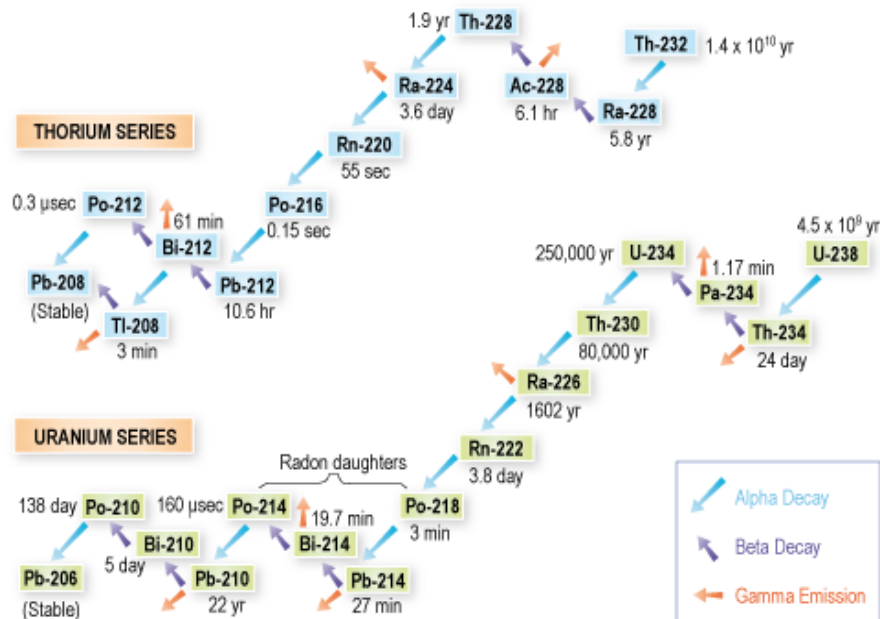


Figure 13. Radionuclides decay series⁸⁴

Table 6 shows the important gamma energies and photon yields of the relevant when considering using ^{214}Pb and ^{214}Bi measurements for ^{226}Ra determinations⁸⁴.

If chemistry, e.g. a liquid extraction, is performed on a soil sample and the liquid is separated from the soil sample, then, when counting the liquid, the following two extreme scenarios are possible^{6,92,93}:

1 Radium is extracted into the liquid but neither lead nor bismuth is extracted into the liquid. The liquid must be sealed to prevent the loss of radon gas and bismuth and lead must be allowed to grow into the sample by allowing twenty days to elapse before measurement of the ^{214}Pb and ^{214}Bi .

2 Radium is not extracted but bismuth and lead are extracted. In this scenario, it is not possible to use the measurement of lead or bismuth to measure radium as both will decay away rapidly.

Table 6. Half – life, gamma energy and photon yield values for ^{226}Ra , ^{214}Pb , ^{214}Bi and ^{235}U ²

Radionuclide	Half - life	Gamma Energy (keV)	Photon yield (%)
^{226}Ra	1620 years	186	3.53
^{214}Pb	26.8 minutes	242	7.19
		295	18.3
		352	35.3
^{214}Bi	19.7 minutes	609	46.2
^{235}U	7.038 x 10 ⁸ years	143	10.6
		186	57.2

When counting the soil, the opposite occurs if the soil sample is measured after treatment and separation of the soil and liquid phases i.e. ^{6,92,93}:

1 Radium is extracted into the liquid and lead and bismuth remain in the soil. It is not possible to measure radium in the soil as both lead and bismuth will decay away rapidly.

2 Radium remains in the soil and the lead and bismuth are extracted into the liquid. The soil must be sealed to prevent the loss of radon gas and bismuth and lead must be allowed to grow into the sample by allowing twenty days to elapse before measurement of the ^{214}Pb and ^{214}Bi .

1.3.3 The use of gamma spectrometry to measure known activities of a ^{226}Ra standard

When solutions are spiked with ^{226}Ra , the direct measurement of ^{226}Ra by gamma ray spectroscopy is possible because of the absence of ^{235}U . The sample does not have to be sealed to prevent radon loss.

1.4 The Needle's Eye Site

Needle's Eye is a natural analogue site located in South-West Scotland near the town of Dalbeattie, which is on the North coast of the Solway Firth (National Grid Reference NX 916562) (Figure 14).

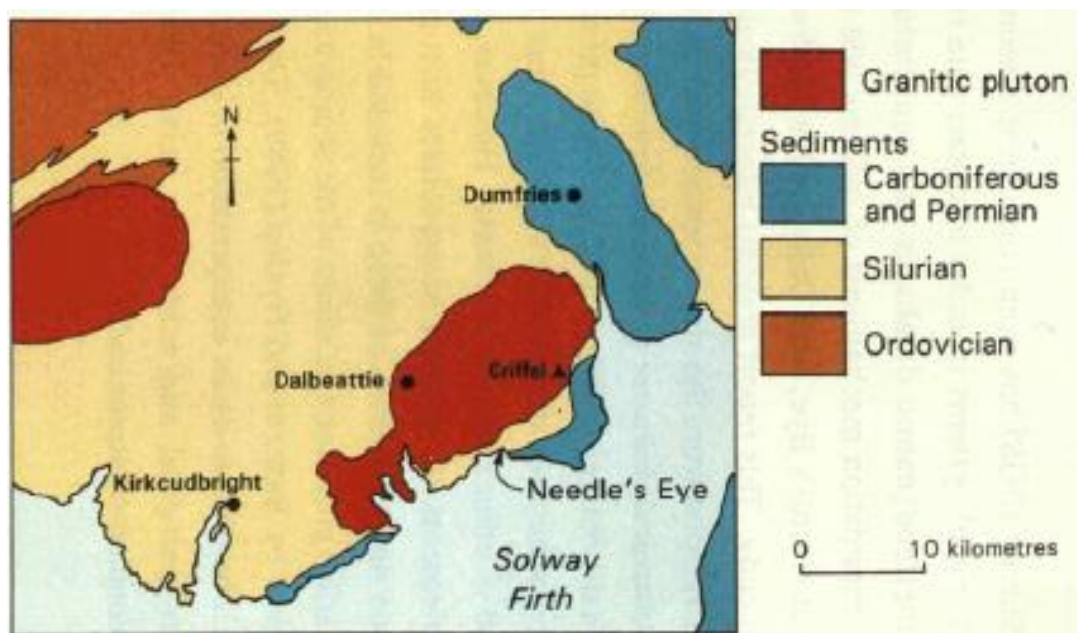


Figure 14. Situation and geology of the Needle's Eye sampling area¹

The Needle's Eye site is delimited to the north by the cliff top at Nether Clifton and to the South by the tidal creek of the Southwick Water. The site is mainly resting on relatively low-lying

ground that varies from 2 to 6 m thickness above ordnance datum (AOD) developed on the estuarine – intertidal mudflats (shallow – sloped shoreline, with expanses of fine sediment) of the Mersehead Sand^{1,94}.

1.4.1 Geology of study area

The geological setting of Needle’s Eye site is characterised by the Late Caledonian (397 ± 2 million years) Criffel pluton (intrusive igneous rock) which was responsible for the thermal metamorphism⁹⁵ of the Silurian (i.e. 24.6 million years⁹⁶ sediments and limestone (CaCO_3) (Figure 16). This metamorphic complex is concentrically zoned from an outer metaluminous hornblende, $\text{Ca}_2(\text{Mg, Fe, Al})_5(\text{Al, Si})_8\text{O}_{22}(\text{OH})_2$ (a dark green to black mineral of the amphibole group, calcium magnesium iron and hydroxyl aluminosilicate), granodiorite (igneous rock containing quartz (SiO_2), and plagioclase $\text{NaAlSi}_3\text{O}_8 - \text{CaAl}_2\text{Si}_2\text{O}_8$) (Figure 15) to a core of peraluminous (igneous rocks that have a molecular proportion of aluminium oxide higher than the combination of sodium oxide, Na_2O , potassium oxide, K_2O , and calcium oxide, CaO) muscovite ($\text{KAl}_2(\text{Si}_3\text{Al})\text{O}_{10}(\text{OH,F})_2$) granite^{1,8,94}.

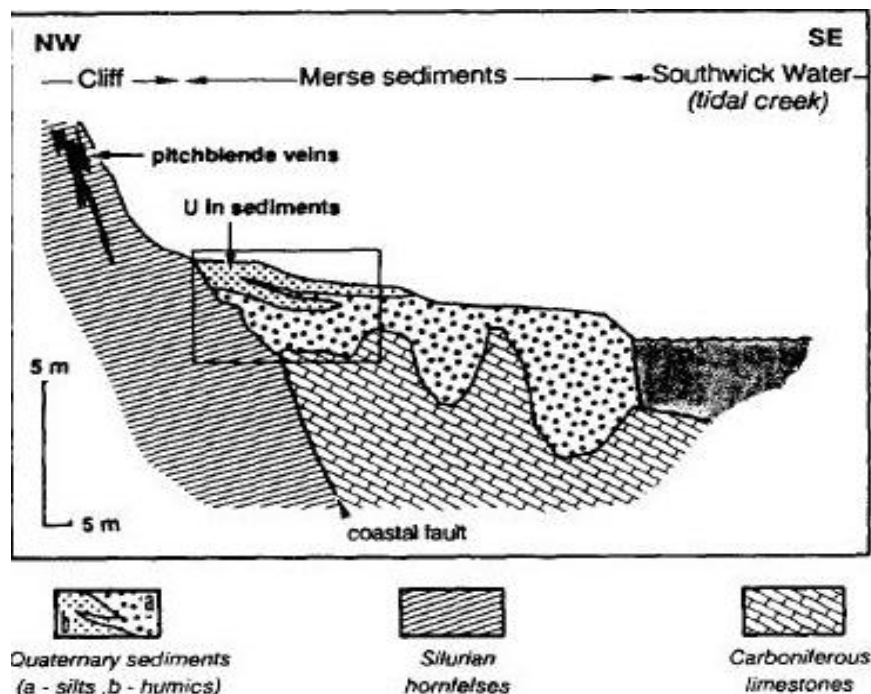


Figure 15. Uranium mineralisation at Needle’s Eye⁹⁴

In 1985, Stephens⁹⁷ et al., recorded a rare - earth element (REE) zonation, where REE contents decrease progressively towards the centre. The southeast margin of pluton is characterised by

a series of related porphyritic granite (a very large potassium feldspar, KAlSi_3O_8 – $\text{NaAlSi}_3\text{O}_8$ – $\text{CaAl}_2\text{Si}_2\text{O}_8$, phenocrysts in a phaneritic (coarse-grained) groundmass) that occur in clusters trending generally north-westerly⁹⁸.

The Quaternary sediments contain mainly siltstones and greywackes (i.e. sandstones that generally include chlorite $(\text{Mg,Fe})_3(\text{Si,Al})_4\text{O}_{10}$, biotite $(\text{K,Mg,Fe})_3(\text{AlSi}_3\text{O}_{10})(\text{F,OH})_2$ and illite $((\text{K,H}_3\text{O})(\text{Al,Mg,Fe})_2(\text{Si,Al})_4\text{O}_{10}[(\text{OH})_2,(\text{H}_2\text{O})]))$ ^{99,100} and demonstrate hornfelsed aureole (a metamorphic rock with fine texture)¹⁰¹ (Figure 16) where the mineralisation is concentrated.



Figure 16. Hornblende granodiorite

The contrast between the Lower Palaeozoic (geological era from 541 to 252.17 million years ago)^{102,103} rocks and the Carboniferous sediments (interbedded limestone sand shales) to the South is caused by a major East - West fault. This fault is also responsible for the long straight coastal feature as it surrounds the base of the cliffs. Further tectonic activity, generated from

the development of cross - faults that occur parallel to the fault that affects the Silurian sediments by means of shearing, brecciation (fragments of older rock fused together) and silicification (the replacement of a rock or of the remains of an organism with silica, as in petrified or silicified wood, or silicified limestone)^{1,8,94}.

Polymetallic mineralisation is observed within a number of steeply inclined veins at the Northwest cross-fractures cutting the north-easterly coastal fault¹. The veins reach their maximum development in the hornfels (a dark, fine-grained metamorphic rock consisting largely of quartz, biotite, a dark-brown to black lustre owing to small crystals of black mica, cordierite $(\text{Mg,Fe})_2\text{Al}_4\text{Si}_5\text{O}_{18}$), garnet $\text{X}_3\text{Y}_2(\text{SiO}_4)_3$, and andalusite Al_2SiO_5) within 10 - 30 m North of the fault, but apart from that mineralisation rarely occurs^{8,94}.

The veins appear mainly in clusters where the fault changes direction and slip off the main structure. The point where the fault approaches the granodiorite is frequently concentrated near the margins of acidic dykes and it is characterised by the highest vein mineralisation intensity compared to the rest of the site⁹⁴. However, the implied structural relationship has not been proven. On the other hand, the Carboniferous sediments demonstrate limited mineralisation and it is assumed that it is acting as a seal to mineral fluids migration in the fractured hornfels, as they have been relatively soft¹⁰⁴.

Miller and Taylor⁸ reported that at least one vein at Needle's Eye contains uranium. This vein continues under the mudflat sediments and goes through the Carboniferous (geologic period and system that spans 60 million years from the end of the Devonian period 358.9 million years ago, to the beginning of the Permian Period, 298.9 million years)⁹⁶ rocks. The British Atomic Energy Division, after a systematic radiometric survey (1957 - 1961), discovered the presence of uranium mineralisation that appears in the form of pitchblende - bearing veins (on structures crosscutting the coast fault) in the cliff of the Colvend and Southwick coasts⁸.

The source of uranium at this site is a major vein of uraninite (UO_2) (variety pitchblende) (Figure 17) (a form of the mineral uraninite, a black, grey, or brown mineral which consists mainly of uranium dioxide (UO_2) and is the chief ore of uranium, occurring in brown or black pitch-like masses and containing radium) in the Criffel granodiorite associated with hydrocarbon, chalcopryrite, native bismuth and hematite in a quartz-carbonate gangue and secondary uranium minerals (triuranium octoxide, U_3O_8 , an oxidised form of UO_2 in the

presence of O₂), and forms a granodiorite rock formation (i.e. cliff) characterised by the faulted rocks that intruded and are situated against the carboniferous limestones (CaCO₃) underlying the Solway Firth flood plain^{8,94}. This cliff is aged, and groundwater movement occurs through fissures located in the mineralised area that drains into the connecting soil and sediment. The carboniferous limestone is surrounded by an anoxic, organic - rich soil of varying thickness from 5 to 10 m and is separated from the attached saltmarsh (an area of coastal grassland that is regularly flooded by seawater) by a vegetated silt deposit 5 - 10 m wide. The saltmarsh sediments spread up to 55 m towards the seaward edge^{94,104}.



Figure 17. Example of pitchblende sample (UO₂ (yellow colour), azurite (blue colour, Cu₃(CO₃)₂(OH)₂), malachite (green colour, Cu₂CO₃(OH)₂))¹⁰⁵

In general, the Needle's Eye natural analogue site has been extensively characterised, mainly with respect to geology, hydrology, uranium source, basic geochemistry, sediment characteristics and accumulation rates.^{5,89} More specifically it was reported that, groundwater from the cliff has elevated ²³⁸U concentrations (~ 1 Bq L⁻¹) and the ²³⁴U/²³⁸U activity ratio for

the dissolved uranium in these groundwaters was 0.94; as groundwater flows towards the sea, the anoxic soil retards migration of uranium (UO_2 , UO_2CO_3) in solution; and colloidal transport of uranium (UO_2 , UO_2CO_3) persists in the anoxic soil. While basic features of the source term and uranium distribution and migration have been established^{8,94}.

1.4.1.1 Boulder Clay (deposit of clay)

The Needle's Eye area was completely submerged beneath a thick ice sheet that covered most of Scotland during the last Pleistocene glaciation^{8,94} (the process or state of being covered by glaciers or ice sheets during geological epoch which lasted from about 2,588,000 to 11,700 years ago)^{106,107}.

Extensive ground moraine (a mass of rocks and sediments carried down and deposited by a glacier, typically as ridges at its edges or extremity) or boulder clay over the majority of the region due to the ice sheets deposition^{8,94}. This boulder clay forms corrugated sheets at the lowest part of the slopes while thickening into the valleys and developing terraces by the main water paths. The type of the clay boulder varies from place to place depending on the nature of the underlying bedrock. Hence on Palaeozoic (from the Greek palaios (παλαιός), "old" and zoe (ζωή), "life", meaning "ancient life, refers to the geological era between the Precambrian aeon and the Mesozoic era)^{102,103} sedimentary bedrock (solid rock underlying loose deposits such as soil or alluvium)^{108,109} it generally has a matrix consisting of tough, tenacious clay (illite, $\text{K,H}_3\text{O}(\text{Al,Mg,Fe})_2(\text{Si,Al})_4\text{O}_{10}[(\text{OH})_2,(\text{H}_2\text{O})]$) however in granitic areas it is grittier and less cohesive^{8,94}. The majority of clay consists of nearby derived material that is inclosing boulders from local granitic plutons and country rocks and in the cases, where the sources of these boulders were identified, they indicated transport from North or Northwest^{8,94}.

1.4.1.2 Intertidal and Estuarine Deposits

The Needle's Eye base bedrock consists of Quaternary (post - glacial) marine erosion with the developed of sea stacks, a wave cut platform and small caves across the cliffs (forming the characteristic natural arch). Following eustatic (changes to sea level due to water volume alteration) elevation of the land subsequent the postglacial unloading of ice raised these structures over the high tide mark, a common characteristic of the Solway Firth coast^{1,8,94}.

The deposits of the raised beach lay directly upon the eroded bedrock surface. These deposits are particularly well developed where streams have breached the precipitous coastline and extensive areas of beach deposit are found at the extrusion of all major streams. The site is located at the edge of a deposit that covers the foot of an ancient cliff line and forms a prominent mudflat and saltmarsh for about a mile wide, extending from Nether Clifton to Southerness.⁹⁰ The deposits of this beach consist of well-stratified sand and fine gravel, associated in places with finely laminated estuarine clays (illite, $(K,H_3O)(Al,Mg,Fe)_2(Si,Al)_4O_{10}[(OH)_2,(H_2O)]$). The southern limit of the Needle's Eye Natural Analogue site research area is delineated by the tidal creek of the Southwick Water which cuts through the deposits of the mudflat exposing Carboniferous limestone and shale bedrock in the base of the channel^{1,8,94}.

The soil-sediment profile consists of a strongly stratified sequence of sands, gravels, silts and organic materials ("peats"). The drift sequence is about 2 m thick and rests directly on bedrock. At the bottom of the sediment pile about 10 cm of gravel and pebbles rest on a smooth, horizontal bedrock surface. Well-rounded pebbles, up to 25 cm diameter, comprise locally derived granodiorite, hornfels and limestone with less common pebbles of vein quartz. The pebble bed is overlain by a layer of homogenous, buff coloured, fine to medium sand. The top part grades into overlying grey laminated silts and fine sands. A sub-horizontal band of sub-spherical patches of concentrically zoned black and orange stained sediment appears. SEM analysis showed a precipitation of fine grained, often spongy textured, interstitial manganese rich (black colour) and iron rich (orange colour) oxides and hydroxides^{1,8,94}.

1.4.1.3 Uranium Locations

Various studies reported that in Needle's Eye site uranium is mainly hosted in the carbonate vein as pitchblende (UO_2). Miller and Taylor⁸ in 1966 showed with the help of energy dispersive X-ray analysis (EDXA) that the content of thorium is very low and that the earliest mineralisation consists of quartz and K-feldspar and occurs in the band adjacent to the granodiorite rock. Granular intergrowths of K-feldspar and quartz occur as relict patches largely replaced and enclosed within later dolomite ($CaMg(CO_3)_2$) and calcite ($CaCO_3$). Tetragonal crystals of an yttrium phosphate mineral (probably xenotime; YPO_4) are abundant within the K-feldspar-quartz relicts. These are later than the quartz-K-feldspar mineralisation and are particularly concentrated along the quartz grain boundaries within the relicts or along

the surfaces of dolomite rhombus at the margins of the relicts. Micaceous hematite (MIO) is closely related to the alteration of the quartz-K-feldspar relicts and is sometimes seen, accompanied by fine secondary TiO_2 , replacing associated muscovite $(\text{KAl}_2(\text{AlSi}_3\text{O}_{10})(\text{F,OH})_2)^{1,8,94}$. Therefore, the solubility of oxidising waters is expected to be high, an assumption reinforced by observing the decomposition of pitchblende^{1,8,94}.

Parnell¹¹⁰ (1988) and Eakin¹¹¹ (1989) reported contents of 4.5% and 35.89% by weight of uranium respectively in hydrocarbons from this locality. Track registration techniques showed that the hydrocarbon mass itself contains negligible esoteric uranium, but fission track distributions indicate a close association of significant levels of uranium with grain surfaces or internal cracks. Back Scattering Electron Microscopy (BSEM) observation of these fractures and grain surfaces identified very fine-grained uranium (\pm bismuth) - silicate as coatings and replacements of the immediately underlying hydrocarbon substrate. The uranium silicate possesses no morphological characteristics to aid precise identification but possible identifications would be coffinite $(\text{U}(\text{SiO}_4)_{1-x}(\text{OH})_{4x})$, uranothorite $(\text{U,Th})\text{SiO}_4$ or soddyite $(\text{UO}_2)_5\text{Si}_2\text{O}_4 \cdot 2\text{H}_2\text{O}$. The cracks in the hydrocarbon are later than those in the pitchblende and do not appear to be infilled by calcite $(\text{CaCO}_3)^1$.

Scanning electron microscope (SEM) examination of open fracture surfaces of hydrocarbons from this locality collected from exposed outcrop and loose blocks from the earlier trenching revealed a much more complex association of uranium. Several fracture surfaces in hydrocarbon reveal the presence of peculiar uraniferous filaments of organic origin. These filaments form loops and may "bridge" one another. They display dendritic "fruiting bodies" and fine branching porous "microfilaments" or "hyphae" penetrate from the main filaments into the surrounding hydrocarbon. These features are present only on fracture surfaces and not in the bulk of the hydrocarbon. Often a mineralised tangled mass of filaments coats the hydrocarbon surface adjacent to the main filaments. Under high magnification the filaments display evidence of a cellular structure. The associated mineralisation is complex. The central core of the main filaments and cells is mineralized with a dense bismuth - sulfur phase containing minor amounts of copper, nickel, zinc, arsenic and selenium and may correspond to bismuthinite (Bi_2S_3) or some other bismuth - sulfosalt (general formula $\text{A}_m\text{B}_n\text{S}_p$). The walls of the cells and filaments are mineralised by uranium and calcium and in some cases by possible native selenium. The fine filaments around the main filaments are enriched in uranium, calcium

and vanadium whilst aggregated fine plates of a calcium - uranium - rich mineral appears to nucleate within the fine filaments - mucilage mass^{1,8,94}.

Fission track prints also show the common occurrence of fine disseminations of uranium along grain surfaces of pyrite (FeS_2), chalcopyrite (CuFeS_2) and galena (PbS) reported by Miller and Taylor⁸, the previously mentioned sulphides (S^{2-}) were not seen in the present study after the XRD analysis. This association is considered to be quantitatively more important than the hydrocarbon association, in view of the frequency of the sulphides and the tendency of most to become altered within the weathering zone. BSEM shows that the main phase hosting uranium in this association is a uranium - silicate (possibly coffinite, $\text{U}(\text{SiO}_4)_{1-x}(\text{OH})_{4x}$ but no distinctive morphology is shown to aid identification). The uranium - silicate is fine grained and nucleates largely upon chalcopyrite (CuFeS_2) surfaces, replacing the underlying sulphide substrate where it may also accompany galena (PbS) and bismuth - sulphide replacement of chalcopyrite (CuFeS_2). Fission tracks concentrated around other sulphides [pyrite (FeS_2), sphalerite (Zn,FeS)] are similarly associated with uranium - silicate, invariably replacing chalcopyrite (CuFeS_2) overgrowths^{1,8,104}. In addition to enrichments associated with surface - active amorphous iron oxides (hematite Fe_2O_3 , goethite $\text{FeO}(\text{OH})$, ferrihydrite $\text{Fe}^{3+}_{10}\text{O}_{14}(\text{OH})_2$) weathering products, minor secondary uranium - arsenic - lead - silicate phases occur replacing dolomite, $\text{CaMg}(\text{CO}_3)_2$. Hydrated uranium silicate minerals are the most common secondary minerals regionally¹.

1.4.1.4 Granodiorite

Granodiorite is a coarse-grained plutonic rock containing quartz (SiO_2) and plagioclase ($\text{NaAlSi}_3\text{O}_8$ - $\text{CaAl}_2\text{Si}_2\text{O}_8$), between granite and diorite in composition. The presence of uranium minerals in the marginal phases of the pluton within and above the cliff at the analogue site has important implications in the modelling of dispersion in groundwater. No systematic sampling has been carried out at present but a preliminary study of samples from elsewhere in the background granodiorite has demonstrated their potential for inclusion as source-terms¹.

Accessory uranium bearing minerals so far recognised include common zircon (ZrSiO_4), sphene (CaTiSiO_5), and apatite $\text{Ca}_5(\text{PO}_4)_3(\text{F,Cl,OH})$ with, less frequently, allanite ($(\text{Ce,Ca,Y,La})_2(\text{Al,Fe}^{3+})_3(\text{SiO}_4)_3(\text{OH})$), thorite ($\text{Th,U}\text{SiO}_4$) and uraninite (UO_2). By analogy with other plutons in the province, additional minerals such as monazite ($(\text{Ce,La,Nd,Th})\text{PO}_4$) and

xenotime ($Y(PO_4)$) are also likely to occur in parts of the fractionation sequence. Zircon, sphene and apatite are usually relatively stable minerals and are not important sources of labile uranium¹. The allanite is turbid, brown and very inhomogeneous due to patchy metamictisation (a natural process resulting in the gradual and ultimately complete destruction of a mineral's crystal structure, leaving the mineral amorphous. The affected material is therefore described as metamict). In places, this is developed to a high degree, with only rare earth carbonate (CO_3^{2-}) remaining. Both minerals are included in primary Ti-biotite, $Ti-K(Mg,Fe)_3(AlSi_3O_{10})(F,OH)_2$, which has been altered to chlorite, $(Mg,Fe)_3(Si,Al)_4O_{10}$, with the release of microcrystalline anatase (TiO_2), hematite (Fe_2O_3) and possibly non - crystalline equivalents. Autoradiography and electron microprobe study has shown that uranium has been mobilised from metamict areas and re - adsorbed locally by these amorphous or microcrystalline phases¹.

1.4.1.5 Silurian Hornfels

The only work to date on the "background" Silurian (geological era 443 to 416 million years ago)⁹⁶ country rocks have been confined to that described above on samples from close to the uraniumiferous vein mineralisation. Some indication is given by study of thin sections that these rocks may contain significant levels of uranium bearing detrital (any disintegrated material; debris) accessory minerals. In addition, initial field examination of the cliff section indicates that secondary dispersion of uranium on fracture surfaces or in association with oxidation products may well be widespread (Figure 18)¹.

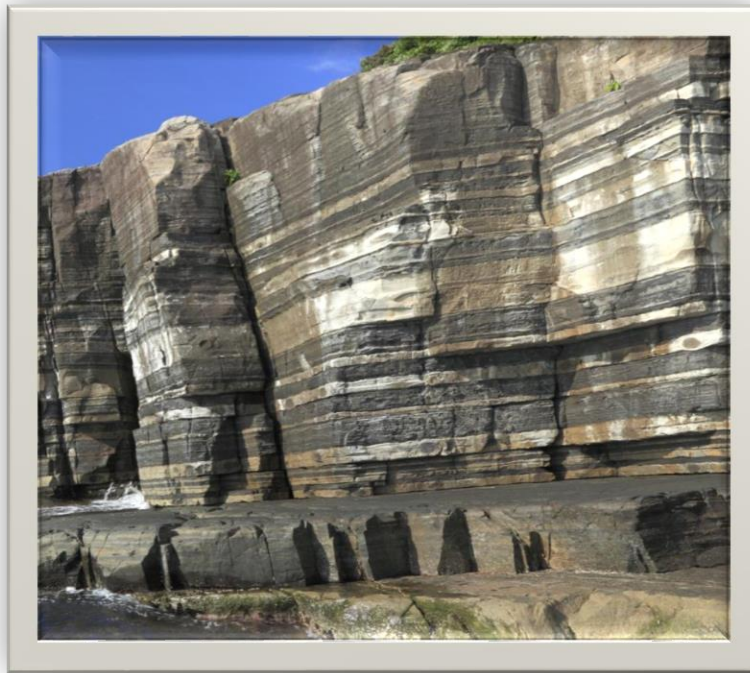


Figure 18. Silurian hornfels¹¹²

1.5 Aims and Objectives

As stated in Section 1.1, the principal focus of the Lo-RISE research project is to outline the key chemical, biological and physical processes that govern radionuclide mobility through the environment at natural analogue sites. The research reported in this thesis is in line with the aims and objectives of the Lo-Rise project by investigating radium speciation in the surface environment and in determining whether radium is mobile through the surface environment at Needle's Eye natural analogue site.

Therefore, this thesis reports the:

- measurement of the radioactivity levels of ^{226}Ra in soil samples.
- characterisation of soil samples from the site to determine radium speciation in soils samples.
- use of leaching techniques (batch experiments) to speciate radium in soil samples and, to determine whether radium is potentially mobile.
- use of column experiments to determine whether radium is mobile through surface soils.

Chapter two – Experimental Work

Chapter 2. Experimental work

2.1 Research Planning

The Needle's Eye site is a complex area which is highly disturbed by the intense research activity in the 60s and 70s. Therefore, the present sampling fieldwork focused on extracting soil samples from the undisturbed areas of the site and restricting the number of soil samples taken from the organic pit to two. Permission for visiting and sampling the Needle's Eye site was granted by Scottish Wildlife Trust and Scottish Natural Heritage bodies with the help of Dr Margaret C. Graham.

2.2 Sampling

Three sampling expeditions were conducted at Needle's Eye site. The first in September 2014, the second in October 2016 and the third in March 2017. During the first visit (reconnaissance visit), soil samples were collected for the general characterisation and understanding of the site by measuring ^{226}Ra activity concentration levels and soil particle/texture analysis. During the second and the third visits to the Needle's Eye site, soil samples were collected from the same stations as described later in Section 2.2.2.

2.2.1 First sampling visit

For the first visit to Needles Eye, soil samples were collected by using an auger soil sampler (Figure 19).



Figure 19. Auger soil sampler¹¹³

Unfortunately, this soil sampling technique is not the most suitable one because it does not allow precise extraction depths of soil to be sampled. In addition, it is not possible to extract intact soil cores (which are significantly more representative samples). Another problem that emerged with the soil samples from the first visit on the site was that the samples were collected from disturbed areas (areas highly excavated in the past by other researchers). Therefore, it was decided to improve the sampling technique/approach for soil samples by taking advice from a consultant at the British Geological Survey (BGS) in order to improve the quality of the samples taken (*see later in this Section 2.2.1*).

In general, the site is characterised as highly disturbed because of the intense sampling excavations that occurred previously. The selection of the sampling stations was driven by the need to be the most representative for the study area with respect to the number of samples taken from the organic pit and to avoid the areas where *Holy grass*¹¹⁴ grows. Therefore, a simple random sampling method was chosen (Figure 20).

A random sampling method was used in all three visits because it is less biased by the sampler than judgment sampling. Random sampling is needed where the soil differences are not immediately noticeable by colour, texture, etc. and selection of representative samples becomes more difficult)¹¹⁵.

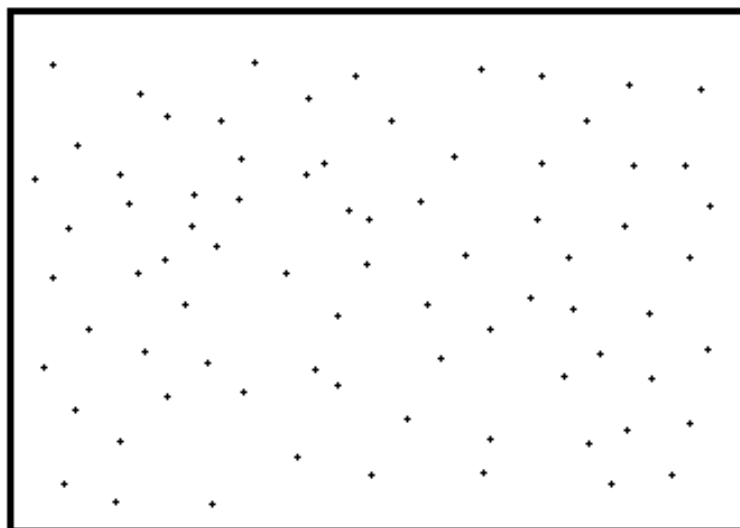


Figure 20. Example of simple random sampling

2.2.2 Second and third sampling visits

During the second and third visit to the Needle's Eye site a different sampling approach was applied compared to the first visit. Five different sampling stations were chosen (described later in this *Section 2.2.2*) as advised by the BGS consultant, Dr Anthony Milodowski. Advice was taken to improve the sampling methodology and to understand where human activity could alter environmental impact on the samples and their subsequent analyses.

NE1: this sampling station is located at the west side of the Needle's Eye area next to the main walk - path that leads to the site. Two sediment core samples, labelled as NE1-a and NE1-b of 14 and 20 cm length respectively, were extracted from the benthos of the stream. The reason for selecting this sampling station was in order to investigate whether the radium is mobilised into the stream or not.

NE2: this sampling station is located ~ 10 m away from the stream, as described above, and on the edge of Pit 3, as shown in Figure 23. This location was intensively sampled by BGS and is highly disturbed as described by Basham et al¹ (1989). Two soil core samples, labelled as NE2-a and NE2-b of 19.5 and 22.7 cm length respectively, were extracted from this sampling station.

NE3: this sampling station is located in between Pit 3 and Pit 1 (Figure 22), as described by Basham et al¹ (1989). This station is situated in the highly organic area of the site (> 18 % organic carbon by weight⁹⁹) and aligned with one of the main metalliferous veins. This area is slightly disturbed by human activity. Two soil core samples, labelled as NE3-a and NE3-b of 39 and 27.8 cm length respectively, were extracted from this sampling station.

NE4: this sampling station is located within the secondary highly organic area of the site and undisturbed when compared to NE3. It was chosen as it was expected to demonstrate similarly high concentrations of radionuclides like the previous sampling station, as both locations (NE3 and NE4) are closely located to the cliff. Two soil core samples, labelled as NE4-a and NE4-b of 33.2 and 39 cm length respectively, were extracted from this sampling station.

NE5: this sampling station is located at the east side of the research area near to a local stream that flows to the sea. This sampling station was used as a control sample. Two soil core samples,

labelled as NE5-a and NE5-b of 24.5 and 24.4 cm length respectively, were extracted from this sampling station.

Table 7. Sampling stations coordinates used during visit two and three at the site

Sampling Station ID	N	W
NE1	54°53.307'	003°41.571'
NE2	54°53.315'	003°41.563'
NE3	54°53.336'	003°41.540'
NE4	54°53.335'	003°41.532'
NE5	54°53.327'	003°41.523'

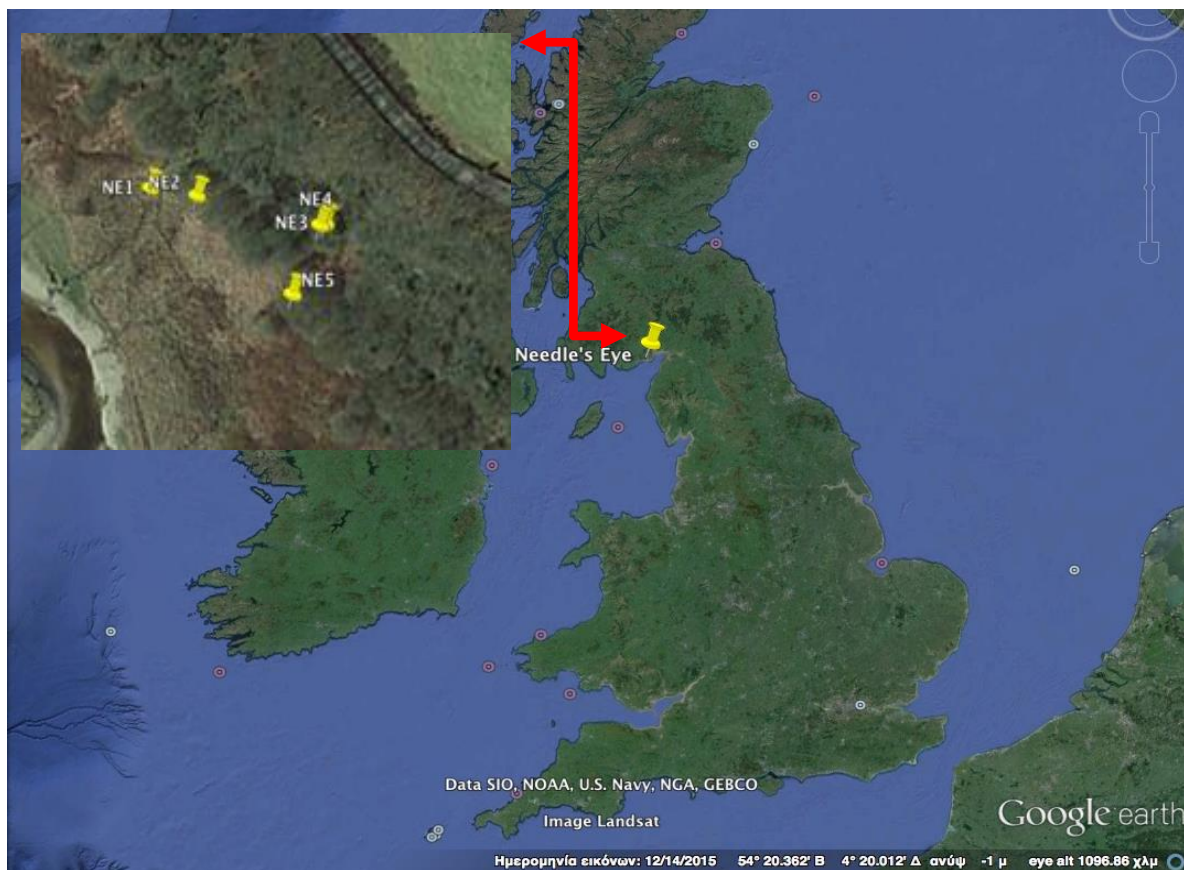


Figure 21. Sampling area¹¹⁶

Figure 21 shows the map with the five sampling stations (i.e. latitude and longitude). The GPS device that was used was the eTrex[®] 20x manufactured by GARMIN. All core samples were extracted using a 12.7 cm diameter plastic tube and a mallet as shown in Figure 23. The soil

core samples were sealed (with plastic bags and tape) and transferred to the Radiochemistry Laboratory at Loughborough University for further analysis.

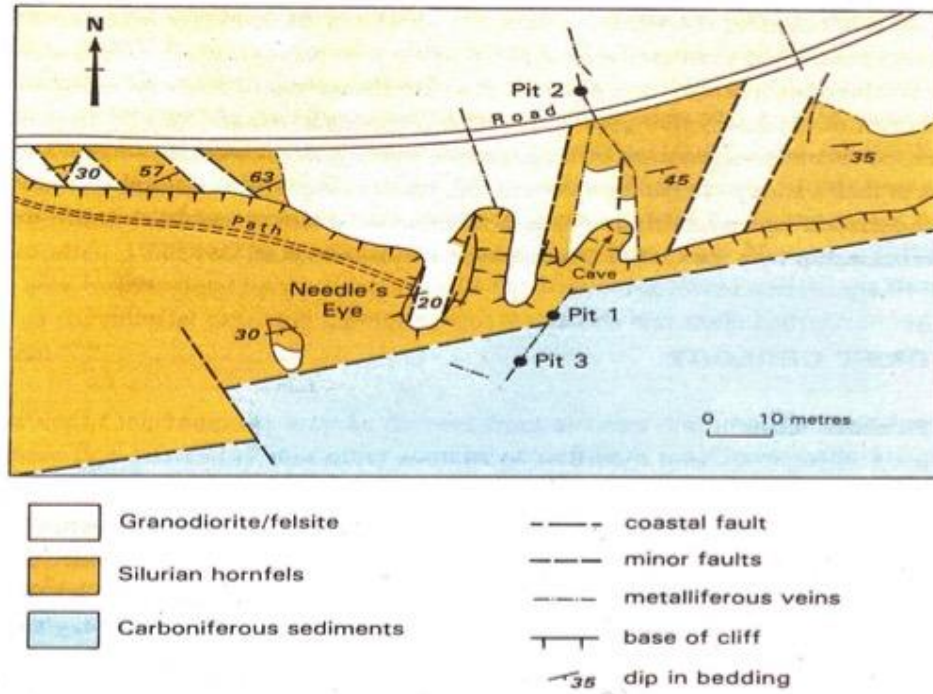


Figure 22. Pit locations used by BGS⁵



Figure 23. Sampling tools (plastic tube and mallet)

2.3 Soil Sample Preparation

The soil samples from all three sampling visits were taken out of the plastic pipes (samplers) or plastic bags (this applies to the samples taken during the first visit on the site) and dried for approximately 24 hours (or more than 24 hours in some cases until the sample demonstrated constant weight) in an oven at 100°C to remove the moisture content¹¹⁷. An example of a dried soil sample is shown in Figure 24.



Figure 24. Example of dried soil core sample

After drying, all soil core samples were cut into two pieces (sub - samples). All soil cores were cut at the point where a change in content was observed. Later in each individual sub - sample plant remains (roots, leaves, etc) and small rocks were removed, and all samples were sieved through a 2 mm sieve (for the samples from the first and third visit, Figure 25) and through 2 mm, 1 mm, 250 μm , 125 μm and 0.063 mm sieves (for the samples of the second visit) in order to investigate potential association of ²²⁶Ra with different soil size particles.



Figure 25. Sieve shaker

After the sieving stage, all samples from each individual size fraction were homogenised using a planetary ball mill (Fritsch Pulverisette 7, 12', 800 rpm) with zirconia pots and balls (Figure 26), and ground to a fine powder using a silicon carbide grinding bowl and ball. This was carried out because a homogenised sample is more representative of a bulk sample. Finally, the samples were stored in plastic pots in a dark, cool area, ready for further analyses.



Figure 26. Ball mill

2.4 Analyses of the soil samples

2.4.1 Gamma spectrometry

The detector used was a Canberra BE2820 HPGe with a carbon epoxy window with cryostatic cooling system (CP-5SL). The FWHM (Full Width at Half Maximum): of ^{57}Co (122 keV was 583 eV] and for ^{60}Co 1725 eV at 1332.5 keV. For the determination of ^{226}Ra , the photo peak at 186.3 keV was used.

After the sample preparation procedure, as described in *Section 2.3*, the soil samples were placed in 50 mL yellow top polypropylene pots, with dimensions 55 x 44 mm. The soil samples that were analysed by gamma spectrometry (Figure 27).



Figure 27. Soil sample ready for gamma spectrometry analysis

Pulse height spectra were collected for various times from one hour to twenty - four hours. The resulting spectra were analysed by using Genie 2000 V3.2 (2009v.) which is an analysis software package, incorporating LABSOCS S573 (geometry calibration tool). Genie software uses a standard radionuclide library, tailored to NORM, to analyse the soil samples.

An international certified reference standard (Amersham No. 94) was used on a daily basis as a quality control procedure to ensure that the photon peaks of the above-mentioned radionuclides did not drift.

2.4.1.1 Standardisation of the gamma spectrometer

As with all analytical techniques, for gamma spectrometry to produce reliable and accurate results the spectrometer must be calibrated and tested correctly¹⁰¹⁻¹⁰⁵.

Testing and standardisation included four different procedures which were carried out to determine whether the gamma spectrometer was working correctly. Those procedures included: counting efficiency (CE), minimum detectable activity (MDA), energy tolerance and consideration of errors^{6,92}.

2.4.1.2 Counting Efficiency.

Determination of the activity present in a sample is straightforward if the counting efficiency of the detector is known. Counting efficiency varies with gamma photon energy and can be determined by measurement of a standard containing a mixture of gamma emitting radionuclides or, by calculation^{6,92}.

If measurements of counting efficiency for a given sample-detector geometry are performed, care must be taken that the calibrated sample geometry and matrix is similar to the unknown sample since variations in these affect the counting efficiency. If unknown samples come in different sizes, densities and materials the differences between the calibrated sample and the unknown samples must be recognised and appropriate corrections to the counting efficiency applied. The uncertainty of the measured efficiency is limited by the uncertainties of the calibrated activities; usually, these amount to 1 %^{6,92}.

Alternatively, the counting efficiency can be calculated. The calculations are performed by the Monte – Carlo method or by analytical methods. The main disadvantage of calculations is that their results depend on data on the internal construction of the detector that are not very well known^{5,6}.

The counting efficiency in this research was calculated automatically with Genie 2000 V3.2.1 (2009) spectral analysis software, which incorporates LABSOCS S573. This software tool gives the opportunity to the user to define the geometry parameters of the sampler. The software using this information generates the counting efficiency automatically. It should be noted that counting efficiency and geometry calibration is needed in each individual sample.

2.4.1.6 Preliminary counting of Needles Eye samples

Tables 16 -19 show the results of ^{226}Ra , and its progenies, in various samples and container packaging of the preliminary measurements of Needle's Eye samples from the second visit. The samples were contained in polythene bottles as shown in Figure 27.

Table 8. Preliminary results of ^{226}Ra , ^{235}U , ^{214}Bi and ^{214}Pb distribution for Needle's Eye samples in a YP-P-W container packaging, analysed for 1 hour

Sample	Mass (g)	^{226}Ra (Bq kg ⁻¹)	^{235}U (Bq kg ⁻¹)	^{214}Bi (Bq kg ⁻¹)	^{214}Pb (Bq kg ⁻¹)	Ra/Bi	Ra/Pb
NE1 2mm	25±0.1	2.06±0.41	0.13±0.02	0.61±0.07	0.62±0.06	3.42	3.37
NE1 1mm	25±0.1	<i>1.05±0.21</i>	<i>0.06 ±0.01</i>	<MDA	<i>0.23±0.02</i>	<i>4.56</i>	<i>4.56</i>
NE1 250µm	25±0.1	1.12±0.22	0.07±0.01	<MDA	0.32±0.03	3.5	3.5
NE1 125µm	25±0.1	0.32±0.08	0.02±0.01	<MDA	0.09±0.01	10.66	3.55
NE1 0.063µm	25±0.1	<i>0.33±0.10</i>	<i>0.02±0.01</i>	<MDA	<i>0.05±0.02</i>	3	6.6
NE2 2mm	25±0.1	2.42±1.20	0.17±0.05	1.38±0.09	1.43±0.13	1.75	1.69
NE2 1mm	25±0.1	3.05±1.24	0.17±0.04	2.08±0.10	1.95±0.17	1.46	1.56
NE2 250µm	25±0.1	5.98±2.07	0.28±0.06	3.92±0.16	3.75±0.34	1.52	1.59
NE2 125µm	25±0.1	2.00±0.90	0.10±0.03	1.21±0.07	1.12±0.10	1.65	1.78
NE2 0.063µm	25±0.1	2.22±0.82	0.08±0.03	0.93±0.06	0.91±0.08	2.38	2.43
NE3 2mm	25±0.1	3.67±2.10	0.45±0.06	0.76±0.08	0.85±0.08	4.82	4.31
NE3 1mm	25±0.1	<i>5.43±2.77</i>	<i>0.54±0.08</i>	<i>2.02±0.13</i>	<i>2.00±0.18</i>	2.68	2.71
NE3 250µm	25±0.1	8.75±3.79	0.60±0.12	5.05±0.34	4.99±0.46	1.73	1.75
NE3 125µm	25±0.1	<i>27.0 ±10.3</i>	<i>1.65±0.28</i>	<i>18.1±0.78</i>	<i>17.4±1.59</i>	<i>1.49</i>	<i>1.55</i>
NE3 0.063µm	25±0.1	<i>31.6±10.2</i>	<i>1.39±0.27</i>	<i>17.2±0.79</i>	<i>16.8±1.53</i>	1.83	1.88
NE4 2mm	25±0.1	3.64±1.28	0.17±0.03	2.40±0.12	2.21±0.20	1.51	1.64
NE4 1mm	25±0.1	3.23±1.10	0.13±0.03	1.56±0.10	1.44±0.13	2.07	2.24
NE4 250µm	25±0.1	3.14±0.92	0.09±0.03	1.63±0.07	1.50±0.13	1.92	2.09
NE4 125µm	25±0.1	3.47±1.59	0.18±0.06	2.05±0.15	2.09±0.19	1.69	1.66
NE4 0.063µm	25±0.1	2.55±0.92	0.08±0.03	1.25±0.12	1.23±0.11	2.04	2.07
NE5 2mm	25±0.1	0.48±0.12	0.03±0.01	<MDA	0.16±0.02	9.6	3
NE5 1mm	25±0.1	0.42±0.09	0.02±0.01	0.15±0.02	0.15±0.01	2.8	2.8
NE5 250µm	25±0.1	0.49±0.13	0.03±0.01	<MDA	0.18±0.02	8.16	2.72
NE5 125µm	25±0.1	0.19±0.06	0.01±0.01	<MDA	0.09±0.01	9.5	2.11
NE5 0.063µm	25±0.1	0.26±0.06	0.01±0.01	<MDA	0.11±0.01	8.66	2.36

Note: the results presented in *italics* are from spectra which where energy peaks have drifted out of the counting channel. YP = yellow pot, P = parafilm, W = wax.

Table 9. Preliminary results of ^{226}Ra , ^{235}U , ^{214}Bi and ^{214}Pb distribution for 1 kBq ^{226}Ra spike (counted in 14 replicates) sample within a YP-P-W-T container packaging, analysed for 1 hour

Ra Spike	Mass (g)	^{226}Ra (Bq kg⁻¹)	^{235}U (Bq kg⁻¹)	^{214}Bi (Bq kg⁻¹)	^{214}Pb (Bq kg⁻¹)	Ra/Bi	Ra/Pb
Rep. 1	47±0.1	13.9±3.7	0.87±0.9	5.45±2.33	2.82±1.67	2.55	4.92
Rep. 2	47±0.1	13.8±3.7	0.86±0.9	4.49±2.11	3.99±1.99	3.07	3.45
Rep. 3	47±0.1	13.5±3.6	0.84±0.9	4.41±2.10	3.83±1.95	3.06	3.52
Rep. 4	47±0.1	13.5±3.6	0.84±0.9	4.41±2.10	3.83±1.95	3.06	3.52
Rep. 5	47±0.1	27.2±5.2	1.71±1.3	10.9±3.30	10.1±3.17	2.49	2.69
Rep. 6	47±0.1	27.1±5.2	1.70±1.3	11.4±3.37	10.4±3.22	2.37	2.60
Rep. 7	47±0.1	20.3±4.5	1.27±1.12	11.9±3.44	10.9±3.30	1.70	1.86
Rep. 8	47±0.1	22.5±4.7	1.41±1.18	13.6±3.68	12.1±3.47	1.65	1.85
Rep. 9	47±0.1	22.5±4.7	1.41±1.8	13.6±3.68	12.1±3.47	1.65	1.85
Rep. 10	47±0.1	22.5±4.7	1.41±1.18	12.4±3.52	11.8±3.43	1.81	1.90
Rep. 11	47±0.1	22.5±4.7	1.41±1.18	12.4±3.52	11.8±3.43	1.81	1.90
Rep. 12	47±0.1	22.5±4.7	1.41±1.18	14.8±3.84	13.5±3.67	1.52	1.66
Rep. 13	47±0.1	22.2±4.7	1.39±1.17	13.4±3.66	12.8±3.57	1.65	1.73
Rep. 14	47±0.1	22.4±4.7	1.40±1.18	15.4±3.92	14.7±3.83	1.45	1.52

Note: the results presented in *italics* are from spectra which where energy peaks have drifted out of the counting channel. YP = yellow pot, P = parafilm, W = wax, T = tape

Table 10. Preliminary results of ^{226}Ra , ^{235}U , ^{214}Bi and ^{214}Pb distribution for a ^{226}Ra source (counted in 9 replicates) and a radium contaminated watch sample (counted in 4 replicates) analysed for 1 hour

Sample	Container	Mass (g)	^{226}Ra (Bq kg ⁻¹)	^{235}U (Bq kg ⁻¹)	^{214}Bi (Bq kg ⁻¹)	^{214}Pb (Bq kg ⁻¹)	Ra/Bi	Ra/Pb
Ra source 1	Sealed	5	3288±57.3	206±14.31	5752±75	3659±60	0.57	0.89
Ra source 2	Sealed	5	773±27.8	48.5±6.96	1399±37	894±30	0.55	0.86
Ra source 3	Sealed	5	797.8±28.2	50±7.07	1492±38	897±30	0.53	0.88
Ra source 4	Sealed	5	12118±110	760.6±27.5	18965±137	13246±115	0.63	0.91
Ra source 5	Sealed	5	4602±67.8	288±16.9	7179±84	5135±71	0.64	0.89
Ra source 6	Sealed	5	4602±67.8	288±16.9	7179±84	5135±71	0.64	0.89
Ra source 7	Sealed	5	4215±64.9	264±7.74	7311±85	4579±67	0.57	0.92
Ra source 8	Sealed	5	964±31.04	60±7.93	1580±39	1081±32	0.61	0.89
Ra source 9	Sealed	5	1014±31.84	63±8.27	1600±40	1077±32	0.63	0.94
Watch 1	N/A	7	1092±33.04	68.5±4.21	443±21	418±20	2.46	2.61
Watch 2	N/A	7	284±16.85	17.8±4.19	110±10	109±10	2.58	2.6
Watch 3	N/A	7	281±16.76	17.6±4.17	122±11	117±10	2.3	2.4
Watch 4	N/A	7	1163±34.71	73±8.54	470.6±21	450.4±21	2.47	2.58

Note: the results presented in *italics* are from spectra which have drifted

Table 11. Preliminary results of ^{226}Ra , ^{235}U , ^{214}Bi and ^{214}Pb distribution for a soil test sample (10 replicates) within a variety of container packaging, analysed for 1 hour

Sample	Mass (g)	^{226}Ra (Bq kg ⁻¹)	^{235}U (Bq kg ⁻¹)	^{214}Bi (Bq kg ⁻¹)	^{214}Pb (Bq kg ⁻¹)	Ra/Bi	Ra/Pb
Test 1	59.23±0.1	24.8±4.98	1.00±1.00	13.1±3.61	13±3.60	1.89	1.9
Test 2	59.23±0.1	24.7±4.97	0.98±0.99	16.5±4.06	16±4.00	1.49	1.54
Test 3	59.23±0.1	24.7±4.97	0.98±0.99	16.5±4.06	16±4.00	1.49	1.54
Test 4	59.23±0.1	20.1±4.48	1.23±1.10	19.2±4.38	19.2±4.38	1.04	1.04
Test 5	59.23±0.1	26.2±5.11	0.86±0.92	19.8±4.45	19.9±4.46	1.32	1.31
Test 6	59.23±0.1	25.7±5.07	0.99±0.99	19.7±4.43	20.1±4.48	1.3	1.27
Test 7	59.23±0.1	23.1±4.80	1.11±1.05	21.2±4.60	20.7±4.55	1.08	1.11
Test 8	59.23±0.1	23.1±4.80	1.11±1.05	21.2±4.60	20.7±4.55	1.08	1.11
Test 9	59.23±0.1	23.7±4.86	1.00±1.00	21.5±4.63	20.6±4.53	1.1	1.15
Test 10	59.23±0.1	24.7±4.97	1.00±1.00	21.6±4.64	21.1±4.53	1.14	1.17

Note: the results presented in *italics* are from spectra which where energy peaks have drifted out of the counting channel. YP = yellow pot, P = parafilm, W = wax, T = tape

In Tables 16 - 19, YP is a yellow top pot with dimensions 55 x 44 mm and a screw lid. P refers to parafilm tape wrapped around the lid and T refers to Teflon tape that was wrapped around the screw thread of the plastic pot lid, and W for wax that was used to cover the crack between the lid and the pot.

The results shown in the Tables 16 - 19 show that ^{226}Ra is not in secular equilibrium with its daughters ^{214}Pb and ^{214}Bi as should be expected. When equilibrium is achieved the ratios of $^{226}\text{Ra}/^{214}\text{Pb}$ and $^{226}\text{Ra}/^{214}\text{Bi}$ are 1. The majority of the measurements give ratios greater than one, which demonstrates that secular equilibrium is not occurring and that the measured ^{226}Ra activities are higher than those of the $^{214}\text{Pb}/^{214}\text{Bi}$ daughters. Possible reasons for these discrepancies are:

i) Instrumental problems:

- a) Photo peak drift where the peaks of interest (^{226}Ra , ^{214}Bi and ^{214}Pb) are drifting out of the regions of interest in the gamma spectrum and therefore ^{226}Ra , ^{214}Bi and or ^{214}Pb are not been fully measured. All the spectra from the samples shown

in the Table were re-examined and possible drift noted. As can be seen in the Table, the spectra which drifted did not show a ratio of one but, in addition to these, the spectra that did not show any drift also did not show a ratio of one. Therefore, drift of the photo peak alone was not the only reason for the apparent lack of attainment of secular equilibrium. However, after noting the lack of secular equilibrium, the gamma spectrometer was checked for drift by using a ^{152}Eu standard source.

- b) Use of the wrong counting efficiencies. Counting efficiency is defined as the measured counts per second divided by the number of Becquerels in the sample for a radionuclide of particular gamma photon energy (Equation 17) ⁶.

$$\text{Counting efficiency} = \frac{\text{Measured photopeak activity}}{\text{Theoretical photopeak activity}} \quad \text{Equation 4}$$

The counting efficiency is used in the calculation to convert observed, measured count rate to Becquerels. Genie, the software used to calculate activities uses the counting efficiencies of ^{226}Ra , ^{214}Bi and ^{214}Pb to calculate the activities of ^{226}Ra , ^{214}Pb and ^{214}Bi . At the start of the project, the instrumentation was calibrated for counting efficiency by using an Eckert & Ziegler Isotope Products ^{226}Ra standard solution (^{226}Ra , 370 kBq +/- 15%, 5 mL fill in 5 mL FSA). Again, after noting the lack of secular equilibrium, the instrument was regularly checked to ensure the correct counting efficiencies of the photo peaks.

Counting efficiency is also affected by geometry which can be altered by the mass of the sample in the counting pot. The results in Tables 16 - 19 show that equilibrium was not achieved by changing the mass of the sample in the counting pot.

- c) Subtraction of background during the calculation of activities. The background was regular recorded, and the new values used in calculations of activities.
- ii) Loss of radon. Radon gas is an intermediate between ^{226}Ra and ^{214}Bi and ^{214}Pb and must not be lost from the container that holds the sample. If there is loss of

^{226}Ra then equilibrium will not be reached between ^{226}Ra and ^{214}Bi and ^{214}Pb and the measurement of either ^{214}Bi or ^{214}Pb cannot be used to determine the activity of Ra. All of the samples shown in Tables 16 - 19 were measured in a plastic pot and, even though some of the measurements were made with Teflon tape and/or were sealed with wax, the results of the measurements show that equilibrium was not achieved. To check whether loss of ^{222}Rn by possible diffusion through the plastic container, cylindrical aluminium containers with dimensions 53 x 27.5 mm were purchased online from Amazon and used in future measurements.

iii)

Table 12. Gamma - ray absorption experiment

Al thickness (mm)	122 keV peak	245 keV peak	344 keV peak
0.02	23.63	76.5	46.8
0.22	24.33	73.5	46.6
0.23	24	76.8	49.1
0.26	23.1	75	46.8
0.31	23.1	73.4	45.8
0.4	23.1	75.9	46.3
0.5	22.8	74.7	45.6
0.61	22.9	75.7	46.9
0.63	23.3	76.2	47.6
0.69	23.6	76.4	47.8
0.81	23.3	75.8	47.7
0.93	22.7	73.8	44
1.16	23.6	77.6	48.3
1.19	22.5	73.5	45.1
1.6	23.8	79.7	48.9
1.87	23.6	76.6	48
2.06	22.6	75.8	45.9
2.62	24.2	79	49.3
3.22	23.7	76.7	47.8
4.87	24.2	79.9	48.4
5.64	26.3	77.8	49.6
6.35	24	78.4	49.3

To investigate whether the use of aluminium pots would attenuate the low energy gamma photons (186 keV) from ^{226}Ra , a set of measurements were taken using a ^{152}Eu standard source (122 keV, 245 keV and 344 keV) and aluminium absorbers of known thickness. The measurements were taken using a ^{152}Eu sealed source and the results are shown in Table 20 and Figure 49 below.

The aim of this experiment was to investigate the attenuation of different gamma ray energies (122 keV, 245 keV and 344 keV) by different thicknesses of aluminium. These energies were chosen because they provide a range of energies around the 186 keV peak of ^{226}Ra . Values in bold represent the thickness of the aluminium pot used in this research.

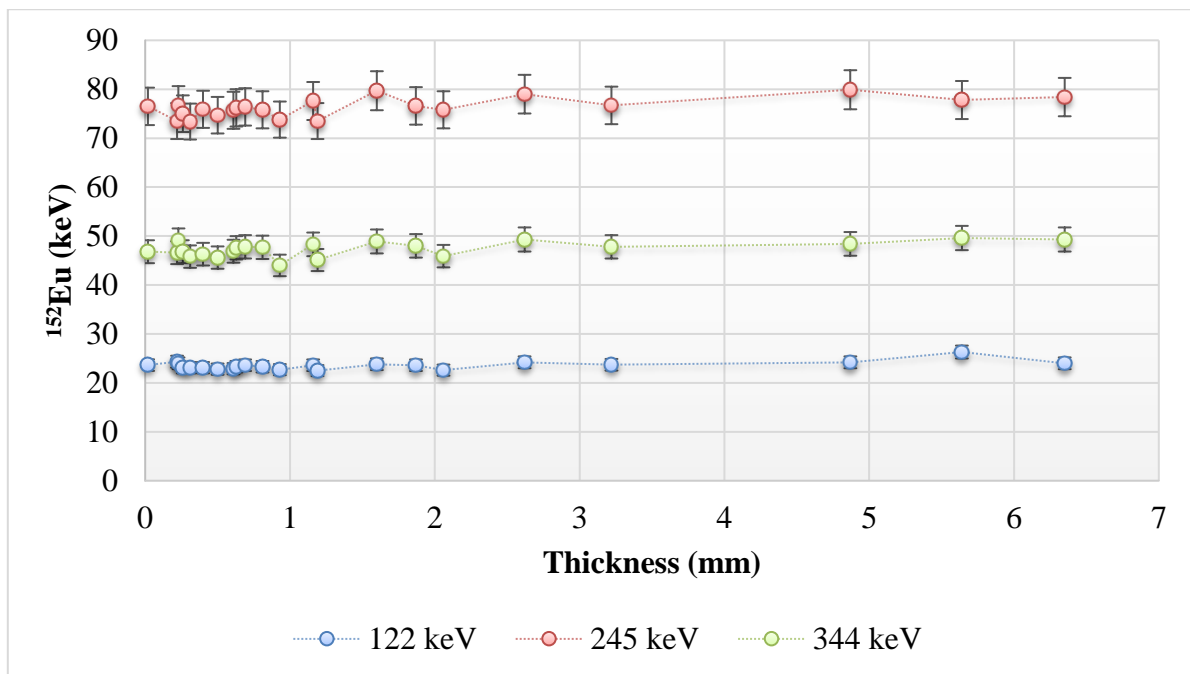


Figure 28. Plot to determine the extent of ^{152}Eu gamma photon attenuation as a function of aluminium thickness

The results shown in Figure 48 demonstrate that when using a thickness of 1.16 mm (bold in Table 17), which is the same thickness as that of the base of the aluminium can, there is no evidence of attenuation of gamma photons emitted from ^{226}Ra .

To investigate further the effect of time after sealing an aluminium pot on the attainment of secular equilibrium, aluminium sealed aluminium pots containing samples of NE1-b and NE3-b soils were sealed and then counted after various times

Table 13. Shows the results from the measurement of sample NE1-b and the results for sample NE3-b as a function of time after placing the sample into the aluminium pot

Sample	Time (days)	²²⁶ Ra (Bq kg ⁻¹)	²³⁵ U (Bq kg ⁻¹)	²¹⁴ Pb (Bq kg ⁻¹)	²¹⁴ Bi (Bq kg ⁻¹)
NE1-b	1	7.64 ± 4.02	0.72 ± 0.72	4.95 ± 0.46	5.08 ± 0.31
NE1-b	2	10.05 ± 4.79	0.8 ± 0.15	6.05 ± 0.56	6.08 ± 0.39
NE1-b	6	38.92 ± 13.5	1.99 ± 0.37	21.9 ± 1.92	23.6 ± 0.9
NE1-b	7	45 ± 13.4	1.63 ± 0.34	23.3 ± 2.04	24.2 ± 0.94
NE1-b	9	43.4 ± 13.5	1.73 ± 0.35	24.3 ± 2.13	24.6 ± 0.93
NE1-b	10	39.9 ± 13.6	1.96 ± 0.36	24.6 ± 2.16	25.3 ± 1
NE1-b	13	41.1 ± 13.2	1.8 ± 0.34	24.7 ± 2.16	24.8 ± 0.93
NE1-b	14	24.7 ± 2.16	1.66 ± 0.32	24.1 ± 2.13	25.3 ± 0.95
NE1-b	15	41.8 ± 13.1	1.73 ± 0.34	24.2 ± 2.11	25.3 ± 0.95
NE1-b	16	41.6 ± 13.1	1.75 ± 0.34	24.2 ± 2.13	25.9 ± 0.95
NE1-b	20	40 ± 12.9	1.73 ± 0.34	29.7 ± 2.59	31.04 ± 1.11
NE1-b	21	41.4 ± 13.2	1.73 ± 0.36	31.3 ± 2.74	33.1 ± 1.17
NE1-b	22	38.6 ± 13.1	1.87 ± 0.36	32.5 ± 2.83	34.4 ± 1.2
NE1-b	23	44.2 ± 13.6	1.7 ± 0.36	34.1 ± 2.45	36.4 ± 1.24
NE1-b	24	3250.6 ± 1097.9	138.7 ± 30	2709.3 ± 234.6	2630 ± 105.8
NE3-b	1	7.51 ± 0.48	0.92 ± 0.17	7.17 ± 0.66	7.04 ± 0.4
NE3-b	2	10 ± 4.88	0.81 ± 0.17	7.6 ± 0.67	7.19 ± 0.47
NE3-b	4	8.92 ± 0.49	0.89 ± 0.17	7.2 ± 0.66	7.05 ± 0.42
NE3-b	5	9.84 ± 4.81	0.84 ± 0.16	7.48 ± 0.69	7.24 ± 0.44
NE3-b	8	9.03 ± 4.75	0.84 ± 0.16	7.3 ± 0.67	7.16 ± 0.42
NE3-b	9	749.9 ± 388	68.4 ± 13.5	576.7 ± 53.5	533.3 ± 30.7
NE3-b	10	8.81 ± 4.88	0.88 ± 0.17	7.17 ± 0.66	7.47 ± 0.43
NE3-b	11	9.32 ± 4.88	0.86 ± 0.17	7.11 ± 0.66	7.24 ± 0.42
NE3-b	15	8.05 ± 4.57	0.85 ± 0.16	7.47 ± 0.69	7.52 ± 0.44
NE3-b	16	9.01 ± 4.54	0.79 ± 0.16	7.13 ± 0.42	7.26 ± 0.67
NE3-b	17	11.8 ± 4.45	0.63 ± 0.14	7.48 ± 0.69	7.25 ± 0.44
NE3-b	18	9.7 ± 4.95	0.83 ± 0.18	8.02 ± 0.72	8.35 ± 0.45
NE3-b	19	757.7 ± 391.2	67.1 ± 14	632.8 ± 58.6	584.4 ± 39.4

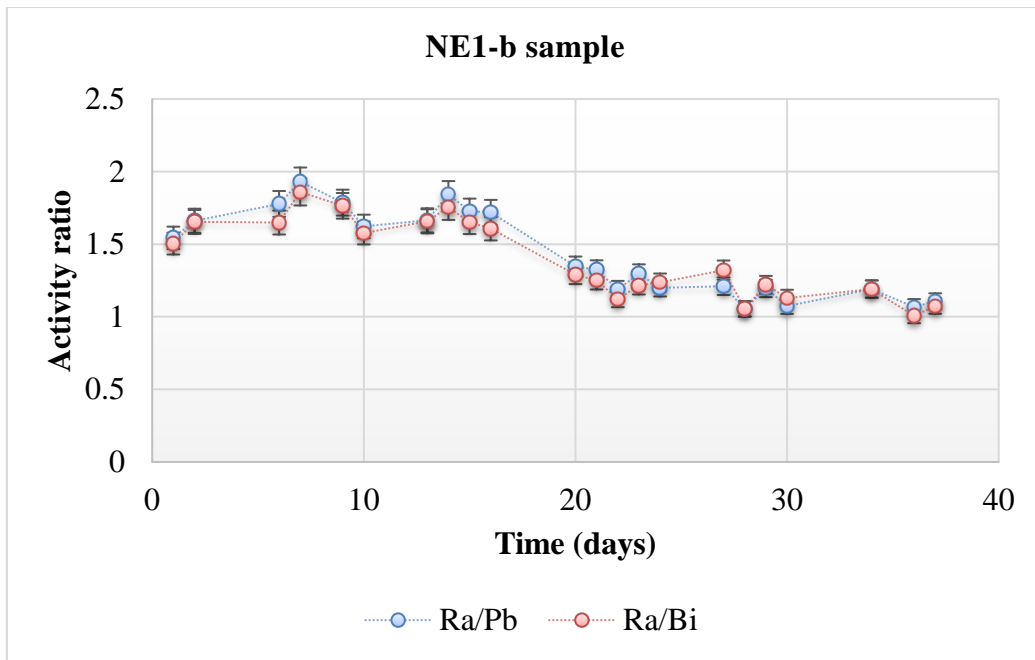


Figure 29. Ra/Pb and Ra/Bi activity ratios for the NE1-b sample in the aluminium pot

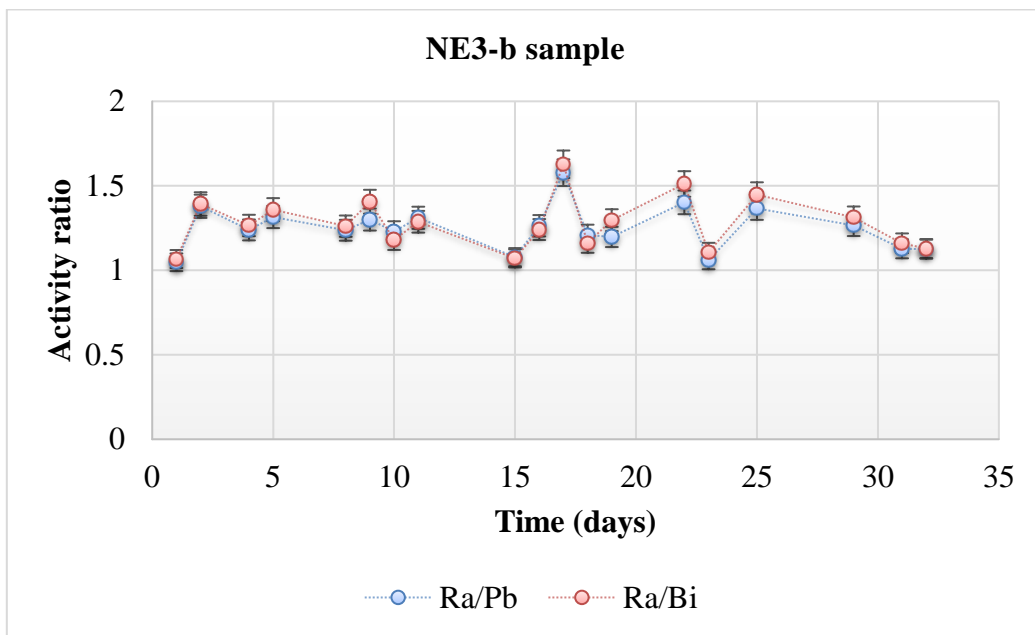


Figure 30. Ra/Pb and Ra/Bi activity ratios for NE1-b sample in the aluminium pot

The results shown in Table 18 and in Figures 29 and 30 show that the use of aluminium pots to count samples NE1-b and NE3-b have been partially successful in containing the radon gas and with Ra/Pb and Ra/Bi ratios of approximately 1.2 for NE1-b and 1.2 to 1.3 for NE3-b. These ratios are much closer to the expected value of 1.0 than those from the measurements taken when using plastic pots.

Therefore, for the further gamma measurements of the soil samples from Needle's Eye site were made in aluminium pots as they provide better containment of radon (Figure 31).



Figure 31. Aluminium pots used in this research project

2.4.1.7 ^{235}U interference calculations and the use of the Genie program

As stated previously, the presence of ^{235}U in a sample can interfere with the measurement of ^{226}Ra because of the closeness of the energies of their gamma photons (185.7 keV for ^{235}U and 186 keV for ^{226}Ra). At the head of the chain, in which ^{226}Ra is a member is ^{238}U which is 99.28% of natural uranium. The remaining 0.72% of natural uranium is ^{235}U . As ^{226}Ra is a progeny of ^{238}U , it is inevitable that ^{235}U will also be present in samples that contain ^{226}Ra .

To further investigate the possible interference of ^{235}U when measuring ^{226}Ra , a calculation was made to estimate the contribution of ^{235}U when measuring e.g. 1 kBq of ^{226}Ra . Assuming secular equilibrium in the ^{238}U chain, 1 kBq of ^{238}U should be present alongside 1 kBq of ^{226}Ra . The calculation below shows that if 1 kBq of ^{226}Ra was measured, a contribution of 46 Bq would arise from the overlap of ^{235}U . Say 1 kBq ^{238}U is in equilibrium with 1 kBq ^{226}Ra ,

$$^{238}\text{U} \text{ 1000} = \frac{0.693}{4.468 \times 10^9 \times 365 \times 24 \times 3600} \times N = \mathbf{2.0332 \times 10^{20}} \quad \text{Equation 5}$$

$$\text{Mass } ^{238}\text{U} = \frac{2.0332 \times 10^{20}}{6.023 \times 10^{23}} \times 238 \text{ g} = \mathbf{80.33 \times 10^{-3} \text{ g of } ^{238}\text{U}}, \text{ Mass } ^{235}\text{U} = \frac{0.73}{100} \times 80.33 \times 10^{-3} \text{ g} =$$

$$\mathbf{0.586 \times 10^{-3} \text{ g of } ^{235}\text{U}}, N \text{ of } ^{235}\text{U} = \frac{0.556 \times 10^{-3}}{235} \times 6.023 \times 10^{23} = \mathbf{0.01502 \times 10^{20}},$$

$$\text{Bq } ^{235}\text{U} = \frac{0.693}{2.2195 \times 10^{16}} \times 0.01502 \times 10^{20} = \mathbf{46.9 \text{ Bq}}$$

The conclusion from the foregoing calculation is that the contribution of ^{235}U to the ^{226}Ra measurement is not the reason for the apparent lack of secular equilibrium between ^{226}Ra and ^{214}Pb and ^{214}Bi .

Genie 2000 is a computer software supplied by Canberra to collect gamma spectra and to process the measurements so as to provide results expressed in e.g. Bq kg^{-1} . To check that Genie is using the correct calculations to deliver the activity concentration of a radionuclide, the following calculations were carried out:

- a) Manual subtraction of interference of ^{235}U from the total peak counts to provide the peak counts from ^{226}Ra .

The following calculation uses the results reported by Genie from the measurement of NE1 measured on 27th February 2017 (Table 14). NE1-b mass = 40 g, counting time = 3619 seconds

Table 14. ^{235}U and ^{226}Ra calculations for NE1-b sample

Radionuclide	Energy keV	Yield%	Counting Efficiency	Peak Counts	Activity Bq kg^{-1}	Corrected activity Bq kg^{-1} (mean)
^{235}U	143.8	10.6	0.05	1860	1.52×10^2	1.11×10^2
	185.7	57.2	0.035	14100	2.80×10^2	
^{226}Ra	186.2	3.53	0.035	14100	44.6×10^2	26.95×10^2

Total counts at 186 keV

$$C_T = {}^{226}\text{Ra}_{\text{counts}} + {}^{235}\text{U}_{\text{counts}} \Leftrightarrow {}^{226}\text{Ra}_{\text{counts}} = C_T - {}^{235}\text{U}_{\text{counts}} = \mathbf{14100} - {}^{235}\text{U}_{\text{counts}}$$

²³⁵U counts at 186 keV

$$2.80 = \frac{\text{counts}}{3619} \times \frac{1}{0.035} \times \frac{1}{0.572} \times \frac{1}{40} \Leftrightarrow \text{counts} = \mathbf{8115}$$

$${}^{226}\text{Ra Bq kg}^{-1} = \frac{(14100-8115) \times 10^2}{3619} \times \frac{1}{0.039} \times \frac{1}{0.0353} \times \frac{1}{40} = \mathbf{33.46 Bq kg}^{-1}$$

The calculated value of $33.46 \times 10^2 \text{ Bq kg}^{-1}$ compares to the Genie 2000 calculated value of 26.95 Bq kg^{-1} . Therefore, the ‘*interference corrected*’ value of Bq kg^{-1} of ²²⁶Ra as reported by Genie 2000 takes into account the interference from ²³⁵U.

If $1.52 \times 10^2 \text{ Bq kg}^{-1}$ of ²³⁵U would have been used for the calculation of ²³⁵U in the ²²⁶Ra peak, then $18.1 \times 10^2 \text{ Bq kg}^{-1}$ would have been calculated. Genie 2000 probably uses an average of $2.16 \text{ Bq} \times 10^2 \text{ kg}^{-1}$ ²³⁵U which calculates as ²²⁶Ra interference corrected result of $25.81 \times 10^2 \text{ Bq kg}^{-1}$ which compares more favourably with the Genie 2000 reported value of $26.95 \times 10^2 \text{ Bq kg}^{-1}$.

- b) Use of Genie to report the interference corrected value for ²²⁶Ra.

Table 15 contains Genie reported measurements for the NE1-b.

Table 15. Measurements for NE1-b sample

Original Peak Area	Corrected Peak Area	Identified Radionuclides (²²⁶ Ra Bq kg ⁻¹)	Interference Corrected Radionuclides (²²⁶ Ra Bq kg ⁻¹)
14100	14100	44.61 ± 7.85	26.95 ± 8.50

The corrected area is the background corrected area and not the corrected area resulting from the subtraction of ²³⁵U counts. Using the calculation reported by Gilmore⁶:

$$\text{Corrected } {}^{226}\text{Ra (Bq kg}^{-1}\text{)} = 0.5709 \times \text{Apparent } {}^{226}\text{Ra}$$

For the NE1-b sample as used in the manual calculation,

$$\text{Corrected } ^{226}\text{Ra (Bq kg}^{-1}\text{)} = 0.5709 \times 44.6 = 25.46 \text{ Bq kg}^{-1}$$

25.46 Bq kg⁻¹ compares favourably with the value reported by Genie of 26.9 Bq kg⁻¹.

The following calculation confirms the factors used to correct the total 186 keV photo peak for interference from ²³⁵U to report the corrected value for ²²⁶Ra activity concentration.

$$\text{Activity (Bq)} = \lambda N \quad \text{Equation 6}$$

where:

$$\lambda = \text{Decay constant (s}^{-1}\text{)}$$

$$N = \text{Number of atoms}$$

Decay constant:

$$\lambda = \frac{\ln(2)}{\text{half-life (s)}} \quad \text{Equation 7}$$

Assuming secular equilibrium in the ²³⁸U chain, 1000 Bq of ²³⁸U should be present alongside 1000 Bq of ²²⁶Ra. The calculation on page 101 shows that, if ²³⁸U and ²³⁵U are in their natural abundance states (²³⁸U 99.274%, ²³⁵U 0.720%) then 1000Bq of ²³⁸U has a mass of 80.33 x 10⁻³ g and the mass of ²³⁵U is 0.586 x 10⁻³ g. The activity of ²³⁵U is 46.89 Bq.

Therefore,

$$1000 \text{ Bq } ^{226}\text{Ra} = C_{Ra} \times \frac{1}{\gamma\text{yield}} \times \frac{1}{CE},$$

$$\gamma\text{yield} = 0.0359,$$

$$CE = \text{counting efficiency}$$

$$C_{Ra} = 1000 \times \gamma\text{yield} \times CE$$

$$45.49 \text{ Bq } ^{235}\text{U} = C_U \times \frac{1}{\gamma\text{yield}} \times \frac{1}{CE} \Leftrightarrow \gamma\text{yield} = 0.572 \Leftrightarrow C_U = 46.89 \times \gamma\text{yield} \times CE$$

So,

$$\text{Total Peak Counts} = C_{Ra} + C_U = (1000 \times \gamma\text{yield} \times CE) + (46.89 \times \gamma\text{yield} \times CE)$$

$$= (1000 \times 0.0359 \times CE) + (46.89 \times 0.572 \times CE) = 35.9CE + 26.82CE = CE(35.9 + 26.82) = \mathbf{62.72CE}$$

Contribution to 186 keV peak:

$${}^{226}\text{Ra} = \frac{35.9CE}{62.72CE} = \frac{35.9}{62.72} = 0.5724$$

$${}^{235}\text{U} = \frac{26.02CE}{62.72CE} = \frac{26.77}{62.72} = 0.4268$$

The calculated value of 0.5724 is similar, but slightly different, to that quoted by Gilmore⁶ and previously quoted by Giles¹⁷¹ (0.571). Using 0.571 value, the interference corrected activity concentration for ²²⁶Ra is 25.46 Bq kg⁻¹ whereas using 0.5724, the calculated value is 25.53 Bq kg⁻¹. The Genie quoted value for the interference corrected ²²⁶Ra activity concentration is 26.95 Bq kg⁻¹. Within the error quoted by Genie these values are in good agreement.

When Genie detects the presence of ²³⁵U in a sample (by cross reference to 143.8 keV peak), the Genie software subtracts the contribution of ²³⁵U from the total 186 keV photo peak and thus reports correctly the ²²⁶Ra activity concentration. To confirm this, further, an aqueous ²²⁶Ra spiked standard was measured by gamma spectrometry. The ²²⁶Ra solution does not contain ²³⁵U and the “original peak area” as reported by Genie software should be the same as the “corrected peak area” and the activity concentrations of the “identified nuclides” should be the same as that of the “interference corrected report”. The values shown below in Table 16 reported by Genie show that this is the case for an aqueous ²²⁶Ra spiked solution.

Table 16. Results for ²²⁶Ra spike solution at the 186 keV photo peak

Original Peak Area (counts)	Corrected Peak Area (counts)	Identified Radionuclides (²²⁶ Ra Bq kg ⁻¹)	Interference Corrected Radionuclides (²²⁶ Ra Bq kg ⁻¹)
8660	8660	33.72 ± 5.96	33.72 ± 5.96

The conclusion to the forgoing discussion is that although, normally, ^{226}Ra can only be measured directly by gamma spectrometry using the 186 keV photo peak of ^{235}U , and therefore ^{238}U , are absent from an environmental sample. If $^{238}\text{U} - ^{235}\text{U}$ are present in the sample, then the use of a computer software such as Genie, subtracts the contribution of ^{235}U for the photo peak allowing the ^{226}Ra activity to be reported accurately. The above calculations and considerations give confidence in the use of Genie 2000 software package for reporting activity of ^{226}Ra in an environmental sample.

2.4.2 pH Determination

For the determination of the pH of the soil water, suspensions of 1:10 solid to liquid ratio, i.e., 1 g in 10 mL of deionised H_2O were prepared in polypropylene tubes and then shaken gently overnight to equilibrate⁶⁴. pH measurements were obtained with a Hanna Instruments HI 98129 pH EC TDS Conductivity Tester Meter ORIGINAL.

The pH meter required calibration before pH measurements, and this was achieved by immersing the pH electrode into buffers (test solutions of known pH) and then adjusting the meter accordingly. Three buffer solutions (by SIGMA - ALDRICH) were used to calibrate the pH meter, of pHs 10.01, 7.00 and 4.01.

2.4.3 X-Ray Diffraction

The identification and quantification of the different mineral phases that are present in soil samples can be challenging. Powder X-ray diffraction (PXRD) is the most commonly used technique for the phase identification of crystalline phases in soil samples. PXRD cannot be used for the analysis of non – crystalline or poorly crystalline phases. Every PXRD pattern occurs as a sequence of reflections which can be matched using the ICDD database to identify known phases in a sample. The quality of the generated pattern is affected by the crystal system, as well as the space group and cell parameters in such a way that an individual phase produces a unique pattern that can be matched in the same way as a fingerprint¹¹⁸.

X-rays have the ability to irradiate the analysed material, in a way that the incident X-rays can interact with the electrons that are present in the sample, and this process leads to X-ray

scattering as a result of the interactions with the electrons of the atoms that are present in the analysed material¹¹⁸.

2.4.3.1 Generation of X-rays

The generation of X-rays results from the interaction of a beam of particles of high energy, such as electrons, with matter. The production of electrons occurs by increasing the temperature of a filament, the electrons then accelerate in a vacuum assisted with a high electric field from 20 to 60 kV towards an anode, i.e. a metal target. The generated electric current varied from 5 to 100 mA. The described process is inefficient as 99 % of the energy generated by the beam heats the metal target and only 1 % produces X-rays¹¹⁸.

The generation of a continuous white radiation (i.e. spectrum of X-rays), is a result of the collision (i.e. electrons – metal target). The shortest wavelength (λ_{\min}) of the spectrum is controlled by the maximum energy loss (E_{\max}) and is expressed by the Equation 21¹¹⁸:

$$E = e V = h c / \lambda \quad \text{Equation 8}$$

Where,

e = the charge on the electron,

V = the accelerating voltage,

h = Planck's constant,

c = the speed of light.

Another practical expression of Equation 21 can be:

$$\lambda = 12.398 / V$$

Where,

V = in kilovolts,

λ = wavelength expressed in Angstroms ($1 \text{ \AA} = 0.1 \text{ nm}$).

Both equations show that higher the acceleration of the X-ray generator voltage, the shorter will be the λ_{\min} that can be attained. When the value of the wavelength is approximately expressed by the $1.5 \times \lambda_{\min}$ then the intensity of the X-ray spectrum reaches its maximum value. Longer wavelengths can be attained by processes of multiple collisions¹¹⁸.

2.4.3.2 PXRD principle

It was discovered by Max von Laue¹¹⁹ (1912) that crystalline substances can act as three-dimensional gratings for X-ray wavelengths similar to the spacing of planes in crystal lattice. Nowadays, PXRD technique is a common tool for the investigation and identification of crystallised materials¹¹⁸.

It is reported that within the X-ray region, the electromagnetic radiation may have relatively short wavelengths. Thus, it is expected that X-rays can be more penetrative when they have high energies compared to visible, UV rays, or radio waves¹¹⁸.

Crystalline materials have ordered three-dimensional arrangements of their atoms with characteristic interplanar or diffraction spacing (*d*-spacing). As the spacing between atoms is on the same order of magnitude as X-ray wavelengths (1-3 Å), crystals can diffract the radiation¹¹⁸.

The Bragg Equation 22:

$$n\lambda = 2d \sin\theta \quad \text{Equation 9}$$

Where,

λ = any given wavelength,

θ = certain angle of diffraction for a given diffraction spacing (*d*)

n = number of wavelengths

The use of powdered samples aims to achieve the maximum degree of completely random orientation of the crystals of the material, and therefore, diffraction from all possible angles simultaneously¹¹⁸.

PXRD is at best a semi-quantitative method for crystalline phases. Factors such as the nature of sample and its composition, operators' skill level and operating conditions of the diffractometer employed can allow more accurate quantification¹¹⁸.

2.4.3.3 Phase Identification by Powder X-ray Diffraction

In the present study, the characterisation of Needle's Eye soil samples was carried out using a Bruker D8 Discover powder diffractometer operating with monochromatic cobalt $\text{K}\alpha_1$ radiation and position sensitive detector in transmission mode.

All soils were crushed and sieved through a 2 mm mesh and homogenised with a ball mill. After homogenising, 0.1 g of each sample was placed between two layers of Scotch Magic Tape (Figure 32) ready for further analysis.



Figure 32. Soil sample ready for PXRD analysis

Data were collected from each sample for a period of 23 hours using the PXRD control software, DIFFRAC plus. The samples were run from 10° to 80° with 0.014step size and 9745 steps. The patterns were evaluated using the EVA software and the phases identified by comparison with the ICDD (International Centre for Diffraction Data) database. The phase ID

data from the PXRD analysis were supported by X-ray fluorescence spectroscopy as described in Section 2.4.4.4.

2.4.4 Elemental Analyses

Elemental analyses of the Needles Eye samples were achieved by using Inductively Coupled Mass Spectrometry (ICP - MS), Inductively Coupled Optical Emission Spectroscopy (ICP - OES), X-ray fluorescence (XRF) and CHN elemental analysis. Both ICP techniques are destructive spectroscopic methods that are used to quantify the concentrations of species present in solution. The main difference between these two methods is detection. ICP-MS uses mass spectrometry for detection¹²⁰, whereas ICP-OES uses optical emission spectrometry from the ionisation of elements¹²⁰. It should be noted that ICP-MS method is more sensitive than the ICP-OES¹²⁰. The instruments used were a Perkin Elmer (ICP - MS) and a Thermo Scientific (ICP - OES), Bruker S1 TITAN 600 (XRF) and an Exeter Analytical CE-440 analyser (optimised for C, H and N analysis).

2.4.4.1 Inductively Coupled Plasma (ICP)

Plasma is an ionised gas that is electronically neutral, and the noble gas argon can be used for the production of plasma due to its high ionisation energy (17.76 eV) and chemical inertness. Inductively coupled plasma refers to the type of plasma source in which the energy is supplied by electric currents that are produced by electromagnetic induction^{121,122}.

The generation of a magnetic field, when passing a high frequency electric current through cooled induction coil, is responsible for plasma coupling. The induction can generate a rapidly oscillating magnetic field with a vertical orientation coil. Tesla coil sparks initiate the ionisation of the argon flow and the resulting ions and associated electrons interact with the fluctuating magnetic field. This interaction can generate enough energy to ionize more argon atoms by collision excitation. The electrons generated within the fluctuating magnetic field accelerate vertically to the torch (Figure 33)^{121,122}.

Further ionization is produced when cations and electrons collide with argon at high speeds, a phenomenon known as eddy current, which reaches a steady state because of high electron density after 2 milliseconds. A plasma is created in the top of the torch with a ranging

temperature from 6000 to 10000 K, characterised by a long and well-defined tail on top of the high temperature point. The torch is a spectroscopic source that contains atoms and ions of the analyte that have been excited after heating the plasma^{121,122}.

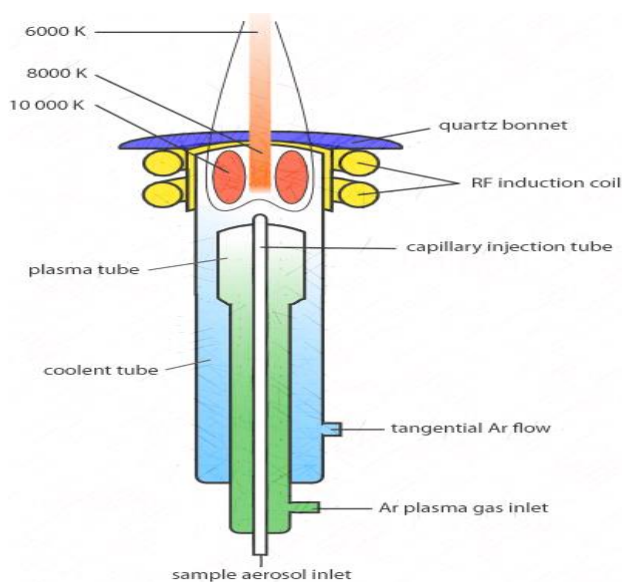


Figure 33. Plasma torch¹²³

2.4.4.2 Inductively Coupled Plasma Mass Spectrometry (ICP – MS)

ICP-MS is a type of mass spectrometry that is capable of detecting metals and several non-metals at concentrations as low as one part in 10^{12} (part per trillion). This can be achieved by the ionization of the sample in an inductively coupled plasma followed by separation and quantification of the ions by mass spectrometry. ICP-MS can analyse and measure simultaneously, multiple elements within a range of sub ppt to high ppm concentration levels in the same run¹²⁰.

The electrostatic lenses focus the ions from the ICP source. The ions are positively charged, as well as the electrostatic lenses that also have positive charge which assists in the formation of the ion beam which is focused on the aperture entrance of the mass spectrometer. Mass to charge ratio separation occurs when the ions enter the mass spectrometer. The most common spectrometer that is used is a quadrupole mass filter. Detectors that are usually used for the ICP-MS technique include a channel electron multiplier (CEM). However, discrete dynode detectors are recently being used to replace the CEM. Discrete dynode detectors have wider linear dynamic ranges in general when compared to CEMs, which is essential when using ICP-

MS for elemental analysis, because the concentrations can vary from sub ppt to high ppm. A number of electrons are released when the ions hit the active surface of the detector, subsequently the ions strike the next surface of the detector and this is when the signal is amplified. Finally, by the use of the calibration standards the amplified signal can be measured and related to the number of the atoms for each individual element (Figure 34) ¹²⁰.

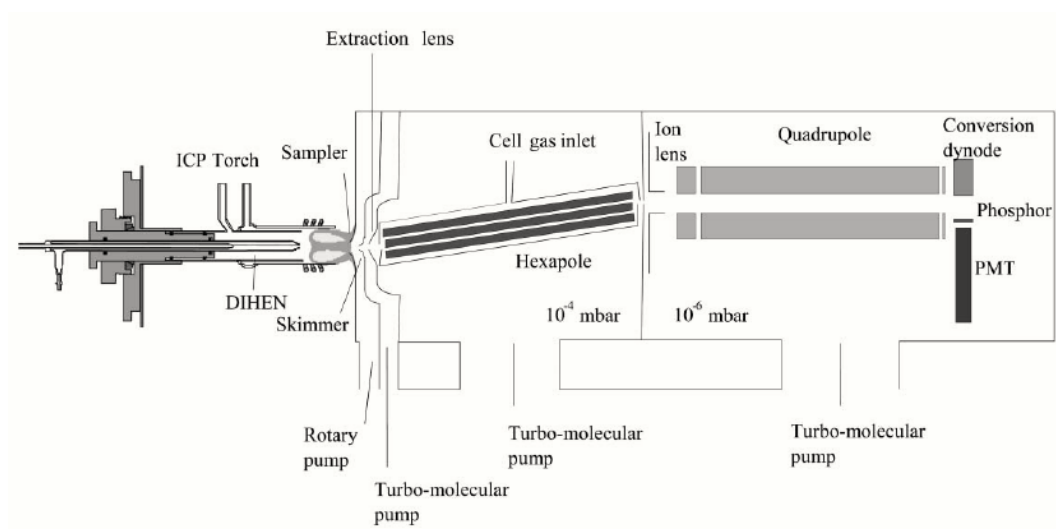


Figure 34. ICP-MS schematic

2.4.4.2 Inductively Coupled Plasma Optical Emission Spectrometry (ICP – OES)

ICP-OES is useful for measuring concentrations at ppm levels. The technique measures the wavelength of characteristic electromagnetic radiation of the emitting species ¹²⁰.

In this project ICP-OES has been used to measure a variety of elements at more concentrated levels, whereas ICP-MS was used to measure low levels of uranium and thorium isotopes in the samples ¹²⁰.

In the ICP-OES method, a number of processes occurs when the analyte enters the central channel. The series of processes that occur, include: desolvation of the sample, the decomposition of the matrix, and the excitation of the resulting analyte that produces molecular, atomic and ionic species for various energy levels. An amount of the resulting energy is expressed in an electromagnetic form of radiation of a specific wavelength which is characteristic for the species that are emitting the radiation. The specific wavelengths of interest are identified by a monochromator and subsequently the detector is responsible for the

measurement of the emitted light intensity. The concentrations of the elements that are under investigation can be quantified by their emitted light intensity (Figure 35)¹²⁰.

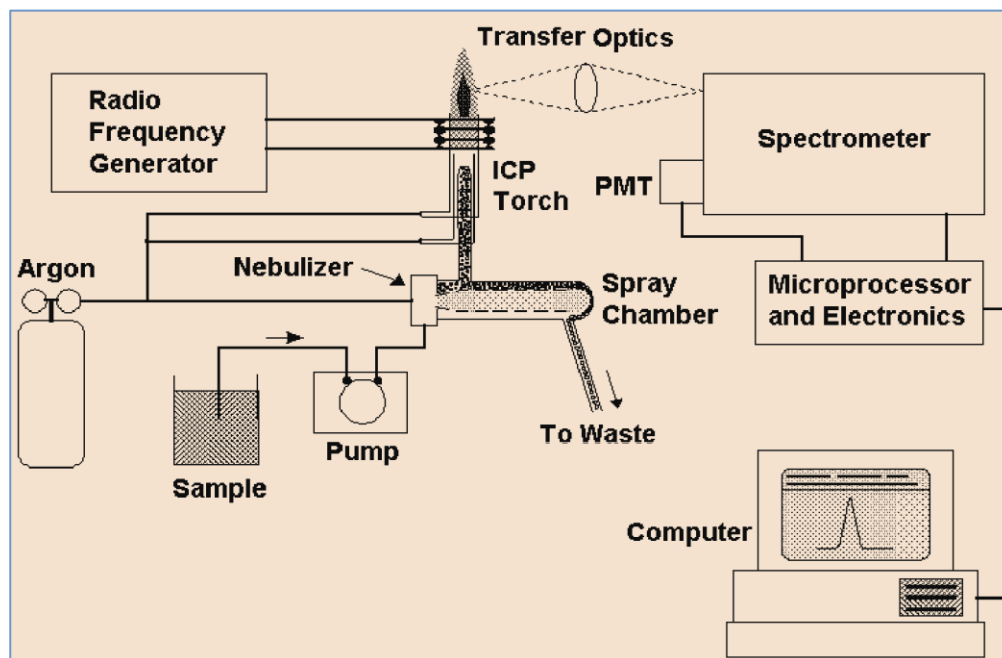


Figure 35. ICP-OES schematic

2.4.4.3 Sample preparation for ICP-MS and ICP_OES – Wet digestion microwave assisted

A weighed amount of soil from each of the sample stations was dried, to constant weight, overnight in an oven at 100 °C in order to remove any moisture content within the soil samples. All soil samples were digested by using the USEPA method 3052¹²⁴ – microwave assisted acid digestion of siliceous and organically based matrices. Accurately weighed samples of 100 ± 2 mg were used for wet digestion and placed into Teflon tubes with an addition of 5 ± 0.1 mL HF (hydrofluoric acid) and 9 ± 0.1 mL of HNO₃ (nitric acid). All samples were digested in triplicates)¹²⁴.

After microwave treatment, the digested samples required quenching with H₃BO₃ (boric acid) to neutralise the HF. A stock solution of saturated H₃BO₃ (5 g boric acid in 100 mL⁻¹ dH₂O) was prepared by warming the solution on a hot plate. About 40 mL of this saturated H₃BO₃ solution were added to each vessel containing HF. All digestions were conducted using CEM

Mars 2000 microwave. Subsequently, each sample was filtered through a syringe attached to a 0.22 μm filter discs.

Microwave Methods¹²⁴: a) 12 pots - easy prep: 25 minutes ramp to 180°C, 15 minutes hold time, 30 minutes to cool down, and b)_Boric 12 pots – easy prep: 20 minutes ramp to 170°C, 10 minutes hold time, 30 minutes cool down.

For each sample, a 3 ± 0.1 mL aliquot was taken from the digestion liquid. This was placed in a 15 mL polypropylene centrifuge tube. About $3 \text{ mL} \pm 0.1$ of 2% HNO_3 were added to make the total volume up to 6 ± 0.1 mL. The samples were then analysed for uranium using ICP-MS and for other metals using ICP-OES. All samples were analysed in triplicate for statistical purposes (i.e. standard deviation, etc).

ICP-MS standards were made up using uranium Spex CertiPrep 1000 mg L^{-1} uranium solution of 250, 200, 150, 100, 75, 50, 25, 10, 5, 2, 1, 0.5 and 0.1 ppb (w.v). Blanks without uranium were also made containing only 2% HNO_3 . The samples and standards were run on the Agilent 7700 ICP-MS using a 1 ppb (w.v) solution of indium as an internal standard.

ICP-OES standards were made up using a 100 mg L^{-1} 28 element standard solution of 100, 75, 50, 25, 10, 5, 1 and 0.5 ppm (w.v). Blanks were also made containing only 2% HNO_3 .

2.4.4.4 X-ray fluorescence spectrometry (XRF)

X-ray fluorescence spectrometry (XRF) was used to determine bulk elemental composition. This technique provides a non – destructive elemental analysis for a quantification of nearly any element from magnesium to uranium. This information can support the PXRD by narrowing the elemental search range. Approximately 5 ± 0.1 g of powdered soil sample from the Needle's Eye site was analysed using a Bruker S1 TITAN 600 tube based handheld XRF analyser. The S1 TITAN 600 uses a large area CUBE(TM) SDD detector to give incredibly fast analysis times (Figure 36).

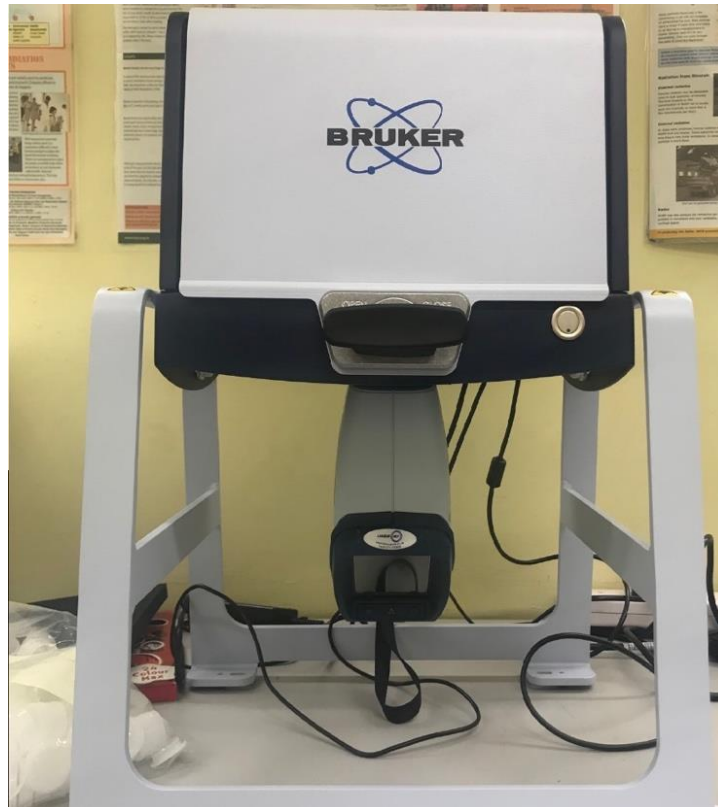


Figure 36. XRF spectrometer

The XRF method involves a process whereby electrons are displaced from their atomic orbital positions, and then higher energy electrons take up these vacant positions releasing some of their energy which is characteristic of a specific element¹²⁵. This release of energy is then registered by the detector in the XRF spectrometer, which in turn categorises the energies by element¹²⁵. An X-ray tube, located in the analyser, emits an X-ray beam which interacts with the atoms in the material under investigation resulting in electron displacement from their orbitals of the atom¹²⁵. The electron displacement occurs because of the difference in the energies of the primary X-ray beam, which is emitted by the analyser and the energy which binds the electrons in their orbitals. This process occurs when the beam energy of the X-ray is higher than the energy that binds the electrons. The orbitals of the atoms are determined by the specific energies of the electrons which are fixed. The atom becomes unstable when vacancies occur into the orbital of the electrons. This instability of the atom is corrected immediately when the vacancies are filled when the available electrons move from higher to lower orbitals to fill the vacancies exist. Figure 37 represents an example of displacement that fill vacancies in lower orbitals¹²⁵.

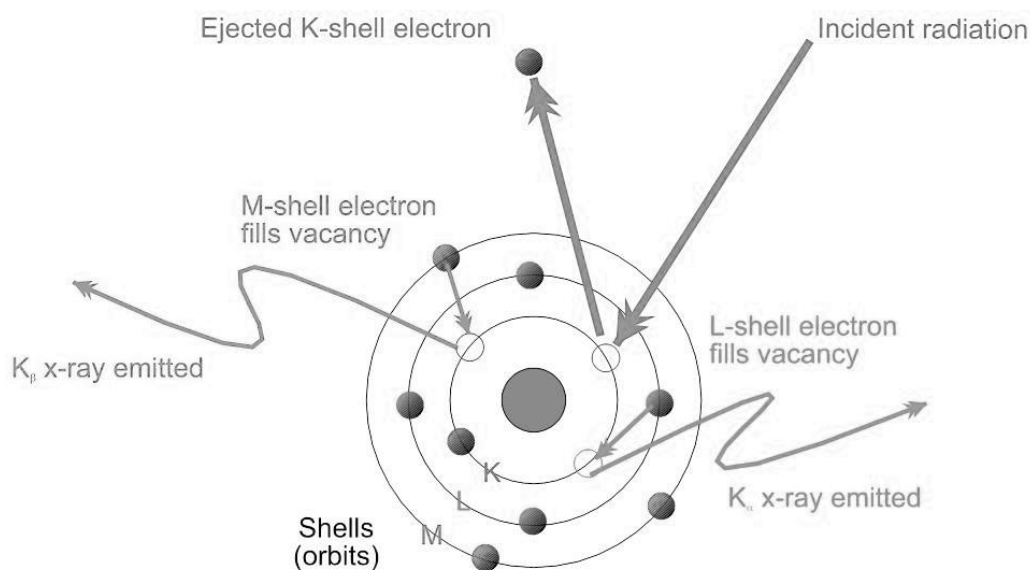


Figure 37. XRF working principle¹²⁶

The binding energies of the electrons increase as they move further from the nucleus of the atoms. Therefore, when an electron moves from a higher electron shell to another which is closer to the nucleus, the electron loses energy. This energy loss can be expressed as the difference between the energies of the two electron shells and can be determined by the distance between them. Each element has a unique distance between the two orbitals (higher and lower). The identification of the element present in the sample can be quantified by the emanated energy loss, because every element has a unique loss during the fluorescence process. The detection of the individual energies of fluorescence are characteristic to the elements that are present in the analysed sample¹²⁵. To determine the quantity of each element, present in the Needle's Eye topsoil and sequential extractions residues, the proportion (i.e. sacrificial samples) in which the individual energies appear was calculated by the XRF instrument and the S1 TITAN/Tracker 5' software that Bruker S1 TITAN 600 XRF uses for generating data after each analysis.

2.4.4.5 C, H, N elemental analysis

Elemental analysis for C, H, N was carried out using an Exeter Analytical CE-440 analyser. The sample to be analysed was weighed into a disposable tin capsule of approximately 2 mg weight. The sample then was inserted into a nickel sleeve and inserted into a high temperature

furnace where it was combusted in pure oxygen under static conditions at 975 °C. At the final stage of the combustion process, a dynamic burst of oxygen was added to ensure total combustion of all inorganic and organic substances. An initial exothermic reaction occurs raising the temperature of combustion to over 1800 °C¹²⁷.

The products of the combustion process go through specialised reagents used for the elemental carbon, nitrogen, and hydrogen production, as well as, carbon dioxide (CO₂), nitrogen (N₂), water (H₂O), and nitrogen oxides. The interference of the halogens, sulfur and phosphorous can be removed from the combustion tube by these reagents. The removal, from the reduction tube, of the excess oxygen, and the reduction of nitrogen oxides to elemental nitrogen occurs when the gasses are passed over a pure copper wire at 620 °C. The gasses then go through a mixing chamber which ensures that the mixtures achieves homogeneity at constant pressure and temperature¹²⁷.

The mixture then goes through a number of high precision thermal conductivity detectors, which each contain a pair of thermal conductivity cells. A water trap is present between the first two cells. The differential signal between the cells is proportional to the trap water concentration, equivalent to the amount of hydrogen in the original sample. Between the next two cells is a carbon dioxide trap for measuring carbon. Lastly, nitrogen can be quantified by measuring a helium reference¹²⁷.

2.5 Loss on Ignition (LoI)

Loss on Ignition (LoI) analysis was used to determine the percentage of natural organic matter (%NOM) contained in a soil sample and to support the mineral phase identification by PXRD analysis. Two temperatures were used to distinguish between organic (500°C) and inorganic carbon bound as carbonates (1000°C). The LoI analysis does not involve the use of any chemicals, only the use of a muffle furnace and a balance.

The content of water in soils, the bulk density, the organic matter, and the carbonate content can be determined by measuring the weight loss of a material (i.e. soil sample) which is exposed to sequential heating^{128–130}.

Carbon dioxide (CO₂) and ash are the oxidation products of organic matter when a soil sample is ignited at temperatures within the range of 200 to 500 °C. For temperatures varying from 700 to 900 °C the carbon dioxide (CO₂) is released from the inorganic carbonate minerals. Recording the sample weights before and after the controlled ignition is essential for the determination of the weight losses that are associated with water (H₂O) and carbon dioxide (CO₂) evolution, and this loss can be later quantified as organic matter, carbonate, and water content of each individual sample under investigation¹²⁸⁻¹³⁰.

In the present study, for the LoI analyses 1.0 ± 0.1 g of sample was placed into a crucible of pre-weighed constant weight. The samples were placed in a muffle furnace for 24 hours at 500 and then at 1000 °C and then were allowed to cool before being reweighed (Figure 38). The weight lost during the heating period was calculated and an average taken from three replicates.

NOM determinations are usually based on one of two methods. Firstly, the weight loss removal of the organic matter content from the mineral fraction by oxidation using hydrogen peroxide (H₂O₂) or by controlled ignition, and the secondly the quantification of constituent that can be found to be a relatively consistent percentage of soil organic matter such as carbon or nitrogen¹²⁸⁻¹³⁰.



Figure 38. Example of a soil sample from Needle's Eye after LoI (left side crucible containing soil sample, right side empty aluminium pot)

The difference in weight between the 500 and 1000 °C controlled ignitions can be assumed to result as a loss of carbon dioxide (CO₂) during carbonate mineral breakdown. However, loss on ignition techniques are not designed to indicate which kind of carbonate minerals may be present within the investigated samples¹²⁸⁻¹³⁰.

On the other hand, significant quantities of lattice bound hydroxides (OH⁻) can be found within clay minerals and therefore, these ions may be released as water evaporates at high temperatures. All data from the 500 and 1000 °C LoI experiments are reported as a weight loss percentage (Weight % LoI, 500 or 1000 °C)¹²⁸⁻¹³⁰.

2.6 Soil Texture Analysis

One of the most important measurements of soil characterisation refers to size particle distribution and texture, associated with pore volume. The soil texture analysis refers to the proportion of ions for each class (i.e. sand, silt, and clay) present in a sample. The limitation in specifying the diameter of each class can be different and depend on the organisation (i.e. USDA, IAEA, etc.) that provides a definition. It is essential to distinguish two different but overlapping definitions for the term clay by means of soil texture analysis. The USDA¹³⁵ classification (Figure 39¹³⁵) refers to clay for these particles with size smaller than 2 micrometres. Another definition for clay minerals refers to particles that have characteristic mineralogy similar to the layer of the aluminosilicate group which include kaolinite (Al₂Si₂O₅(OH)₄), montmorillonite ((M₁,M₂)_{0.33}(Al,Mg)₂(Si₄O₁₀)(OH)₂·nH₂O), etc^{133,134,136}.

The size of most clay mineral particles is small enough to be included in the clay class, as described above. However, some non - clay minerals such as feldspars or quartz (SiO₂) can often be dissolved before getting to small sizes. The physicochemical behaviour of clay mineral particles in soil can be related with small particle size which is related to high specific area (i.e. surface area per unit mass or volume of particles), while their mineralogy suggests high surface charge properties¹⁴¹.

The main features of soil texture analysis include the destruction or dispersion of inert soil into discrete units by mechanical or chemical means, and then the separation of the soil particles by

sieving methods. Chemical dispersion can be achieved by the removal of cement substances, i.e. organic matter and iron oxides, subsequent to the replacement of calcium and magnesium ions, characterised by their tendency to bind soil particles together into cultivation areas, with sodium ions, that are responsible of surrounding soil particles with a hydrated ions coating¹³³⁻¹³⁶.

Soil texture analysis was determined using the hydrometer method after oxidising OM with hydrogen peroxide. Calcium and magnesium ions were removed from the solution by using 5% (v.v) sodium hexametaphosphate (NaPO₃)₆¹³³⁻¹³⁶. The soil texture analysis is expressed by Equation 25^{133,134}:

$$\rho = \rho_l + (c/1000)*(1 - \rho_l/\rho_s) \quad \text{Equation 10}$$

Where,

ρ = density

ρ_l = the density of liquid,

ρ_s = the particle density, (all in g L⁻¹)

c = hydrometer scales

The large size of hydrometer bulb necessary to give adequate sensitivity reduces the depth discrimination of the instrument, but this limitation can be overcome by a simple correction.

Calculations^{133,134}:

1. Temperature (T) correction factor, where T may be different in each reading,

$$T = (\text{Observed temperature} - 20^\circ\text{C}) * 0.3 \quad \text{Equation 11}$$

2. Corrected 40-second reading (A),

$$40\text{-sec}(c) = 40\text{-sec} - \text{Blank} + T \quad \text{Equation 12}$$

3. Corrected 2-hour reading (B),

$$2\text{-hr}(c) = 2\text{-hr} - \text{Blank} + T \quad \text{Equation 13}$$

4. $\% \text{Sand} = 100 - 2 \times (A+T)$ Equation 14

5. $\% \text{Clay} = 2 \times (B + T)$ Equation 15

6. $\% \text{ Silt (0.05 - 0.002 mm)} = 100\% - (\% \text{sand} + \% \text{clay})$ Equation 16

The soil particle size experiment provides information regarding the nature and the provenance. Particle size can influence a variety of other soil properties such as sedimentary sequences (stratigraphy), lithofacies (mappable subdivision of a designated stratigraphic unit), reactive properties (specific surface area, reaction kinetics), thermal properties (heat capacity, thermal conductivity), hydraulic properties (bulk density, porosity, residual water content, water retention, relative permeability), natural isotope abundance (^{40}K , ^{238}U , ^{232}Th , gross gamma – ray response), etc^{157,158}.

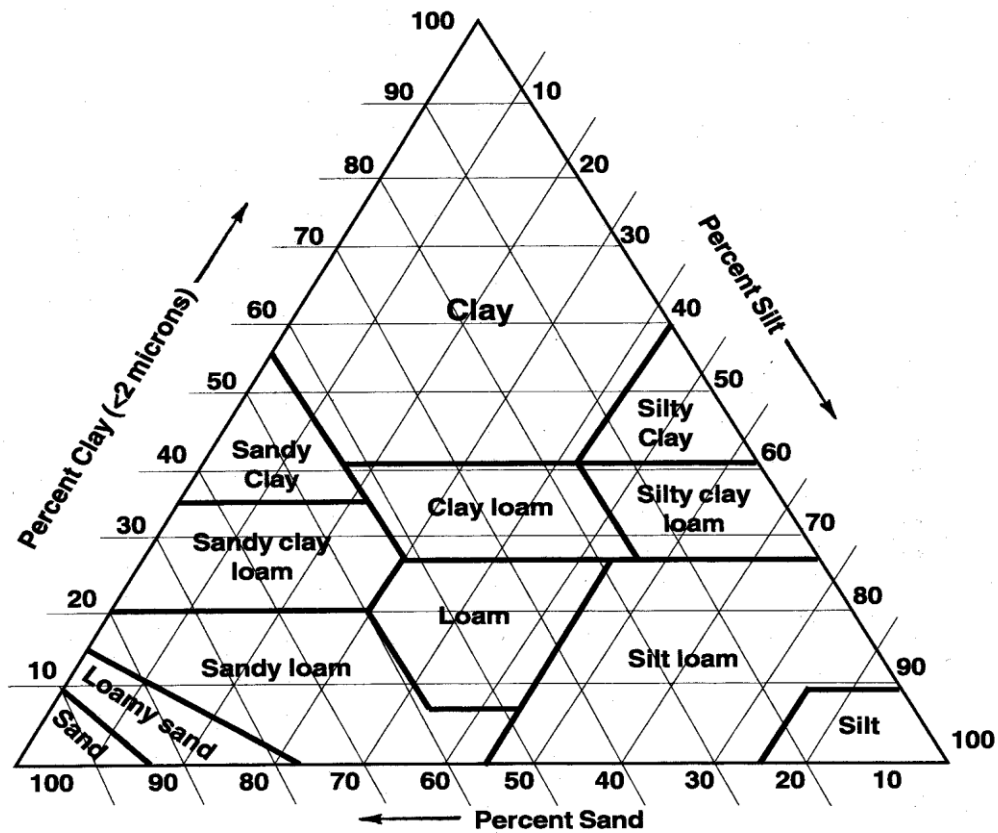


Figure 39. Soil texture triangle¹³⁵

The parameters that were determined during the particle size analysis (hydrometer method) were the percentage of sand, silt and clay in the inorganic fraction of soil. This method is based on Stokes'¹⁵⁹ law governing the rate of sedimentation of particles suspended in water. According to this law, a spherical object of known size descends through a liquid solution. This object can reach a terminal velocity that can be determined as the equivalent of the time needed to pass from two marks on the tube. The Stokes's law can be expressed by the Equation 33¹⁵⁹:

$$\frac{\pi D^3 g (\rho_s - \rho_l)}{6} = 3\pi D \eta U \quad \text{Equation 17}$$

Where,

D = diameter,

g = gravitational constant,

ρ_s = effective solid density,

ρ_l = liquid density,

η = liquid viscosity, and

U = H/t settling velocity (height/time)

The soil particle size experiment provides information regarding the nature and the provenance. Particle size can influence a variety of other soil properties such as sedimentary sequences (stratigraphy), lithofacies (mappable subdivision of a designated stratigraphic unit), reactive properties (specific surface area, reaction kinetics), thermal properties (heat capacity, thermal conductivity), hydraulic properties (bulk density, porosity, residual water content, water retention, relative permeability), natural isotope abundance (⁴⁰K, ²³⁸U, ²³²Th, gross gamma – ray response), etc^{157,158}.

Further investigation for the identification of the clay minerals that may be present, in the soils from Needle's Eye, was supported by a deflocculation method. Approximately 1 g (in duplicate) of soil was initially rinsed with 5% (v.v) ammonia solution as a dispersant and centrifuged for 1 hour. Each sample was centrifuged for 4 minutes at 1000 rev. per minute so that the clay fraction remained in suspension. The isolated clay fraction was then applied in vacuo to glass tiles to give a uniform coating. The coated tiles were left overnight in desiccators to dry¹³⁷.

2.7 Scanning Electron Microscopy / Energy Dispersive X-ray spectroscopy (SEM/EDX)

Morphology and elemental distribution of soil samples from Needle's Eye were analysed using a Hitachi TM 3030 Scanning Electron Microscope (SEM) (Hitachi High-Technologies Europe GmbH, Krefeld, Germany) equipped with an Energy Dispersive X-ray spectrometer (EDX) (Oxford Instruments X-Max, Abingdon, United Kingdom). The Silicon Drift Detector (SDD) of 30 mm² with an electron beam current set to 20 keV, allowed identification and quantification of elements present in the soil samples (Figure 40).



Figure 40. SEM/EDX equipment

To prevent from charging during SEM, samples were coated with a gold-palladium alloy (Figure 41) in an 80:20 weight ratio, for 90 s at 25 mA using a sputter coater (Quorum Q150T, Quorum, Edwards, Hastings, UK)^{138,139}.



Figure 41. Au/Pd coating

Electrons are produced at the top of the column, and subsequently are accelerated down passed through a combination of lenses and apertures to produce a focused beam of electrons which hits the surface of the sample. During this stage of the process the sample is mounted in the chamber area, and then both the chamber and the column, by assisting pumps, are evacuated, unless the instrument operates at low vacuums. The design of the SEM microscope defines the level of the vacuum (Figure 42)^{138,139}.

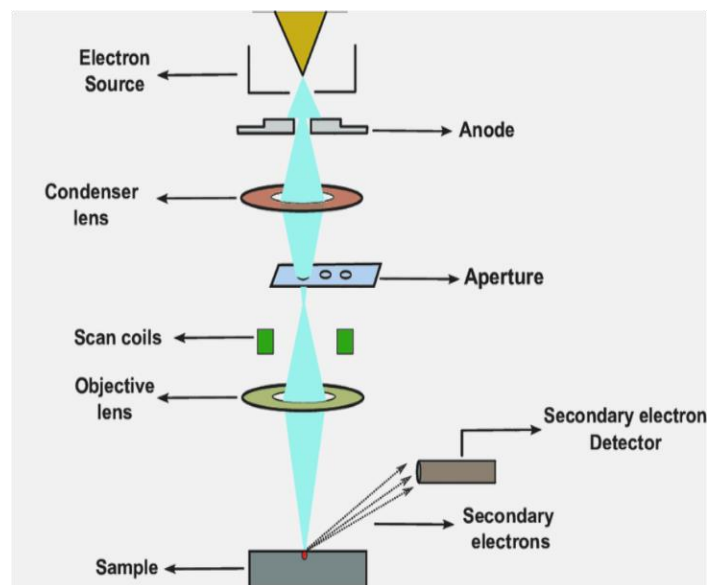


Figure 42. Schematic of SEM/EDX¹⁴⁰

Scan coils, located above the objective lens, control the position of the electron beam that hits the samples. Furthermore, the scan coils allow the scanning of the electron beam on the surface of the sample. The scanning electron beam provides information of the scanned sample area. A number of produced signals is a result of the interaction between sample and electron^{138,139}.

Images are produced by the electron scanning of the sampling with a high energy beam of electrons. Backscattered secondary electrons are produced when the sample interacts with the sample, by characteristic X-rays. Several or one detector produce images, displayed in a PC monitor, after collecting X-ray signals. The electron beam hit the surface of the analysed sample and can penetrate the sample up to a depth of a few microns. The penetration depth depends on the density of the sample and the acceleration of the voltage. Interactions within the sample may be responsible of secondary electrons and X-rays. Generally, factors like the electron spot size and the volume of interaction of the electron beam with the analysed sample can affect the level of the maximum resolution obtained during the scanning^{138,139}.

For the SEM/EDX analysis dried homogenised samples were used. A very small portion of soil sample was placed carefully with a spatula on cuvettes that were previously coated with carbon stickers (Figure 43). The samples were then coated with a gold/palladium alloy in an 80:20 ratio, for 90 seconds at 25 mA using a sputter coater in order to prevent charging during the analysis^{138,139}.

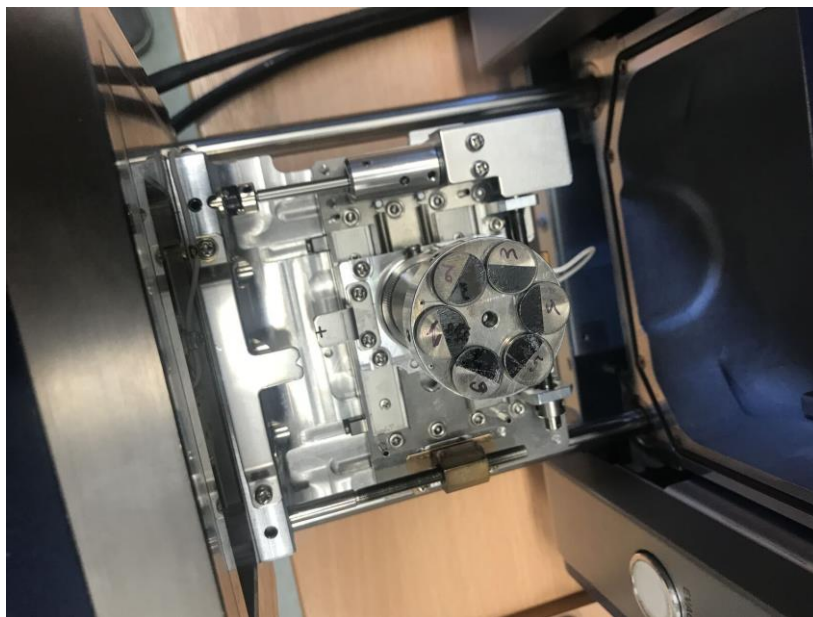


Figure 43. SEM/EDX sample holders containing samples ready for analysis

2.8 Liquid Scintillation Counting (LSC)

Liquid scintillation counting (LSC), is an analytical technique which is usually used for the quantification of alpha or beta emitting radionuclides. LSC was developed in the early 1950s to aid the measurement of ^3H and ^{14}C ^{141,142}. Broser and Kallman¹⁴³, discovered that certain organic compounds (scintillators) fluoresce after their exposure to ionising radiation. Every fluorescence event can be caused by a radioactive decay event, and the frequency of these events is equivalent to the number of radioactive atoms present in the sample^{141,142}.

The radioactive decay is responsible for the excitation energy of the aromatic solvent molecules that reaches the scintillator. This excitation energy can be absorbed by the scintillator which is responsible for the production of the electrons' excitation states which subsequently decay to the ground state and produce a characteristic pulse light. The pulse light can be detected by the photomultiplier tubes (PMTs) of the liquid scintillation counter (Figure 44)^{141,142}.

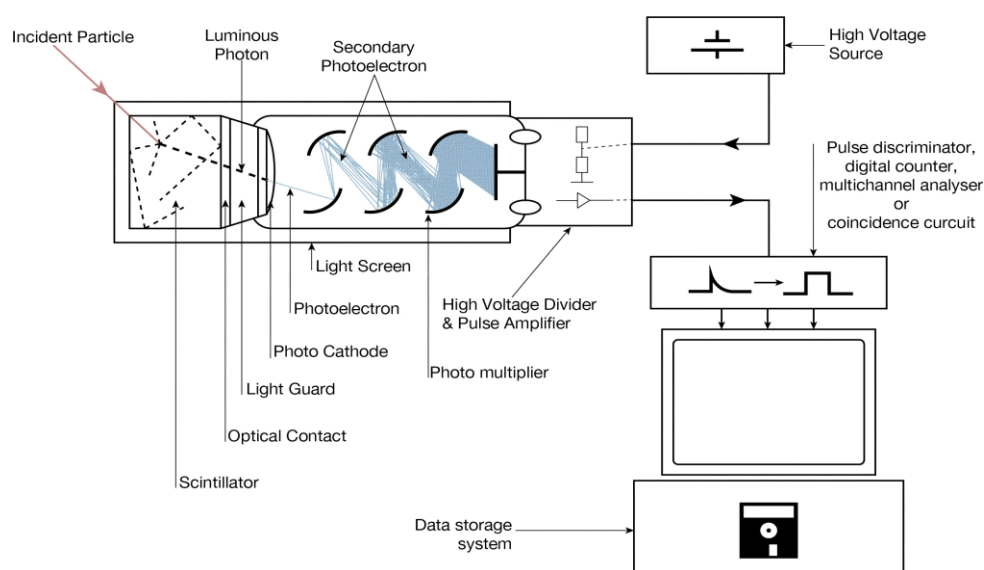


Figure 44. LSC schematic

2.9 UV/visible spectroscopy – Absorbance spectroscopy

2.9.1 General information

UV/visible spectroscopy refers to absorption spectroscopy in the ultraviolet (UV) and visible spectral regions. This technique uses light in the visible and adjacent ranges and is usually used

in analytical chemistry for the quantitative determination of different analytes, such as organic compounds, transition metal ions and biological macromolecules¹⁴⁴. In the present study it was used for the quantification of organic compounds extracted from soil samples taken from the Needle's eye site.

The principle of ultraviolet visible absorption is that the molecule, that contain π -electrons or non-bonding electrons (n-electrons), absorbs energy in the form of ultraviolet or visible light by exciting electrons to higher anti-bonding molecular orbitals¹⁴⁴.

The absorbance of a solution is described by the Beer – Lambert law, as the equivalent concentration of the absorbing species in the solution and the path length. Thus, a UV/visible spectroscopy can be used for the determination of the concentration of the absorber in a solution (after initial calibration of the instrument), for a fixed path length¹⁴⁴.

The wavelengths of absorption peaks can be correlated with the types of bonds in a given molecule and are essential for determining the functional groups within a molecule. The Woodward – Fieser rules, define a set of empirical observations used for the λ_{\max} prediction. λ_{\max} is defined as the wavelength of the most intense UV/visible absorption, for organic compounds (i.e. dienes and ketones)¹⁴⁴.

The absorption spectrum can be affected by the pH of the solution, the nature of the solvent, the temperature, the high electrolyte concentrations, the presence of interfering substances, and experimental variations, i.e. the slit width (effective bandwidth) of the spectrophotometer. These variables must be considered and controlled during the UV/visible analysis for the determination of the present substances¹⁴⁴.

This method is most often used in a quantitative way to measure the concentrations of the absorbing species in present solution, by using the Beer – Lambert law (Equation 32)¹⁴⁴:

$$A = \log_{10} \left(\frac{I_0}{I} \right) = \varepsilon \times c \times L \quad \text{Equation 18}$$

Where,

A = the measured absorbance (in Absorbance Units (AU)),

I_0 = the intensity of the incident light at a given wavelength,

I = the transmitted intensity,

L = the path length through the sample,

c = the concentration of the absorbing species, and

ϵ = a constant known as the molar absorptivity or extinction coefficient, characteristic for every wavelength and species.

The ϵ constant defines a fundamental molecular property in a given solvent, at a particular temperature and pressure, and has units of $\text{L M}^{-1}\text{cm}^{-1}$.

The UV/visible spectrometer comprises of a light source, a sample holder, a diffraction grating in a monochromator or a prism that separates the different wavelengths of light, and the detector. The radiation source is usually a Tungsten filament of a 300 to 2500 nm sensitivity, a H_2 arc lamp, that is continuous over the ultraviolet region from 190 to 400 nm, Xenon arc lamp, which is continuous from 160 to 2000 nm, or the modern light emitting diodes (LED) for the visible wavelengths. The detector consists of a photomultiplier tube, a photodiode, a photodiode array or a charge coupled device (CCD). A combination of single photodiode detectors and photomultiplier tubes is used along with a scanning monochromator that filters the light in a way that only a single wavelength at a time reaches the detector. The scanning monochromator is responsible for moving the diffraction grating step by step to each wavelength so that the intensity can be measured as a function of wavelength¹⁴⁴.

In this research a Varian Cary Series Type 50 Bio UV Spectrophotometer was used. UV measurement of purified humic acid (HA) solutions at 250 nm, 350 nm and 450 nm occurred along with Specific wavelength assignment mode with baseline correction using 0.1 mol dm^{-3} MES.

2.9.2 Calibration of UV/visible spectrophotometer

A solution of potassium permanganate (KMnO_4), and dilutions of that solution, were measured to determine the linearity of measurements when using the UV/Visible spectrophotometer. The graph shown in Figure 45 shows that the instrument is linear when measuring absorbance values of 3 and below.

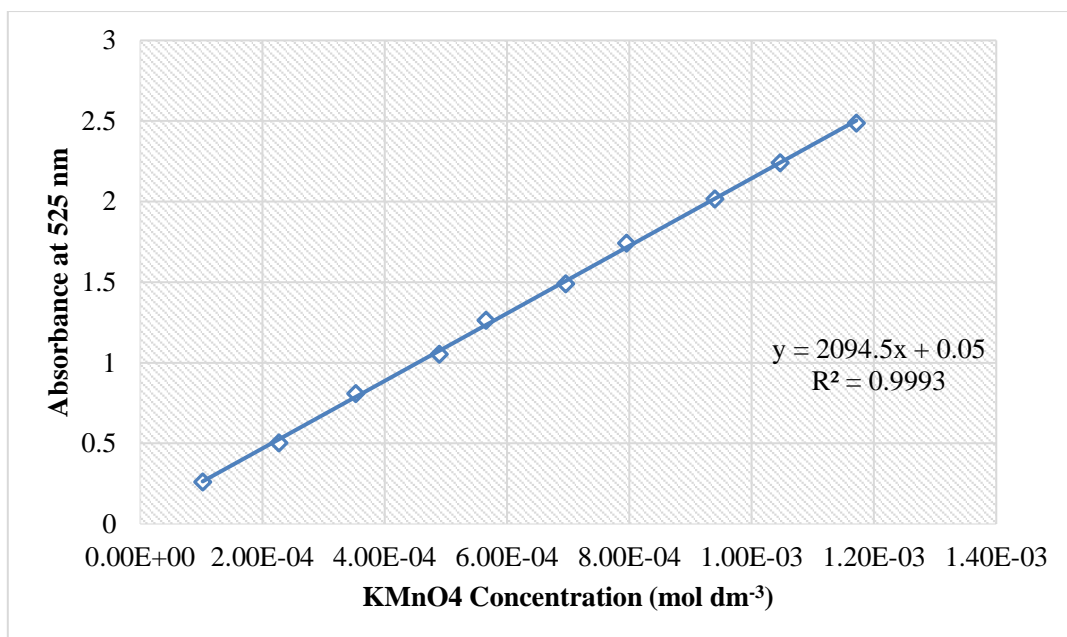


Figure 45. KMnO₄ calibration graph

Purified humic material (HA) was prepared by placing approximately 2 g of commercially available Sigma – Aldrich sodium humate into a 2 L conical flask and then adding approximately 1900 mL of dH₂O together with 4 mL 0.1 mol L⁻¹ NaOH. This was then sonicated until all the sodium humate was dissolved. Once the sodium humate was dissolved, the pH of the solution was lowered to 2 by adding drops of conc. HCl. The humate was allowed to precipitate overnight. After the precipitation was completed, the yellow solution (FA fraction) was decanted off and the remaining (darker) humic fraction filtered through a 0.45 µm cellulose membrane using a magnetic filter funnel and a pump. The remaining solid was dried in a desiccator to produce purified Sigma – Aldrich sodium humate. The dried solid was further washed, precipitated out of solution, separated and dried several times (usually 3 - 4 times) until no FA fraction was visible¹⁴⁵.

Solutions of purified HA were prepared with concentrations varying from 0.5 to 100 ppm (w.v). the UV/visible absorption of each solution was measured, and Figures 46 to 48 show the results at 250, 350 and 450 nanometres.

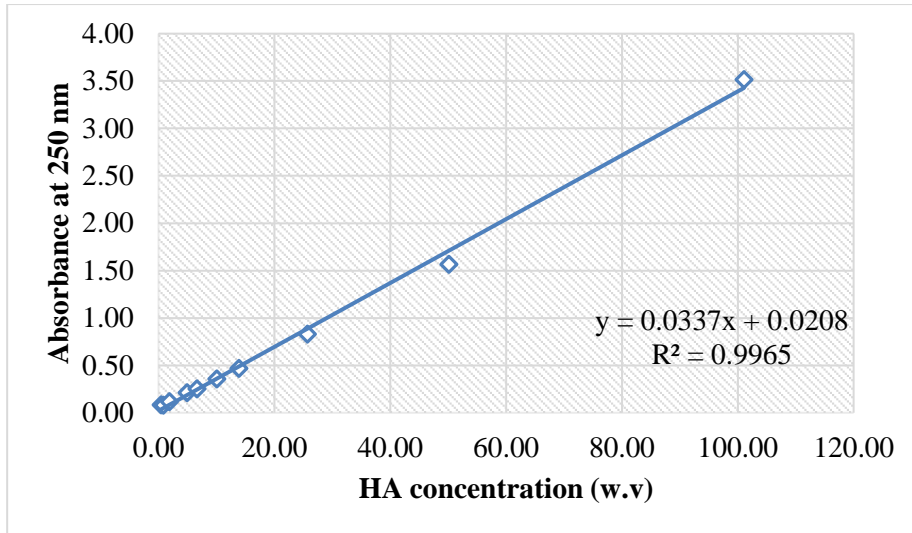


Figure 46. HA calibration graph 250 nm

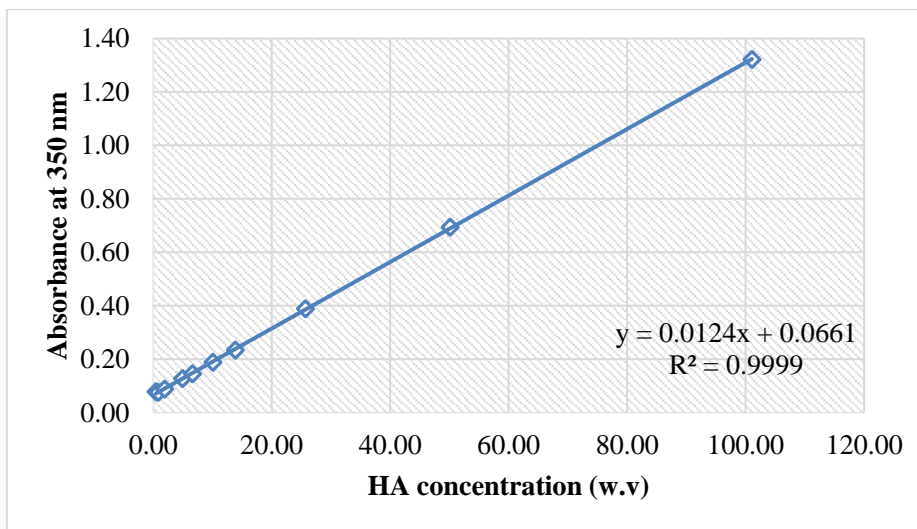


Figure 47. HA calibration graph 350 nm

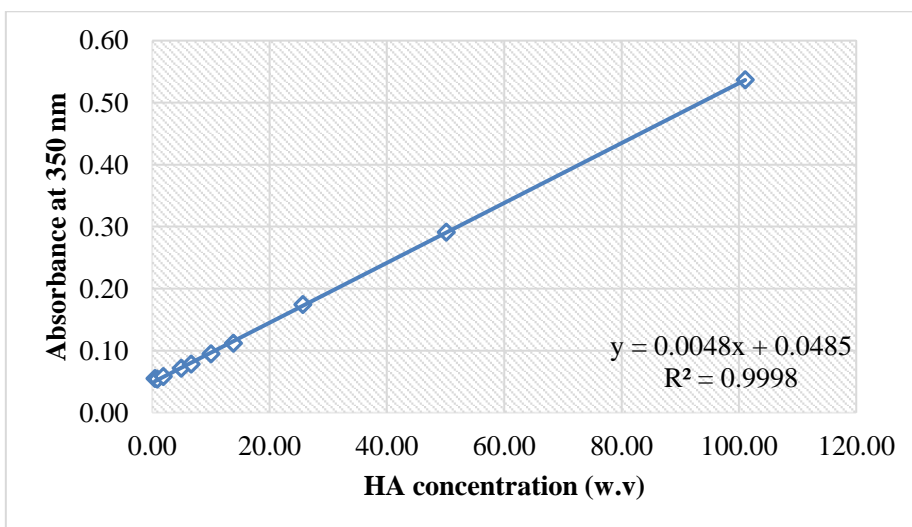


Figure 48. HA calibration graph 450 nm

2.10 Binary Experiments

The sorption of ^{226}Ra onto topsoil (NE4_T) was investigated by the batch technique. The batch adsorption or static equilibration technique can be used to calculate the capacity of solids and solid components that are responsible for removing chemical constituents from solution phase. More specifically, an aqueous solution that contains solutes of known concentrations is mixed with a known mass of adsorbent, at a recorded temperature, for a given period of time. Subsequently, the solution is then separated from the adsorbent with a pipette and then analysed in order to determine any changes of the solute concentration. The concentration of solute that was sorbed by the adsorbent can be assumed to be the equivalent of the difference between the initial concentration (i.e. before contact with adsorbent) and the concentration of the solute after the mixing time.

For the investigations reported here, the solid adsorbent material was topsoil (NE4_T). The solution phase contained BaCl_2 at varying concentrations in addition to trace concentrations of ^{226}Ra . Three sets of sorption experiments were carried out so as to quantify the distribution ratio (R_d , the ratio of the concentration of ^{226}Ra in the solid to the ratio of ^{226}Ra remaining in solution) of ^{226}Ra :

1. ^{226}Ra spiked equilibrated water (eqH₂O) - NE4_T
2. ^{226}Ra spiked demineralised water (dH₂O) - NE4_T
3. ^{226}Ra spiked demineralised water (dH₂O) – prewashed NE4_T

Soil equilibrated water was prepared by adding approximately 1 g of NE4_T to 50 mL of dH₂O. The mixture was agitated for 24 hours and then filtered and counted at a NaI gamma counter. Soil equilibrated water was used to provide, as much as possible, the environmental conditions pertaining to the Needle's Eye site.

2.10.1 ^{226}Ra spiked equilibrated water (eqH₂O) - NE4_T

For this set of binary experiments, three replicates were prepared by adding approximately 0.1 g of NE4_T to 9 mL of eqH₂O containing varying concentrations ($0.1 - 10^{-5} \text{ mol dm}^{-3}$) of the

carrier BaCl₂ (aq) of the carrier solution (Figure 49). All 3 replicates were then spiked with 500 Bq ²²⁶Ra standard (approximately 0.0061 mL ²²⁶Ra standard). The samples were then left for 6 days, with constant agitation, to equilibrate.

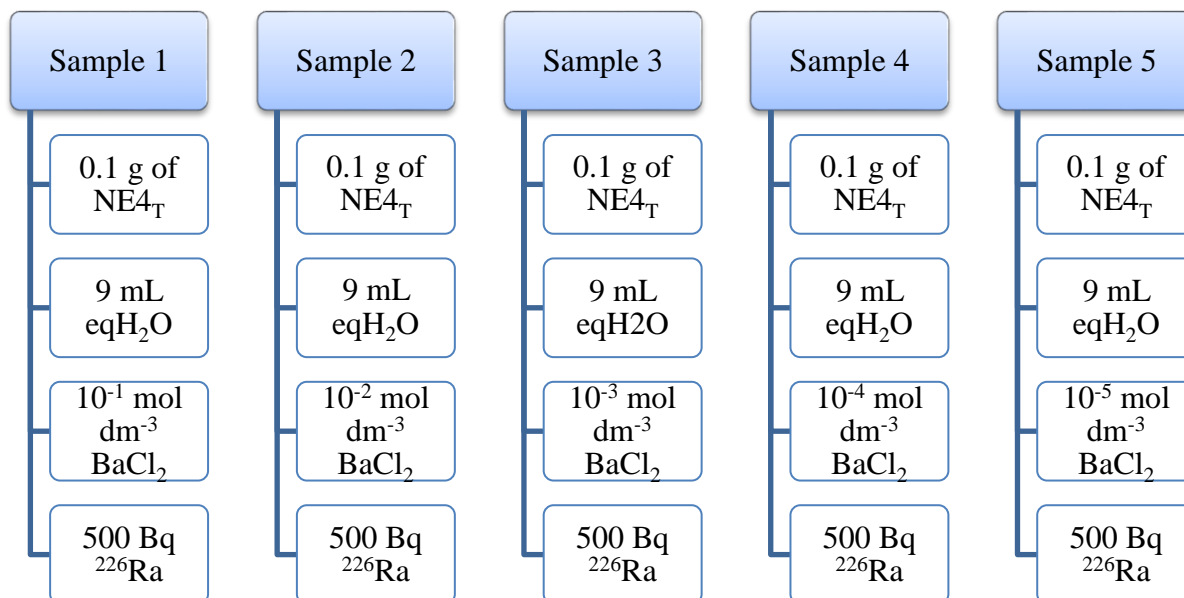


Figure 49. Sample preparation for the first set of binary experiments

After six days of agitation the samples were set aside to settle for about one hour. Subsequently, the supernatants were filtered, and 2 mL of each sample were transferred in plastic vials and counted with a gamma counter for ²²⁶Ra. The full counting channel window of 0 to 2000 keV was used. The samples were counted to at least ten thousand counts (i.e. 2σ, 2 % error).

2.10.2 ²²⁶Ra spiked demineralised water (dH₂O) - NE4_T

For this set of binary experiments, approximately 0.1 g of NE4_T, in 3 replicates, were added to 9 mL of dH₂O containing varying concentrations (0.1 – 10⁻⁵ mol dm⁻³) of BaCl₂ (aq) carrier solution (Figure 50). All replicates were spiked with 500 Bq of ²²⁶Ra standard (approximately 0.0061 mL ²²⁶Ra standard). The samples were then left for 6 days, with constant agitation, to equilibrate.

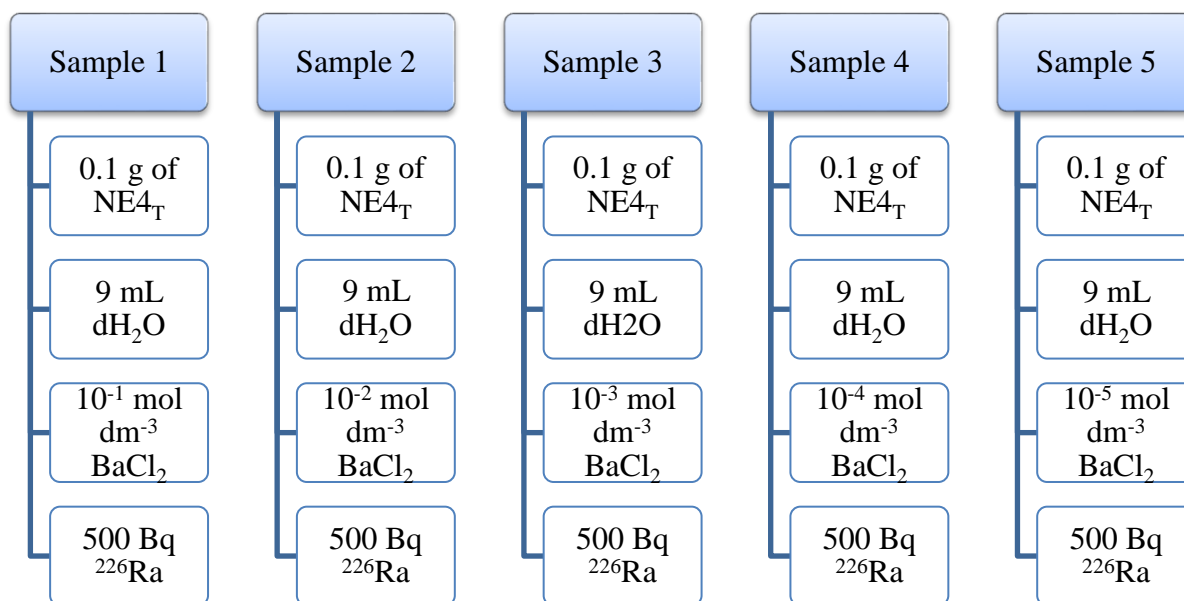


Figure 50. Sample preparation for the second set of binary experiments

After six days of agitation the samples were set aside to settle for about one hour. Subsequently, 2 mL of each sample were transferred in plastic vials and counted with a gamma counter for the γ energy of ²²⁶Ra. The full counting channel window used 0 to 2000 keV was used. The samples were counted to at least ten thousand counts (i.e. 2σ , 2 % error).

2.10.3 ²²⁶Ra spiked demineralised water (dH₂O) - NE4_T

For this set of binary experiments, in approximately 0.1 g of NE4_T, in 3 replicates, were added to 9 mL of dH₂O containing varying concentrations ($0.1 - 10^{-5}$ mol dm⁻³) of the BaCl₂ (aq) carrier solution (Figure 51). Finally, all replicates were spiked with 500 Bq of ²²⁶Ra standard (approximately 0.0061 mL ²²⁶Ra standard). The samples were then left for 6 days, with constant agitation, to equilibrate.

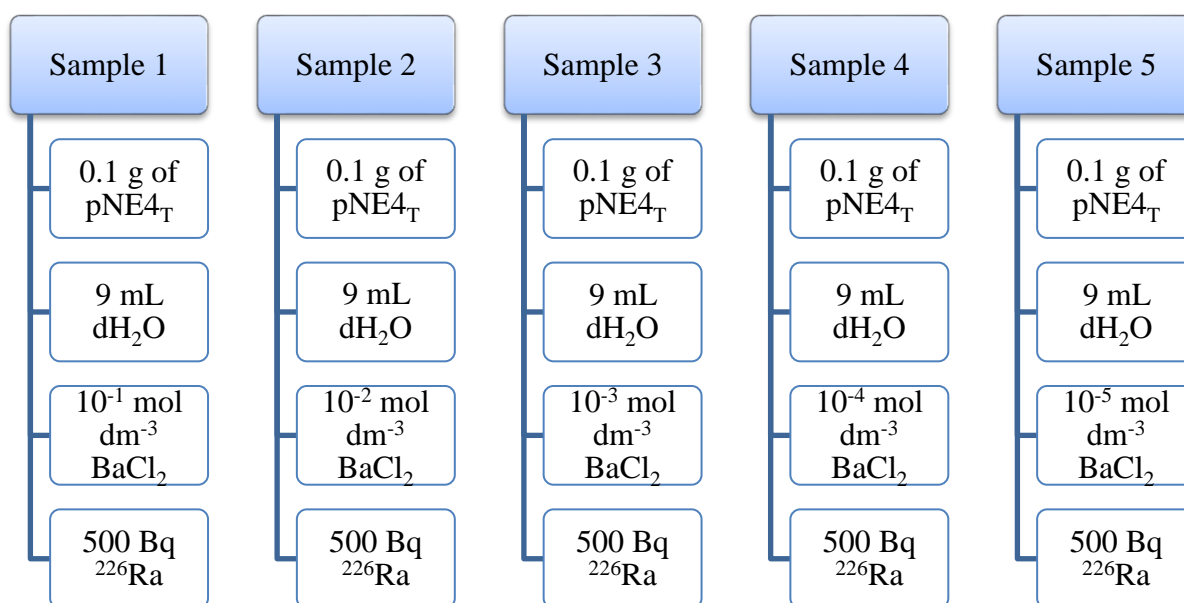


Figure 51. Sample preparation for the third set of binary experiments

After six days of agitation the samples were set aside to settle for about one hour. Subsequently, 2 mL of each sample were transferred in plastic vials and counted with a gamma counter for the γ energy of ²²⁶Ra. The full counting channel window used 0 to 2000 keV was used. The samples were counted to at least ten thousand counts (i.e. 2σ , 2 % error).

2.11 Column Experiments

Static batch experiments have been used in the present study to investigate the potential mobility of ²²⁶Ra. To further investigate radium mobility, column experiments were used containing NE4_T soil material and ²²⁶Ra solution (²²⁶Ra spiked eqH₂O) was passed through the column. The purpose of using topsoil material of the study area, as well as, eqH₂O was to duplicate the environmental conditions of Needle's Eye and investigate the potential mobility of ²²⁶Ra under these conditions.

For this experiment a borosilicate glass column was used with an internal diameter of 1 cm and height 55 cm. About 2 g of NE4_T were placed in the column providing a depth of 5 cm of soil of diameter 1 cm. the volume of soil used in the column was therefore 3.92 cm³ (Figure 52).

The porosity of the topsoil sample was measured by using 300 Bq ml^{-1} of a tritium tracer (HTO). HTO was passed through the column with a flowrate of about $1 \text{ cm}^3 \text{ h}^{-1}$. In total $33, 0.5 \text{ cm}^3$, HTO fractions were collected and analysed by liquid scintillation counting (Perkin Elemer Tricarb 2100 TR) by using a counting window between 2 and 18 keV.

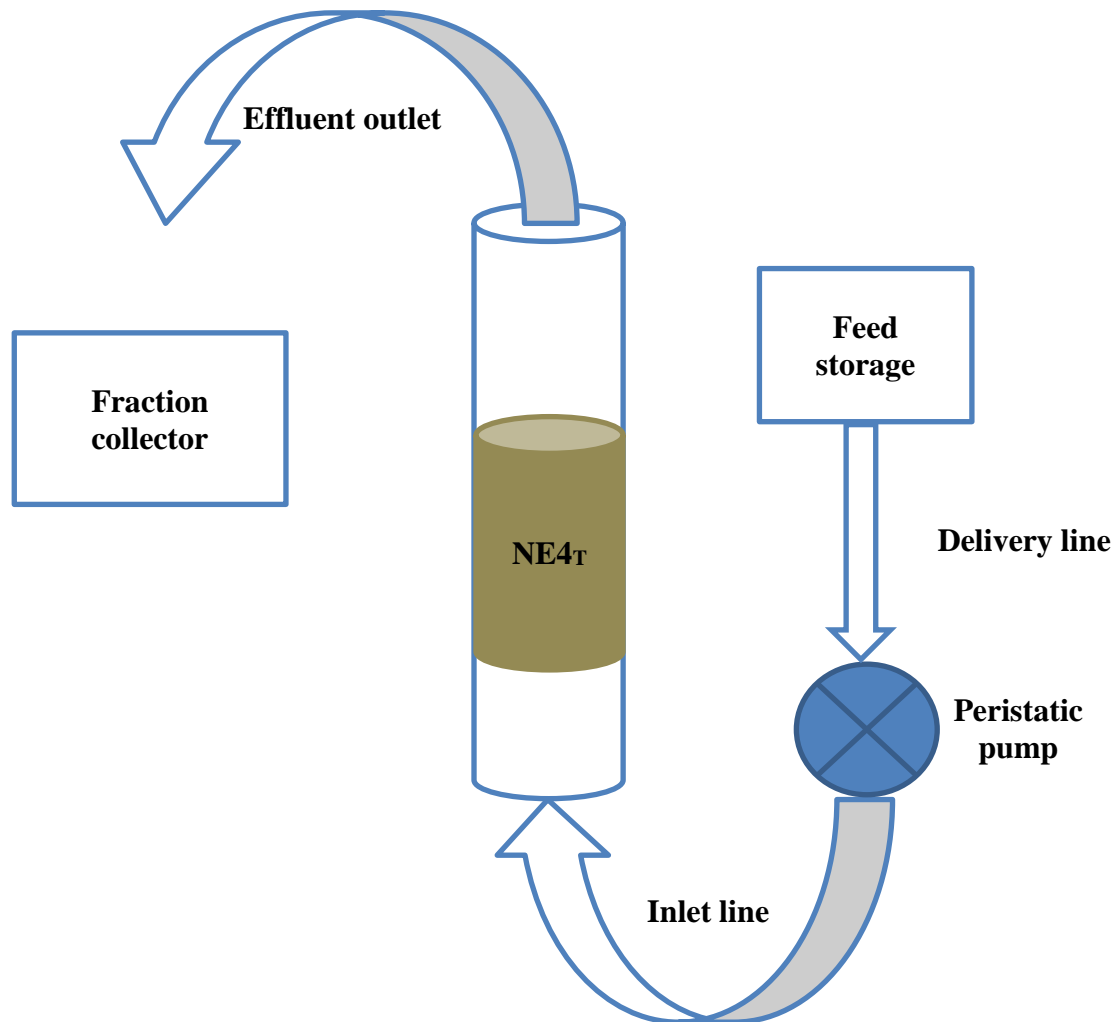


Figure 52. Schematic setup of column experiment

2.12 Sequential Extractions

2.12.1 Sequential extraction introduction

The toxicity of radionuclides and trace metals in the environment can be associated with their bioavailability and mobility which can be affected significantly by their specific chemical behaviour, as well as their binding with the constituents present in the environment. These

elements can be dangerous when they can be found in significant concentrations in the environment. Determining the available concentration of these elements in the environment may not provide enough information about their potential risk, because their behaviour and potential bio-availability is subject to the environment conditions that may affect their potential mobility^{146,147}

Sequential extraction methods can be used for the determination of mobile forms which allow a better understanding of any environmental contamination risk. Tessier¹⁴⁶ et al., developed one of the first sequential extraction methodologies which was able to provide information about the potential mobility of heavy metals such as, Cd, Cu, Co, Fe, Mn, Pb, Ni, and Zn, in sediments. The Tessier method can provide information about the different forms of trace metals in the sediments, as well as physicochemical availability, mobilisation, and transportation.

The sequential extraction method offers a good evaluation of contamination in different mineral phases^{148,149}. The application of sequential extraction experiments is used to investigate any potential relationship of radionuclides with different mineral fractions by using a series of reagents of increasing leaching and their ability to remove particular mineral fractions. These processes can be characterised as rather subjective due to the lack of specificity of the extractants, the presence of poorly defined mineral fractions and the unsuitability of certain procedures for different sediments, and therefore any conclusions must be presented with caution^{146,147}. However, although precise conclusions cannot be drawn, the sequential extractions can be useful for getting comparative results of the affinity between radionuclides and different mineral fractions¹⁴⁹.

Further characterisation of the NE4_T sample was achieved by using the sequential extraction method, as described by Tessier et al¹⁴⁶. The Tessier method was used to investigate the potential mobilisation of ²²⁶Ra from soil into solution.

Using the Tessier method, the solid material can be partitioned into five specific fractions (F1 – F5) that can be selectively extracted by the use of appropriate reagents. The fractions are described below.

2.12.2 Methodology

In this investigation, sintered crucible filters (grade 4) were used to separate the solid from the solution.

2.12.2.1 F1 – Exchangeable Fraction

Approximately 1 g, in three replicates (Rep. 1-3), of previously dried and homogenised soil sample, was added to a 30 mL volume sintered crucible. Approximately 8 mL of 1M MgCl₂, pH 7.0 were added to the soil and agitated for 1 hour at room temperature. The solution phase was separated from the solid phase by suction using a vacuum pump and a Büchner flask. It should be noted that the Replicate 1 sample was a “sacrificial” sample as a small amount of sample was removed from the resulting residues after each sequential extraction stage and was used for SEM/EDX, XRF and PXRD analysis. Therefore, the results of ²²⁶Ra activity are presented but not included in the average calculation using sequential extraction stage 2 and onwards.

2.12.2.2 F2 – Bound to Carbonates Fraction

In this stage of the sequential extractions, the residues from the F1 stage were re-weighed (without removing them from the sintered crucibles). The residues were then leached at room temperature with approximately 8 mL of 1M NaOAc adjusted to pH 5.0 using HOAc. Continuous agitation was maintained for 6 hours and the solution phase was separated from the solid phase using a vacuum pump and a Büchner flask.

2.12.2.3 F3 - Bound to Iron and Manganese Oxides Fraction

In this stage of the sequential extractions, the residues from the F2 stage were re-weighed, without removing them from the sintered crucibles. The residues were then contacted with 20 mL of 0.3M Na₂S₂O₄ + 0.175M Na-citrate + 0.025M H-citrate in 25% (v.v) HOAc at 96 ± 3 °C with occasional agitation for six hours. The solution phase was extracted using a vacuum pump and a Büchner flask.

2.12.2.4 F4 - Bound to Organic Matter Fraction

In this stage of the sequential extractions, the residues from F3 stage were re-weighed without removing them from the sintered crucibles. To the residues, about 3 mL of 0.02M HNO₃ were added and the mixtures were heated to 85 ± 2 °C for 2 hours with occasional agitation. Subsequently, a second 3 mL aliquot of 30% H₂O₂ (adjusted to pH 2.0 with HNO₃) was added and the mixtures were heated again to 85 ± 2 °C for 3 hours with intermittent agitation. After cooling, 5 mL of 3.2M NH₄OAc in 20% (v.v) HNO₃ were added and the samples were diluted to 20 mL with dH₂O and agitated continuously for 30 minutes. The addition of NH₄OAc is designed to prevent adsorption of extracted metals onto the oxidised soil.

2.12.2.5 F5 – Residual

In the final stage of the sequential extractions, the residues from the F4 stage were re-weighed without removing them from the sintered crucibles. To the residues, a mixture of 2 mL of HClO₄ and 10 mL of HF were added, and the sample was digested to near dryness; subsequently a second addition of 1 mL of HClO₄ and 10 mL of HF was made and again the mixture was evaporated to near dryness. Finally, 1 mL of HClO₄ alone was added and the sample was evaporated. The residue was dissolved in 12M HCl and diluted to 25 mL. The resulting solution was spiked with H₃BO₃ to neutralise HF and analysed with gamma spectroscopy.

2.13 Non – sequential extraction

NOM content of NE_{4T} was investigated further by measuring the humic, fulvic and humin content of the soil by separating them into humic acid (HA), humin (HU) and fulvic acid (FA) fractions. To separate the soluble fraction of NOM (HA and FA) from the insoluble fraction of NOM (HU), 3 replicated of approximately 1 g (Rep. 1 – 3) of topsoil sample were taken from the three 20 g NE_{4T} replicas respectively and then: i) 20 ml of 0.1M NaOH, ii) 0.1M HNO₃, iii) dH₂O were added and agitated for approximately 24 hours (Figure 53). The samples were then filtered through coarse and 0.45 µm filters using a vacuum pump. The filtrates were then analysed for their ²²⁶Ra content using γ spectrometry, and then by UV/visible absorption for

the quantification of HA and FA. UV/visible absorption measurements were taken by filling a 0.1 cm quartz cuvette with each sample and recording the absorbance spectra for each sample at 250, 350 and 450 nm on a UV Type Varian Cary Series 50 Bio Spectrophotometer.

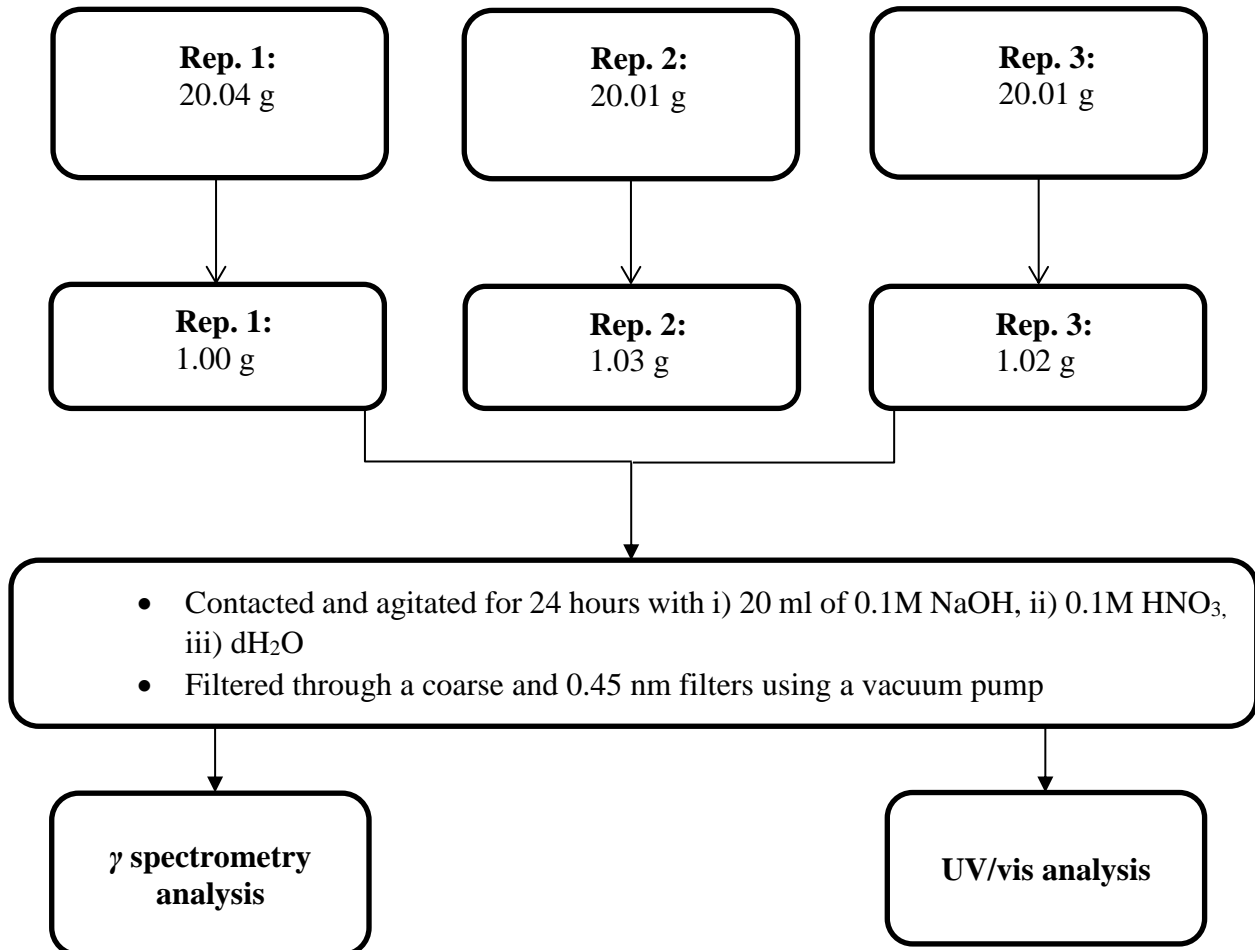


Figure 53. Preparation of samples UV/visible absorption and γ spectrometry analysis

2.14 Topsoil

2.14.1 Introduction – Why study topsoil?

Soil structure is the arrangement of soil particles (sand, silt, clay and organic matter) into granules, crumbs or blocks. The shape (colour, size of soil particles, etc.) of the soil is based on its physical, chemical and biological properties. Topsoil occurs in the upper layer of soil (Figure 54). The highest concentrations of microorganisms and organic matter can be found in

these top two to eight inches of soil. However, the amount of organic matter varies in different soil types¹⁵⁰.

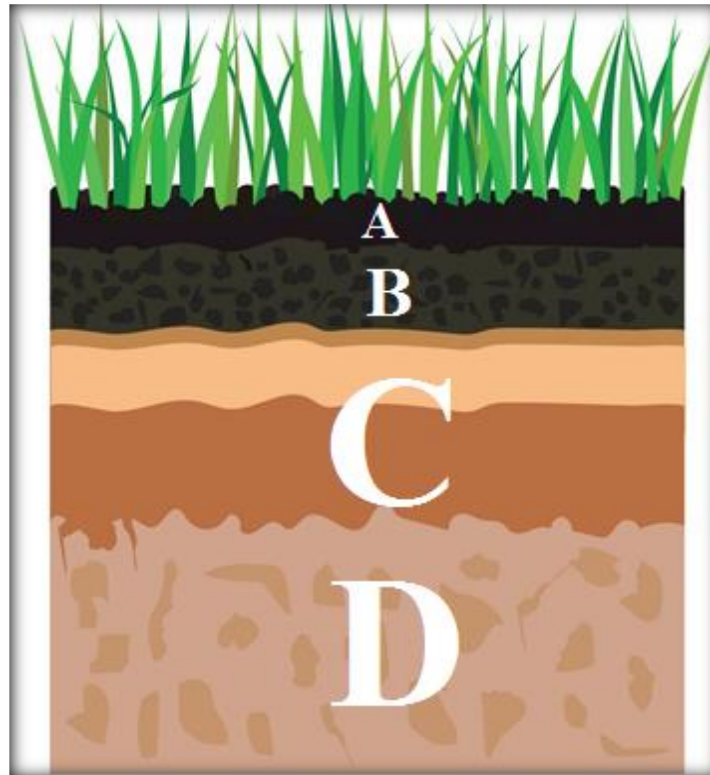


Figure 54. Soil sections (A: Soil organic material, B: Topsoil, C: Subsoil, D: Bedrock)

Furthermore, most of the earth's biological soil activities (nutrient cycling, soil decomposition, tec.) can be found in the topsoil layer. Topsoil is also the layer in which plants concentrate their roots¹⁵⁰.

The importance of topsoil is that it is the most fertile portion of soil and the most valuable. It requires about 500 years under natural conditions to produce an inch of topsoil. In addition, topsoil is a perfect blend of structural media and nutrient material. Topsoil's natural fertility promotes greener, thicker, healthier grass and reduces the amount of amendments, and organic material required for plants to be sustainable. Most of the properties we associate with topsoil are: good nutrient supply, tilth, drainage, aeration, water storage, etc., because topsoil is rich in organic matter and contains a huge diversity of life¹⁵⁰.

The chemistry of topsoil can provide a database that identifies areas of elevated topsoil concentrations of potentially harmful chemical elements and can be used in conjunction with

proposed soil screening values (i.e. EU environmental regulations) for assessing ecological risks and/or the soil guideline value, which is already a threshold used in the preliminary assessments for land contamination¹⁵⁰.

2.14.2 Needle's Eye topsoil

The area of interest at Needle's Eye is mostly an organic rich peaty area which is anoxic at depth and is situated along the base of a cliff which contains enhanced amounts of uranium. The uranium is strongly associated (> 95%) with soil organic matter¹⁵¹. Therefore, this locality provides a unique opportunity to study the interaction of ²²⁶Ra with humic substances under entirely natural conditions. Thus, topsoil sample located at the NE4 sampling area (*Section 1.5*) was analysed and characterised in order to identify the potential association of ²²⁶Ra with NOM.

Undisturbed topsoil sample (NE4 topsoil) was collected from the peaty area of the site (NE4 location, see Figure 19), in which uranium and NOM are known to accumulate in abundance. The topsoil sample was amorphous peat, geologically originated to the Crowdy series (the Crowdy series is an amorphous peat soil at least 40 cm thick and, at times, up to 1 m deep over mineral substrates, characterised usually by a black or dark brown peaty soil horizons that may include thin semi – fibrous bands)^{152,153}. The litter layer (3 – 5 cm depth) was removed before sampling. The NE4 topsoil sample of the underlying uranium – NOM containing peat was cut out with a spade (20 x 20 x 20 cm) and the top layer was replaced. The topsoil sample (NE4_T) was placed in polythene bag, labelled and stored at 4°C until further analysis.

2.14.3 NOM characterisation of NE4_T

The absorption of radionuclides and heavy metals to NOM is an important mechanism that controls metal concentrations in aqueous systems. The effect of NOM on metal ion sorption to mineral surfaces is a complex function of the environment in which the minerals and ions reside, as well as the source^{154,155}. In the present work NOM characterisation was achieved by LoI (500 and 1000°C) and non-sequential experiments (Sections 2.5 and 2.13)

The presence of NOM either in or in the surroundings of radioactive contaminated lands is of major concern because of their potential to enhance mobilisation of metal contaminants away

from the contaminated sites. The presence of dissolved organic and inorganic substances may affect the sorption behaviour of metal ions into rocks and minerals significantly. Sorption of these organic ligands can affect metal sorption by i) Alteration of the mineral surface charge (electrostatic environment). For example, the sorption of anions may result in changes in surface charge favourable for sorption of cationic metals, ii) Forming tertiary surface complexes by ligand sorption at the surface site and aqueous complexation with metal ions, iii) Metal ligand complexation formation in the aqueous phase, iv) Competition of the ligand with metal for the mineral surface sites, v) Formation of surface precipitates at the water/mineral interface, and vi) Dissolution of the mineral^{156,157}.

Conditions that may promote enhanced mobility of contaminant metals in a typical water fracture where reactive mineral surfaces are present vary but often include high concentrations of organic ligands, low concentrations of competing cations, organic ligands with slow biodegradation rates and kinetically inert and very strong ligand - metal stability constants. Under certain conditions metal sorption may be favoured over the formation of an aqueous metal complex, or if the complex has formed, it may co-adsorb to the mineral phase rather than dissociate prior to adsorption. In general, it is reported in the literature that complexing organic ligands enhance the adsorption of metals at low pH and, because of the formation of aqueous metal ligand complexes, can reduce metal adsorption at higher pH^{157,158}.

2.15.4 Preparation of NE4_T bulk sample

The NE4 topsoil sample (NE4_T) was removed from the polythene bag and dried at 110 °C to constant weight for approximately 24 hours. Subsequently, the NE4_T sample was sieved through a 1 mm sieve and homogenised with a mortar. The total mass after homogenisation was 120.13 g (initial mass before drying 143.4 g, mass after drying 122.32 g, total mass after plants, roots, etc. removal 120.13 g).

Chapter three – Results and Discussion

Chapter 3. Results and Discussion

3.1 Results of the analyses of the samples from the first visit to Needle's Eye

3.1.1 Soil Particle Size and Physicochemical Characterisation

The results presented in Table 17 show the soil texture (particle size) classification of the soil samples from the Needle's Eye site.

Table 17. Soil particle fractions for Needle's Eye soil samples

Sample	Sand (%)	Silt (%)	Clay (%)
NE-A	15.0 ± 9.4	83.3 ± 9.4	1.7 ± 0.1
NE-B	9.5 ± 1.8	87.7 ± 2.7	2.6 ± 0.9
NE-C	6.5 ± 3.0	90.2 ± 4.4	3.2 ± 1.7
NE-D	33.7 ± 8.4	63.1 ± 7.6	3.1 ± 1.9

Table 17 above shows the distribution of sand, silt and clay percentages in soil samples taken from different sampling stations and in different depth profiles. For the NE-A sampling station the percentage (%) in the soil sample for sand was found to be 15.0 ± 9.4, for silt 83.3 ± 9.4 and for clay 1.7 ± 0.1. For NE-B sampling station the percentage (%) in the soil samples for sand was 9.5 ± 1.8, for silt 87.7 ± 2.7 and for clay 2.6 ± 0.9. For NE-C sampling station the percentage (%) in the soil samples for sand was found to be 6.5 ± 3.0, for silt 90.2 ± 4.4 and for clay 3.2 ± 1.7. For NE-D sampling station the percentage (%) in the soil samples for sand was found to be 33.7 ± 8.4, for silt 63.1 ± 7.6 and for clay 3.1 ± 1.9.

Figure 55 shows the distribution of soil particles, within Needle's Eye soil samples, in a textural triangle as introduced by Bouyoucos¹²². All soil samples were characterised by their textural content as silt / silt loam type.

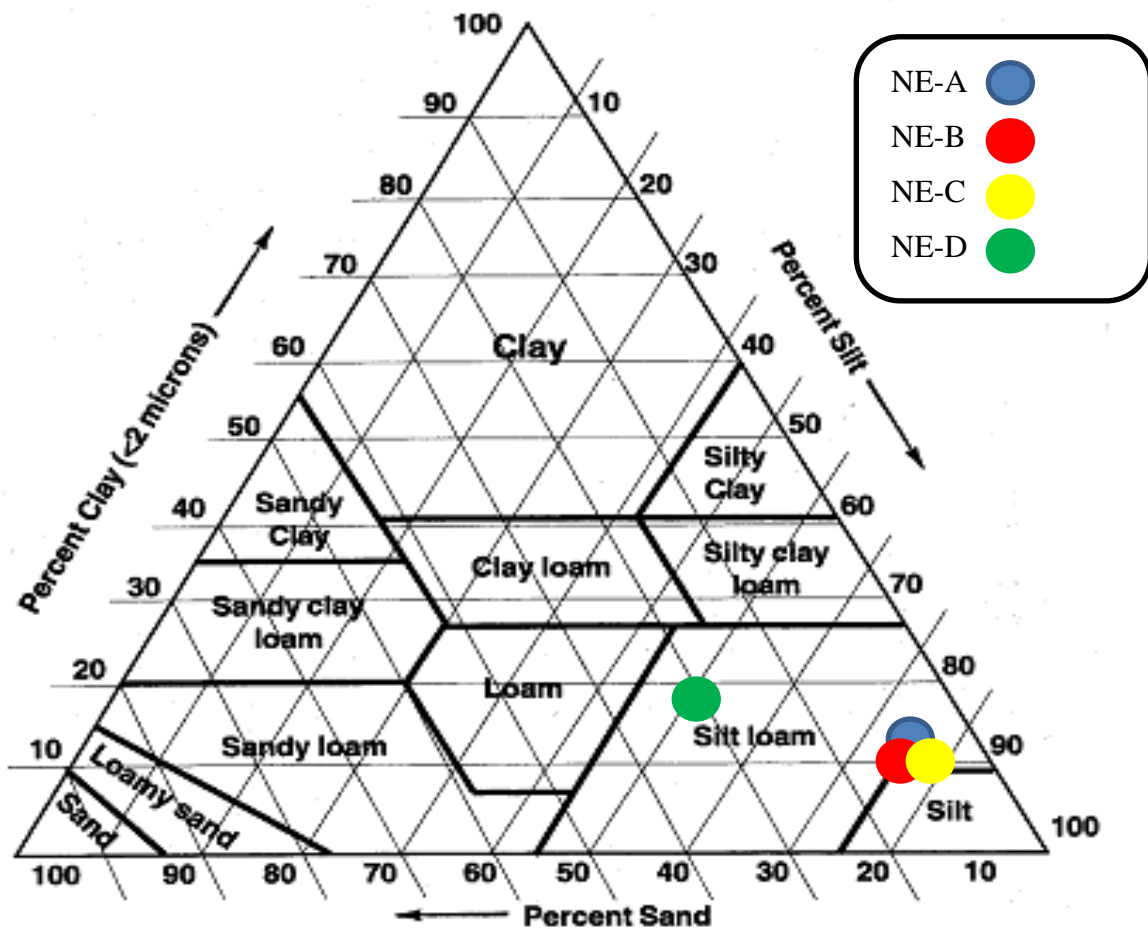


Figure 55. Soil particle distribution in a textural triangle

3.1.2 Gamma Spectrometry Analysis

The soil samples from the Needle’s Eye site, collected in September 2014, were found to contain significantly higher activity concentrations ^{226}Ra compared to the values shown in Sections 1.3.3.1 and 1.5.1.

The results presented in Table 18 show the activity concentrations for ^{226}Ra , ^{214}Pb and ^{214}Bi (^{238}U series) in different depths from four different sampling stations. Figure 56 shows the distribution of activity ratios between $^{226}\text{Ra}/^{214}\text{Bi}$ and $^{226}\text{Ra}/^{214}\text{Pb}$.

Table 18. ²³⁸U chain radionuclides in soil samples from Needle’s Eye

Sample	²¹⁴ Pb (Bq kg ⁻¹)	²²⁶ Ra (Bq kg ⁻¹)	²¹⁴ Bi (Bq kg ⁻¹)
NE-A	1.25x10 ² ± 0.08x10 ²	2.15x10 ² ± 0.33x10 ²	1.30x10 ² ± 0.10x10 ²
NE-B	2.61x10 ² ± 0.23x10 ²	4.72x10 ² ± 0.39x10 ²	2.27x10 ² ± 0.23x10 ²
NE-C	5.99x10 ² ± 0.93x10 ²	9.92x10 ² ± 1.33x10 ²	5.68x10 ² ± 1.02x10 ²
NE-D	0.42x10 ² ± 0.10x10 ²	0.42x10 ² ± 0.02x10 ²	0.35x10 ² ± 0.1x10 ²

Comparing the average activity concentrations of Needle’s Eye samples for ²²⁶Ra as presented in Table 18, ²²⁶Ra activity concentration was found to vary from 0.4x10² ± 0.02x10² to 9.92x10² ± 1.33x10² Bq kg⁻¹, which is significantly lower when compared to the values as reported in “Table 2.” where the concentrations varied from 7.4x10² to 280x10² Bq kg⁻¹, for soil types of clay and loam respectively. Previous work at Needle’s Eye site by Basham et al¹., reported activity concentration of ²³⁸U ~ 1 Bq kg⁻¹, which is significantly less when compared to the average ²²⁶Ra specific ~ 4.3x10² Bq kg⁻¹, as shown in Table 18. The high average activity concentration for ²²⁶Ra may be a result of the contribution of the several metalliferous uranium veins in the Needle’s Eye site, as mentioned in *Section 1.5.1*.

The activity ratios (Figure 56) between ²²⁶Ra and ²¹⁴Bi varied from 1.20 ± 0.06 to 2.07 ± 0.31 and between ²²⁶Ra and ²¹⁴Pb varied from 1.20 ± 0.04 to 1.81 ± 0.31. Therefore, it was concluded that secular equilibrium was not achieved between ²²⁶Ra/²¹⁴Bi and ²²⁶Ra/²¹⁴Pb. This disequilibrium may occur due to the constant loss of radon, which is the immediate decay product of radium, which disturbs the secular equilibrium. Finally, radium may have migrated to its present location at a time significantly less than that required by its daughter products to reach secular equilibrium. On the contrary, greater leaching of the daughters may occur compared to the leaching of radium.

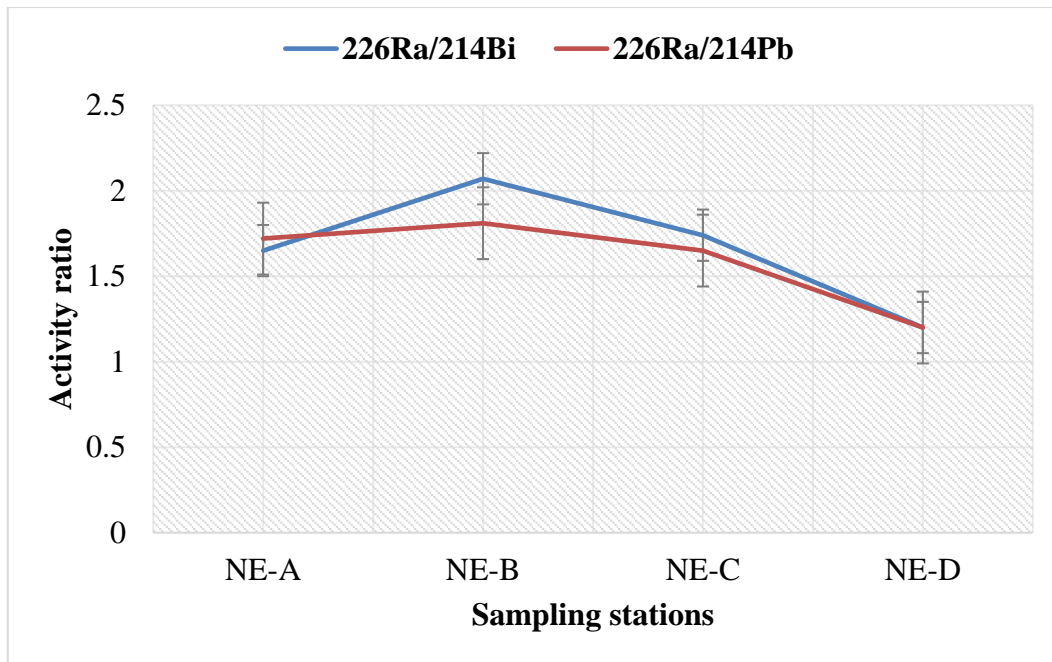


Figure 56. $^{226}\text{Ra}/^{214}\text{Bi}$ and $^{226}\text{Ra}/^{214}\text{Pb}$

In conclusion, the overall results from the first visit at the Needle's Eye site showed that:

1) The activity concentrations for ^{226}Ra in this study were significantly higher ($4.43 \times 10^2 \pm 0.52 \times 10^2 \text{ Bq kg}^{-1}$) compared to the activity concentrations reported in Table 2, where ^{226}Ra was shown to vary from 7.4×10^2 (USA, clay type soil) to $280 \times 10^2 \text{ Bq kg}^{-1}$ (Russia, loam type soil) and in previous study¹ for Needle's Eye (1 Bq kg^{-1}) for ^{238}U .

2) The soil particle size analyses indicated that the soil samples can be classified as Silt type, which may include mineral phases such as illite ($(\text{K},\text{H}_3\text{O})(\text{Al},\text{Mg},\text{Fe})_2(\text{Si},\text{Al})_4\text{O}_{10}[(\text{OH})_2,(\text{H}_2\text{O})]$), kaolinite ($(\text{Al}_2\text{Si}_2\text{O}_5(\text{OH})_4)$), and montmorillonite ($(\text{Na},\text{Ca})_{0.33}(\text{Al},\text{Mg})_2(\text{Si}_4\text{O}_{10})(\text{OH})_2 \cdot n\text{H}_2\text{O}$) and mica group minerals (e.g. biotite, $\text{K}(\text{Mg},\text{Fe})_3\text{AlSi}_3\text{O}_{10}(\text{F},\text{OH})_2$, muscovite, $\text{KAl}_2(\text{AlSi}_3\text{O}_{10})(\text{F},\text{OH})_2$), however, the PXRD analysis did not identify these mineral phases. Compared to the literature as described in Section 1.5, activity concentrations for ^{226}Ra were not reported in similar classified soil samples. Therefore, it can be assumed that silt – silt loam classified soils may host significant activity concentrations for ^{226}Ra . Further investigation in order to determine whether there is any correlation between the soil particle size classification and the reported activity concentrations of ^{226}Ra was conducted during sampling visit two and three.

3.2 Results from the Second Visit on the Site

A second sampling visit to Needle's Eye was made to obtain samples from the undisturbed areas of the site.

3.2.1 Gamma Spectrometry Analysis

The soil samples from the Needle's Eye site, collected in October 2015, were found to contain significantly higher activity concentrations of ^{226}Ra , compared to the values shown in *Sections 1.3.3.1 and 3.1*) and to previous research visit that was done at Needle's Eye site (see *Section 1.5.1*).

More specific, the results from the second visit at Needle's Eye for ^{226}Ra varied from $0.19 \times 10^2 \pm 0.06 \times 10^2$ to $31.65 \times 10^2 \pm 10.24 \times 10^2$ Bq kg⁻¹, whereas, the results from the first visit varied from $0.42 \times 10^2 \pm 0.02 \times 10^2$ to $9.92 \times 10^2 \pm 1.33 \times 10^2$ Bq kg⁻¹. Furthermore, the ^{226}Ra results from the second visit at Needle's Eye were significantly higher when compared to the ^{226}Ra results shown in Table 2 which varied from 7.4×10^2 to 280×10^2 Bq kg⁻¹ representing various places worldwide.

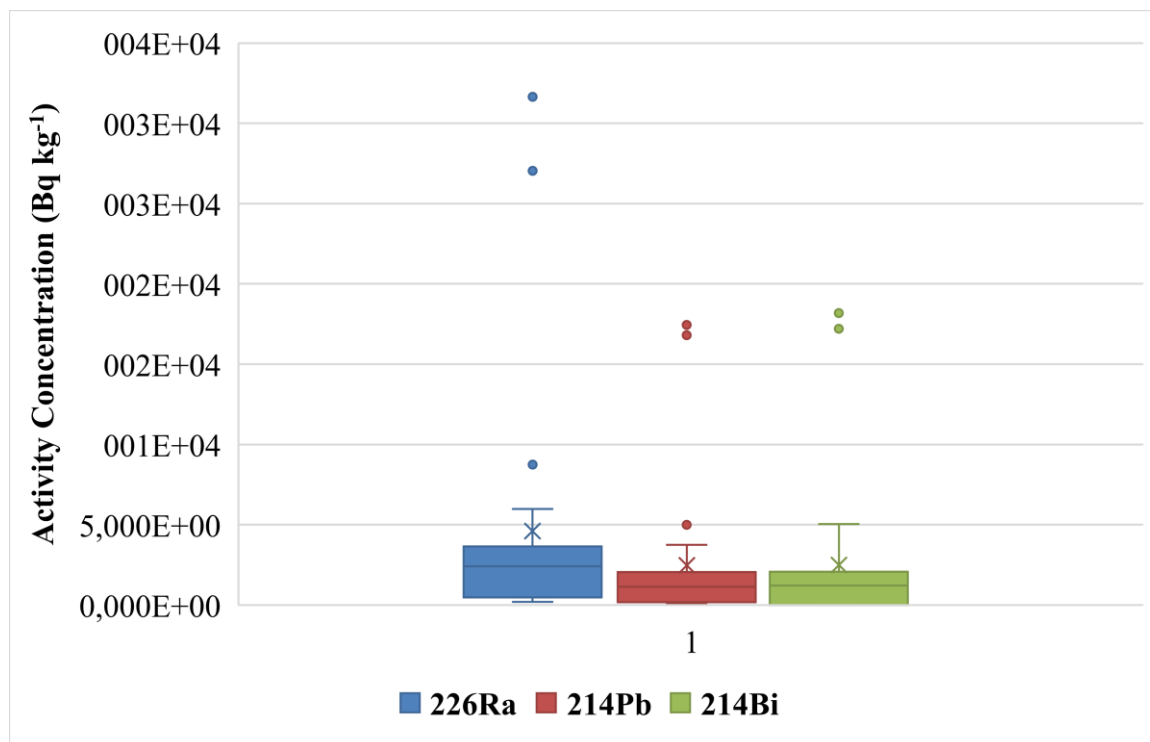


Figure 57. Activity Concentrations

Figure 57 shows that the activity concentrations (Bq kg^{-1}) for ^{226}Ra in NE1 samples varied from $0.32 \times 10^2 \pm 0.08 \times 10^2$ to $2.06 \times 10^2 \pm 0.41 \times 10^2$ with an average value of $1.62 \times 10^2 \pm 0.34 \times 10^2$, for NE2 samples varied from $2.00 \times 10^2 \pm 0.90 \times 10^2$ to $5.98 \times 10^2 \pm 2.07 \times 10^2$ with an average value of $5.22 \times 10^2 \pm 2.07 \times 10^2$, for NE3 samples varied from $3.67 \times 10^2 \pm 2.10 \times 10^2$ to $31.65 \times 10^2 \pm 10.24 \times 10^2$ with an average value of $25.51 \times 10^2 \pm 9.73 \times 10^2$, for NE4 samples varied from $2.55 \times 10^2 \pm 0.92 \times 10^2$ to $3.64 \times 10^2 \pm 1.28 \times 10^2$ with an average value of $5.34 \times 10^2 \pm 1.94 \times 10^2$ and for NE5 samples varied from $0.19 \times 10^2 \pm 0.06 \times 10^2$ to $0.49 \times 10^2 \pm 0.13 \times 10^2$ with an average value of $0.36 \times 10^2 \pm 0.09 \times 10^2$.

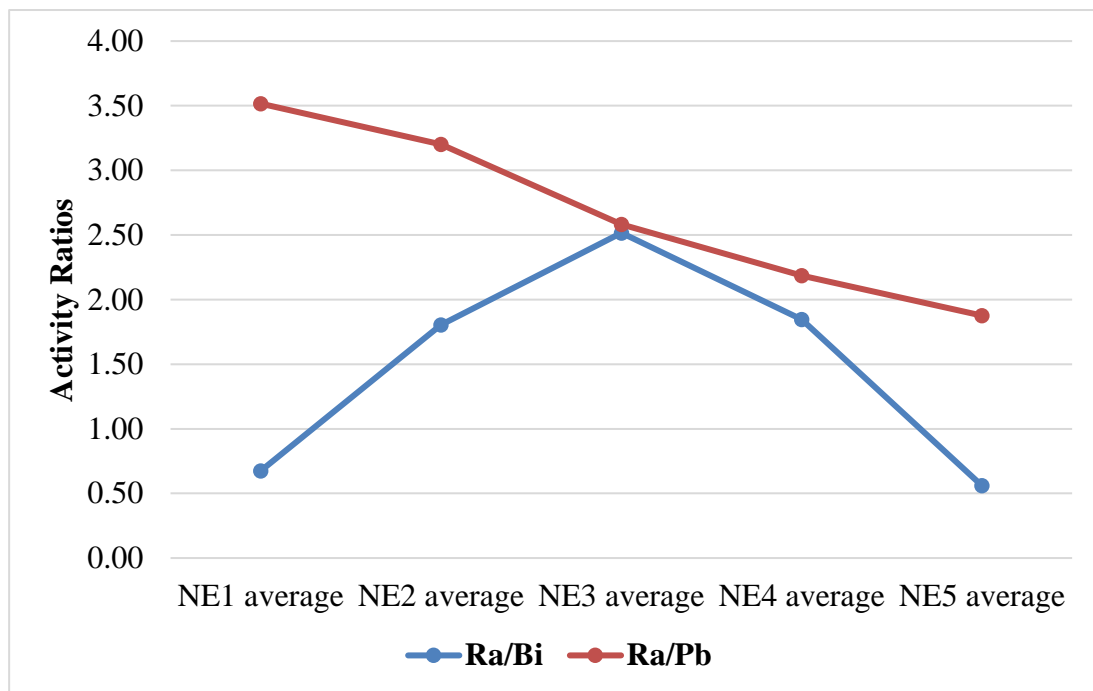


Figure 58. Activity ratios

The average activity ratios (Figure 58) between ^{226}Ra and ^{214}Bi (Ra/Bi) and between ^{226}Ra and ^{214}Pb (Ra/Pb) varied from 0.56 to 2.52 and from 1.88 to 3.52 respectively. Therefore, it was concluded that secular equilibrium was not evident between ^{226}Ra and ^{214}Bi and ^{214}Pb .

In conclusion, it was shown that:

- 1) On average, the highest activity concentrations for ^{226}Ra were located at sampling stations NE3, NE4 as expected from the literature where elevated concentrations of uranium have been reported¹ (see Section 2.2.2.4).

- 2) NE3 and NE4 sampling stations are located within the areas of Needle's Eye site that are characterised by organic rich soil materials hence further investigation will help towards the understanding of any potential association between ^{226}Ra and NOM (*see Section 3.2.3*).
- 3) The results of ^{226}Ra activity concentrations measurements from the second visit to Needle's Eye site show that there is no consistent relationship to the soil particle size.

3.2.2 Elemental Composition

The soil samples from the Needle's eye site were analysed by using ICP - MS for their ^{238}U content.

The average concentrations (mg kg^{-1}) of ^{238}U were found to be for NE1 $313 \times 10^{-3} \pm 16 \times 10^{-3}$, for NE2 $396 \times 10^{-3} \pm 20 \times 10^{-3}$, for NE3 $2154 \times 10^{-3} \pm 108 \times 10^{-3}$, for NE4 $678 \times 10^{-3} \pm 34 \times 10^{-3}$, and for NE5 $362 \times 10^{-3} \pm 18 \times 10^{-3}$. It should be noted that the soil samples for the NE3 and NE4, which were sampled from the peat bog areas of the site, characterised by their organic rich content⁹⁸ (*see Section 1.5.1*) demonstrated considerably higher concentrations of uranium when compared to the other soil samples.

3.2.3 Physicochemical Characterisation

To investigate further any potential association between radium with species in the natural environment at Needle's Eye, Loss on Ignition (LoI) was measured. LoI, as described in *Section 2.5*, is a technique which through careful choice of temperature can differentiate between inorganic and organic carbon-containing phases.

The results obtained from the LoI measurements are shown in Table 19, which also shows the activity concentration of the measured ^{226}Ra . In general, the samples that showed the highest activity concentrations for ^{226}Ra showed the highest percentages LoI. For example, NE3 0.063 mm, which showed the highest measured activity (3200 Bq kg^{-1}) and, the highest value (79.62 %) of LoI.

Table 19. LoI and ^{226}Ra results from Needle's Eye site

Sample	LoI (%)	^{226}Ra (Bq kg ⁻¹)
NE1 2 mm	6.10 ± 2.46	2.06x10 ² ± 0.41 x10 ²
NE1 1 mm	2.10 ± 1.44	1.05 x10 ² ± 0.21 x10 ²
NE1 250 µm	1.03 ± 1.01	1.12 x10 ² ± 0.22 x10 ²
NE1 125 µm	1.45 ± 1.2	0.32 x10 ² ± 0.08 x10 ²
NE1 0.063 mm	0.45 ± 0.17	0.33 x10 ² ± 0.10 x10 ²
NE2 2 mm	8.90 ± 2.98	2.42 x10 ² ± 1.20 x10 ²
NE2 1 mm	17.10 ± 4.14	3.05 x10 ² ± 1.24 x10 ²
NE2 250 µm	41.8 0± 6.45	5.98 x10 ² ± 2.07 x10 ²
NE2 125 µm	0.50 ± 0.18	2.00 x10 ² ± 0.90 x10 ²
NE2 0.063 mm	6.50 ± 2.76	2.22 x10 ² ± 0.82 x10 ²
NE3 2 mm	4.20 ± 2.15	3.67 x10 ² ± 2.10 x10 ²
NE3 1 mm	5.10 ± 2.96	5.43 x10 ² ± 2.77 x10 ²
NE3 250 µm	33.47 ±5.17	8.75 x10 ² ± 3.79 x10 ²
NE3 125 µm	69.30 ± 8.16	27.04 x10 ² ± 10.31 x10 ²
NE3 0.063 mm	79.62 ± 8.98	31.65 x10 ² ± 10.24 x10 ²
NE4 2 mm	1.54 ± 0.36	3.64 x10 ² ± 1.28 x10 ²
NE4 1 mm	0.95 ± 0.34	3.23 x10 ² ± 1.10 x10 ²
NE4 250 µm	0.84 ± 0.14	3.14 x10 ² ± 0.92 x10 ²
NE4 125 µm	1.09 ± 0.65	3.47 x10 ² ± 1.59 x10 ²
NE4 0.063 mm	0.72 ± 0.14	2.55 x10 ² ± 0.92 x10 ²
NE5 2 mm	0.18 ± 0.07	0.48 x10 ² ± 0.12 x10 ²
NE5 1 mm	0.17 ± 0.06	0.42 x10 ² ± 0.09 x10 ²
NE5 250 µm	0.20 ± 0.06	0.49 x10 ² ± 0.13 x10 ²
NE5 125 µm	0.11 ± 0.03	0.19 x10 ² ± 0.06 x10 ²
NE5 0.063 mm	0.16 ± 0.04	0.26 x10 ² ± 0.06 x10 ²

The results shown in Table 19 were statistically processed in order to investigate any potential correlation between ^{226}Ra and LoI. These are shown in Figure 59.

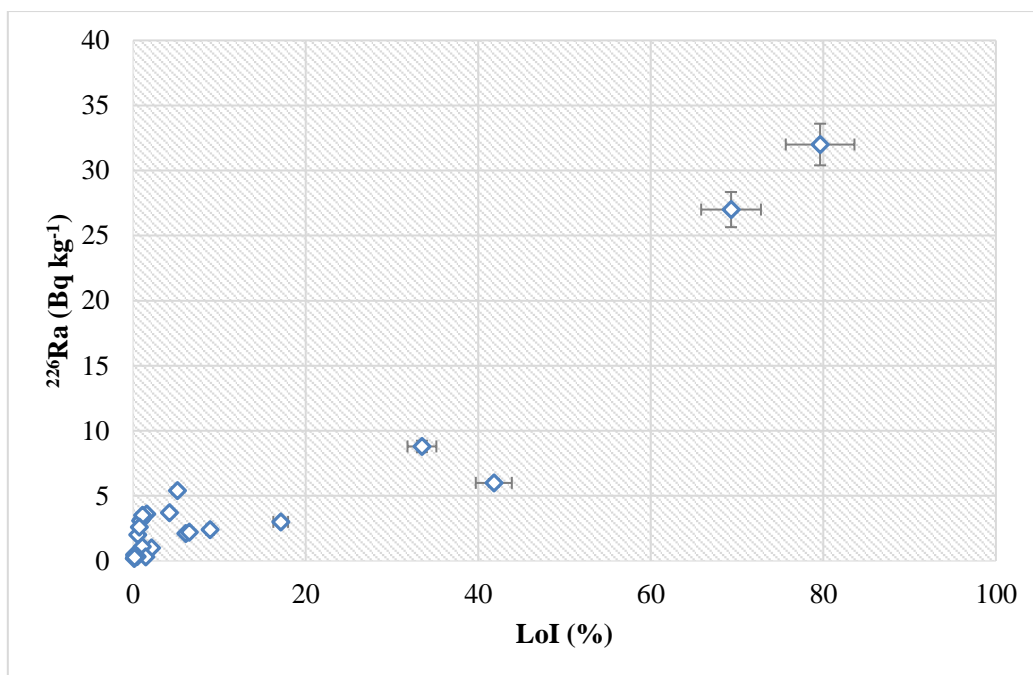


Figure 59. Correlation plot between ²²⁶Ra and LoI

Figure 59 shows a correlation between ²²⁶Ra and LoI. However, the range of values in the graph is not evenly distributed across the linear regression, as most values are situated within the 0 – 10 % of LoI as shown in the graph.

3.2.4 Mineralogical Analyses

Powder X - ray diffraction (PXRD) analyses were performed at the Needle’s Eye bulk (i.e. bulk = undisturbed soil) soil samples. The results of the analysed samples are shown below in Figures 60 - 65. Since X-ray diffraction detects crystalline phases only, any amorphous phase would not be identified e.g. organic matter such as leaf litter where no long-range crystalline order is present.

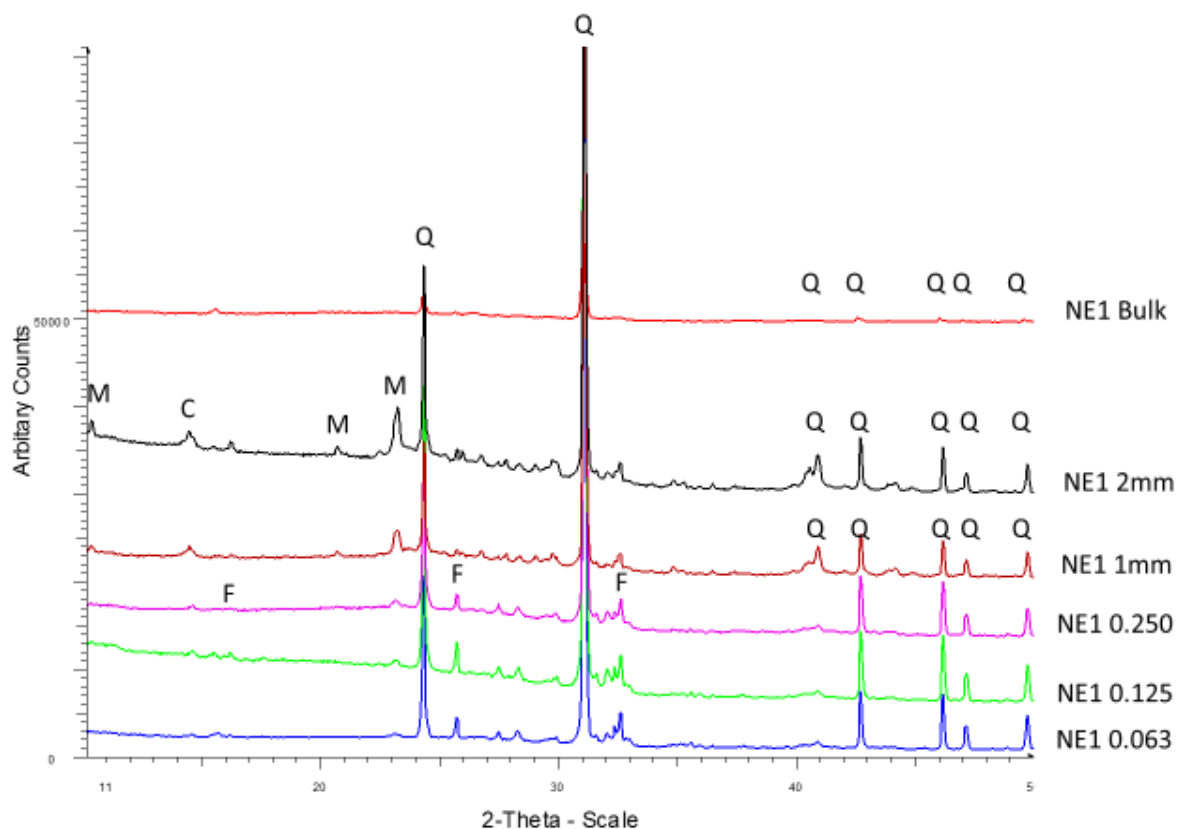


Figure 60. PXRD data of NE1 samples of varying size (Phase Identified: M = Muscovite; C=Chlorite, Q = Quartz, F= Feldspar)

The X-ray diffraction of the bulk NE1 phase (Figure 60) is featureless except for the strong reflections from quartz on a background showing poor crystallinity. In the sieved fraction, the platy crystallites of the layered silicates such as muscovite and chlorite concentrate in the fraction with the largest particle size (2 mm). This is typical for these type of phases as their structure results in making the phases more difficult to break down into the smallest particles. Strong reflections are expected from these phases due to a process known as preferred orientation where the crystallites align easily with one another rather than lying randomly. Although the choice of the transmission mode instrument should minimise this effect, larger particles always tend to align with the tape rather than fall perpendicular to it, meaning fractions with the larger particle sizes will be worst affected.

An expansion of the low angle region of the 2 mm sample from the NE1 phases is given in Figure 61 matched to the ICDD database. The effect of preferred orientation of the layered silicate (mica and clays) can clearly be observed where 00l reflections are enhanced relative to the intensity expected for the database. The identification of the feldspar phase is not clear as

many feldspars exist that have reflections in a similar position in the 2-theta range. Anorthite (calcium rich end of the Ca-Na solid solution – pattern no: 20-0020) is overlaid on the figure.

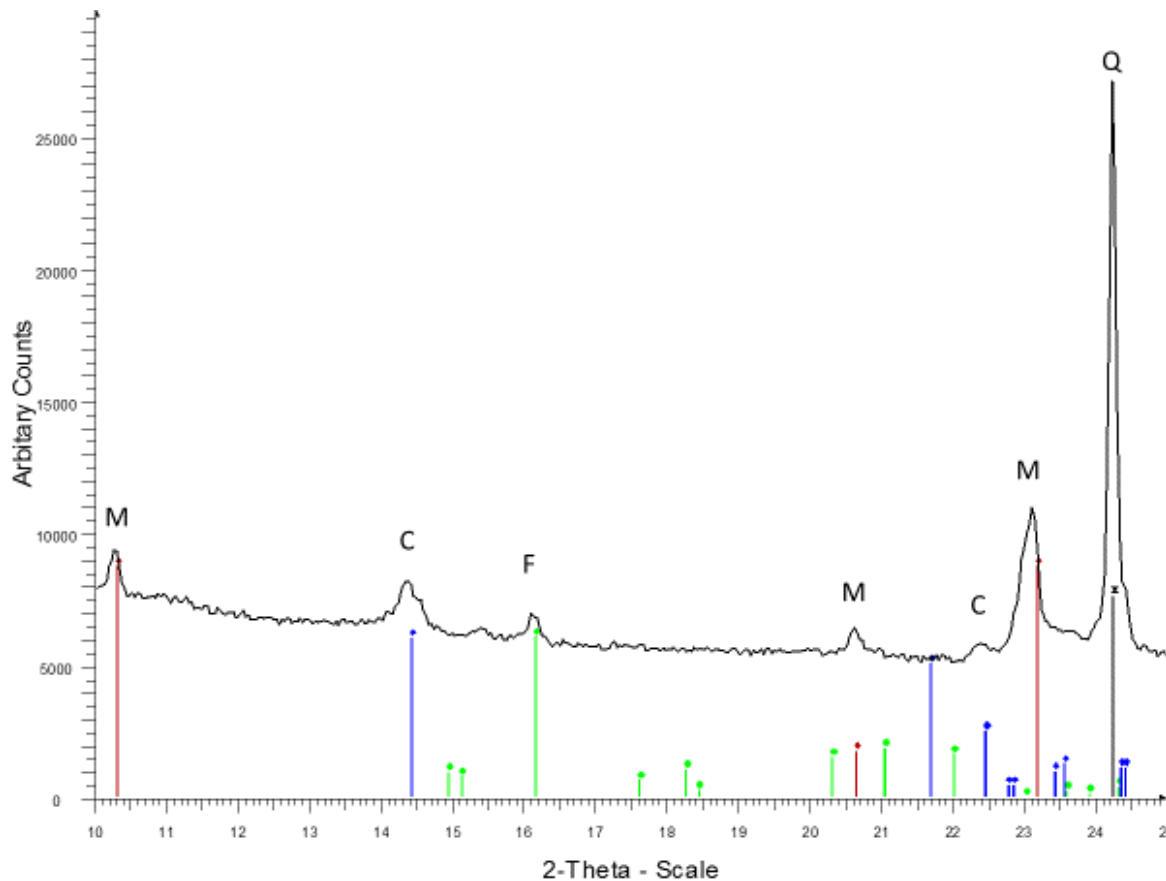


Figure 61. PXR D Data for the 2mm fraction of the NE1 phase. Vertical lines are patterns from the ICDD database where M = muscovite (red - 02-0058), F = anorthite feldspar (green -20-0020), C = Chlorite (blue – 46-1323) and Q = quartz (black – 46-1045)

According to Jamet⁸ et al., and Braithwaite and Knight¹⁶⁰, all these mineral phases have been previously identified at Needle’s Eye, close to the sampling locations of the present study.

Figures 62 - 65 show the powder diffraction patterns of similar phases taken from the NE2, NE4 and NE5 sites. All the patterns are quite similar to that for those seen at the NE1 site with no additional phases identified. The NE3 patterns are particularly featureless only showing signs of feldspar and quartz and little evidence of the clay/mica phases.

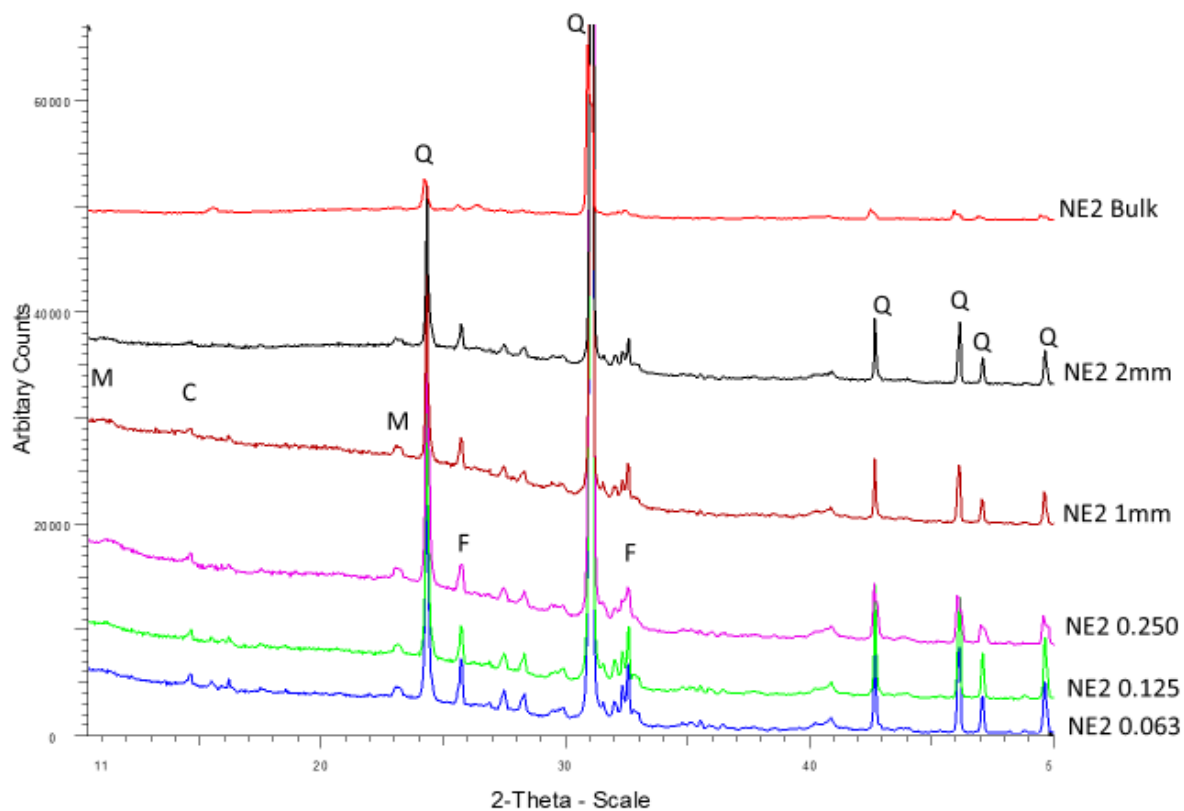


Figure 62. PXRD data of the NE2 samples of varying particle size phase identified: M = Muscovite, C = Chlorite, Q = Quartz, F = Feldspar

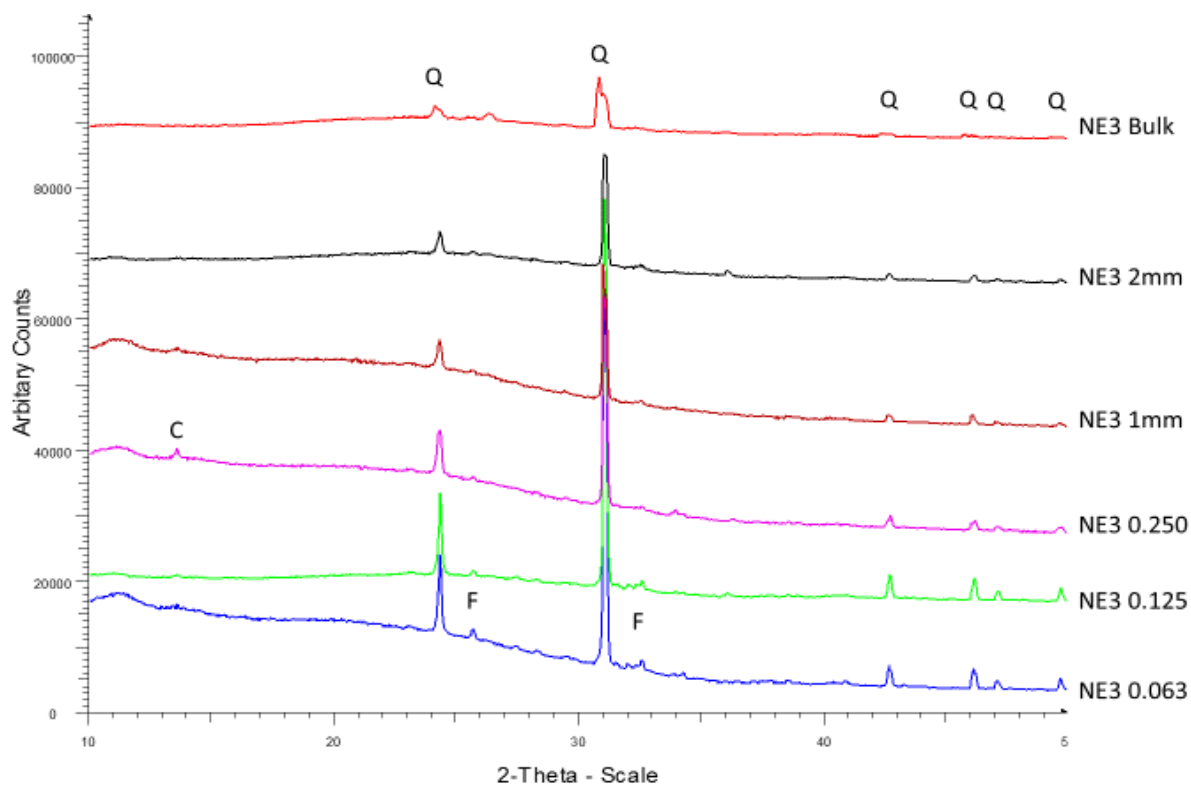


Figure 63. PXRD data of the NE3 samples of varying particle size phase identified: C=Chlorite, Q = Quartz, F= Feldspar

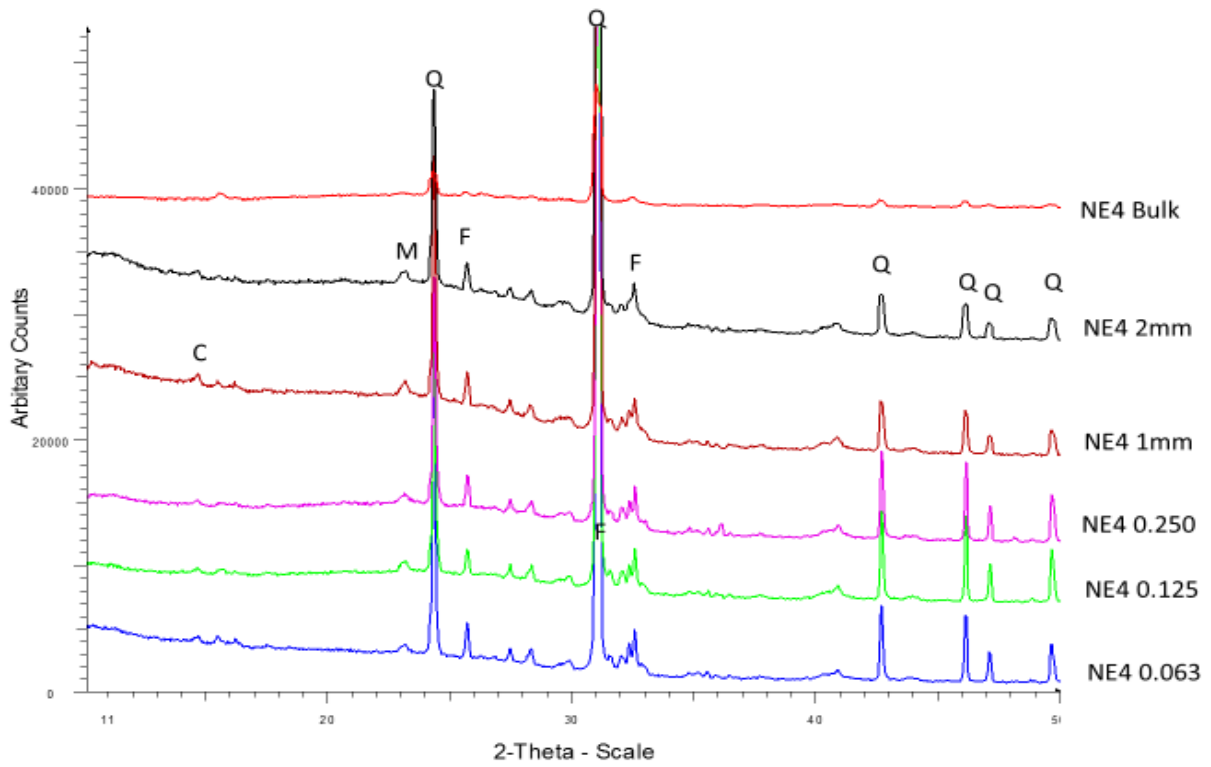


Figure 64. PXRD data of the NE4 samples of varying particle size, phase identified: M = Muscovite, C = Chlorite, Q = Quartz, F = Feldspar

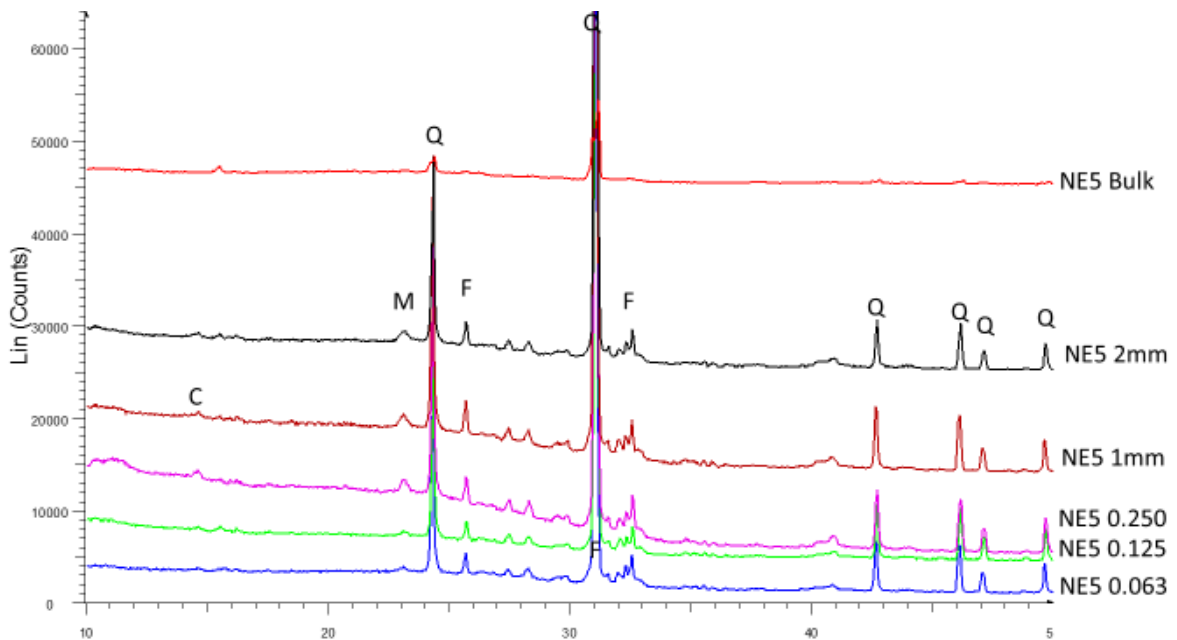


Figure 65. PXRD data of the NE5 samples of varying particle size phase identification: M = Muscovite, C = Chlorite, Q = Quartz, F = Feldspar

According to the literature (Basham¹ et al., Hooker⁸ et al., Jamet⁹⁹ et al., and Braithwaite and Knight¹⁶⁰), there are more than 60 phases associated with the Needle's Eye site. The major phases are quartz (SiO₂), feldspars, dolomite ((Ca,Mg)CO₃), calcite (CaCO₃), gypsum (CaSO₄.2H₂O) and baryte (BaSO₄). Close to the uraninite (UO₂) vein, haematite (Fe₂O₃), chalcopyrite (CuFeS₂), pyrite (FeS₂), sphalerite ((ZnFe)S) and some arsenic phases (FeAs and NiAs) have also been found together with bismuth. Weathering of the silicate minerals can also produce clays and micas such as illite and muscovite. The observation of phases in a powder X-ray diffraction pattern depends on their crystallinity, poorly crystalline/amorphous phases cannot be characterised. This means that the organic material in the pattern does not contribute to the pattern in terms of phase identification, it just adds to the background. The powder diffraction data presented in Figures 83 - 86 are dominated by the reflections from quartz; a highly crystalline well-ordered phase.

The mineral phases analyses (XRD) indicated that mainly quartz (SiO₂), muscovite (KAl₂(AlSi₃O₁₀)(F,OH)₂), chlorite ((Mg,Fe)₃(Si,Al)₄O₁₀) and feldspar minerals e.g. anorthite (CaAl₂Si₂O₈) dominated all Needle's Eye soil samples. This fits with the geology of the Needle's Eye where the main rock formation is granodiorite and the main constituents of this rock are quartz, mica and feldspar.

Though quartz is abundant in nature, it is not one of the most important minerals when considering the migration of uranium. Quartz has no capacity for ion exchange so does not interact with uranium.

Apart from gaseous movement, transport of radionuclides through soil is a consequence of the movement of transporting water. Movement of radionuclides may be retarded by the adsorptive properties of the soil. The ion exchange properties of soil materials play an important role in retaining or transporting the radionuclides released into the soil environment. An understanding of the ion exchange reactions of ²²⁶Ra with soil and its clay fraction are therefore important.

It can be concluded that the results from the XRD analyses are in good agreement with the geology of Needle's Eye site (granite, granodiorite background, *see Section 1.5.1a*), with the background studies (*see Section 1.3.3.2*) and with the soil texture – particle size analysis (*see Section 3.1.2*) which suggested that the soil samples from Needle's Eye site can be characterised as silt rich soils and therefore silt mineral phases should be found.

3.3 Results from the Third Visit on the Site

A third visit to Needle's Eye was made to collect samples from the same sampling stations as visited in the 2nd visit. The new samples were used to investigate the behaviour of ^{226}Ra in bulk samples, and not in different fractions as before (see *Section 3.2*).

3.3.1 Gamma Spectrometry Analysis

Figure 66 shows the gamma spectrometry measurements for ^{226}Ra , ^{214}Pb and ^{214}Bi (^{238}U series).

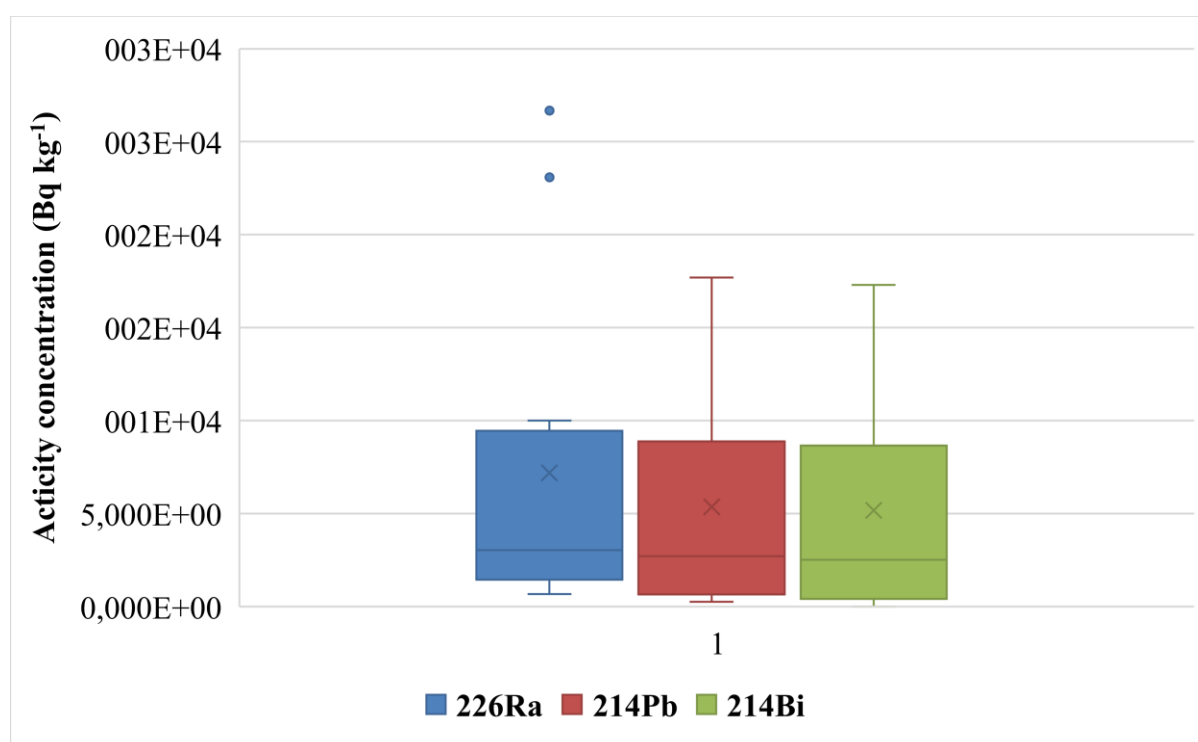


Figure 66. Activity concentrations

The activity concentrations (Bq kg^{-1}) for ^{226}Ra in NE1 samples varied from 0.13×10^2 to 0.27×10^2 with an average value of $0.17 \times 10^2 \pm 0.05 \times 10^2$ (MDA values), for NE2 from 0.14×10^2 to 0.19×10^2 with an average value of $0.16 \times 10^2 \pm 0.02 \times 10^2$ (MDA), for NE3 from $2.41 \times 10^2 \pm 2.00 \times 10^2$ to $4.90 \times 10^2 \pm 0.90 \times 10^2$ with an average value of $3.14 \times 10^2 \pm 0.72 \times 10^2$, for NE4 from $3.23 \times 10^2 \pm 0.90 \times 10^2$ to $26.67 \times 10^2 \pm 6.40 \times 10^2$ with an average value of $15.2 \times 10^2 \pm 11.4 \times 10^2$ and for NE5 from $0.67 \times 10^2 \pm 0.50 \times 10^2$ to $10.00 \times 10^2 \pm 3.20 \times 10^2$ with an average value of $3.49 \times 10^2 \pm 3.75 \times 10^2$ (both MDA and non MDA values and therefore high standard deviation values). Of the twenty samples that were analysed for their radiochemical content eight of them

failed to show any significant values for ^{226}Ra . Therefore, they are excluded from the discussion and conclusion section since no valuable information can be extracted from them.

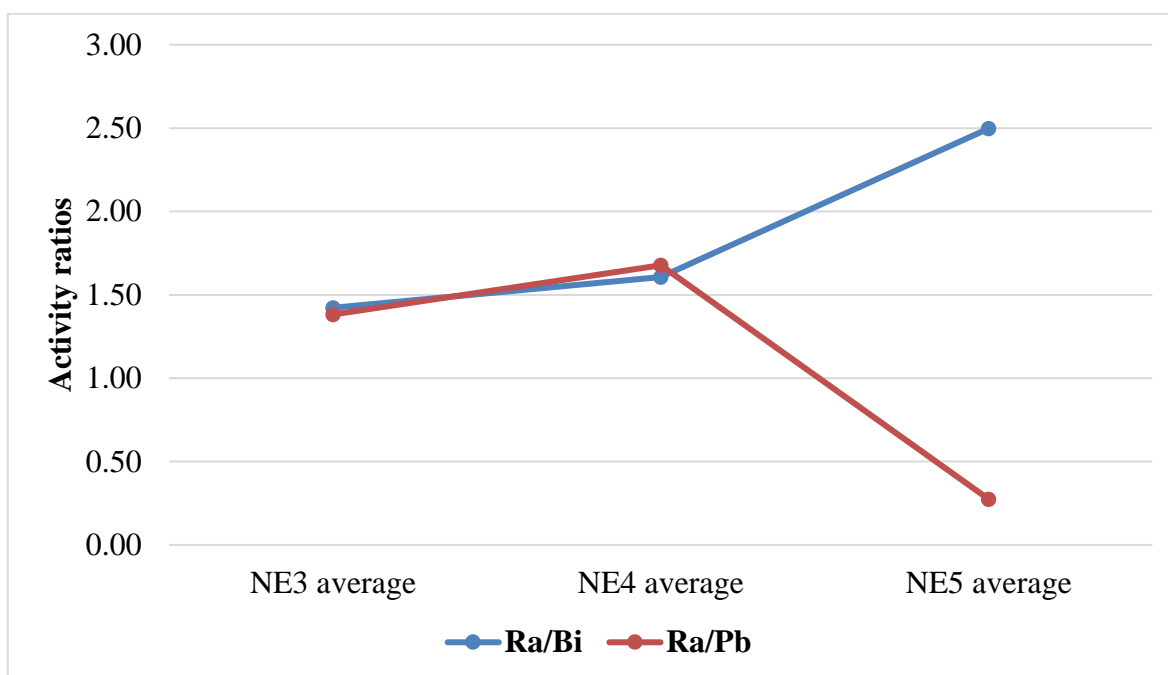


Figure 67. Activity ratios

The activity ratios (Figure 67) between radium and bismuth ($^{226}\text{Ra}/^{214}\text{Bi}$) and between radium and lead ($^{226}\text{Ra}/^{214}\text{Pb}$) showed that secular equilibrium between $^{226}\text{Ra}/^{214}\text{Bi}$ and $^{226}\text{Ra}/^{214}\text{Pb}$ was not achieved.

In conclusion, it was shown that:

1. Considering average values, the highest activity concentrations (Bq kg^{-1}) for ^{226}Ra were located at sampling stations NE3 and NE4, as expected from the literature, where Jamet⁸ et al., reported elevated concentrations of uranium varying from 1.19 to 113 ppb in the organic rich sediments. Furthermore, Basham¹ et al., confirmed, by using the sensitive techniques of autoradiography and fission track registration, a strong association between uranium and organic matter.
2. NE3 and NE4 sampling stations are located within the areas of Needle's Eye site that are characterised by organic rich soil materials. Further investigations were conducted in order to gain a better understanding of any potential association between ^{226}Ra and

other environmental species present at Needle’s Eye (i.e. organics, carbonates, mineral phases, etc.) (see Section 3.3.5).

3.3.2 Physicochemical Characterisation

In previous *Sections 3.2.3* and *3.3.1*, it was noted that there may be a potential association (Figure 68) between the activity concentration of ^{226}Ra and NOM (derived from LoI experiments).

Table 20. ^{226}Ra , Si and Al results from Needle’s Eye site

Sample	LoI (%)	^{226}Ra (Bq kg ⁻¹)	Si (mg L ⁻¹)	Al (mg L ⁻¹)
NE3-a1	21.50 ± 4.63	2.80x10 ² ± 0.55x10 ²	37978.9 ± 1842.3	163.53 ± 3.76
NE3-a2	26.75 ± 5.17	2.41x10 ² ± 2.00x10 ²	21025.6 ± 4842.8	110.10 ± 30.32
NE3-b1	21.53 ± 4.64	2.85x10 ² ± 2.44x10 ²	12850.1 ± 4018.8	62.12 ± 28.61
NE3-b2	34.35 ± 5.86	4.90x10 ² ± 0.90x10 ²	27716.2 ± 8806.9	117.93 ± 58.39
NE4-a1	69.12 ± 8.31	23.08x10 ² ± 6.50x10 ²	54324.4 ± 3528.5	178.93 ± 9.02
NE4-a2	22.05 ± 4.69	3.23x10 ² ± 0.90x10 ²	17005.8 ± 1767.7	98.35 ± 7.78
NE4-b2	23.67 ± 4.86	7.80x10 ² ± 2.50x10 ²	36146.9 ± 4384.8	167.88 ± 13.87

Table 20 above shows the values for LoI (1000 °C) and ^{226}Ra which were measured on bulk soil samples. Only samples that showed significant activity concentrations for ^{226}Ra are shown in Table 20. These results indicate, as the findings presented in *Section 3.2.3*, a relative association between LoI and ^{226}Ra . Though statistically ($R^2 = 0.8822$), it can be concluded by Figure 68, that ^{226}Ra and LoI are strongly associated, this conclusion cannot stand without further investigation as the range of values in the graph is not evenly distributed across the linear regression, and most values are situated below the $< 10 \times 10^2$ Bq kg⁻¹ region and within the 20 – 25 %LoI. Therefore, it cannot be concluded that a simple positive linear correlation of ^{226}Ra – LoI occurs.

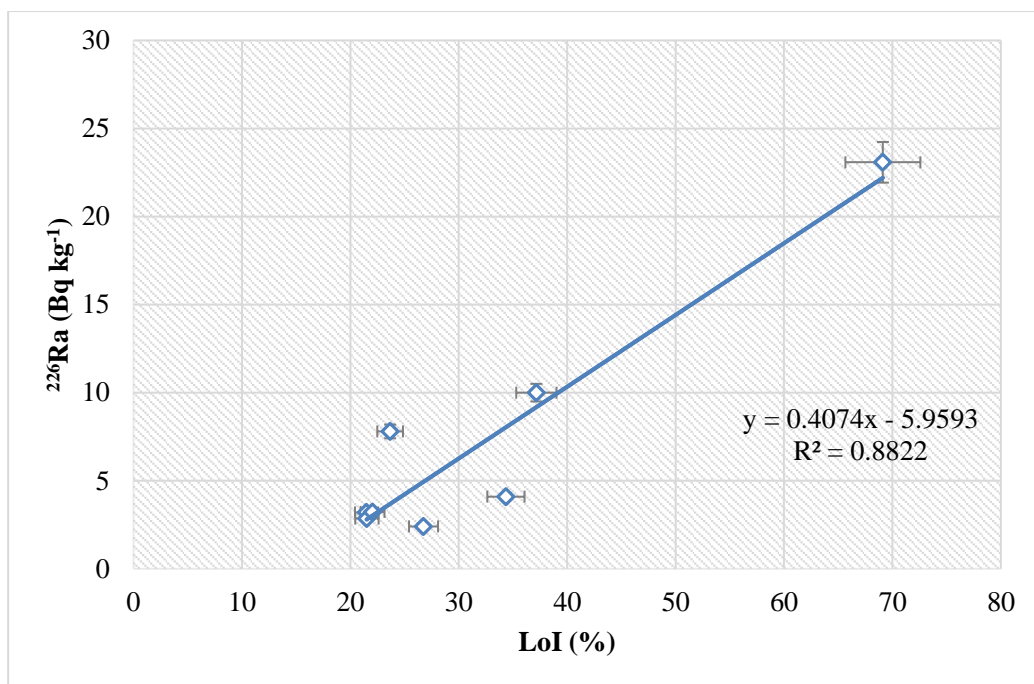


Figure 68. Correlation plot between ²²⁶Ra (significant reported activity concentrations) and LoI

The significantly high concentrations of silicon (i.e. average 29578.3 mg L⁻¹) and aluminium (i.e. average 128.4 mg L⁻¹) present in the soils of Needle's Eye suggest the presence of Al- (e.g. illite) and Si- (e.g. quartz) mineral phases in the soil samples.

3.3.3 Elemental Analysis

The soil samples from Needle's Eye site were analysed by ICP – MS in order to determine the ²³⁸U content. The results for ²³⁸U analysis are shown in Table 21 together with the results of ²²⁶Ra as presented earlier in Table 31 (see Section 3.3.1).

The results in Table 21 show that the activity concentrations (Bq kg⁻¹) for ²³⁸U in NE1 samples varied from 51.9 to 68.4 with an average value of 61.4 ± 7.9, for NE2 samples from 20.2 to 49.7 with an average value of 41.3 ± 12.1, for NE3 samples from 14.6 to 51.7 with an average value of 35.1 ± 7.2, for NE4 samples from 6.6 to 40.4 with an average value of 20.2 ± 1.9 and for NE5 samples from 9.9 to 36.4 with an average value of 17.2 ± 4.62.

Table 21. ^{238}U concentrations in soil samples from Needle's Eye

Sample	^{238}U (Bq kg ⁻¹)	^{226}Ra (Bq kg ⁻¹)
NE1-a1	$67.1 \times 10^2 \pm 5 \times 10^2$	<i>0.16*</i>
NE1-a2	$58.4 \times 10^2 \pm 4.2 \times 10^2$	<i>0.13*</i>
NE1-b1	$68.4 \times 10^2 \pm 17.5 \times 10^2$	<i>0.27*</i>
NE1-b2	$51.9 \times 10^2 \pm 5 \times 10^2$	<i>0.13*</i>
NE2-a1	$46.4 \times 10^2 \pm 8.3 \times 10^2$	<i>0.19*</i>
NE2-a2	$20.2 \times 10^2 \pm 5.5 \times 10^2$	<i>0.15*</i>
NE2-b1	$48.7 \times 10^2 \pm 23.9 \times 10^2$	<i>0.17*</i>
NE2-b2	$49.7 \times 10^2 \pm 10.8 \times 10^2$	<i>0.14*</i>
NE3-a1	$51.7 \times 10^2 \pm 1.8 \times 10^2$	$3.2 \times 10^2 \pm 0.6 \times 10^2$
NE3-a2	$14.6 \times 10^2 \pm 0.94 \times 10^2$	$2.41 \times 10^2 \pm 1.6 \times 10^2$
NE3-b1	$38.8 \times 10^2 \pm 18.9 \times 10^2$	$2.85 \times 10^2 \pm 2.44 \times 10^2$
NE3-b2	$35.2 \times 10^2 \pm 7.1 \times 10^2$	$4.1 \times 10^2 \pm 1.4 \times 10^2$
NE4-a1	$40.4 \times 10^2 \pm 2.8 \times 10^2$	$23.08 \times 10^2 \pm 6.5 \times 10^2$
NE4-a2	$10.7 \times 10^2 \pm 0.95 \times 10^2$	$3.23 \times 10^2 \pm 0.9 \times 10^2$
NE4-b1	$6.6 \times 10^2 \pm 0.33 \times 10^2$	$26.67 \times 10^2 \pm 6.4 \times 10^2$
NE4-b2	$23.1 \times 10^2 \pm 3.5 \times 10^2$	$7.8 \times 10^2 \pm 2.5 \times 10^2$
NE5-a1	$9.9 \times 10^2 \pm 2.09 \times 10^2$	$1.27 \times 10^2 \pm 0.3 \times 10^2$
NE5-a2	$36.4 \times 10^2 \pm 8.4 \times 10^2$	$1.48 \times 10^2 \pm 0.17 \times 10^2$
NE5-b1	$10.9 \times 10^2 \pm 0.59 \times 10^2$	$1.22 \times 10^2 \pm 0.3 \times 10^2$
NE5-b2	$11.07 \times 10^2 \pm 7.3 \times 10^2$	$10 \times 10^2 \pm 3.2 \times 10^2$

* Results in italics represent MDA values

The results in Table 21 suggest that the highest activity concentrations of ^{238}U are mainly located in sampling stations NE1 and NE2 and secondarily in sampling stations NE3, NE4 and NE5. It is tentatively concluded therefore that ^{238}U and ^{226}Ra show different environmental behaviours in their mobilities in soils taken from Needle's Eye. This statement can be supported graphically as is shown in Figure 69.

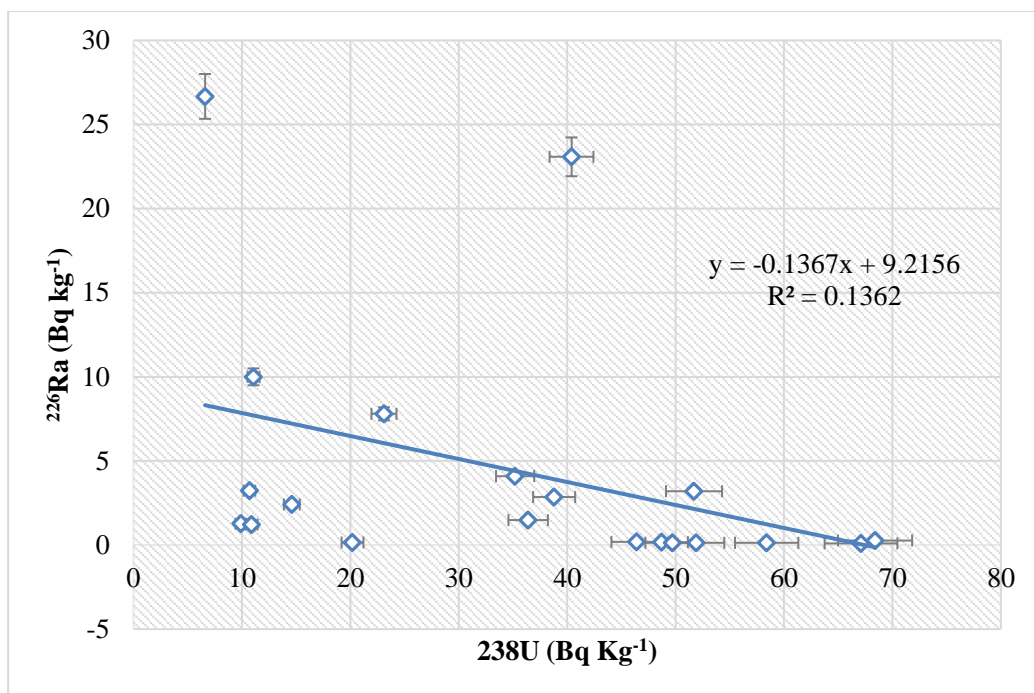


Figure 69. Correlation plot between ^{238}U and ^{226}Ra

Figure 69 shows that there is no correlation between the concentrations of ^{238}U and ^{226}Ra present in the soil samples.

3.3.4 Mineralogical Analyses

Powder XRD results of the samples were collected (Figure 70) to determine the mineralogical phases present in the samples. In order to further investigate the phases, present without the interference of the organic material, which is non-crystalline, PXRD data were recorded on the loss on ignition samples. Data were collected at 500 and 1000 °C as carbonates decompose beyond 1000 °C through loss of CO_2 . To capture carbonate phases which may also be of interest for radium uptake, data were compared at different temperatures and across different sites (NE1 - NE5).

Powder diffraction data recorded on samples combusted at 1000 °C across the different sites are shown in Figure 90, Section 3.3.5.5.2. There is a stark difference between all the other sites and that of NE4. Apart for NE4, the only phases observed in the patterns are quartz and feldspar. Neither of these phases has much relevant sequestration of radium as they contain no exchangeable ions. Further mineralogical analysis is discussed in the next Section 3.3.5.

3.3.5 Results for Needle's Eye NE4 topsoil (NE4_T)

3.3.5.1 Initial γ spectrometry analyses

From the total 120.13 g of the previously dried and homogenised NE4_T sample three replicates (Rep. 1 – 3) of approximately 20 g each were analysed initially for ²²⁶Ra activity concentration (Figure 71).

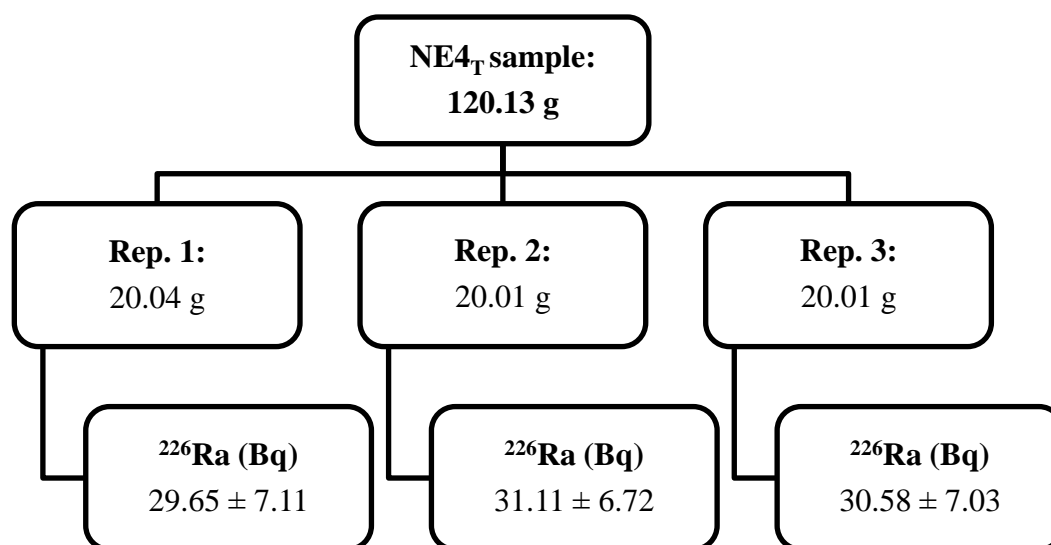


Figure 70. γ spectroscopy analyses of three 20 g NE4_T bulk samples

As expected, the three replicates of 20 g NE4_T samples showed very similar activity concentrations amongst them, with an average value of 30.47 ± 6.95 Bq kg⁻¹. It is noteworthy to mention that the activity concentrations of NE4_T (30.47 ± 6.95 Bq kg⁻¹ average of three), NE4-b1 (30.42 ± 6.52 Bq kg⁻¹) and NE4-a1, (28.09 ± 6.67 Bq kg⁻¹), are very similar with regards to their standard deviation. The reason behind this agreement relies on the fact that the NE4_T, NE4-a1, and NE4-b1 are from the same sampling location.

3.3.5.2 γ spectrometry and LoI analysis of NE4_T samples

The LoI method was applied for all NE4_T replicate samples to estimate the organic and carbonate content of the soils. The LoI method, described in Section 2.5, involves the destruction of the organic matter by igniting the soil at high temperature (approximately 500

and 1000 °C) until constant weight is obtained, after which the loss in weight of the soil is taken as a measure of the organic content.

About 5 g of soil were taken from each 20 g pot. The 5 g samples were firstly analysed by γ spectrometry for 3600 seconds. The 5 g samples were then burned to constant weight at 1000 °C for approximately 24 hours (Figure 72).

As expected, the three 5 g NE4_T replicate reported similar activity concentrations, within the errors, with an average value of 34.37 ± 6.73 Bq kg⁻¹. Furthermore, the 5 g and the 20 g NE4_T samples reported similar activity concentrations for ²²⁶Ra as expected.

The three 5 g NE4_T replicas showed very similar percentage LoI with an average value of 86.05 ± 9.28 %. These results shown in Figure 72 showed that the NOM in this locality of the Needle's eye site is 86.06%, as expected since the NE4 sampling spot is located within the organic peat bog as described in Section 1.5.1.

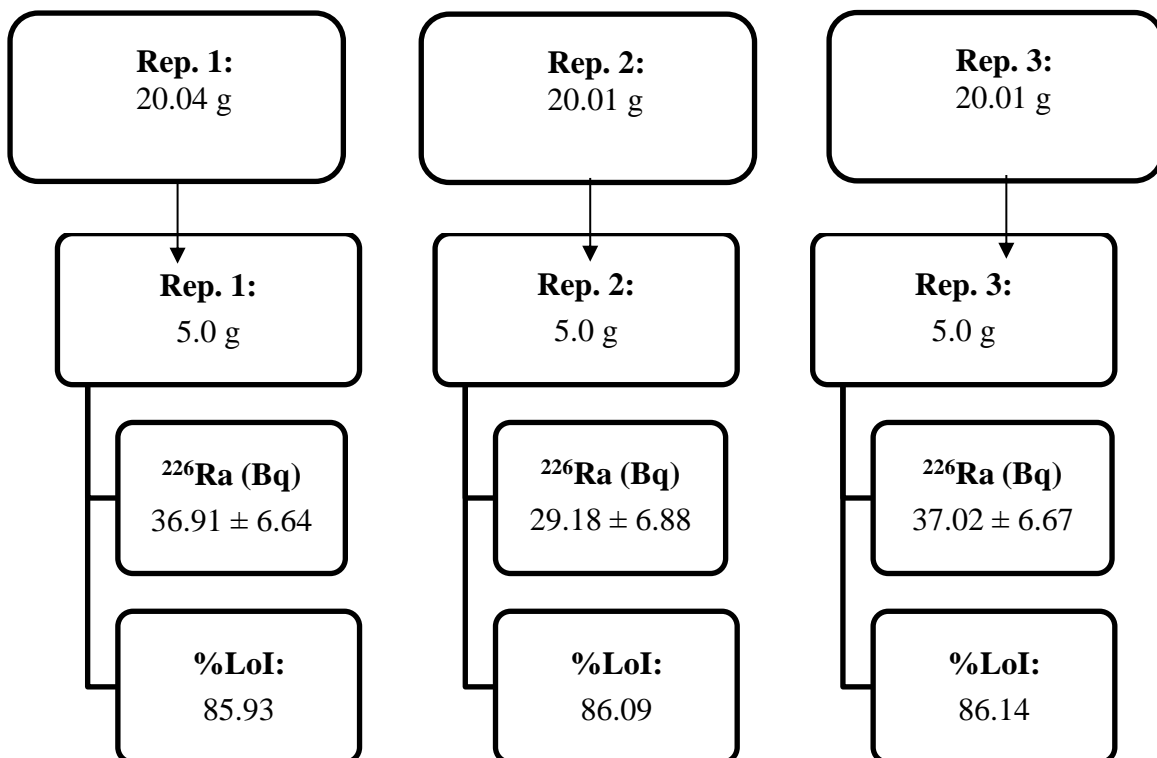


Figure 71. γ spectrometry and LoI analysis to three (3) samples of 5 g

3.3.5.3 Non – sequential extractions

3.3.5.3.1 0.1M NaOH extractions

The results obtained from the 0.1M NaOH extractions, as described in Section 2.14 are shown in Table 22.

Table 22. ^{226}Ra and NOM dissolved by 0.1M NaOH solution extract

Sample	Initial mass (g)	Residue mass (g)	Initial ^{226}Ra (Bq kg^{-1})	^{226}Ra (Bq kg^{-1})		HA/FA extract (mg L^{-1})
				Filtrate	Residue	
Rep. 1	1.00	0.91	34.62 ± 7.27	<0.372	33.37 ± 7.05	63.99 ± 3.25
Rep. 2	1.03	0.89	35.69 ± 7.36	<0.313	38.24 ± 7.96	54.89 ± 5.56
Rep. 3	1.02	0.85	36.89 ± 7.66	<0.296	35.76 ± 7.56	39.27 ± 2.93

The results in Table 22 showed that an average 0.133 g of the NE_{4T} samples were dissolved by the NaOH solution. The 13.1% of the mass loss is the dissolution of HA and FA which is soluble at pHs > 2. The remaining 87% of the insoluble NE_{4T} sample corresponds to humin, which is insoluble at all pHs and clays and minerals not soluble in NaOH.

Comparing the initial activity concentration of ^{226}Ra with the activity concentrations of ^{226}Ra for the filtrate and for the residue showed that ^{226}Ra is not removed from the solid by NaOH solution. This may suggest that there is no direct association between ^{226}Ra – HA and FA. However, it is possible that the Ra was released from HA and FA and then precipitated as $\text{Ra}(\text{OH})_2$.

To determine the concentrations of HA and FA in the NaOH solution, 4 to 6 drops (approximately 0.17 – 0.20 mL) of concentrated HCl were added to reduce the pH of the filtrate < 2 in order to precipitate HA and thereby separate the HA (insoluble for pH < 2) from FA (soluble at all pHs) (Table 23).

Table 23. HA and FA extractions at the 0.1M NaOH solution extract

NE4 _T	FA extract (w.v) 250 nm	FA extract (w.v) 350 nm	FA extract (w.v) 450 nm	HA mass (g)	FA mass (g)
0.1M NaOH Rep. 1	72.88	52.72	22.54	0.02	0.06
0.1M NaOH Rep. 2	83.45	57.74	29.24	0.03	0.11
0.1M NaOH Rep. 3	91.08	63.28	28.99	0.03	0.15

The results from Table 23 showed that in approximately 1 g of the NE4_T sample the content of humin, which is insoluble at all pHs, clays and minerals not soluble in NaOH is on average 88.23 ± 3.43 %, the FA content is on average 10.79 ± 4.38 % and HA content is in average 2.64 ± 0.23 %.

3.3.5.3.2 0.1M HNO₃ extractions

The results obtained from the 0.1M HNO₃ extractions, as described in Section 2.14 are shown in Table 24.

Table 24. ²²⁶Ra and carbonate at 0.1M HNO₃ solution extract

NE4 _T	Initial mass (g)	Residue mass (g)	Initial ²²⁶ Ra (Bq kg ⁻¹)	²²⁶ Ra (Bq kg ⁻¹)		HA/FA extract (mg L ⁻¹)
				Filtrate	Residue	
Rep. 1	1.00	0.8942	37.10 ± 8.02	<0.409	27.25 ± 5.97	3.36 ± 2.15
Rep. 2	1.01	0.9015	37.07 ± 7.73	<0.362	28.85 ± 6.05	2.92 ± 2.24
Rep. 3	1.01	0.9356	39.91 ± 8.34	<0.359	29.55 ± 6.02	2.91 ± 2.33

The results in Table 24 showed that an average 0.096 g of the NE4_T samples were dissolved by the HNO₃ solution. The 10 % of the mass loss is the dissolution of HA and FA which is soluble at pHs > 2. The remaining 90 % of the insoluble NE4_T sample corresponds to the humin, which is insoluble at all pHs and clays and minerals not soluble in HNO₃. Comparing the initial activity concentration of ²²⁶Ra with the activity concentrations of ²²⁶Ra for the filtrate and for the residue showed that ²²⁶Ra is not removed from the solid by HNO₃ solution. This may suggest that there is no direct association between ²²⁶Ra – HA and FA. The filtrates were recounted for longer periods of time of approximately 12 hours to measure more accurately the ²²⁶Ra content and the results are shown in Table 25.

Table 25. Recounted ²²⁶Ra for 0.1M HNO₃ filtrates

NE4 _T	Initial ²²⁶ Ra (Bq kg ⁻¹)	Recounted ²²⁶ Ra (Bq kg ⁻¹)	
		Filtrate	Residue
Rep. 1	37.10 ± 8.02	0.49 ± 0.11	27.25 ± 5.97
Rep. 2	37.07 ± 7.73	0.57 ± 0.11	28.85 ± 6.05
Rep. 3	39.91 ± 8.34	0.51 ± 0.10	29.55 ± 6.02

The recounted filtrates verified that there is no significant evidence of ²²⁶Ra in the filtrates. To determine the concentrations of HA and FA in the HNO₃ solution, 2 drops (approximately 0.10 mL) of concentrated HCl were added to reduce the pH of the filtrate < 2 and to precipitate HA and thereby separate the HA (insoluble for pH < 2) from FA (soluble at all pHs) (Table 25).

Table 26. HA and FA extractions at 0.1M HNO₃ solution extract

NE4 _T	FA extract (w.v) 250 nm	FA extract (w.v) 350 nm	FA extract (w.v) 450 nm	HA mass (g)	FA mass (g)
Rep. 1	18.91	9.18	3.15	0.0023	0.11
Rep. 2	23.13	10.71	3.68	0.0056	0.10
Rep. 3	22.48	10.17	2.60	0.0049	0.07

The results from Table 26 showed that in approximately 1 g of the NE4_T sample the content of humin, which is insoluble at all pHs, clays and minerals not soluble in HNO₃ is on average 91.04 ± 2.21 %, the FA content is on average 9.37 ± 1.69 % and HA content is in average 0.42 ± 0.02 %.

3.3.5.3.3 dH₂O extractions

The results in Table 27 showed that for the NE4_T samples the dH₂O solution extracted an average of 0.04 ± 0.01 g of HA and FA in solution. The 4 % of the mass loss corresponds to HA and FA, whereas, the remaining 96 % of the insoluble NE4_T sample corresponds to humin and mineral phases (i.e. clays). Furthermore, comparing the initial activity concentration of ²²⁶Ra with the activity concentrations of ²²⁶Ra for the filtrate and the residue there is no significant evidence of ²²⁶Ra in the filtrate, suggesting that there is no direct association between ²²⁶Ra – HA and FA in the solution extract.

Table 27. ²²⁶Ra and NOM at dH₂O solution extract

NE4 _T	Initial mass (g)	Residue mass (g)	Initial ²²⁶ Ra (Bq kg ⁻¹)	²²⁶ Ra (Bq kg ⁻¹)		HA/FA extract (mg L ⁻¹)
				Filtrate	Residue	
Rep. 1	1.00	0.95	34.62 ± 7.27	<0.267	36.41 ± 7.49	3.89 ± 2.19
Rep. 2	1.03	0.99	35.69 ± 7.36	<0.275	33.98 ± 7.07	3.73 ± 2.06
Rep. 3	1.02	0.97	36.89 ± 7.66	<0.273	37.22 ± 7.58	3.26 ± 1.79

To determine the concentrations of HA and FA in the dH₂O solution, 3 drops (approximately 0.10 mL) of concentrated HCl were added to reduce the pH of the filtrate < 2 and to precipitate HA and thereby separate the HA (insoluble for pH < 2) from FA (soluble at all pHs) (Table 41).

The results in Table 28 showed that in approximately 1 g of the NE4_T sample the content of humin, clays and minerals not soluble in demineralised water is on average 97.44 ± 2.32 %, the FA content is on average 4.04 ± 0.07 % and HA content is in average 0.42 ± 0.02 %.

Table 28. HA and FA extractions at dH₂O solution extract

NE4 _T	FA extract (w.v) 250 nm	FA extract (w.v) 350 nm	FA extract (w.v) 450 nm	HA mass (g)	FA mass (g)
Rep. 1	13.59	7.89	4.30	0.0025	0.05
Rep. 2	13.12	7.58	1.58	0.0012	0.03
Rep. 3	16.52	9.44	1.98	0.0018	0.04

The results show that, during the non – sequential extractions of the NE4_T sample, no significant association between ²²⁶Ra - HA and/or FA was observed.

In addition to the non – sequential extractions, mineralogy analysis was performed by PXRD to identify the mineral phases after each stage of extraction. The results obtained by the PXRD analysis are shown in Figure 73.

The sampling site closest to the uraninite vein is NE4. This region lies in the most organic rich area of the site with much surface vegetation. As this vein is the source of the radium which transport, we are trying to track, a depth profile was taken below this site to investigate the presence of any other mineral phases. The literature (Basham¹ et al., Hooker⁸ et al., Jamet⁹⁹ et al., and Braithwaite and Knight¹⁶⁰) reports that many mineral phases have been observed at this point associated with the vein – as well as uraninite, various calcium based phases have been observed including gypsum (CaSO₄.2H₂O) and calcite (CaCO₃), dolomite ((Ca,Mg)CO₃), baryte (BaSO₄) has also been found together with large quantities of quartz. Iron minerals such as haematite, goethite and ferrihydrite are also seen together with chalcopyrite (CuFeS₂) and pyrite (FeS₂). Some arsenic phases of iron (FeAs) and nickel (NiAs) have also been taken from this vein. Vitreous black hydrocarbons are seen in the rock, but do not have a defined diffraction pattern. Powder diffraction data of the core drills are dominated by an amorphous background and strong reflections from quartz, in order to glean more information on these

samples from XRD. XRD was performed after various analysis including Loss on Ignition, non-sequential extraction and sequential extraction.

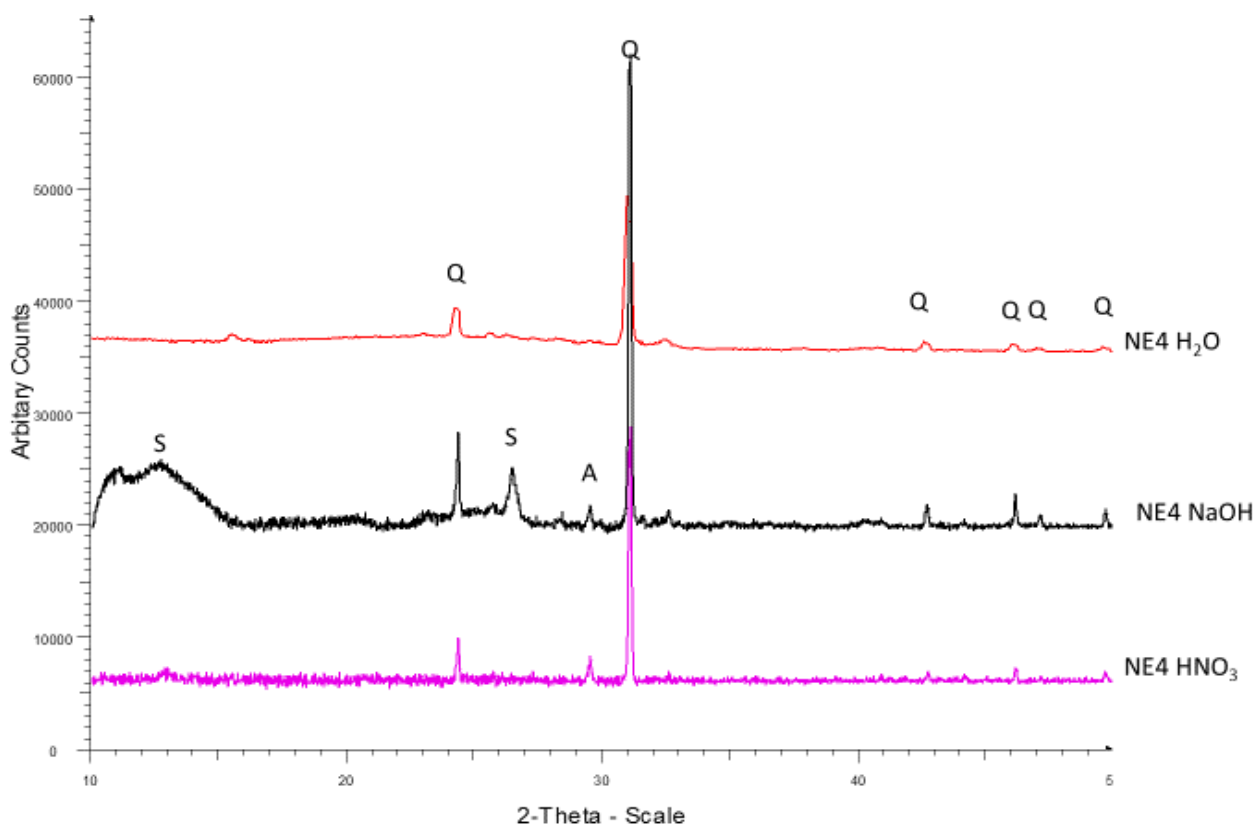


Figure 72. PXRd data of NE4 samples following treatment with dH₂O, 0.1M NaOH, and 0.1M HNO₃, Phase ID: S = sjogrenite MgFe₂(OH)₁₆CO₃(H₂O)₄ (74-1513), A = anhydrite CaSO₄ (37-1496) and Q = quartz (46-1045)

Anhydrite is visible in both the sodium hydroxide and nitric acid extracted phases. Anhydrite is the dehydrated form of gypsum, which has been observed at Needle's Eye on many geological surveys. It is likely that during the drying of these samples, the poorly crystalline hydrated gypsum was dried out through the sample treatment process and hence has become visible in the powder diffraction pattern as anhydrite.

Sulfate phases of calcium and barium are both known to be able to sequester radium by isovalent substitution of the divalent Ca/Ba cations for Ra. The size mismatch between radium and calcium means that much smaller amount of radium can be taken up by the calcium phase compared to barium, but it has been reported by Doerner and Hoskins⁴⁰ and Langmuir and Melchior⁴². The magnesium iron carbonate phase has not previously been reported at Needle's Eye. However, magnesium and iron have both been identified by XRF and ICP, so it could

easily be present. The fact that the reflections from this phase disappear when treated with acid, further suggests that this phase is definitely present as acid would break down this carbonate phase as per the typical carbonate/acid reaction.

3.3.5.4 Sequential extraction analysis on NE4_T and NE4-b1

Sequential extraction experiments, as described in Section 2.13, were used to estimate the association of ²²⁶Ra with different fractions for the samples NE4_T and NE4-b1. The comparison of NE4_T, NE4-b1 and NE4-b2 samples, originating from the same locality (Figure 74), was used to provide information about the behaviour of ²²⁶Ra in different depths, as well as, the effect of different mineralogy (found in different depths) on ²²⁶Ra mobility.

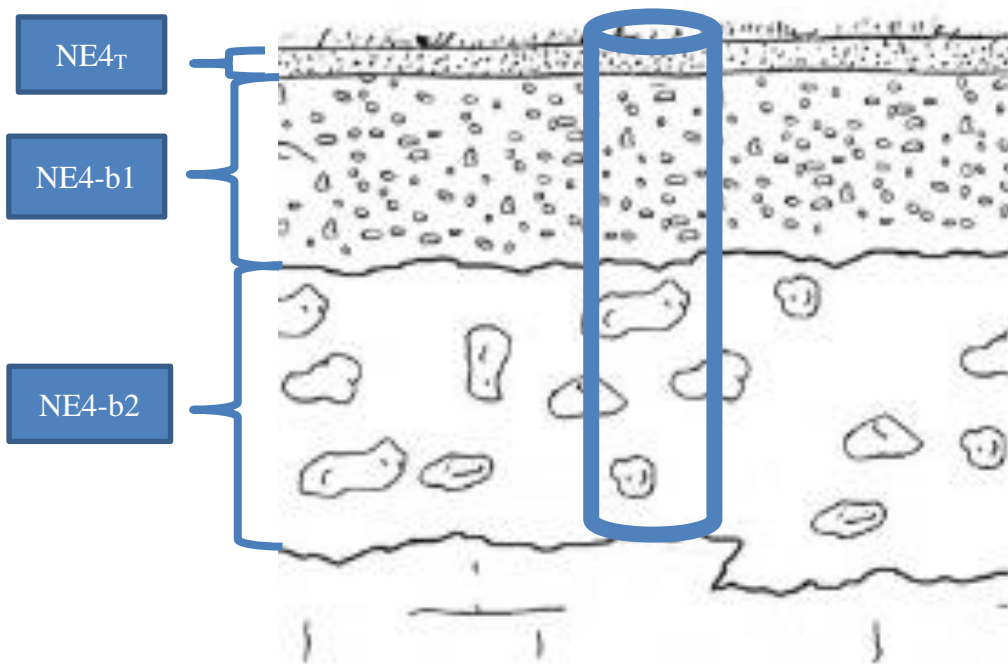


Figure 73. NE4_T, NE4-b1, NE4-b2 samples spatial formation

Prior to the main sequential analysis, the suitability of the sintered crucibles for containing a soil sample when measured by γ spectrometry was evaluated using two NE4_T samples of pre-measured activities of ²²⁶Ra.

Figure 75 shows that, when taking into account the 2σ errors, the two NE4T replicate samples demonstrated similar activity concentrations of ^{226}Ra before and after the use of sintered crucible and therefore, sintered crucibles can be successfully used when measuring soil samples by gamma spectroscopy.

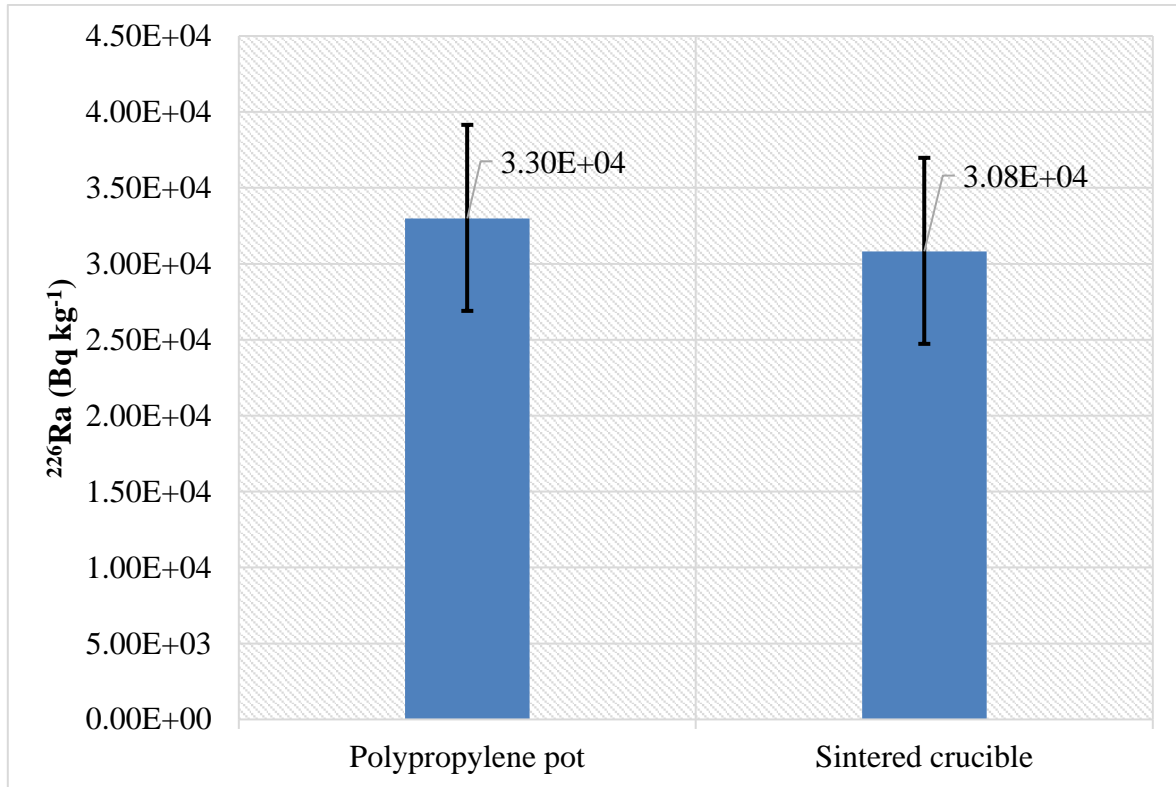


Figure 74. Calibration of γ spectrometer using polypropylene pots and sintered crucibles (average of three)

F1 – Exchangeable Fraction

Because the measurement of activity concentration of the residues during these experiments may give values that are lower than the minimum detectable amounts, it was decided to express the results of the measurements in Bq (referred as ^{226}Ra activity concentration in the sequential extractions section). The results of ^{226}Ra activity concentration (approximate mass = 1.0 g) obtained before the first sequential extraction stage (described in *Section 2.13.2*) are shown in Figure 76.

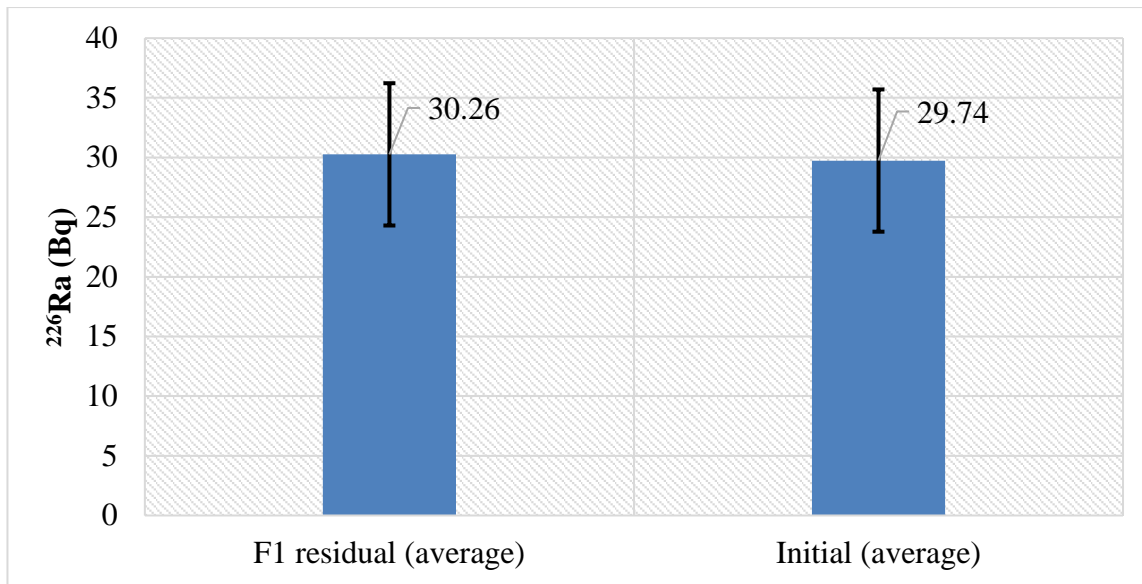


Figure 75. Comparison of F1 residual ^{226}Ra activity to the initial (average of three)

Taking into account the percentage error on the measurement, the first stage of sequential extraction (F1 – Exchangeable bound), showed that no ^{226}Ra loss was detected for the residue.

F2 – Bound to Carbonates Fraction

The results of ^{226}Ra activity obtained after the second sequential extraction stage (described in Section 2.13.2) are shown in Figure 76.

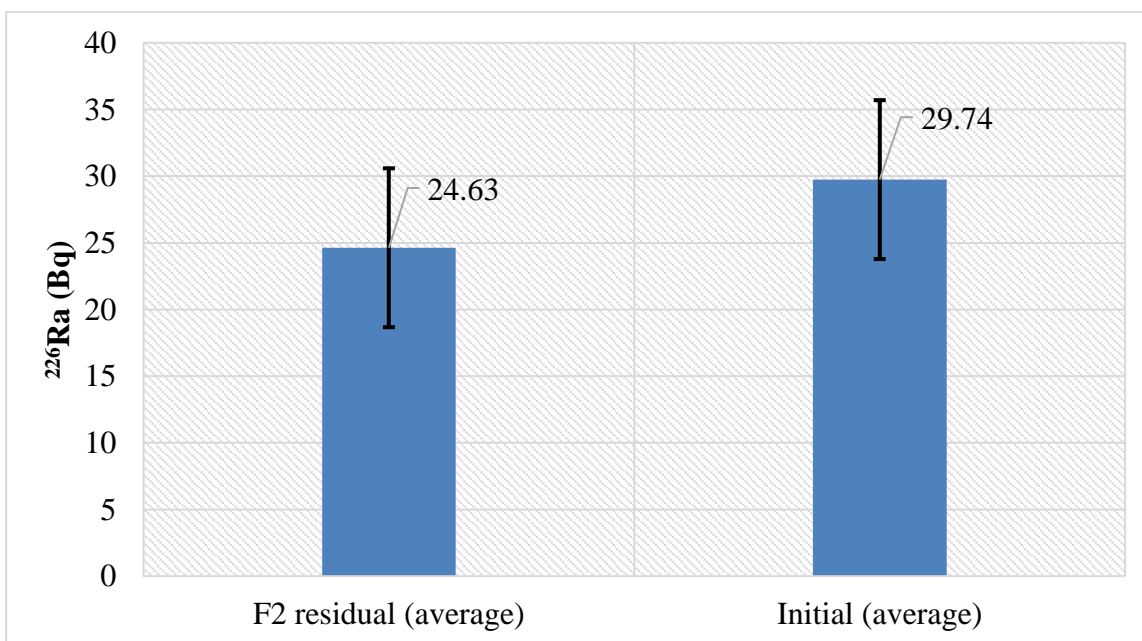


Figure 76. Comparison of F2 residual ^{226}Ra activity to the initial (average of three)

In conclusion, and taking into the percentage error, the second stage of sequential extraction (F2 – Bound to Carbonates), showed that approximately 18.9 % of the initial ^{226}Ra activity was lost from the solid. Compared to the results from the previous stage, in this stage higher levels of ^{226}Ra were reported in the F2 leachates which implies that NaOAc treatment affects ^{226}Ra activity distribution.

Calcite (CaCO_3) and dolomite ($\text{CaMg}(\text{CO}_3)_2$) are two carbonate phases which have been found in previous geological studies at Needle's Eye (Basham¹ et al., Hooker⁸ et al., Jamet⁹⁹ et al., and Braithwaite and Knight¹⁶⁰) close to the uraninite vein. Both of these carbonates have been reported in the literature as being able to take up radium^{49,52,53}. Radium is also known to precipitate from solution at relatively low carbonate concentrations (i.e. partition coefficient λ' from 1.21 to 1.8)⁴⁵. As radium is at the bottom of the group II metals and carbonate solubility falls as the group is descended, RaCO_3 will have extremely low solubility under environmental conditions of near neutral pH. In this case, it is likely that the radium is incorporated into the bulk calcite or dolomite phase rather than being precipitated separately due to the extremely low concentrations observed. All carbonates including calcite and dolomite would be expected to decompose at the acidity provided by the second stage of sequential extraction and release the cations into solution; carbonate decomposes to release carbon dioxide. The loss of radium activity from the solid and increase in the amount of radium seen in solution is therefore likely to be due to radium accumulation in these phases and their decomposition at this pH. Further evidence for the presence of carbonate through PXRD analysis on the products of the sequential extraction is given in Section 3.3.5.5.2.

F3 - Bound to Iron and Manganese Oxides Fraction

The results of ^{226}Ra activity concentration obtained after the third sequential extraction stage (described in *Section 2.13.2*) are shown in Figure 77.

In conclusion, and taking into account the percentage error, the third stage of sequential extraction (F3 – Bound to Fe / Mn Oxides), showed that approximately a further 19.1 % of the initial ^{226}Ra activity concentration was lost from the solid. This means in total 38 % of the initial ^{226}Ra activity has been lost in stages 2 and 3. Overall only 62 % of the initial ^{226}Ra activity concentration now remains in the residue. Compared to the results from the previous stages, in this stage significantly higher levels of ^{226}Ra were reported in the F3 leachates.

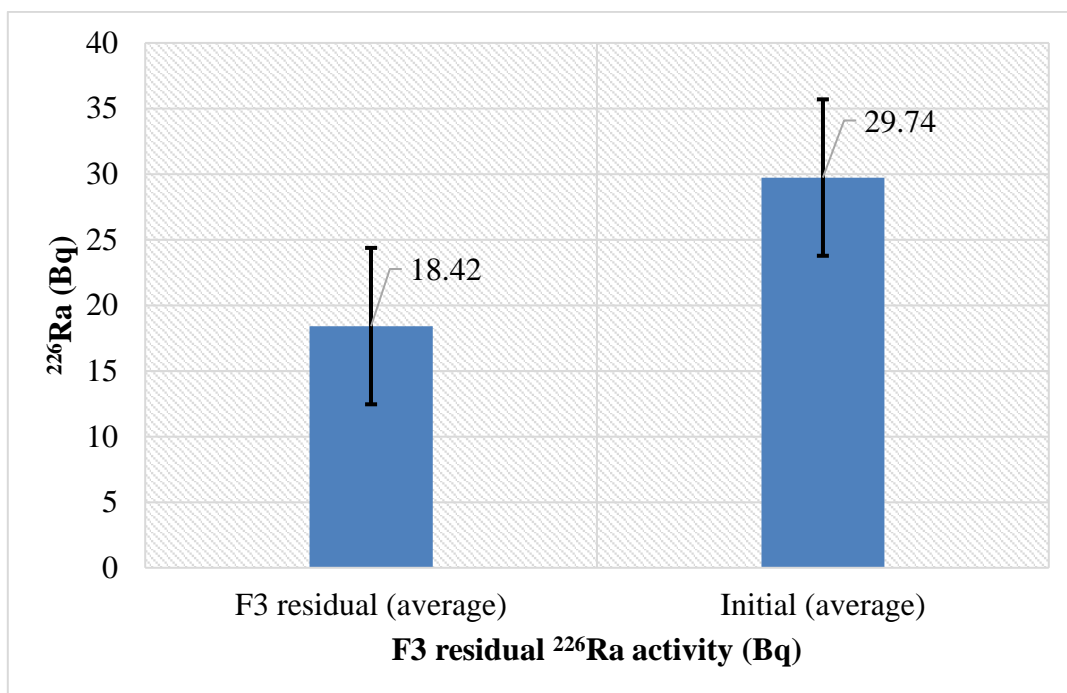


Figure 77. Comparison of F3 residual ^{226}Ra activity to the initial

Ferrihydrite ($(\text{Fe}^{3+})_2\text{O}_3 \cdot 0.5\text{H}_2\text{O}$), a poorly crystalline iron oxide similar to hematite (Fe_2O_3), and goethite ($\text{FeO}(\text{OH})$) are two iron oxide phases which are present in the geology of Needle's Eye site (Basham¹ et al., Hooker⁸ et al., Jamet⁹⁹ et al., and Braithwaite and Knight¹⁶⁰). Both of these oxides, as well as hematite (Fe_2O_3) which is common at Needle's Eye site have been reported in the literature to take up radium^{55,56}. Furthermore, an amount of radium that was mobilised in solution at the F3 stage may be associated with sulfide mineral phases, such as FeS_2 and FeAs that exist at Needle's Eye which fits well with the geological background of the site^{1,8,99,167}.

F4 - Bound to Organic Matter Fraction

The results of ^{226}Ra activity obtained after the fourth sequential extraction stage (described in *Section 2.13.2*) are shown in Figure 78.

Figure 78 shows the results obtained after the F4 sequential extraction stage. It should be noted that the solid fraction is now only one quarter of its original mass. The loss in volume of the sample may have a deleterious effect on the spectroscopic measurements due to the change in geometry resulting from a much smaller sample.

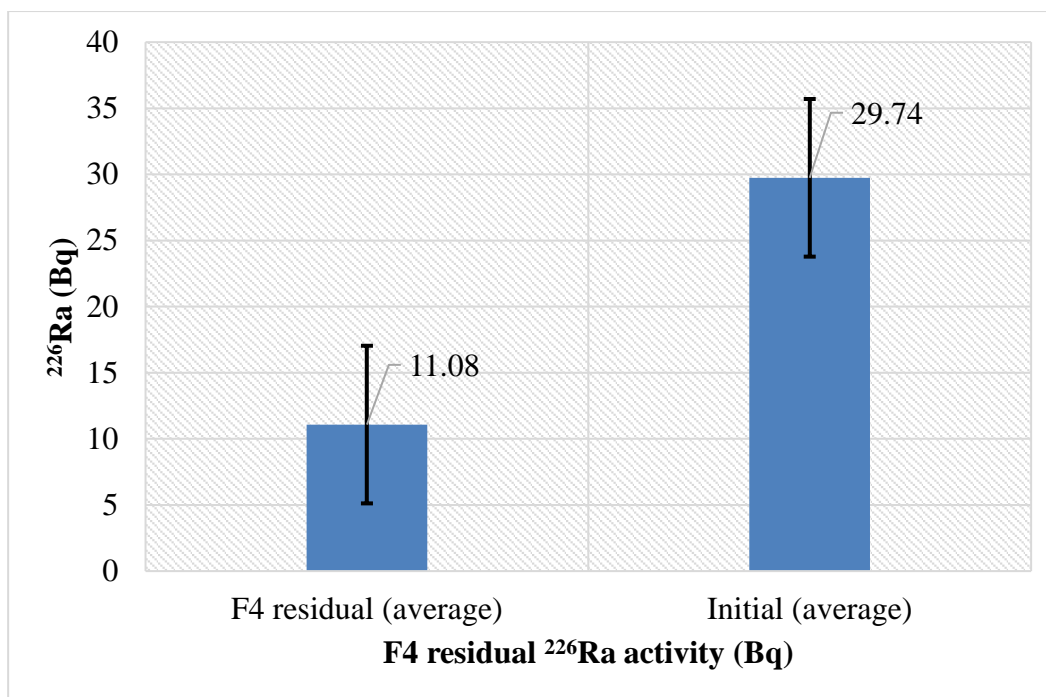


Figure 78. Comparison of F4 residual ^{226}Ra activity to the initial

In conclusion, and with respect to the percentage error, the fourth stage of sequential extraction (F4 – Bound to Organics), showed that approximately a further 26.5 % $[(7.88/29.74) \times 100]$ of the initial ^{226}Ra activity was lost from the residue. This means in total 64.5 % of the initial ^{226}Ra has been lost in stages 2, 3 and 4. Overall only 35.5 % of the initial ^{226}Ra activity concentration now remains in the residue after stage 4. Compared to the results from the previous stages, in this stage significantly higher levels of ^{226}Ra were reported in the F4 leachates. Good agreement is shown between the loss of radium from the residue and that observed in solution for this stage.

Nathwani and Phillips³⁷ reported radium sorption from organic matter at varying concentrations. Moreover, sequential chemical extractions, applied to the organic rich (~ 29 %LoI treatment at 1000 °C) sediments of River Fal in South Terras, Cornwall (England) by Siddeeg^{165,166} et al, to investigate the mobility of radium near an abandoned uranium mine. Approximately 60 %, of the initial ^{226}Ra , was found to be associated with the organic fraction. Further comparison of the sequential extraction results of the present work and the South Terras site is discussed later in this section.

F5 – Residual

In conclusion, and with respect to the percentage error, the fifth stage of sequential extraction resulted in the remainder of the solid being dissolved, approximately 35.5 % of the initial ^{226}Ra activity concentration. No solid residue remained, and all of the ^{226}Ra was extracted into solution. Compared to the results from the previous stages, in this stage significantly higher levels of ^{226}Ra were reported in the F5 leachates. The phases which are resistant to the previous four stages are materials such as the silicates – quartz, feldspars and also sulfates such as gypsum and baryte. Both gypsum ($\text{CaSO}_4 \cdot 2\text{H}_2\text{O}$) and baryte (BaSO_4) are known to occur naturally at Needles Eye. As previously discussed, sulfate solid solutions with barium and radium are well known and have been deliberately used to remove radium from solution. The $(\text{Ba,Ra})\text{SO}_4$ is also known to coprecipitate in pipelines and be extremely resistant to normal treatments to remove standard scales^{2,4759}. PXRD analyses of the residual fraction clearly shows the presence of anhydrite (dehydrated form of gypsum), CaSO_4 by reflections at 29.5 2-theta (Section 3.3.5.5.2). It is very likely that the radium is associated with the sulfate phases.

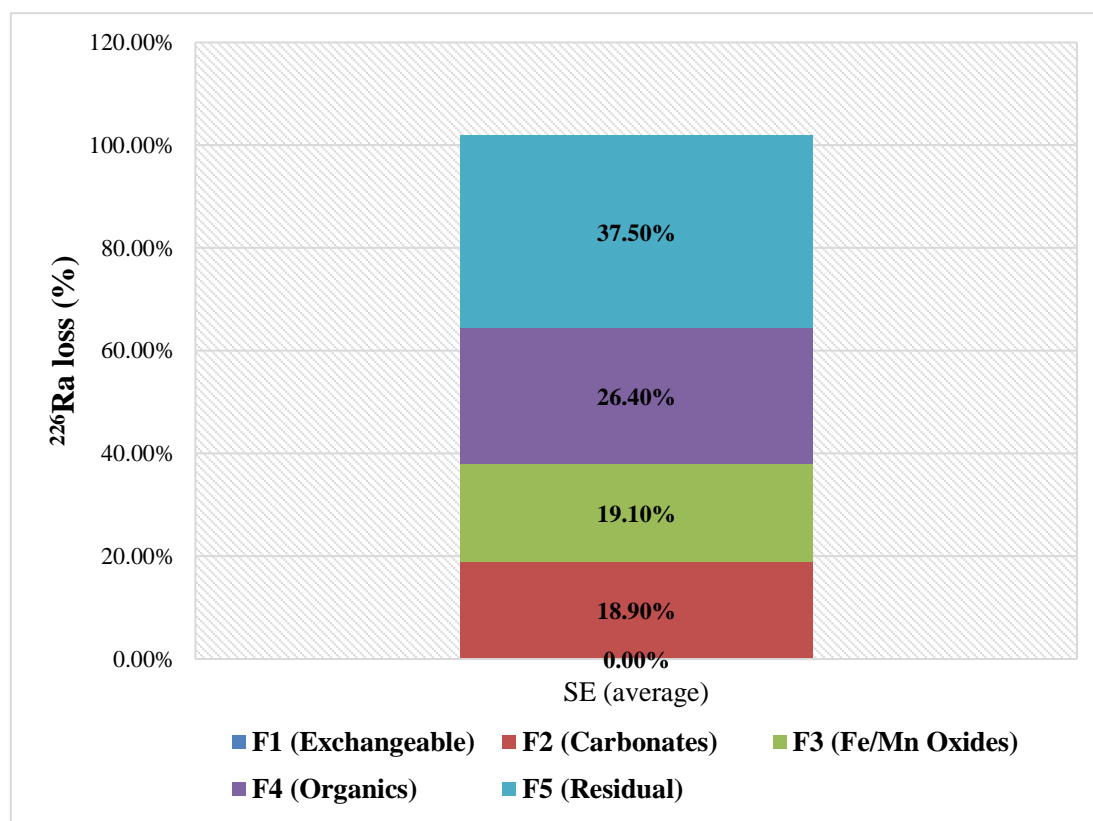


Figure 79. Effect of sequential extractions (SE) on the initial ^{226}Ra activity of NE4_T residues

To summarise, Figure 79 shows the effect of sequential extractions on the initial ^{226}Ra activities as it was reported in the extracted filtrates and the remaining residues. Figure 78 suggests that ^{226}Ra is present in four sequential extraction stages (F2-F5). The majority of ^{226}Ra activity, more than 80 % with respect to the errors, is associated with carbonates, iron and manganese oxides, organics (as humin) and insoluble fraction (likely to be silicates and sulfates).

Sequential extractions on NE4_T were repeated using 6 replicates due to the variability between the results of the radium measured in solution and lost from the solid. It should be noted that one replicate was “sacrificed” after every sequential extraction stage. The “sacrificed” sample was used entirely for XRF analysis. To avoid any confusion between the first and the second set of sequential extraction results, the first of sequential extractions batch will be referred to as “SE” and the second batch referred to as “SQE”. The results of the initial ^{226}Ra activity obtained before the first sequential extraction stage (described in *Section 2.13.2*) are shown in Figure 80.

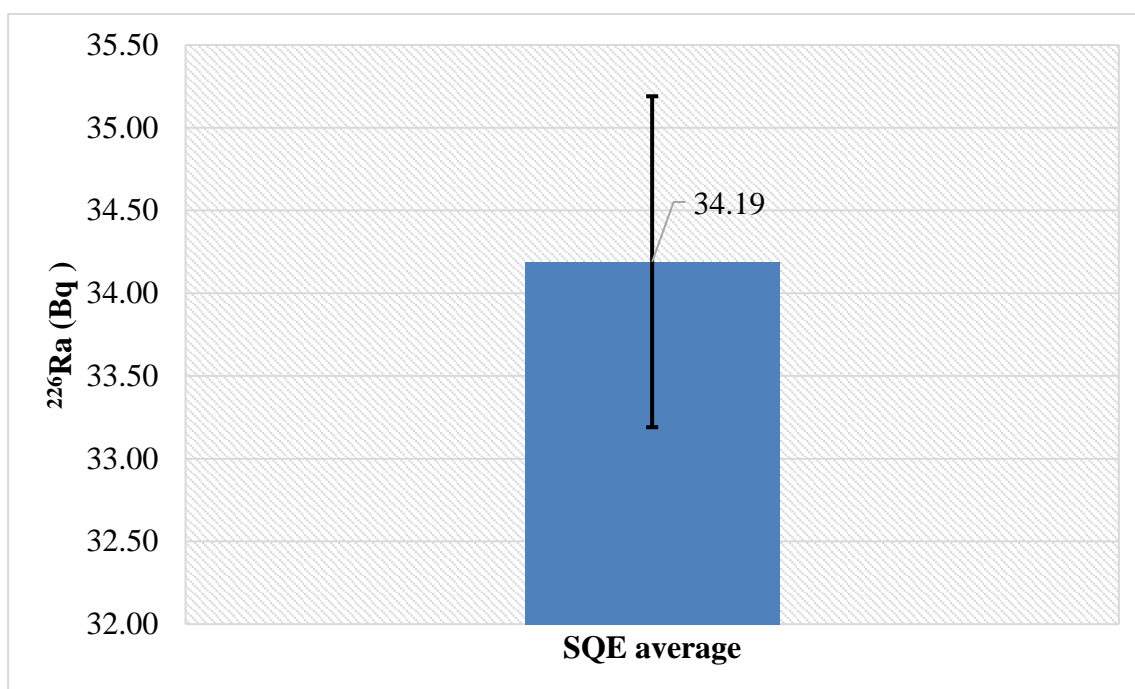


Figure 80. Initial ^{226}Ra activity before sequential extraction treatment

F1 – Exchangeable Fraction (SQE)

The results of ^{226}Ra activity obtained after the first sequential extraction stage (described in *Section 2.13.2*) are shown in Figure 81.

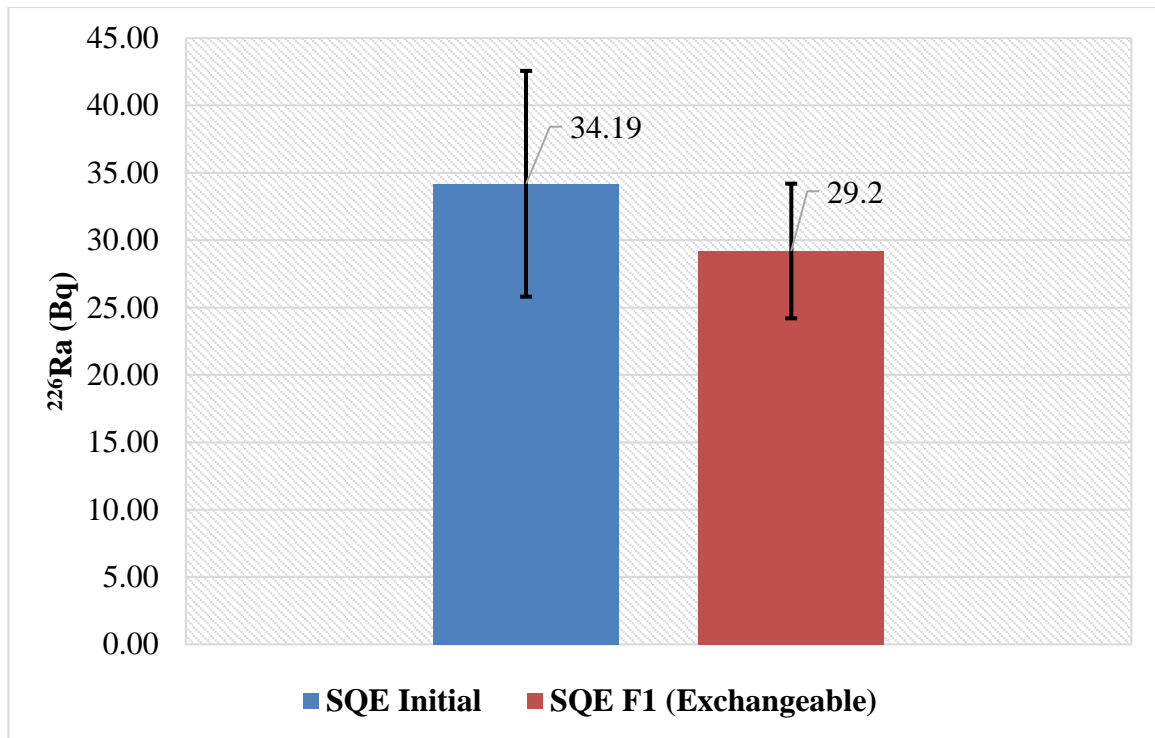


Figure 81. F1 - Exchangeable Fraction results

In conclusion, and taking into account the percentage error, the first stage of sequential extraction (F1 – Exchangeable bound), showed that approximately 14.6 % $[(4.99/34.19) \times 100]$ of the initial ²²⁶Ra activity was lost from the solid. The very low levels of ²²⁶Ra found in leachates imply that MgCl₂ treatment does not affect radium.

F2 – Bound to Carbonates Fraction

The results of ²²⁶Ra activity measured after the second sequential extraction stage (described in 2.13.2 Methodology) are shown in Figure 82.

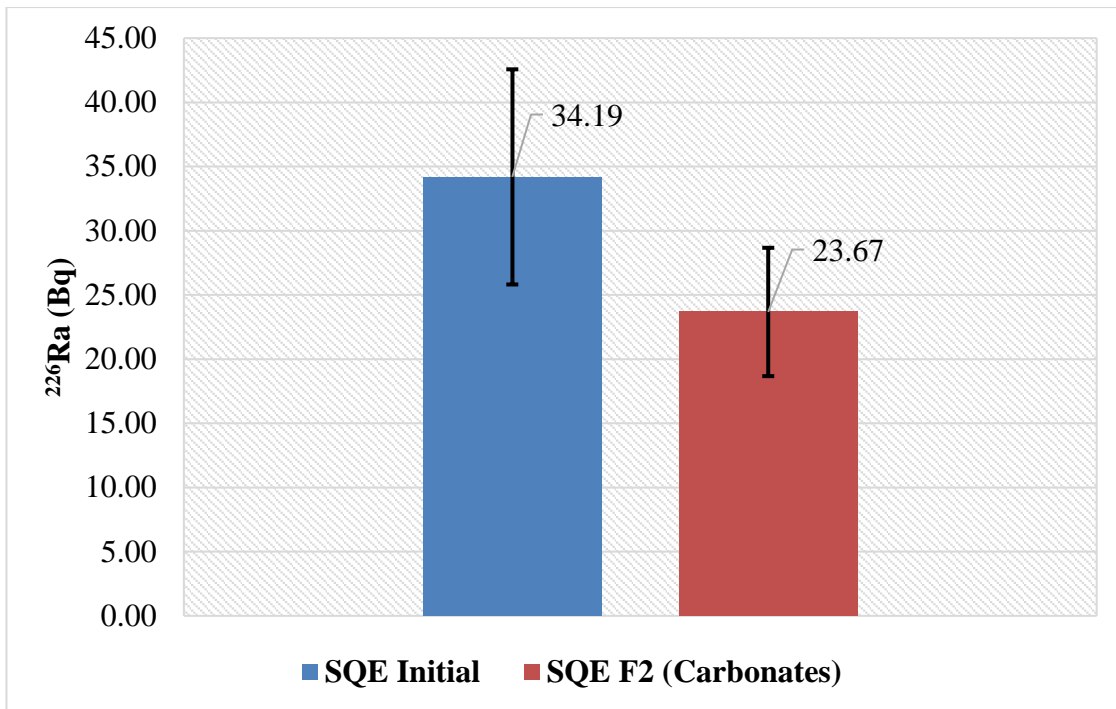


Figure 82. F2 - Bound to Carbonates results

In conclusion, and taking into account the percentage error, the second stage of sequential extraction (F2 – Bound to Carbonates), showed that approximately a further 16.1 % $[(5.41/33.53) \times 100]$ of the initial ^{226}Ra activity was lost from the solid. This means in total 30 % $(100 \times (33.53-23.67)/(33.53))$ of the ^{226}Ra initial activity has been lost in stages 1 and 2. Overall 70 % $(100 - 30)$ of the initial ^{226}Ra activity now remains in the residue. Compared to the results from the previous stage (SE) where about 18.9 % of the initial ^{226}Ra activity accumulatively was lost, whereas in the SQE approximately 30.7 % was lost accumulatively. Although there were differences in the F1 loss between the two sets of sequential extractions, the second stage values of 18.9 % for SE and 16.1 % for SQE respectively are consistent within the limits of experimental error. This proves the relationship between radium sequestration into calcite type phases seen in SE that has also previously been described in literature (Basham¹ et al., Hooker⁸ et al., Jamet⁹⁹ et al., and Braithwaite and Knight¹⁶⁰). This further implies that there is an error in the first set of measurements on the solid phases.

F3 - Bound to Iron and Manganese Oxides Fraction

The results of ^{226}Ra activity obtained after the third sequential extraction stage (described in Section 2.13.2) are shown in Figure 83.

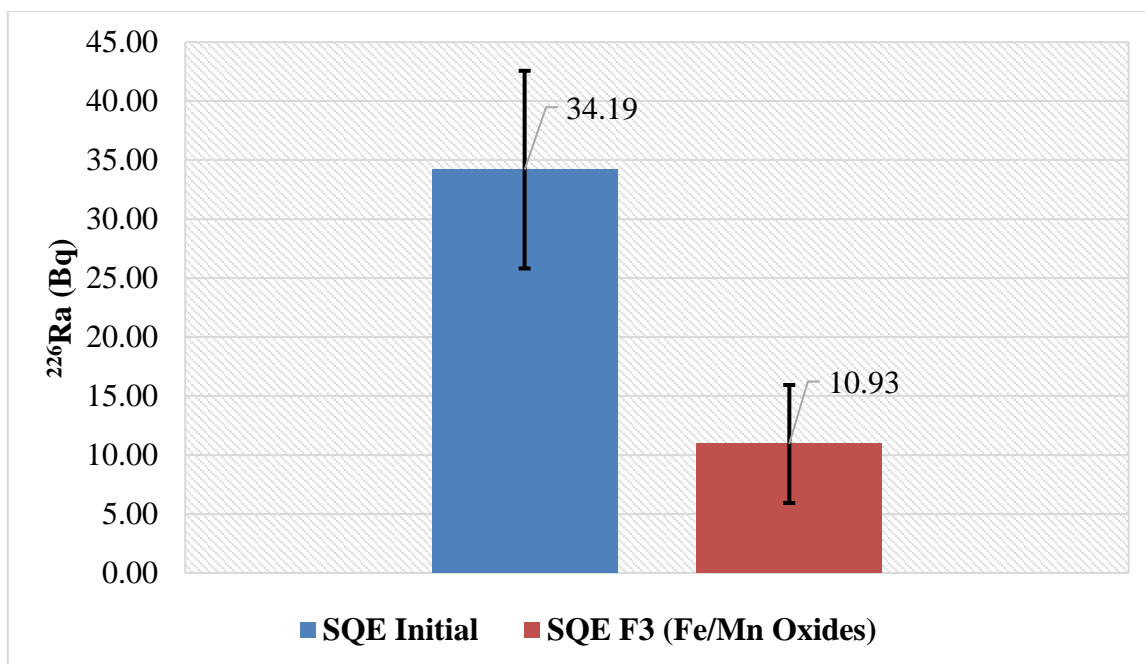


Figure 83. F3 - Bound to Fe / Mn Oxides results

In conclusion, and taking into account the percentage error, the third stage of sequential extraction (F3 – Bound to Fe / Mn Oxides), showed that approximately a further 36.4 % $[(12.46/34.16) \times 100]$ of initial ²²⁶Ra activity was lost from the solid. In total, 32% of the radium now remains in the residue. Compared to the results from the previous stages, in this stage significantly higher levels of ²²⁶Ra were reported in the F3 leachates. This suggests that a significant proportion of the activity is associated with poorly crystalline iron phases which are not easily detected (i.e. absent from the diffraction pattern). LoI however gives evidence for the presence of iron due to the appearance of magnesioferrite phases in the PXRD.

F4 - Bound to Organic Matter Fraction

The results of ²²⁶Ra activity obtained after the fourth sequential extraction stage (described in Section 2.13.2) are shown in Figure 84.

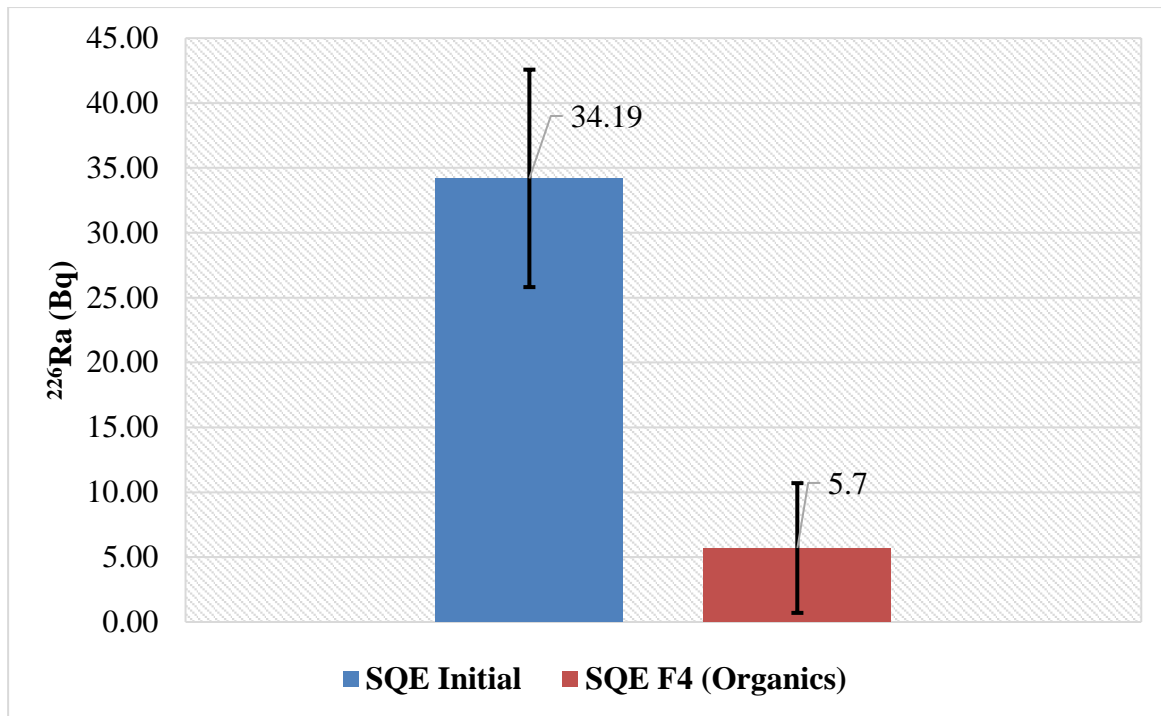


Figure 84. F4 - Bound to Organics results

In conclusion, and taking into account the percentage error, the fourth stage of sequential extraction (F4 – Bound to Organics), a further 13.3% $[(4.54/34.14) \times 100]$ of the initial ²²⁶Ra activity has now been lost from the solid. There is a significant disparity between these results of 19.5% that may be due to a problem with the initial measurements and/or significant loss of solid (ca. one quarter of the original mass remains). Only 18.6 % remains in the residue after F4. There is very poor agreement between the loss of radium from the solid with the amount of radium that is leached into solution in the SQE experiments at stage 4. Compared to the results from SE, the amount of radium retained in the resistant phases is also much lower.

F5 – Residual Fraction

In conclusion, and taking into account the percentage error, the fifth stage of sequential extractions (F5 – Residual Fraction) resulted in the remainder of the solid being dissolved (i.e. accumulated 19.2 % loss from the initial ²²⁶Ra activity). No solid residue remained, and approximately 18.6 % of the initial ²²⁶Ra activity was leached into the solution phase.

Figure 85 shows the effect of sequential extractions on the initial ²²⁶Ra activities as it was measured in the extracted filtrates and residues for both SE and SQE sequential extractions.

Figure 84 shows that ^{226}Ra is present in all five of the sequential extraction solutions. The majority of ^{226}Ra activity, more than 80 %, is associated with carbonates, iron and manganese oxides, organics (as humin) and insoluble fraction (likely to be silicates and sulfates). The major differences between the SQE experiments and the analogous SE group is at stage 1 (where no exchangeable radium should be expected, but it is seen in SQE) and in stage 5 - the residual fraction. It is noteworthy that errors in stage 1 would feed through to stage 5 due to the ‘by difference’ nature of the calculations associated with these experiments. One point to note is that LoI measurements indicate that only 14 % of these samples are mineral phases and most of the sample is organic matter. Of this 14 %, even small variations between condensed silicates (quartz and feldspar) and sulfates would generate a significant difference in the expected radium sequestration as only the sulfate phases (e.g. anhydrite) would be able to take up radium by substitution.

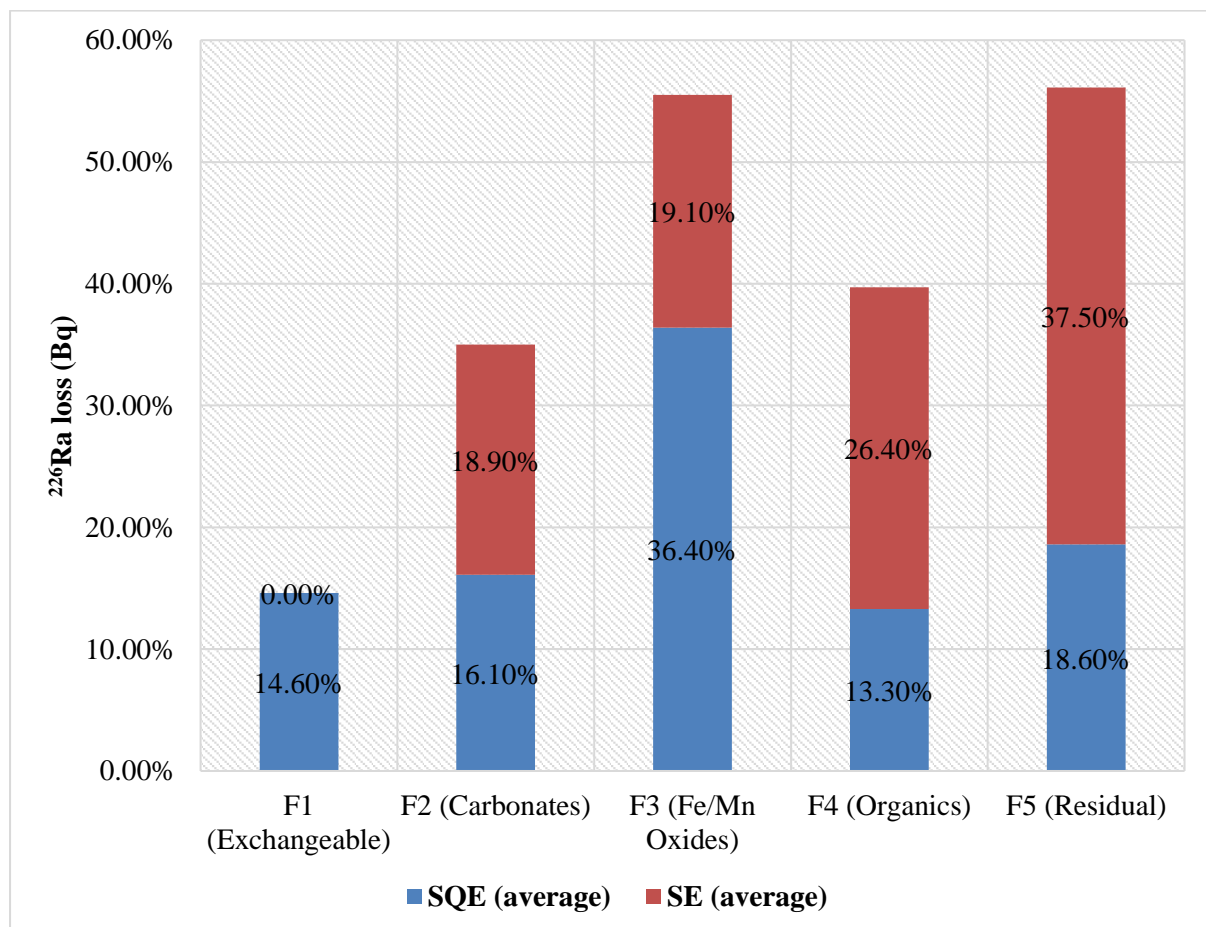


Figure 85. Effect of sequential extractions for SE and SQE on the initial ^{226}Ra activity of NE4_T residues

3.3.5.4.1 Sequential Extractions on deeper soil (NE4-b1)

Sequential experiments, using a deeper soil sample (NE4-b1) taken from the same sampling spot, were carried out to investigate the ^{226}Ra distribution at a different depth to the topsoil (NE4_T). The small sample of NE4-b1 soil only allowed two replicates to be investigated. It should be noted that Replicate 1 was “sacrificed” after every sequential extraction stage. The “sacrificed” sample was used for SEM/EDX, PXRD and XRF analysis.

F1 – Exchangeable Fraction

The results of ^{226}Ra activity measured after the first sequential extraction stage (described in Section 2.13.2) are shown in Figure 86.

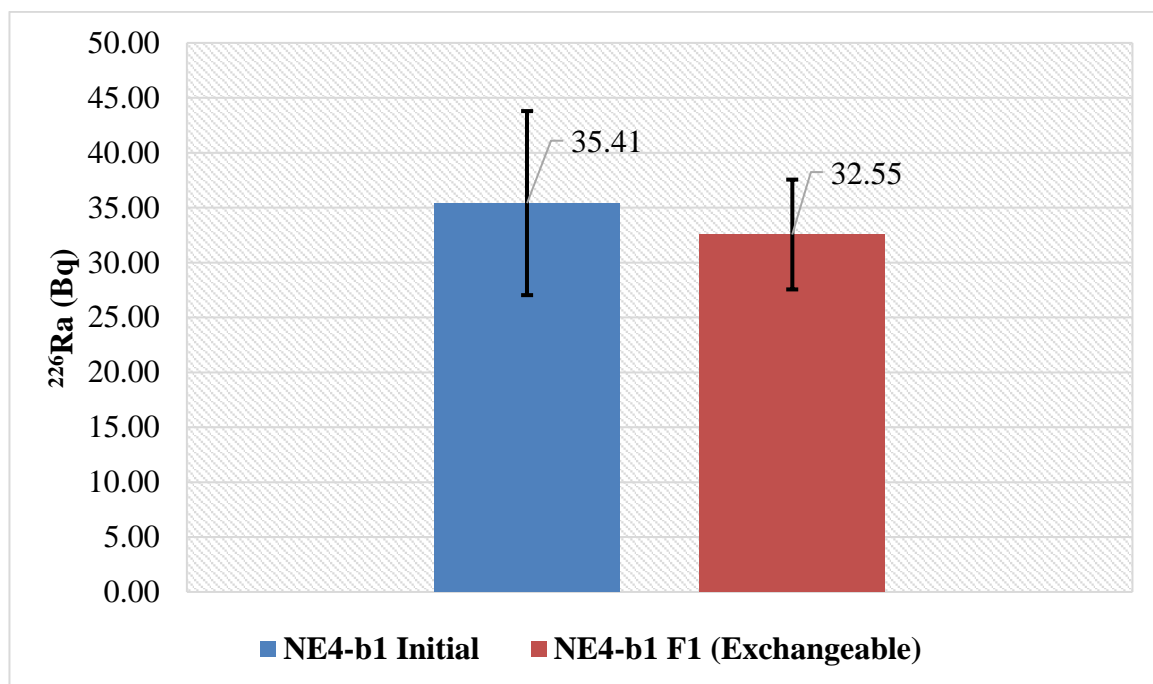


Figure 86. F1 - Exchangeable Fraction results

In conclusion, and taking into account the percentage error, the first stage of sequential extraction (F1 – Exchangeable bound), showed that approximately 8.1 % $[(2.9/35.41) \times 100]$ of the initial ^{226}Ra activity was lost from the soil. The very low levels of ^{226}Ra found in leachates imply that MgCl_2 treatment does not affect the sample very strongly because radium

is a group II species at the bottom of group, and it is not likely to be exchanged for Mg^{2+} which is more mobile².

F2 – Bound to Carbonates Fraction

The results of ^{226}Ra activity measured after the second sequential extraction stage (described in Section 2.13.2) are shown in Figure 87.

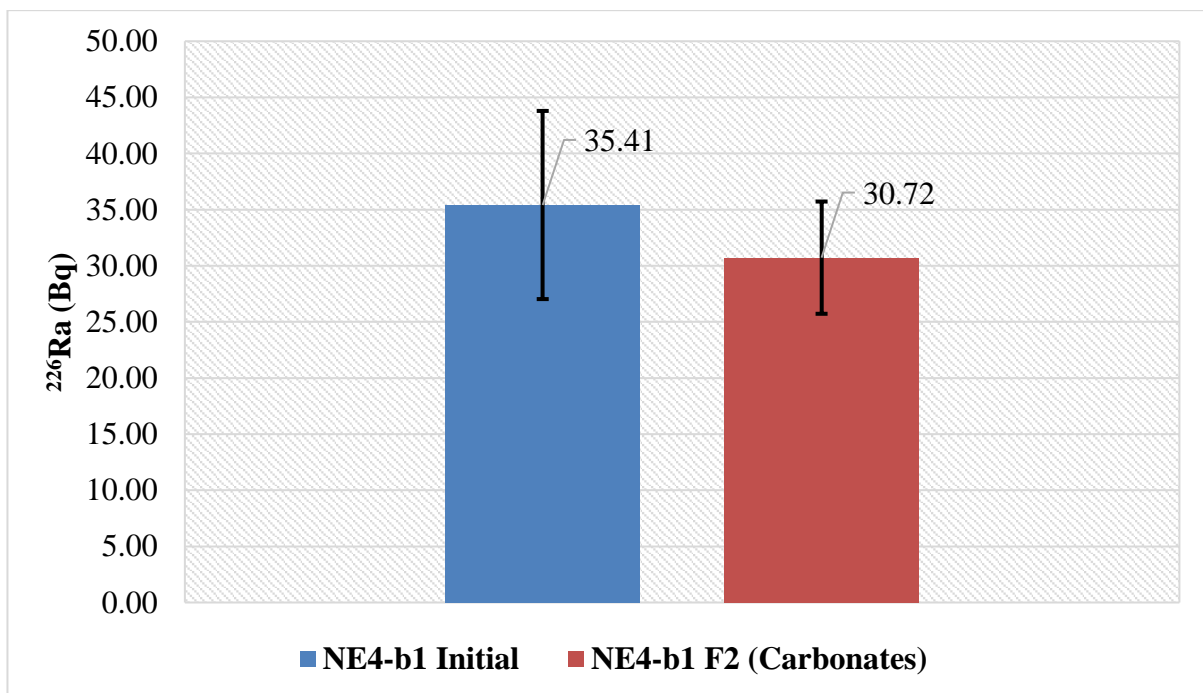


Figure 87. F2 - Bound to Carbonates results

Approximately a further 5.2 % $[(1.83/35.41) \times 100]$ of the initial ^{226}Ra activity was removed from the soil in the second step. In total, 13.3 % (8.1 + 5.2) of the ^{226}Ra has been removed from the initial ^{226}Ra activity of the solid residue leaving 86.7% of the initial ^{226}Ra activity in the residue.

F3 - Bound to Iron and Manganese Oxides Fraction

The results of ^{226}Ra activity measured after the third sequential extraction stage (described in Section 2.13.2) are shown in Figure 88.

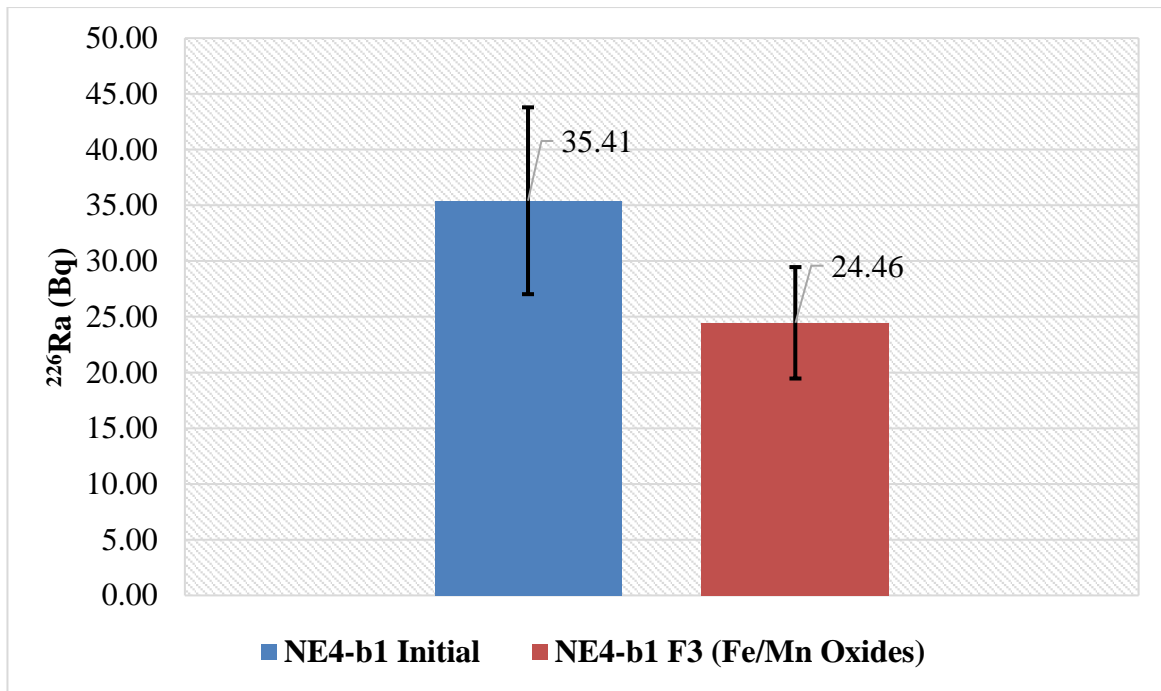


Figure 88. F3 - Bound to Fe / Mn Oxides results

A further 17.7 % $[(6.26/35.41) \times 100]$ of the initial activity from the ^{226}Ra has been lost from the solid. In total, 31 % $(8.1 + 5.2 + 17.7)$ of the initial ^{226}Ra activity has been lost from the solid after 3 sequential extractions. Compared to the results from the previous stages, in this stage significantly higher levels of ^{226}Ra activity were reported in the F3 leachates.

In all three sequential extractions, radium appears to be associated with iron/manganese fractions. While the amount of organic matter might be expected to lessen with depth as leaf litter/plants are concentrated towards the surface, the poorly crystalline iron minerals goethite etc might be expected to remain more constant. The XRF results are consistent between the top and deeper soil where the iron content is ca. 4 wt % (Table 29). After stage 3 of the sequential extractions, the iron content drops significantly to 1 wt % but not to zero. This is because iron can be substituted into the sheet silicates such as chlorite, which is known to be present in these samples. As the silicate phases are very crystalline, they are not broken down by dithionate and this iron is retained in the resistant fraction.

F4 - Bound to Organic Matter Fraction

The results of ^{226}Ra activity measured after the fourth sequential extraction stage (described in Section 2.13.2) are shown in Figure 89.

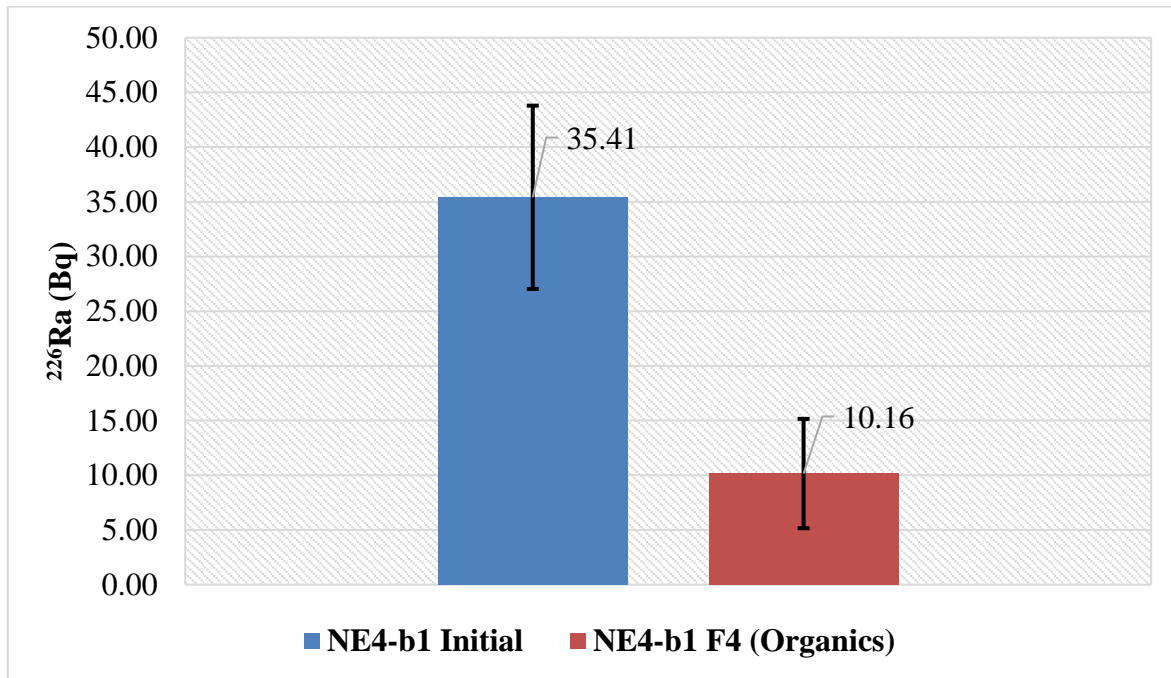


Figure 89. F4 - Bound to Organics results

Approximately 40.4 % $[(14.3/35.41) \times 100]$ of the initial ^{226}Ra activity was lost from the soil, whereas. Compared to the results from the previous stages, in this stage significantly higher levels of ^{226}Ra activity were reported in the F4 leachates.

For NE4-b1, SE and SQE batches the percentage of ^{226}Ra activity that was released into the F4 solution phase are all ca. one third of the total radium content. In contrast, there is a wide variation between the radium measurements on the three batches. This conclusion does not fit with the with organic matter concentration which is greater in topsoil when compared to deeper soil (86.5 % over 34.9 % through LoI). The lack of available NE4-b1 sample (only one replicate used for the sequential extractions of deeper soil) does not allow safe conclusions and therefore, further work should be repeated on more samples from this locality.

F5 – Residual

Approximately 28.7 % $[(10.16/35.41) \times 100]$ was lost from the solid compared to the initial ^{226}Ra activity.

To summarise, Figure 90 shows the effect of sequential extractions on the initial ^{226}Ra activities measured in the residues. Figure 90 suggests that ^{226}Ra is present in all five sequential extraction stages, although in the case of the first stage of the extraction this value is within the error expected for the ^{226}Ra measurement. The majority of ^{226}Ra activity, more than 80 % with respect to the errors, is associated with carbonates, iron and manganese oxides, organics and insoluble fraction (likely to be silicates and sulfates).

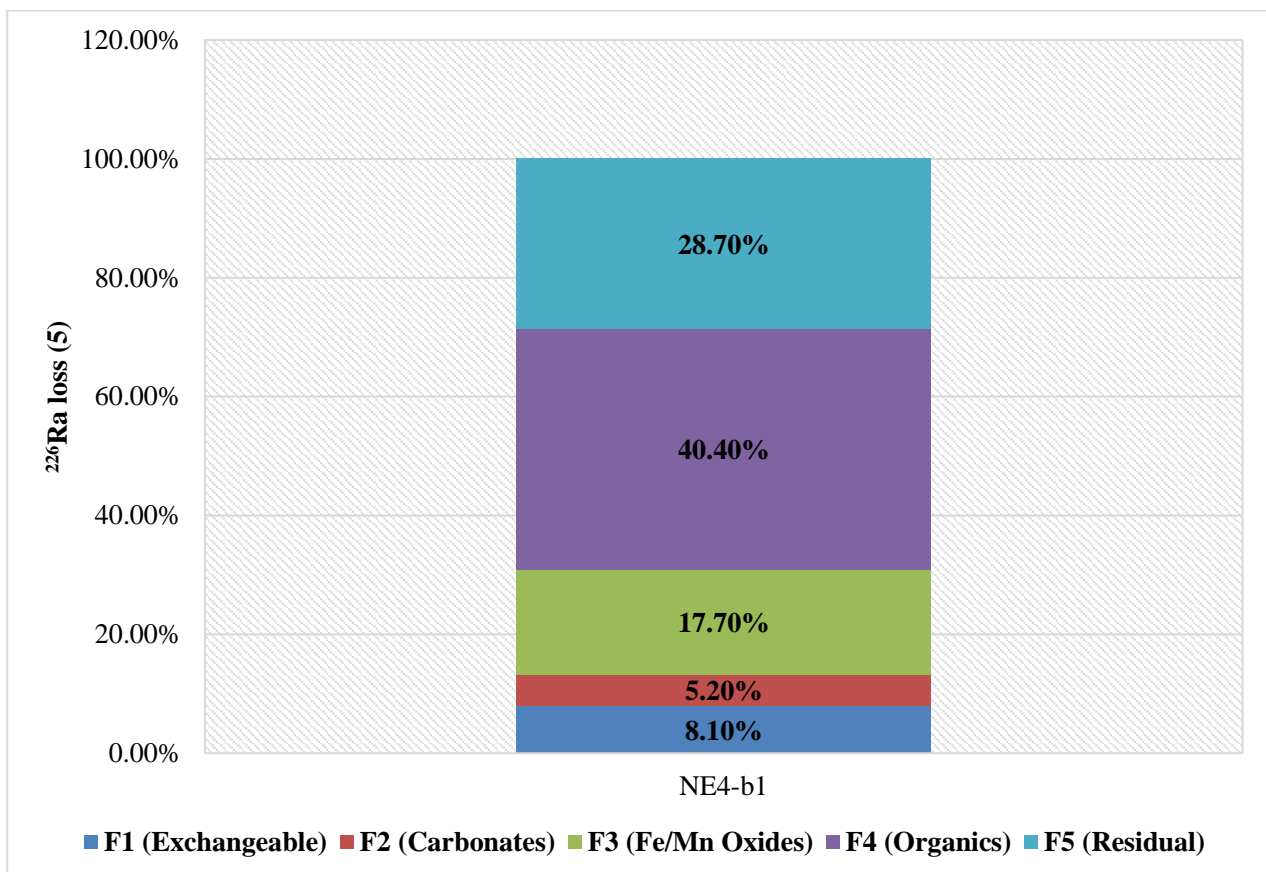


Figure 90. Effect of sequential extractions on the initial ^{226}Ra activity of NE4-b1 residues

Figure 91 below, summarises and compares the results obtained from all three sequential extraction batches.

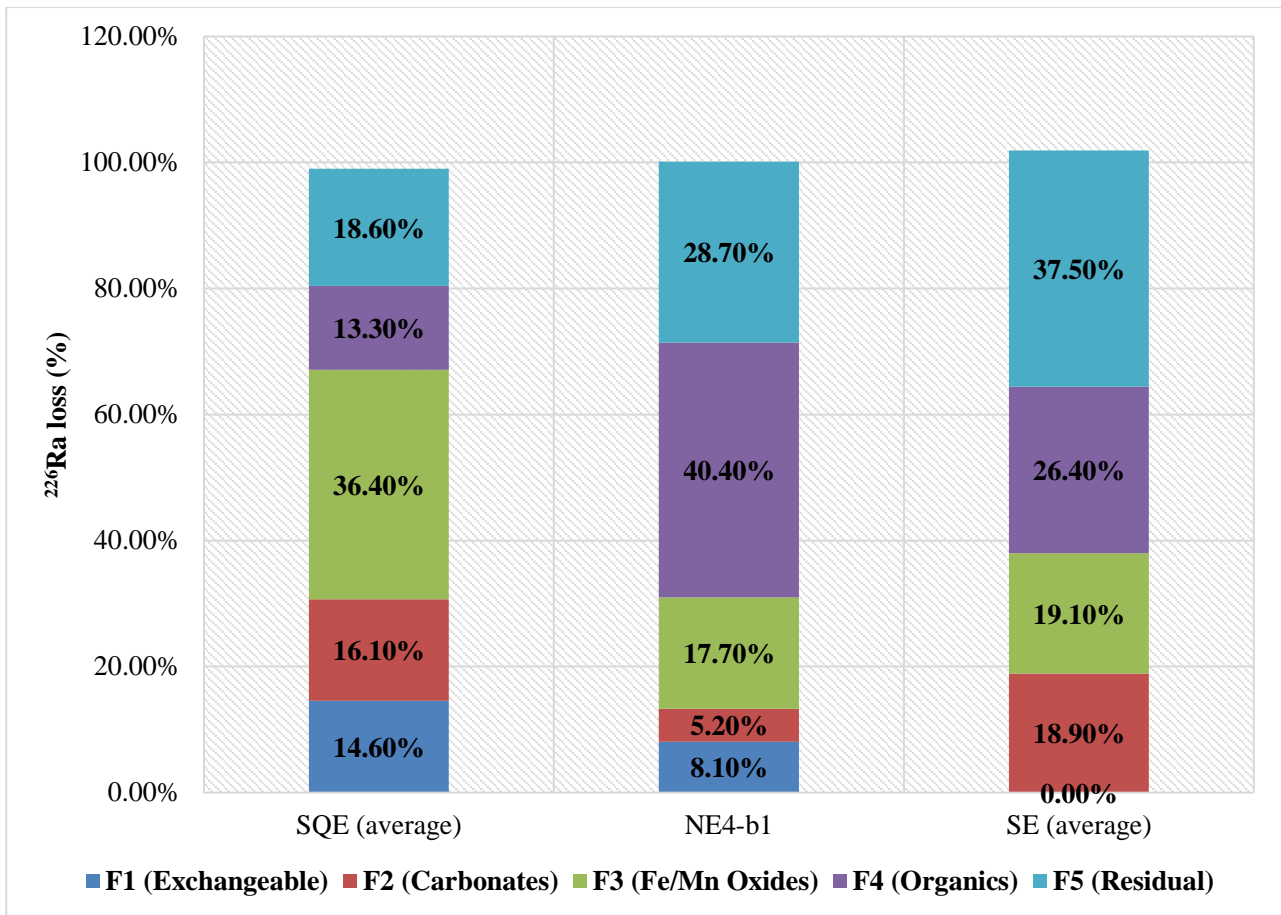


Figure 91. Effect of sequential extractions on the initial ^{226}Ra activity of NE4-b1, SQE and SE residues

Figure 91 shows the comparison of ^{226}Ra activity distribution in the five fractions for residues. ^{226}Ra is unevenly distributed between F1 – F5 sequential extraction fractions. The comparison of the results for SQE, SE and NE4-b1 suggests that:

1. The exchangeable fraction (i.e. fulvic and humic acids) (F1), for both topsoil (from 4.6 to 5.9 %, average value 5.3 %) and deeper soil (3.9 %), has a limited effect on ^{226}Ra distribution. More specifically, ^{226}Ra is unlikely to be mobile in these conditions as radium is not expected to exchange with magnesium; exchange capability falls as group II is descended due to the change in size of the hydrated cation.
2. The carbonate fraction (F2), for the topsoil had a varying effect on ^{226}Ra extraction into solution from between 11.4 to 13.5 % (~ 12.5 %), which was slightly higher when compared to the deeper soil which was 9.8 %. More specifically, it can be assumed that the strong presence of carbonate phases at Needle’s Eye as a result of granodiorite weathering, calcite

(CaCO₃) and dolomite (CaMg(CO₃)), close to the uraninite vein is responsible for the reported radium loss at this stage. Both calcite and dolomite are capable of interacting with radium and therefore, the loss of radium in this stage is likely to be due to radium accumulation in these phases.

3. The Fe/Mn Oxides fraction (F3), for topsoil had a varying effect on ²²⁶Ra extraction into solution from between 28.1 to 30.7 % (~ 29.4 %), which was significantly higher when compared to the deeper soil which had only 17.8 %. More specifically, it can be assumed that the presence of poor crystalline oxides is stronger in the topsoil than the deeper soil as a result of the Criffel plutonic intrusion at Needle's Eye site, such as ferrihydrite ((Fe³⁺)₂O₃·0.5H₂O), goethite (FeO(OH)), and hematite (Fe₂O₃), may be responsible for the radium loss at this stage.

4. The organic fraction (F4), for topsoil had a varying effect on ²²⁶Ra extraction into solution varied from 27.0 to 32.8 % (~ 29.9 %), which was slightly higher than the deeper soil which had 37.7 %. More specifically, the significant loss of radium that was reported at this stage may be due to the strong presence of organic material (LoI ~ 86 %) which have been reported to sorbe radium concentrations⁴¹. It is noteworthy to mention that approximately 86 % of the topsoil and 35 % of the deeper soil (Ne4-b1) is organic matter based on LoI measurements at 1000 °C. Only 30 – 40 % of the radium is associated with these fractions, implying inorganic phases play a major role in the retaining radium at Needle's Eye. Weight losses using LoI at the lower temperature of 500 °C, where carbonates are retained (as evidenced in the XRD pattern), were only 1 – 2 % lower than those at 1000 °C suggesting that carbonates only make up a very small fraction of these samples but have a major effect on radium sequestration with ca. 15 – 20 % of the radium being associated with it. This shows the crucial effect of carbonate concentration on preventing the movement of radium in the environment in agreement with previous studies^{44,48,49}.

5. A significant proportion of the radium ca. 22.8 % (avg. 26.7 and 19.2 %) in topsoil and 18.9 % in deeper soil, is associated with the residual fraction, where the radium is likely to be coprecipitated in anhydrite phase (CaSO₄). Both anhydrite and baryte were reported by previous authors after PXRD analysis at Needle's Eye, and radium is known to be able to replace calcium and barium by isovalent substitution. XRD work carried out as part of this study has repeatedly shown the presence of anhydrite together with layered silicates, feldspars and quartz that would be unlikely to retain radium.

Comparing the results, of sequential extractions, from the present research with the results of Siddeeg^{165,166} et al, that investigated radium mobility at the sediments of South Terras (River Fal) in Cornwall (England), it was shown that:

1. The effect of the exchangeable fraction to ²²⁶Ra activity in this research varied from 3.9 (deeper soil) to 5.3 % (topsoil) and for South Terras site varied from 2.2 to 8.9 %.
2. The effect of carbonate fraction to ²²⁶Ra activity in this research varied from 9.8 (deeper soil) to 12.5 % (topsoil) and for South Terras site varied from 13.1 to 15.9 %.
3. The effect of Fe/Mn Oxides fraction to ²²⁶Ra activity in this research varied from 17.8 (deeper soil) to 29.4 % (topsoil) and for South Terras site varied from 1.2 to 1.9 %.
4. The effect of the organics fraction to ²²⁶Ra activity in this research varied from 29.9 (topsoil) to 37.7 % (deeper soil) and for South Terras site varied from 61.8 to 70.0 %.
5. The effect of the residual (in Siddeeg^{165,166} et al research is referred as resistant) fraction to ²²⁶Ra activity in this research varied from 18.9 (deeper soil) to 29.9 % (topsoil) and for South Terras site varied from 6.0 to 18.6 %.

For the South Terras site, radium was found to be associated mainly with the organic fraction (Siddeeg^{165,166} et al, refers to South Terras site as organic rich site due to %LoI 21.0 – 37.0) and less with the residual and carbonate fraction. It should be noted that in the present work the Tessier sequential extraction method was used rather than the Schultz sequential extraction method which was used for the sediments of the South Terras site. The most noteworthy difference between Needle's Eye and South Terras site was the effect of Fe/Mn Oxides to radium mobility, 23.6 % (average value of top and deeper soil) and 1.5 % (average value) respectively. This significant difference may be a result of the different geology of the sites. The geology of Needle's Eye site is characterised by a strong presence of intrusive igneous rock (i.e. pluton) which is rich in iron and manganese oxides, whereas the geology of South Terras mainly consists of grey and brown Lower Devonian slate, which is a metamorphic rock rich in quartz, muscovite, illite. Finally, more significantly the average activity concentrations of ²²⁶Ra that were reported in this research were 30×10^2 Bq kg⁻¹ in topsoil, when compared to

South Terras research as reported by Siddeeg^{165,166} et al. varied from 0.94×10^2 to 1.77×10^2 Bq kg^{-1} . No sulfate phases were observed in the geology of South Terras.

3.3.5.5 Elemental and mineralogical analysis of topsoil and deeper soil

Further investigation of the potential association of ^{226}Ra with different mineral phases was conducted by non-destructive elemental analysis (XRF), mineralogical analysis (PXRD) and morphological analysis (SEM). For these investigations, the samples that were analysed were: NE4_T (topsoil from the locality that showed the highest reported activity concentration of ^{226}Ra reported in this research), NE4-b1 (deeper soil sample from the locality that showed the highest reported activity concentration of ^{226}Ra reported in this research), and NE5_T (control topsoil sample not containing ^{226}Ra).

3.3.5.5.1 XRF analysis

The bulk composition of the ‘sacrificial’ samples from the sequential extractions, mentioned in Section 3.3.5.3, were analysed by XRF and the results obtained are shown in Table 29. It should be noted that ‘Bulk’ sample identification refers to the initial samples before treatment using the sequential extraction reagents treatment.

Table 29. XRF values of bulk and F1 - F4 composition

Sample		MgO (%)	Al ₂ O ₃ (%)	SiO ₂ (%)	K ₂ O (%)	P (%)	S (%)	Cl (%)	Ca (%)	Mn (%)	Fe (%)	U (%)
NE4-b1	Bulk	1.60 ± 0.90	0.97 ± 0.13	5.47 ± 0.10	0.22 ± 0.01	0.17 ± 0.01	1.21 ± 0.07	0.13 ± 0.01	6.39 ± 0.05	0.11 ± 0.01	3.56 ± 0.01	0.16 ± 0.01
	F1	2.41 ± 0.88	0.77 ± 0.15	3.92 ± 0.11	0.16 ± 0.01	0.13 ± 0.01	0.87 ± 0.07	2.10 ± 0.01	2.59 ± 0.01	0.12 ± 0.01	2.42 ± 0.01	0.20 ± 0.01
	F2	1.43 ± 0.88	0.89 ± 0.14	4.11 ± 0.11	0.24 ± 0.01	0.21 ± 0.01	1.47 ± 0.07	0.27 ± 0.01	2.13 ± 0.01	0.29 ± 0.01	4.56 ± 0.01	0.31 ± 0.01
	F3	0.91 ± 0.86	0.28 ± 0.13	1.49 ± 0.11	0.04 ± 0.01	0.01 ± 0.01	4.07 ± 0.07	N/D	0.25 ± 0.01	0.01 ± 0.003	0.64 ± 0.01	0.04 ± 0.01
	F4	1.01 ± 0.78	1.60 ± 0.14	15.64 ± 0.11	0.43 ± 0.02	0.04 ± 0.01	9.46 ± 0.09	N/D	0.20 ± 0.01	0.01 ± 0.003	0.75 ± 0.01	0.01 ± 0.01
NE4 _T	Bulk	1.45 ± 0.88	0.71 ± 0.18	3.35 ± 0.16	0.20 ± 0.01	0.19 ± 0.02	1.24 ± 0.03	0.28 ± 0.02	5.83 ± 0.04	0.29 ± 0.01	4.48 ± 0.04	0.25 ± 0.01
	F1	1.84 ± 0.87	0.61 ± 0.17	2.52 ± 0.14	0.15 ± 0.01	0.15 ± 0.02	0.96 ± 0.03	0.48 ± 0.03	4.63 ± 0.03	0.22 ± 0.01	4.13 ± 0.03	0.20 ± 0.01
	F2	1.17 ± 0.82	0.66 ± 0.17	2.12 ± 0.14	0.12 ± 0.01	0.16 ± 0.02	1.15 ± 0.03	0.14 ± 0.02	2.94 ± 0.03	0.10 ± 0.01	4.33 ± 0.04	0.13 ± 0.01
	F3	N/D	0.33 ± 0.14	1.43 ± 0.11	0.03 ± 0.01	0.04 ± 0.01	9.16 ± 0.08	N/D	0.54 ± 0.01	0.01 ± 0.003	0.99 ± 0.02	0.03 ± 0.01
	F4	1.06 ± 0.64	0.39 ± 0.13	4.78 ± 0.17	0.15 ± 0.01	0.01 ± 0.01	2.34 ± 0.04	N/D	0.44 ± 0.01	N/D	0.35 ± 0.01	N/D

N/D = not detected

Table 29 shows the elemental and oxides composition of the topsoil (NE4_T) and deeper (NE4-b1) sample, after each the sequential extraction procedure. Initially, both bulk samples of NE4-b1 and NE4_T verified the presence of mineral phases described in the literature and during the mineralogical analysis of the second sampling visit (see Sections 1.5.1 and 3.2.4). The geology of Needle's Eye site verifies a strong presence of quartz, feldspars (Ca/Na plagioclase (solid solution) and orthoclase (K-feldspar). Also present are both muscovite mica (K- $\text{AlSi}_3\text{O}_{10}(\text{OH})_2$) and biotite ($\text{K}(\text{Mg,Fe})_3(\text{AlSi}_3\text{O}_{10})(\text{F,OH})_2$) which is similar to muscovite micas but has a mixture of Mg-Fe-K where the K is present in muscovite (i.e. within the layers of the mineral). Furthermore, the weathering of feldspars is expected to produce clay minerals, which are likely to be present and identified by PXRD analysis (see Section 3.3.5.4.2).

The XRF analysis of the bulk (i.e. before sequential extractions treatment) samples of NE4_T and NE4-b1 showed significant concentrations of calcium, $5.83 \pm 0.04 \%$ and $2.13 \pm 0.01 \%$ respectively, which may confirm, supported by the PXRD analysis, the presence of carbonate mineral phases, such as: calcite (CaCO_3) as a decay product of limestone which is present in the geology of Needle's eye site, clay mineral phases (i.e. micas (biotite $\text{K}(\text{Mg,Fe})_3(\text{AlSi}_3\text{O}_{10})(\text{F,OH})_2$, muscovite $\text{KAl}_2(\text{AlSi}_3\text{O}_{10})(\text{F,OH})_2$, and feldspars (anorthite $\text{CaAl}_2\text{Si}_2\text{O}_8$ as a decay product of granite – granodiorite, hornblende).

For the F1 sequential extraction fraction of both samples, Table 29 reports increasing percentages for chlorine due to the 1M MgCl_2 treatment of the soil during the sequential extraction experiments. For the F2 sequential extraction fraction, of both samples, Table 29 reports enhanced percentages of calcium which confirms the presence of calcite in the samples. For the F3 sequential extraction fraction, of both samples, Table 29 reports calcium loss possibly due to the loss of calcite. For the F4 sequential extraction fraction, for both samples, Table 29 reports iron loss which implies the presence of iron oxides in the samples.

Further elemental analysis was conducted to determine the carbon content in the NE4_T and NE5_T samples. The results obtained by the CHN analysis (described in Section 2.4.4.5) are shown in Table 30.

Table 30. CHN and 1000 °C LoI analysis for NE4_T and NE5_T samples

Sample	C (%)	H (%)	N (%)	1000 °C LoI (%)
NE4 _T	40.77 ± 0.40	4.63 ± 0.12	2.50 ± 0.10	86.06 ± 9.28
NE5 _T	30.00 ± 0.60	3.70 ± 0.01	2.33 ± 0.06	62.70 ± 2.30

Table 30 shows the results from the CHN analysis and LoI (after heating at 1000 °C) for both topsoil samples. It should be noted that the average activity concentration of ²²⁶Ra for NE4_T sample is 30.47 ± 6.95 Bq kg⁻¹, whereas the average activity concentration of ²²⁶Ra for NE5_T is 2.72 ± 0.57 Bq kg⁻¹ (NE5_T is a control sample). The comparison of the results shown in Table 68 suggests that for NE4_T sample approximately 40.7 % from the 86.0 % is associated with carbon while the rest 45.3 % may be associated with carbonate and the breakdown of hydrated minerals. For NE5_T sample approximately 30.0 % of the 62.6 % is associated with carbon while the rest 32.7 % may also be associated chlorine, bromine, also water that may be associated with some mineral phases. Finally, the variation in carbon, hydrogen and nitrogen between the two topsoil samples is relatively big as expected from the literature and from the locality from which the samples were taken. Furthermore, the relative high percentages for carbon, in both topsoil samples, are not surprising given the natural origin of the samples and the background geology of the site which is dominated by the presence of limestone (CaCO₃), hornblende (Ca₂(Mg,Fe, Al)₅(Al, Si)₈O₂₂(OH)₂), and granodiorite (rich in calcium).

3.3.5.5.2 Mineralogical Analysis

The powder diffraction data from the sequential extractions are given in Figure 92. Anhydrite is present in these materials along with the magnesium iron carbonate phase which disappears at the point which is expected for carbonates (SEQ2). The halite (NaCl) which appears after treatment with MgCl₂, is likely to be formed from the addition of these chloride ions. Very little washing took place during these experiments as the intention was to maintain constant volume (40 mL) and not dilute the filtrate too much. It is noteworthy that activity is lost on raising the pH to values which decompose the carbonates, implying radium is associated with the carbonates in the sample. Since PXRD detects crystalline phases only, any amorphous

mineral phase would not be identified (e.g. organic matter such as leaf litter where no long-range crystalline order is present).

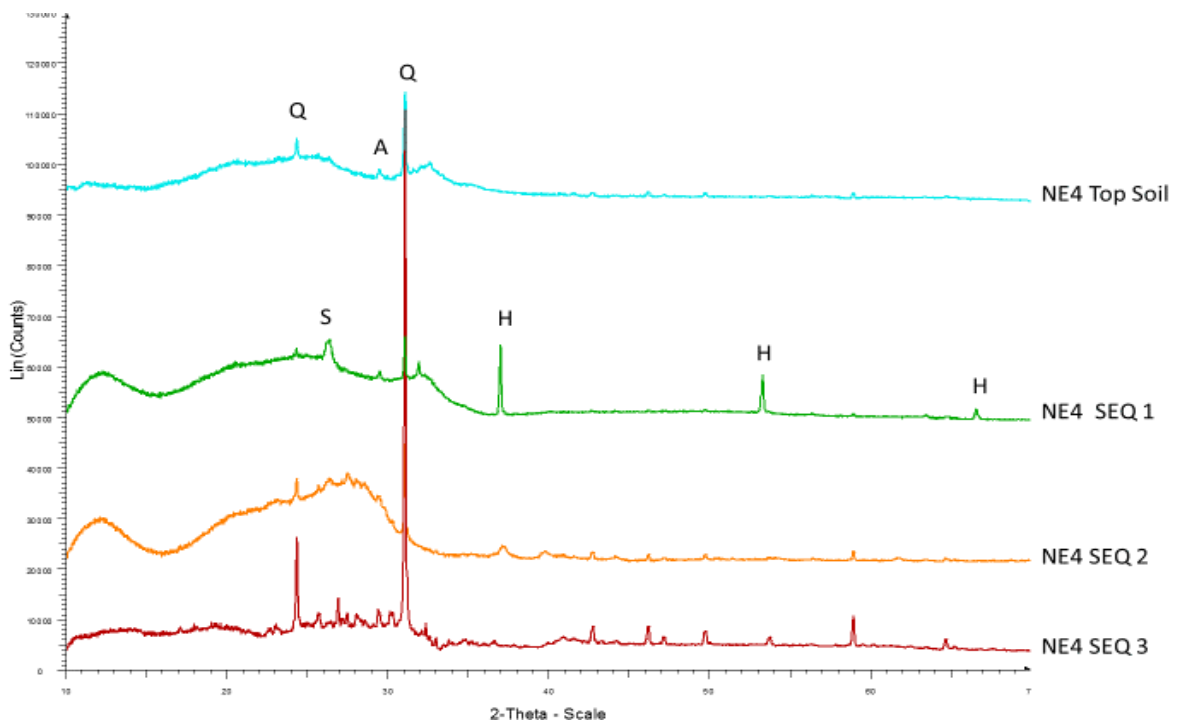


Figure 92. PXRD data on the first three stages of sequential extractions, Phase ID S = sjoegrenite $\text{MgFe}_2(\text{OH})_{16}\text{CO}_3(\text{H}_2\text{O})_4$ (74-1513), A = anhydrite CaSO_4 (37-1496) and Q = quartz SiO_2 (46-1045), H = halite NaCl (70-2509)

To further investigate the phases, present without the interference of the organic material, which is non-crystalline, powder diffraction data were recorded on the samples after combustion. Data were collected at 500 and 1000°C as carbonates decompose beyond 1000 °C through loss of CO_2 . To capture carbonate phases which may also be of interest for radium uptake, data were compared at different temperatures and across different sites.

Powder diffraction data recorded after combustion at 1000°C across the different sites are shown in Figure 93. There is a stark difference between all the other sites and that of NE4. Apart for NE4, the only phases observed in the patterns are quartz and feldspar. Neither of these phases has much interest in sequestration of radium as they contain no exchangeable ions.

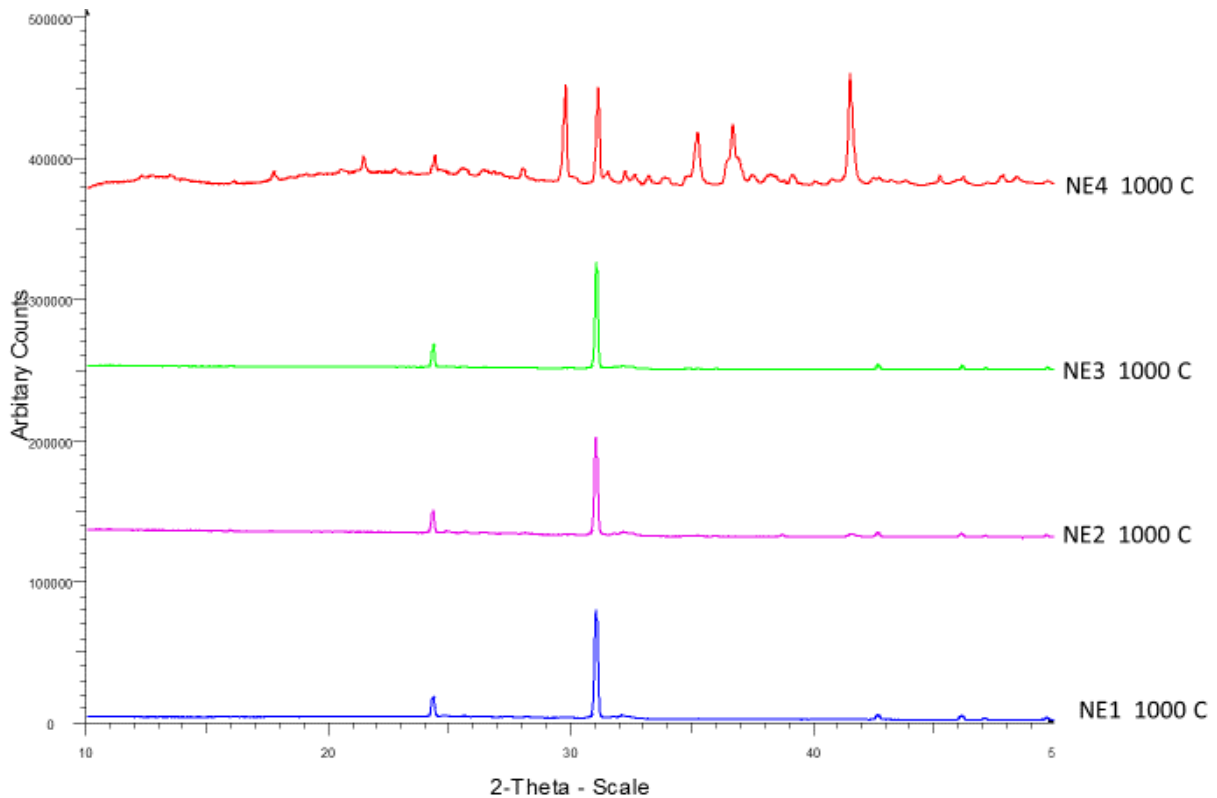


Figure 93. Comparison of LoI of NE4 from those taken at the other sampling sites

Phase identification of the phases in the NE4 file are shown in Figure 92. Prominent phases are anhydrite, gehlenite ($\text{CaSi}_2\text{Al}_2\text{O}_7$), quartz (SiO_2) and magnesioferrite (MgFe_2O_4). The analogous pattern at 500°C (Figure 95) does not show the spinel or gehlenite but shows CaCO_3 as a strongly crystalline component. This is of interest because calcite is another possible sink for radium, as radium can be incorporated onto the calcium site by isovalent substitution^{2,48,53}. A comparison of the loss on ignition diffraction data at different temperatures is given in Figure 93. The vein containing uraninite is described in the BGS survey as being calcite rich (Basham¹ et al.). These XRD data therefore agree with previous work on this area of the site.

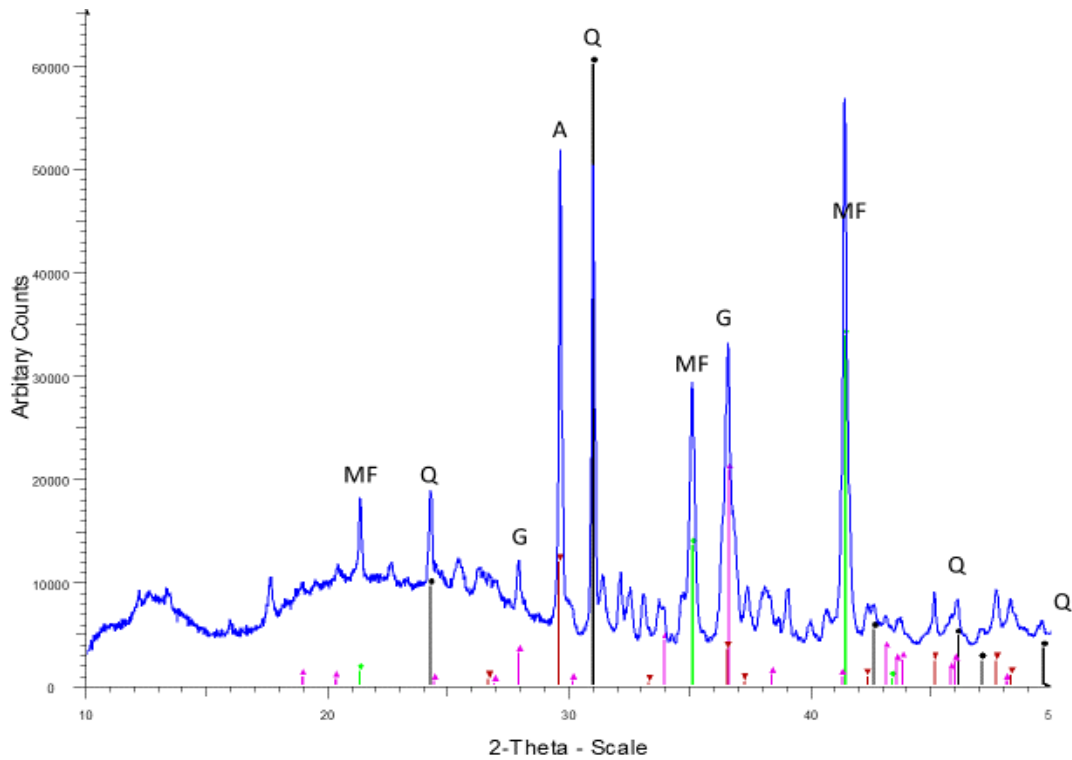


Figure 94. Powder X-ray Diffraction Data of the NE4 topsoil after LoI at 1000 °C, Phase Identified: MF = magnesioferrite (MgFe_2O_4) – green 01-071-1232, Q = quartz – black 46-1045, G = gehlinitite ($\text{Ca}_2\text{SiAl}_2\text{O}_7$) and A = anhydrite (CaSO_4)

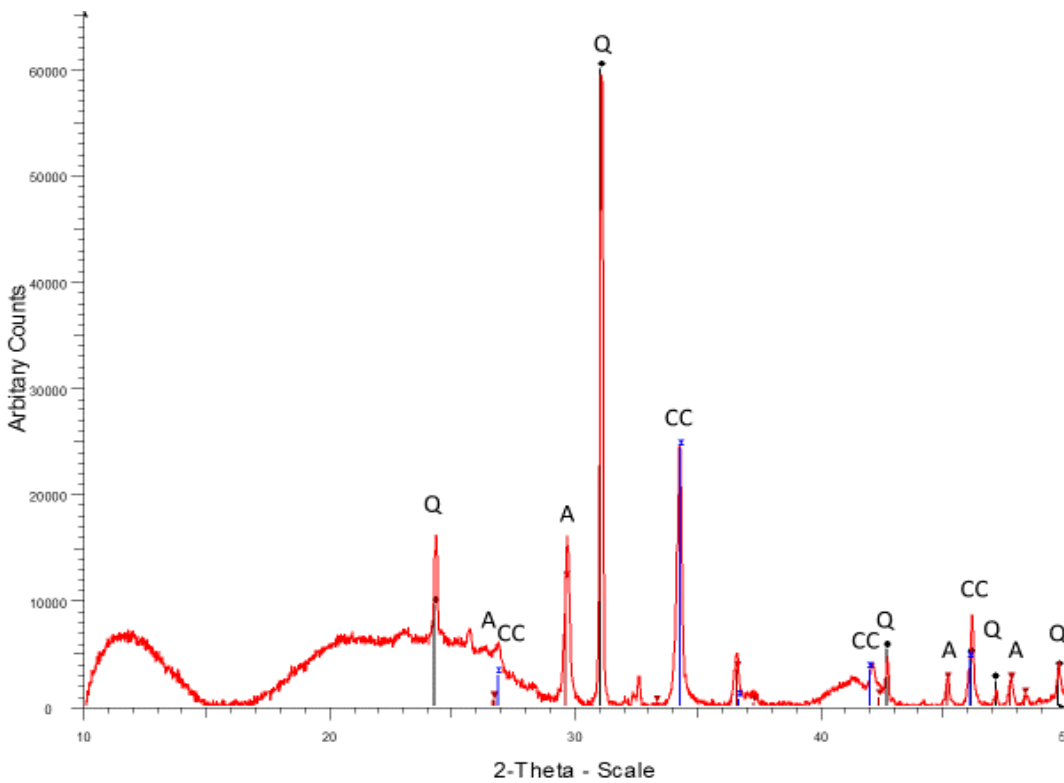


Figure 95. Powder X-ray Diffraction Data of the NE4 topsoil after LoI at 500 °C, Phase identified Q = quartz – black 46-1045, A = anhydrite (CaSO_4), and CC = calcite (CaCO_3)

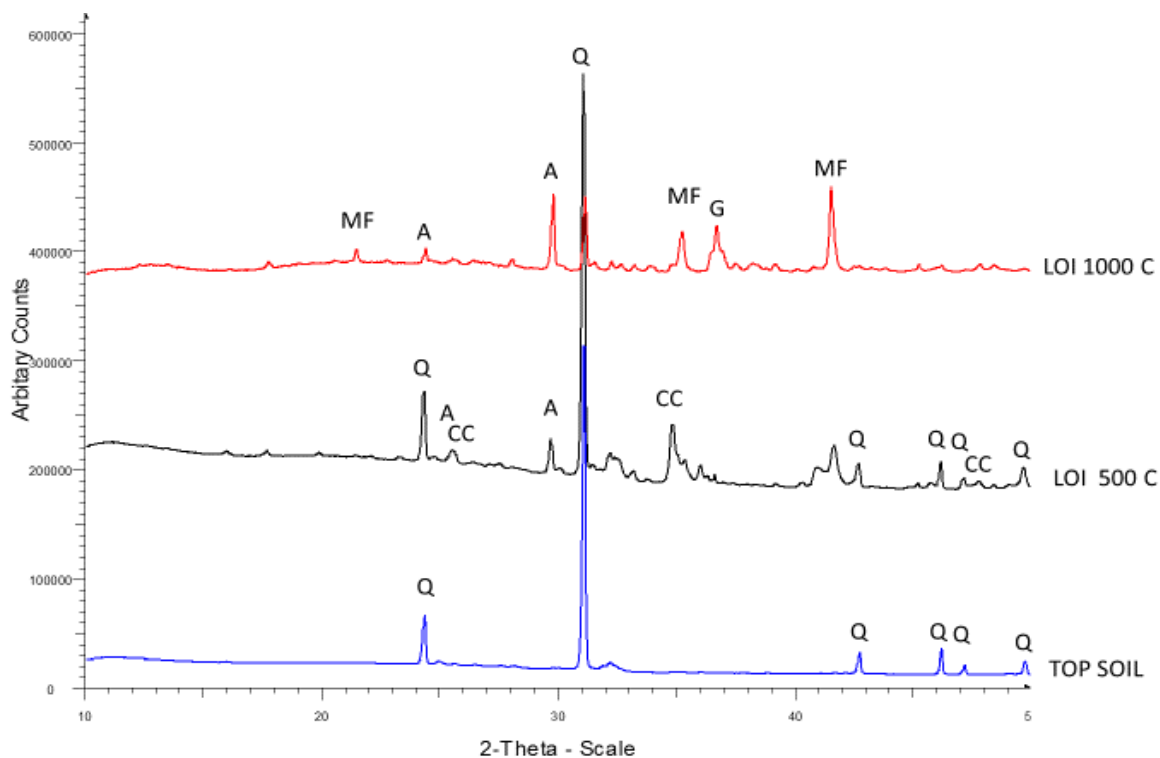


Figure 96. Comparison of Powder X-ray Diffraction Data of the NE4 topsoil after LoI at 500, 1000 °C and bulk top soil, Phase Identified: Q = Quartz SiO_2 (black 46-1045); A = anhydrite (CaSO_4) (red, CC = calcite (CaCO_3))

In conclusion, the mineral phases that were reported in Figures 94 - 96 for the Needle's Eye samples were: anhydrite (CaSO_4), quartz (SiO_2), magnesioferrite (MgFe_2O_4), gehlinitite ($\text{Ca}_2\text{SiAl}_2\text{O}_7$), calcite (CaCO_3).

To summarise, the mineral phases that were identified, by PXRD, in the soils from Needle's Eye site were quartz, and a poorly crystalline mineral of mixed carbonate metal ($\text{Mg,Fe}(\text{CO}_3)$). Moreover, during the acid wash treatment of the samples, the carbonate phase is not present which fits in with the carbonate phase present in the NaOH wash, as expected because carbonate reacts with acid and not with hydroxide. Furthermore, the acid treatment identified the presence of quartz (SiO_2), and sodium chloride (NaCl). The after LoI (500 and 1000°C) patterns identified magnesioferrite ($\text{MgFe}^{2+}_3\text{O}_4$), gehlinitite ($\text{CaAl}_2\text{Si}_2\text{O}_7$), anhydrite (CaSO_4), and quartz (SiO_2). The mineral phase identification of anhydrite (CaSO_4) is considered important as it is likely to interact with radium and remain stable until the sequential extraction F5 residual stage. Finally, a major difference between the 500 and 1000°C LoI treatment was reported in the PXRD patterns as the strong reflections that correspond to calcite (CaCO_3) and

anhydrite (CaSO_4) were reported when the samples were heated at 500°C , which is supported by the geology of the study area (described in Sections 1.5.1 and 3.3.5.3), whereas magnesioferrite ($\text{MgFe}^{2+}_3\text{O}_4$) appears in the patterns as a by-product/ result of the 1000°C LoI treatment.

Further mineralogical analysis of the NE4T and NE4-b bulk and F1 – F4 samples was conducted by SEM/EDX analysis. SEM/EDX imaging was used to investigate the surface topography, crystal form, and mineral chemistry when possible. It should be noted that the soil material was broadly uniform ($\leq 1\text{ mm}$). The backscattered electron imaging aimed to detect the minerals and mineral phases that were identified by PXRD, XRF, and sequential extraction experiments (Figures 97 - 101).

The EDX analyses for NE4T and NE4-b1 samples showed that the elements that are present in the bulk samples are: Si, Ca, Mg, Al, S, Fe, Na and K. For both F1 fraction the elements that are present are: Mg, Cl, Si, Al, S, Ca, Fe and Cu. For both F2 fraction the elements that are present are: Ca, Fe, Na, Al, S, Mg and Si. For both F3 fraction the elements that are present are: Na, Al, Si, S, K, Mg and Fe. Finally, for both F4 fraction the elements that are present are: Si, Al, Fe, K and Mg. To summarise, the results from the SEM/EDX analysis are in agreement with the results as shown in Sections 1.5.1 and 3.3.5.3 on NE4_T and NE4-b and, in this section.

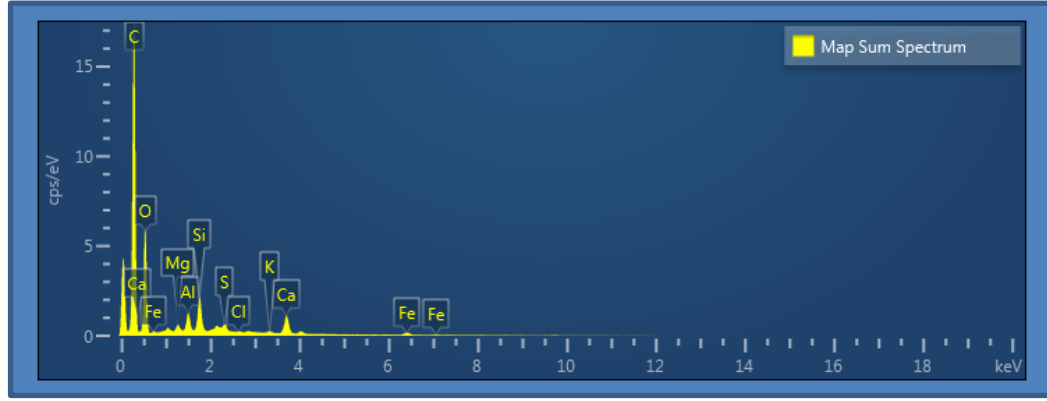
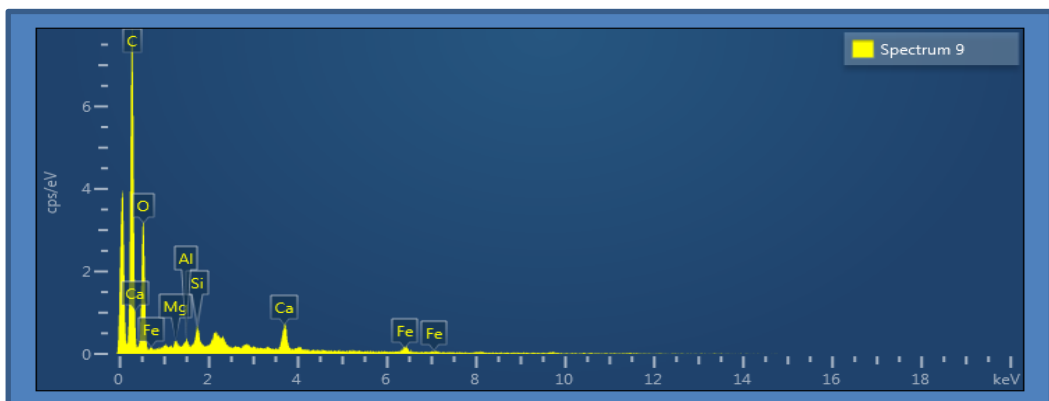
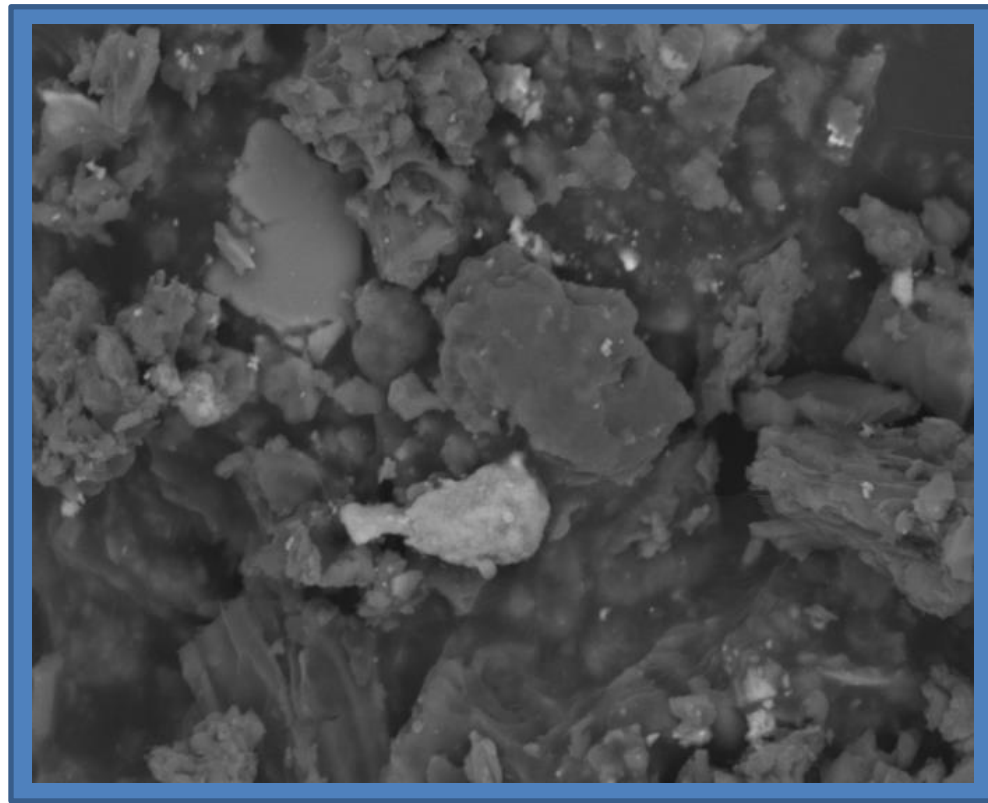
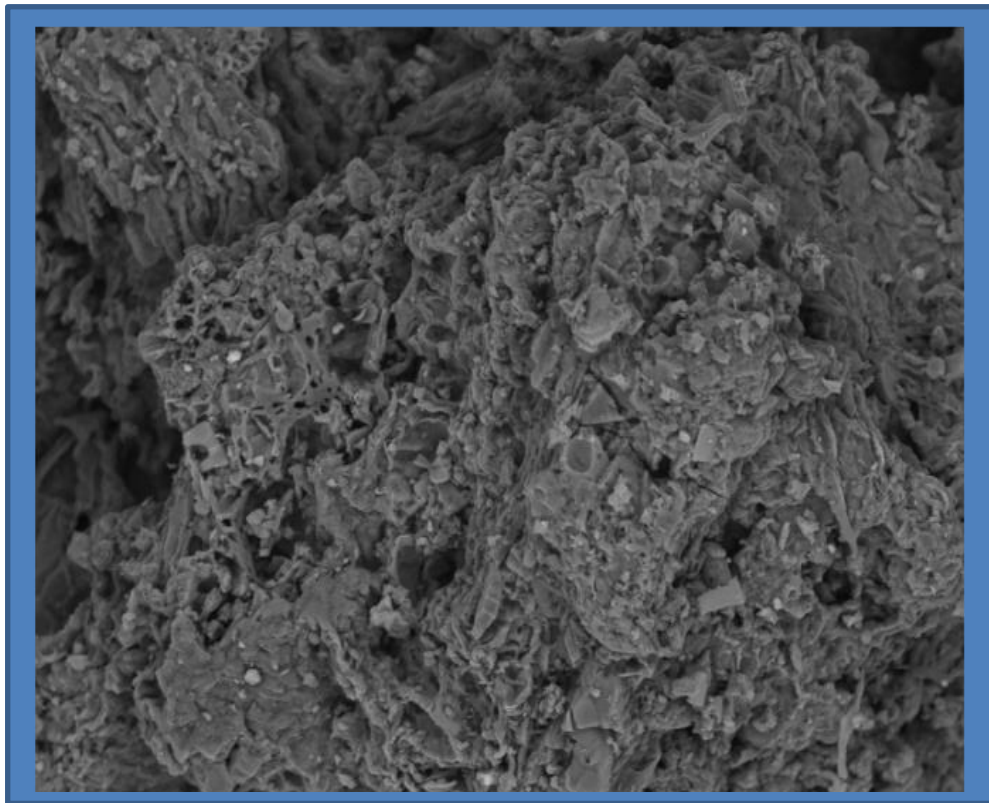


Figure 97. Backscattered electron image (above) and elemental map (below) of NE4_T (left) and NE4-b1 (right) bulk samples

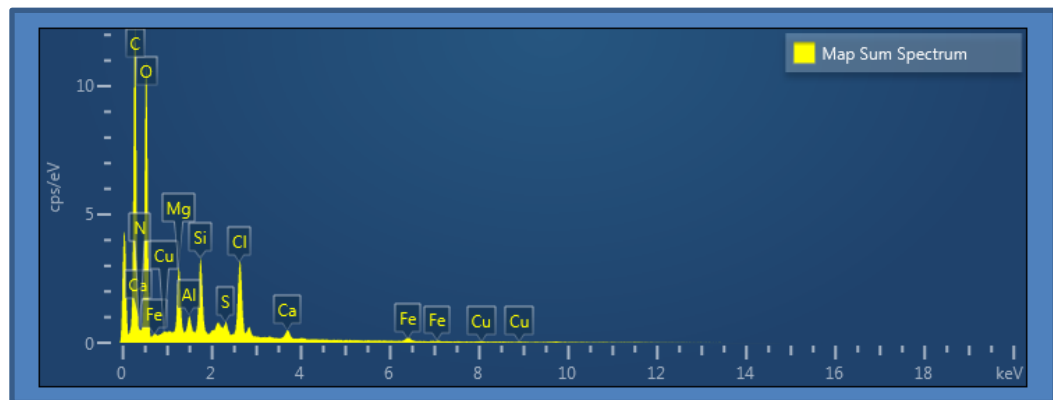
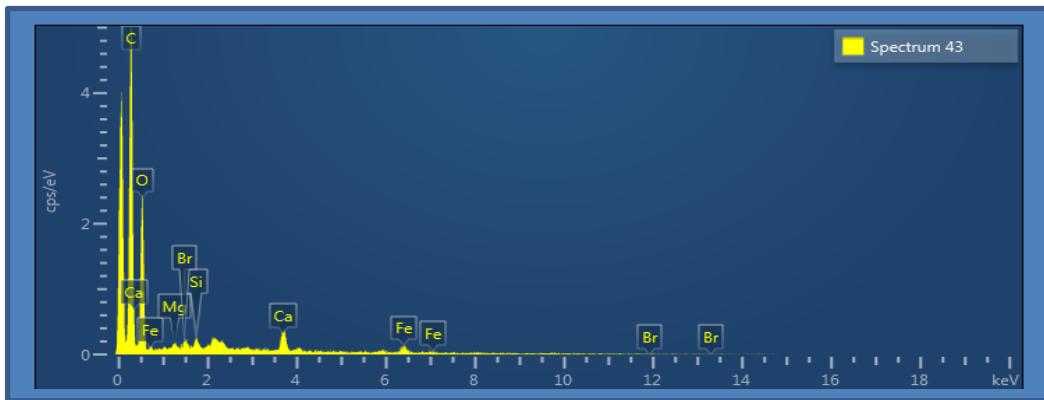
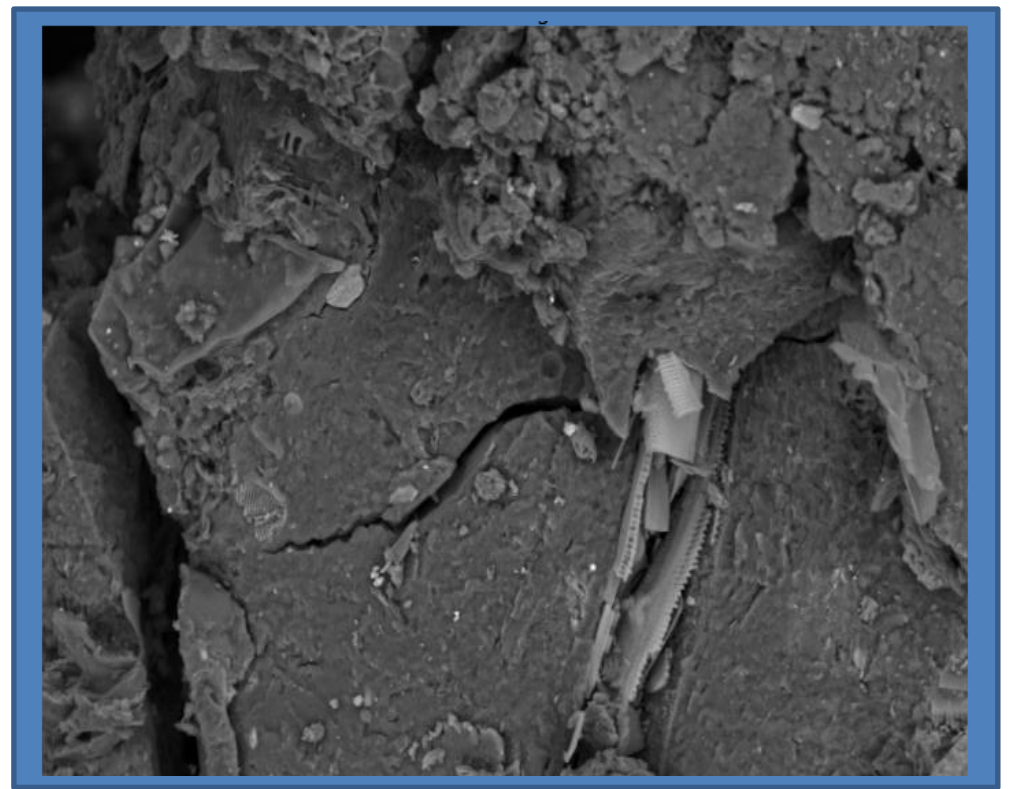
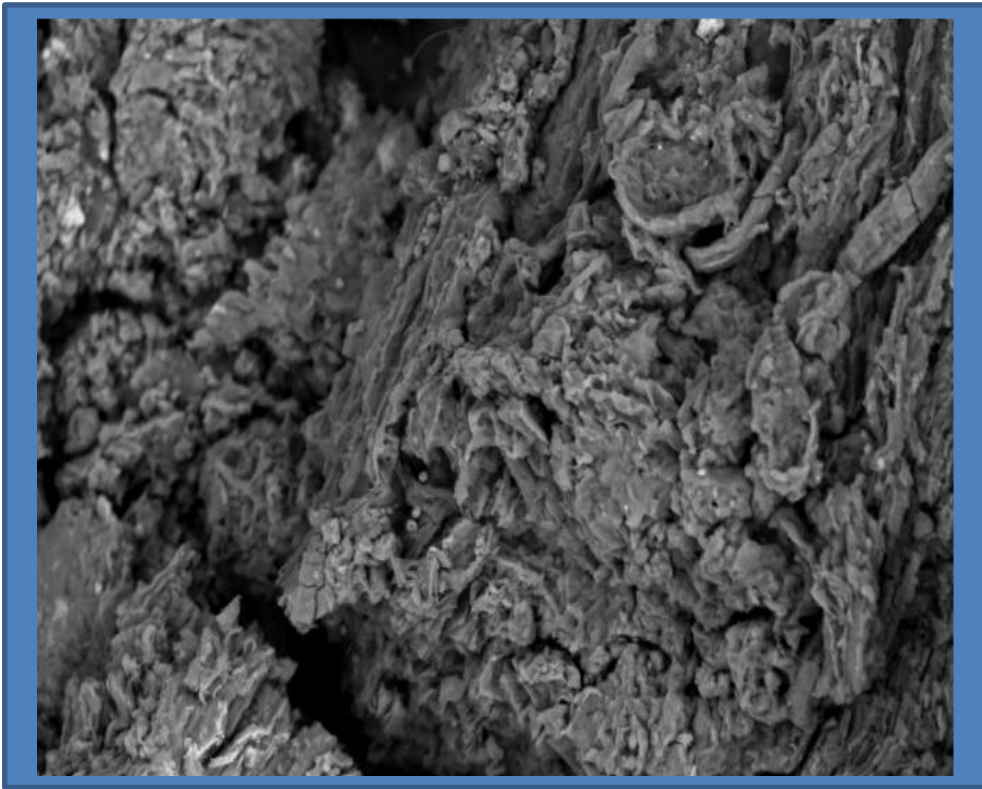


Figure 98. Backscattered electron image (above) and elemental map (below) of NE4_T (left) and NE4-b1 (right) F1 fraction samples

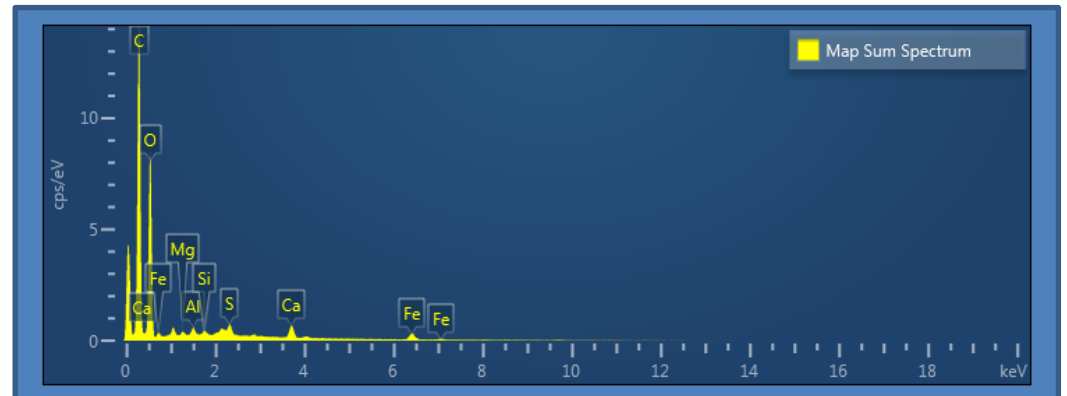
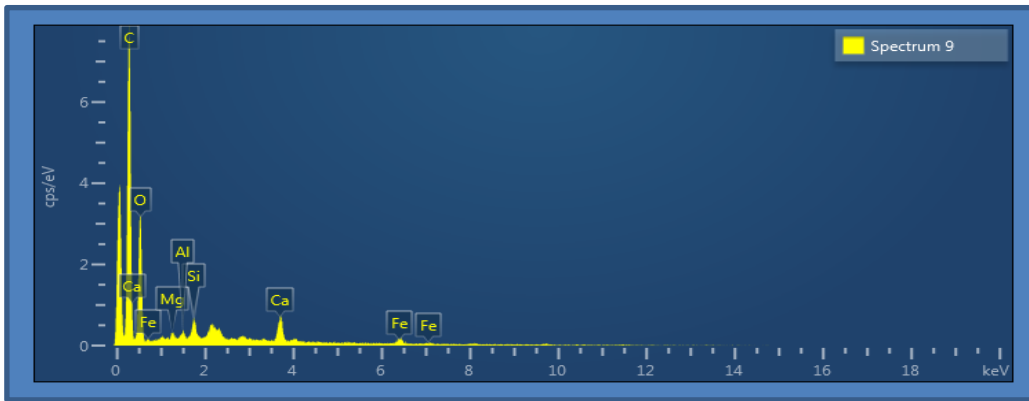
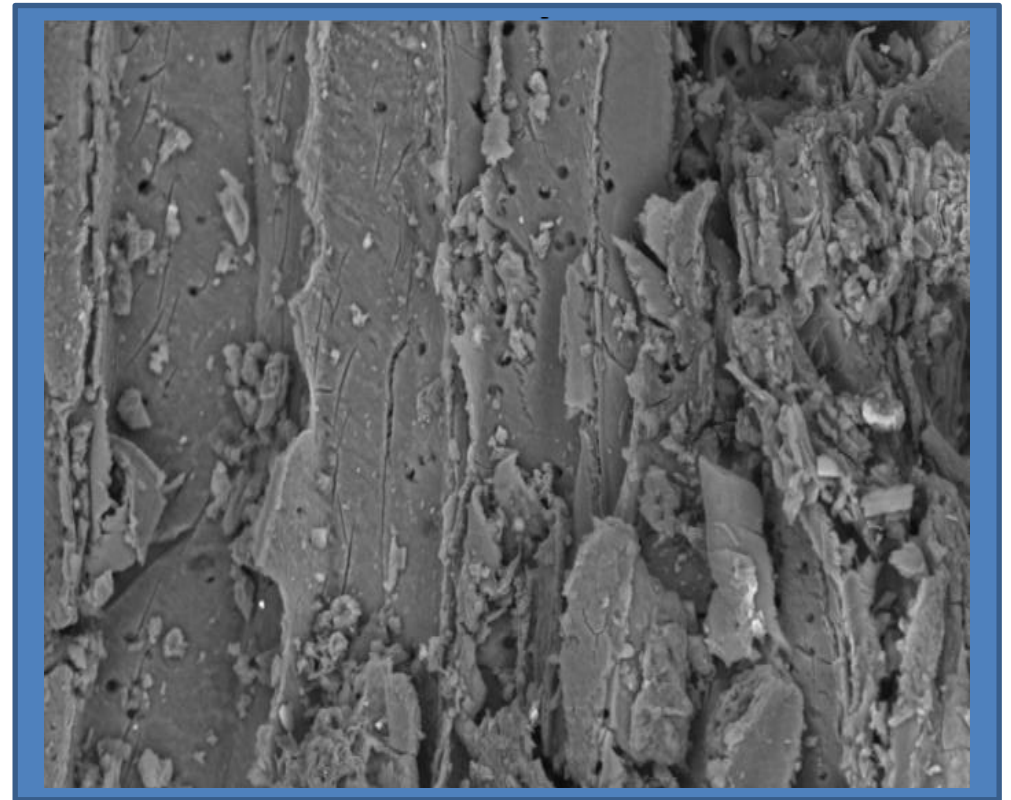
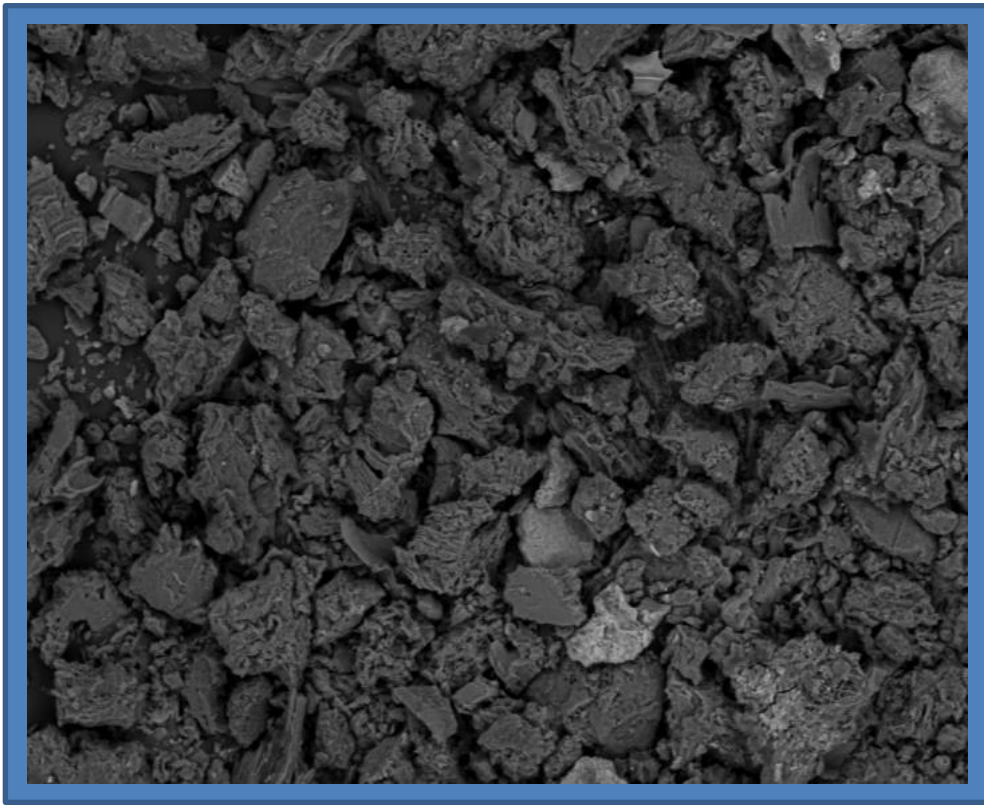


Figure 99. Backscattered electron image (above) and elemental map (below) of NE4_T (left) and NE4-b1 (right) F2 fraction samples

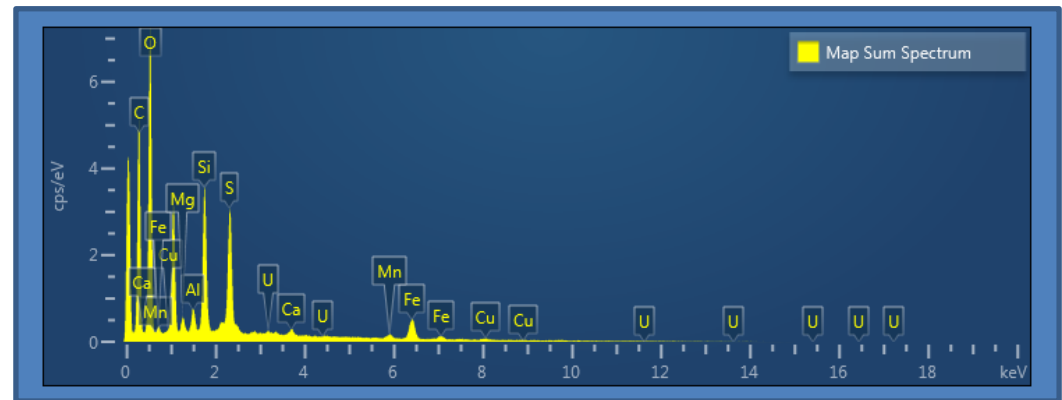
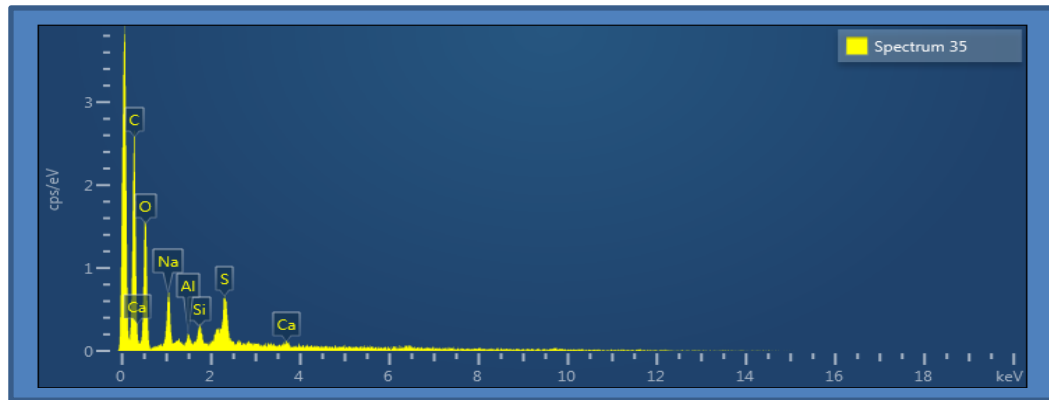
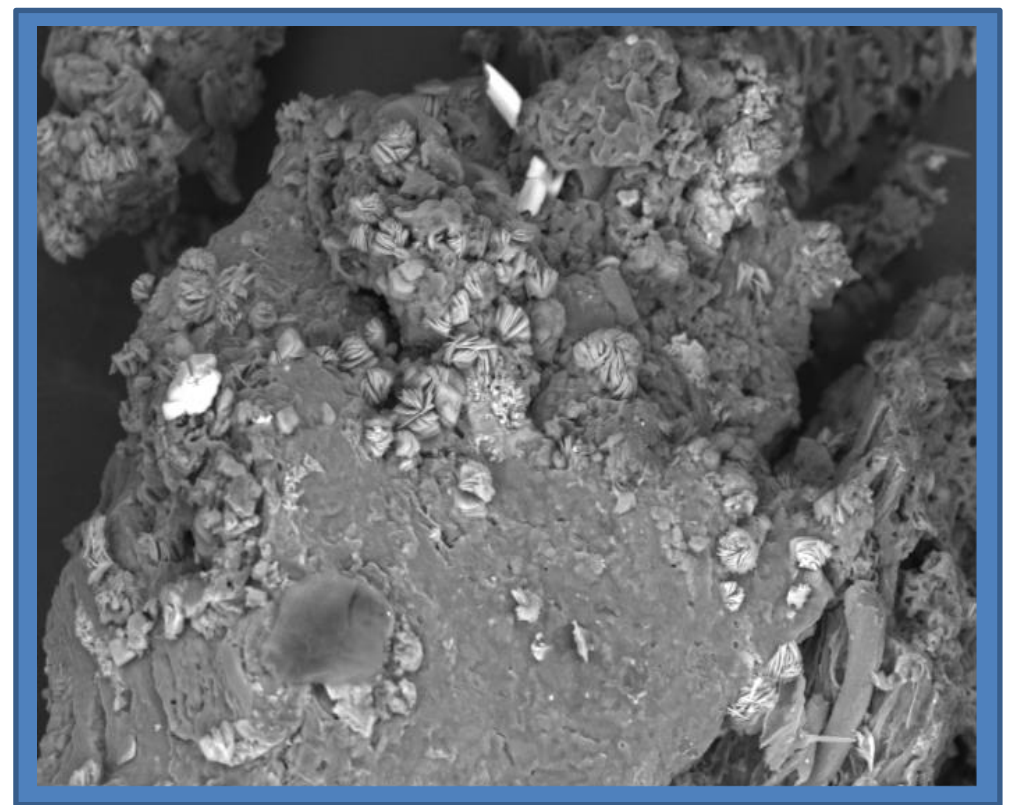
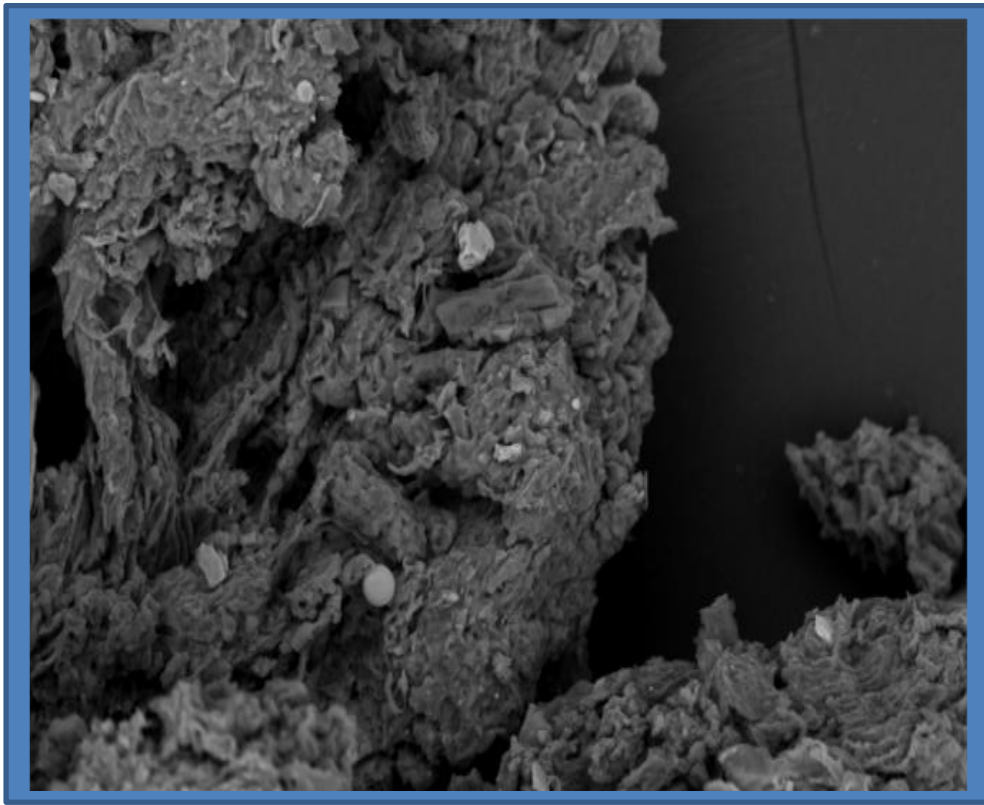


Figure 100. Backscattered electron image (above) and elemental map (below) of NE4_T (left) and NE4-b1 (right) F3 fraction samples

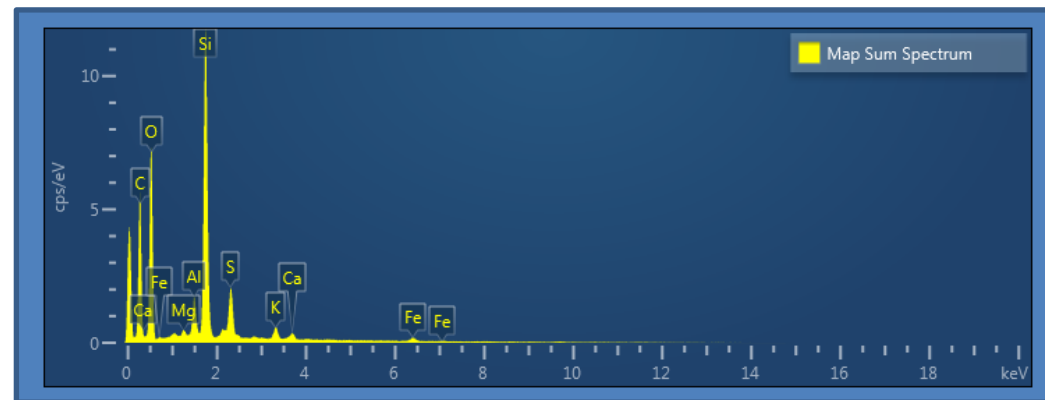
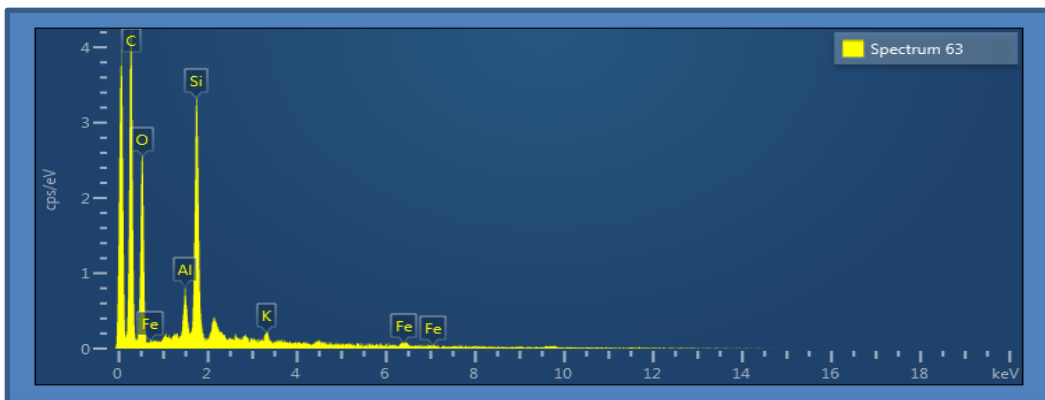
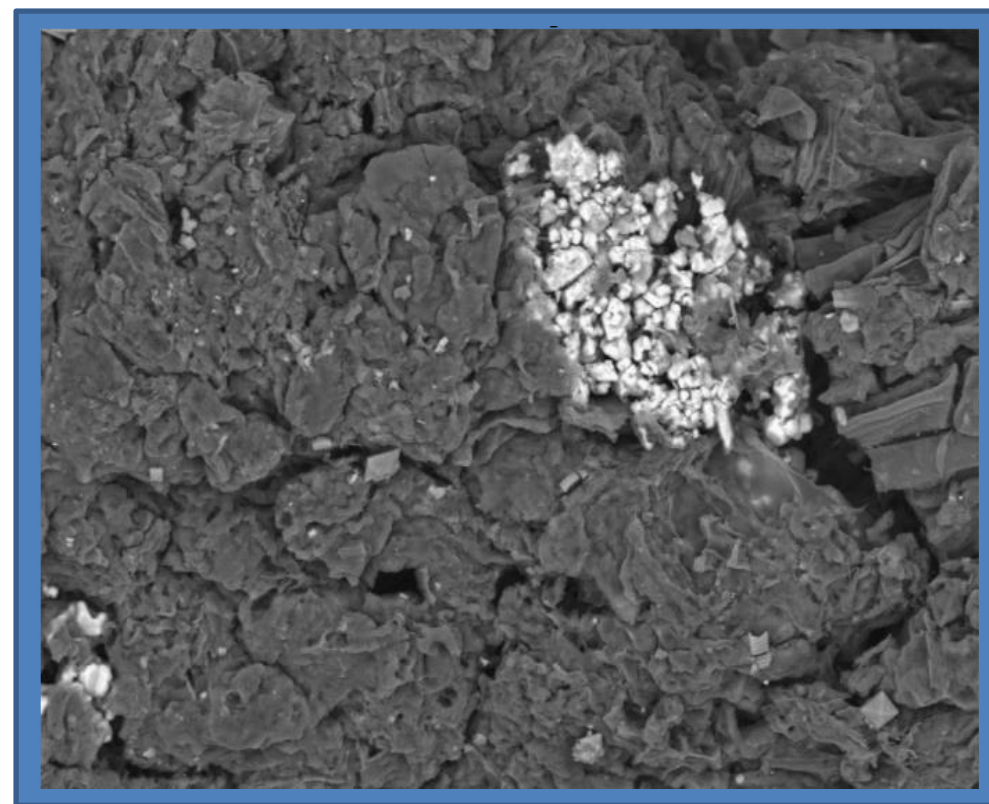
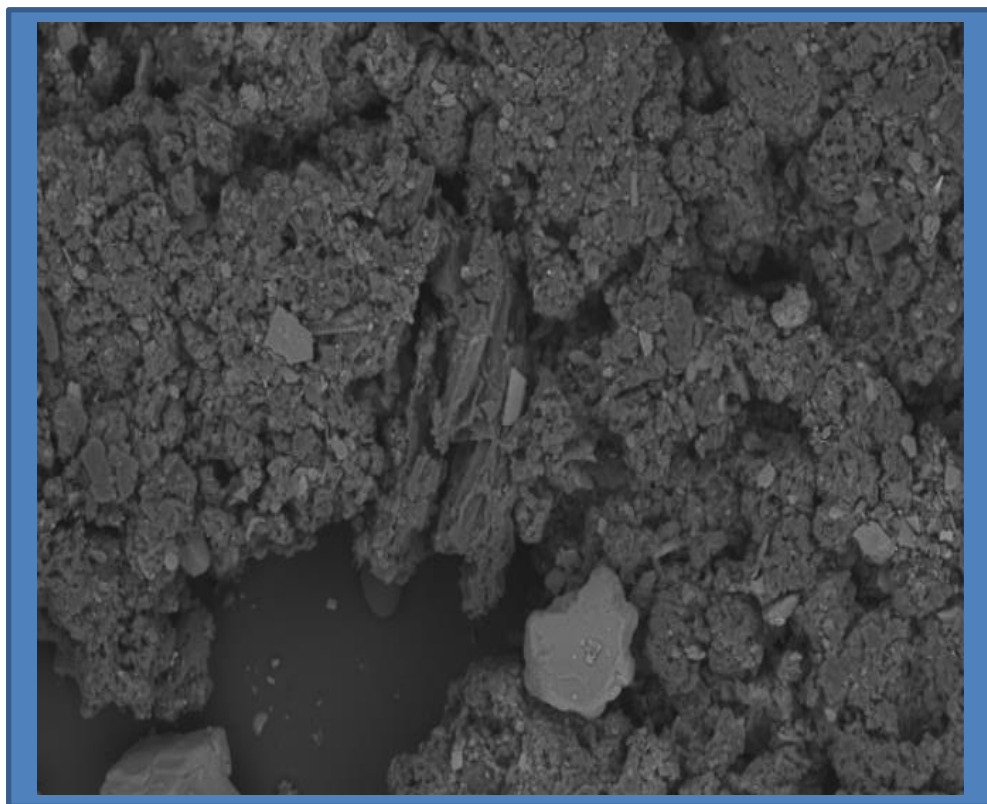


Figure 101. Backscattered electron image (above) and elemental map (below) of NE4_T (left) and NE4-b1 (right) F4 fraction samples

3.3.5.6 Mobility Experiments using Needle's Eye topsoil

3.3.5.6.1 Sorption Experiments

The sorption of ^{226}Ra onto NE4_T soil, using ^{226}Ra spiked eqH₂O, was investigated and the results obtained are shown in Table 31.

Table 31. Sorption results of the first set of binary experiments

Sample	Average R_d ($\text{cm}^3 \text{g}^{-1}$)	Std R_d ($\text{cm}^3 \text{g}^{-1}$)
1	131.96	28.47
2	352.70	173.36
3	444.97	206.06
4	444.42	181.76
5	532.23	164.23

The results are presented in Table 31 and show that the distribution ratio values for ^{226}Ra sorption are similar for the three replicates. In addition, the results show that with increasing concentration of the carrier (BaCl_2) the distribution ratio of ^{226}Ra is decreases (Figure 102).

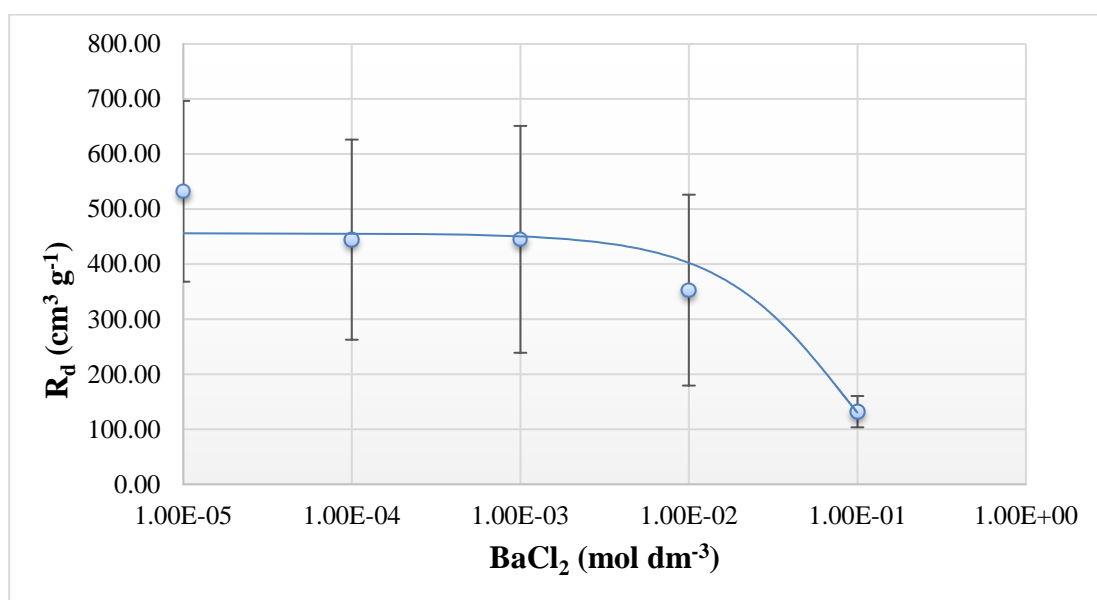


Figure 102. ^{226}Ra sorption to NE4_T using BaCl_2 as a carrier in eqH₂O

Sorption of ^{226}Ra on the solid (NE4_T) was reported as well for concentrations of carrier higher than 0.1 mol dm^{-3} . Finally, Figure 103 shows that R_{d1} value for the first set of binary experiments is $158.3 \text{ cm}^3 \text{ g}^{-1}$.

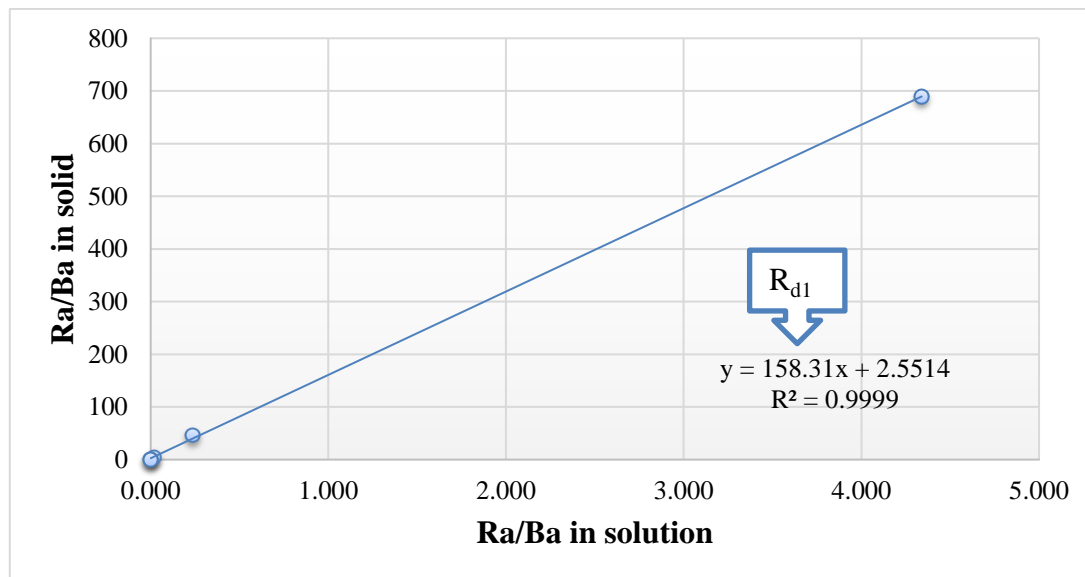


Figure 103. R_{d1} value for the first set of binary experiments

The results obtained from the sorption of ^{226}Ra onto NE4_T soil with ^{226}Ra spiked dH_2O were shown in Table 32.

The results in Table 32 show that amongst the replicates A, B and C the distribution ratio values for ^{226}Ra sorption are similar. In addition, with increasing concentration of the carrier (BaCl_2) the distribution ratio of ^{226}Ra is decreasing (Figure 104).

Table 32. Sorption results of the second set of binary experiments

Sample	Average R_d ($\text{cm}^3 \text{ g}^{-1}$)	Std R_d ($\text{cm}^3 \text{ g}^{-1}$)
1	124.70	39.34
2	227.98	14.42
3	280.97	44.50
4	378.39	19.72
5	353.65	52.65

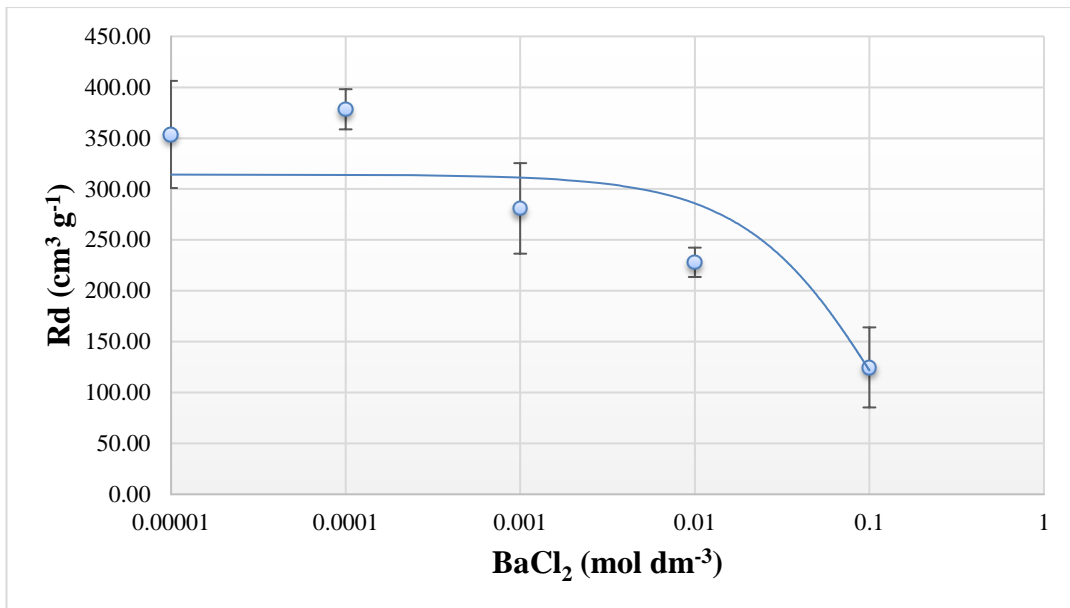


Figure 104. ²²⁶Ra sorption to NE4_T using BaCl₂ as a carrier in dH₂O

Figure 105 shows that the R_d value for ²²⁶Ra decreases as the concentration of BaCl₂ increases. Sorption of ²²⁶Ra on the solid (NE4_T) was reported as well for concentrations of carrier higher than 0.1 mol dm⁻³. Finally, Figure 104 shows that R_{d2} value for the second set of binary experiments is 177.8 cm³ g⁻¹.

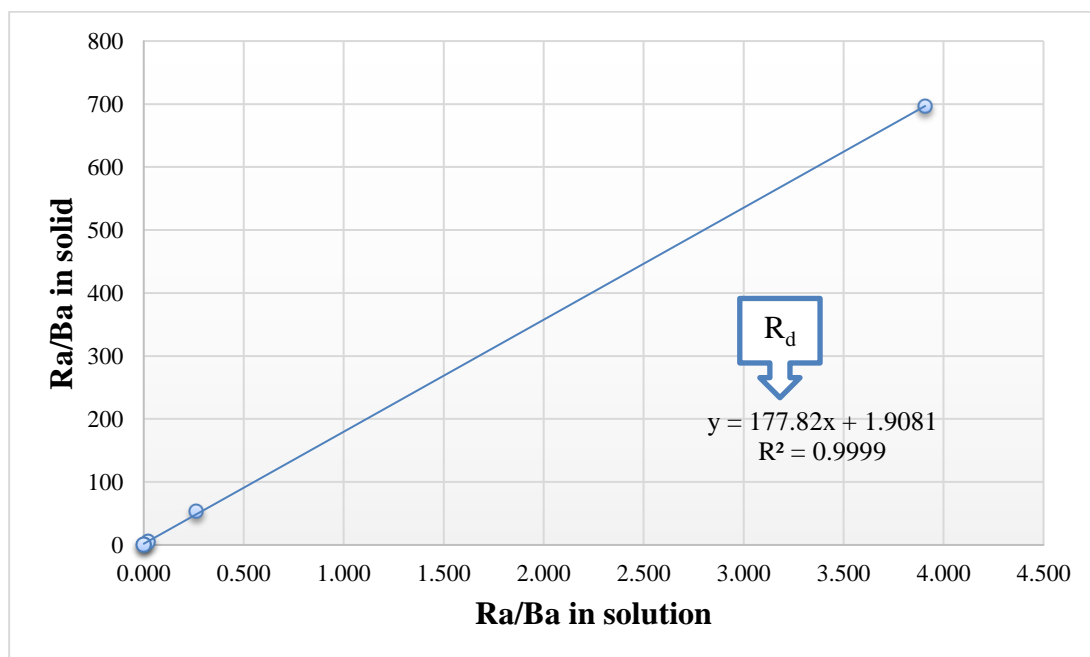


Figure 105. R_{d2} value for the second set of binary experiments

The sorption of ^{226}Ra onto prewashed NE4_T soil with ^{226}Ra spiked dH₂O was investigated and the results obtained are shown in Table 33.

Table 33. Sorption results of the third set of binary experiment

Sample	Average R_d ($\text{cm}^3 \text{g}^{-1}$)	Std R_d ($\text{cm}^3 \text{g}^{-1}$)
1	117.64	16.49
2	217.05	44.50
3	209.50	19.53
4	250.12	79.92
5	293.16	73.51

Figure 106 below shows that the R_d value for ^{226}Ra decreases as the concentration of BaCl_2 increases. Sorption of ^{226}Ra on the solid (NE4_T) was reported as well for concentrations of barium chloride higher than 0.1 mol dm^{-3} . Figure 107 shows that R_{d3} value for the first set of binary experiments is $180.1 \text{ cm}^3 \text{g}^{-1}$.

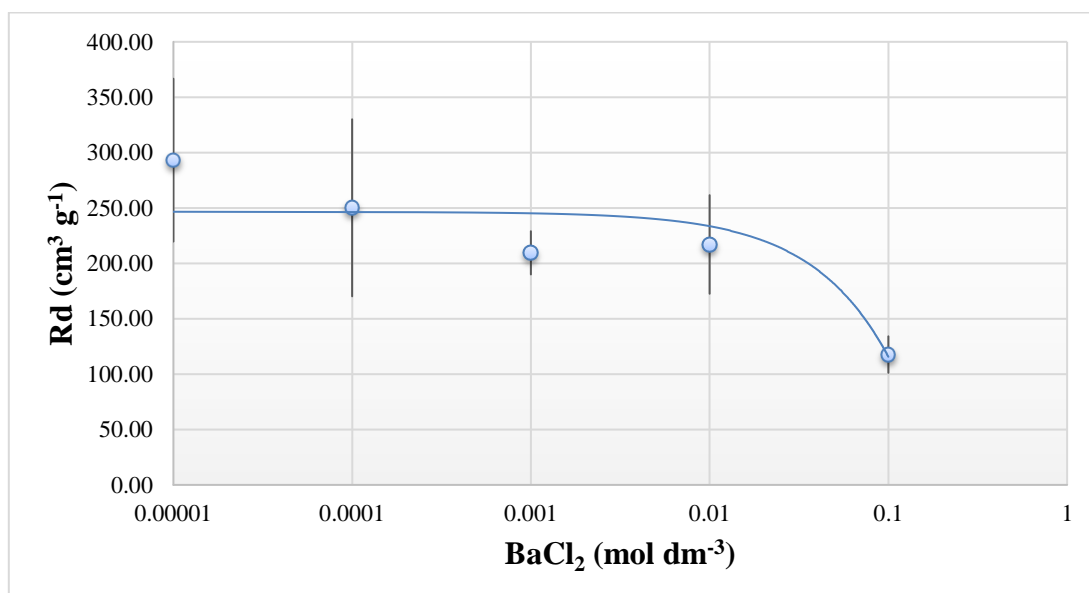


Figure 106. ^{226}Ra sorption to pNE4_T using BaCl_2 as a carrier in dH₂O

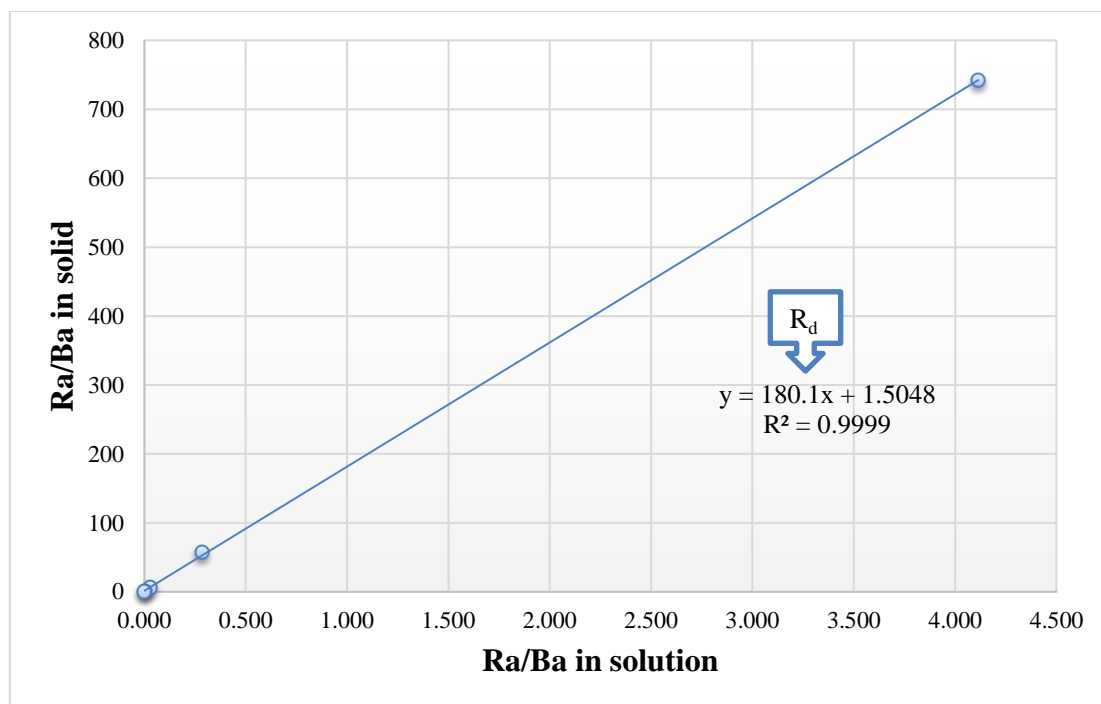


Figure 107. R_d value for the third set of binary experiments

Comparing the findings of all three binary experiments it may be concluded that the distribution ratio values were similar (158.3, 177.8 and 180.1 $\text{cm}^3 \text{g}^{-1}$). The three sets of binary experiments were designed to investigate radium behaviour (i.e. sorption) in a system with excess presence of soluble organic matter (i.e. organic matter contained in the topsoil and organic matter in the equilibrated water), in a system where organic matter is present only in the topsoil that was used, and in a system where the majority of soluble organic matter present in topsoil was removed prior to the experiment. Amongst the three scenarios used in this work the distribution ratio values increased as the available organic matter in aqueous solution decreased (Figure 108).

Table 34 below, presents a comparison of the distribution ratios measured in the present work with the distribution ratios reported in the literature. It should be noted that the literature confuses the distribution coefficient (K_d) with the distribution ratio (R_d). The distribution ratio (R_d) on a soil is defined as the amount of radionuclide or trace metal sorbed per unit mass of the soil solid phase divided by the analytical concentration of the radionuclide or metal in aqueous solution. While the distribution coefficient is a thermodynamic coefficient that is dependent on different thermodynamic properties of a system, the distribution ratio as the name implies is merely an expression relating the quantities of solute adsorbed to that left in solution after equilibrium is reached and is only relevant to the conditions it was measured in.

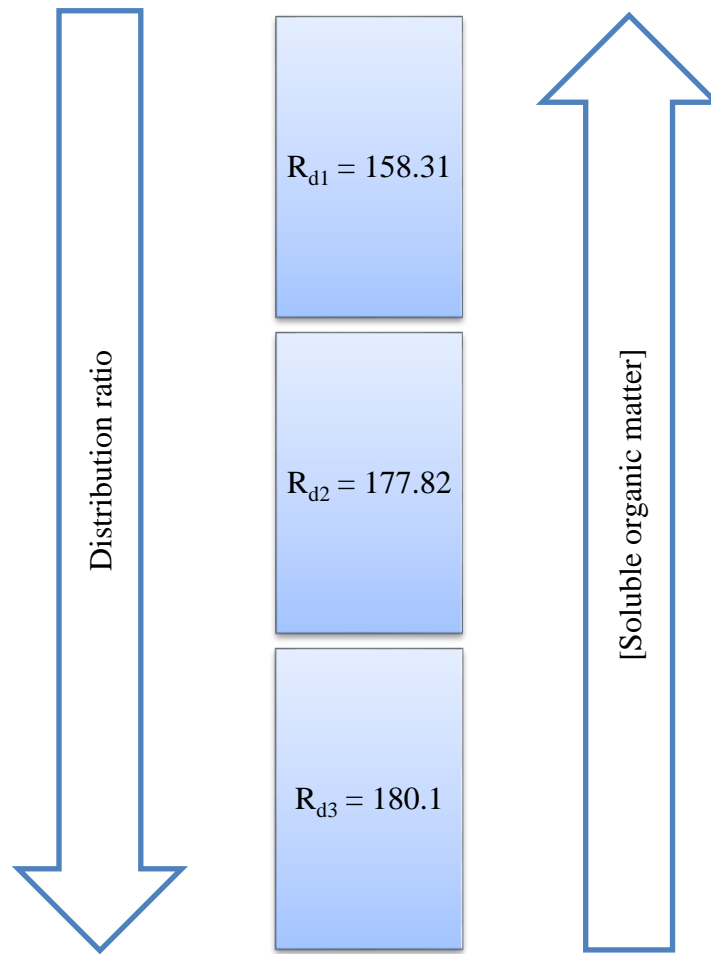


Figure 108. Comparison of distribution ratio values in the present work

Table 34 shows that the levels of ^{226}Ra distribution ratios measured in the present work are significantly less than the values found in the literature. The Table also shows that the mobility of ^{226}Ra in soils with significant amount of organic matter (i.e. soluble) is considerably less compared to the mobility as reported in mediums or materials such as sand, loam, clay, bentonite, illite, other organic groups etc.

Table 34. Comparison of distribution ratio values in the present work with the literature

Source	R _d or K _d	Units	Type of soil/material
Present work R _{d1}	158.31	cm ³ g ⁻¹	Organic rich soil
Present work R _{d2}	177.82	cm ³ g ⁻¹	Organic rich soil
Present work R _{d3}	180.1	cm ³ g ⁻¹	Organic rich soil
Langmuir ¹⁶¹	2,900	mL g ⁻¹	pH 7.58, Kaolinite
Sheppard ¹⁶² et al.	47	L kg ⁻¹	Soil
Sheppard and Thibault ¹⁶³	490	L kg ⁻¹	Sand
	36		Loam
	9,000		Clay
	2,400		Organic groups
IAEA ² and Vandenhove ¹⁶⁴ et al.	49 – 40,000	L kg ⁻¹	Sand
	12 – 120,000		Loam
	696 – 950,000		Clay
	785 - 1890		Unspecified
Ames ¹⁶⁵ et al.	500	mL g ⁻¹	25 ⁰ C, Kaolinite
Tachi ¹⁶⁶ et al.	100 – 10,000	mL g ⁻¹	Bentonite
Ames ¹⁶⁷ et al.	3,800	cm ³ g ⁻¹	25 ⁰ C, Smectites
Ames ¹⁶⁸ et al.	8,500	mL g ⁻¹	25 ⁰ C, Illite
Ames ¹⁶⁹ et al.	3,000	mL g ⁻¹	25 ⁰ C, Fe oxyhydroxides
Haji-Djafari ¹⁷⁰ et al.	12 - 100	L kg ⁻¹	pH 4.5 and 7, respectively, soil

3.3.5.6.2 ²²⁶Ra mobility through top soil in column experiments

The porosity of the top soil sample was measured by using tritiated water (HTO). HTO was passed through the column with a flowrate of about 1 cm³ h⁻¹. In total 33 x 0.5 cm³ HTO fractions were collected and analysed by liquid scintillation counting by using a counting window between 2 and 18 keV. The results are shown in Figure 109.

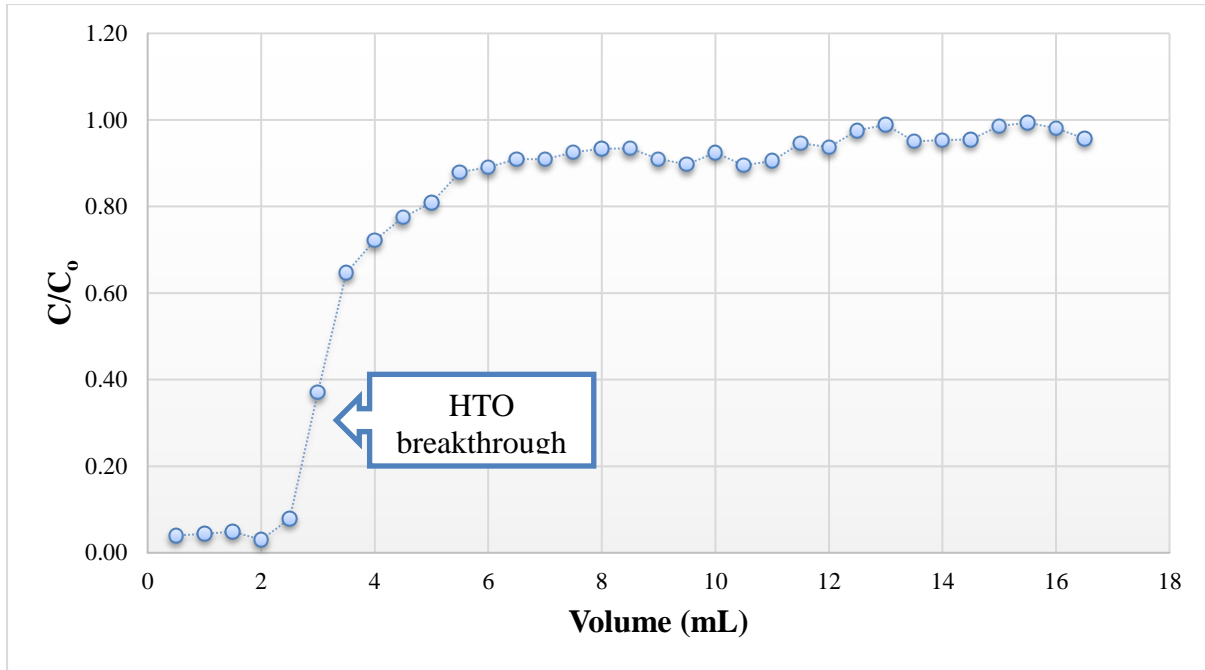


Figure 109. HTO mobility through NE4_T, C₀ = tritium column input concentration and C = tritium column output concentration

Porosity (ϕ) is defined as the fraction of void space in the fraction of the material that may be occupied by water. It is defined by the ratio (Equation 34):

$$\phi = V_v / V_T \quad \text{Equation 19}$$

Where V_v is the volume of the void/space and V_T is the total or bulk volume of material, including the solid and void components. The value of ϕ can be between 0 and 1, or 0 to 100%. In the present experiment, ϕ depends on how the column was packed and is related with the breakthrough of HTO (Figure 108). The higher the ϕ value the more water a solid can hold. Please note that the porosity should not be confused with hydraulic conductivity.

The column used for this experiment was packed to a depth of 5 cm with NE4_T soil and was 1 cm diameter. Therefore, the total volume (V) of the sample was (Equation 35).

$$V = \pi r^2 h \quad \text{Equation 20}$$

$$V = 3.142 \times 0.5^2 \times 5 \Rightarrow V = 3.9275 \text{ cm}^3$$

The volume of the HTO breakthrough (V_v), as shown in Figure 119 is 2.5 cm³. Therefore,

$$\varphi = \frac{2.5}{3.9275} * 100 = 63.6 \%$$

Subsequently, an experiment was designed to determine the mobility and the distribution ratio (R_d) of ^{226}Ra in the column. The point of this experiment was to try to reproduce environmental conditions as much as possible and to answer the question as to whether ^{226}Ra is mobile or not in these conditions. The results from the binary experiments suggested that ^{226}Ra was not mobile and the column experiment was used to confirm this or not. A ^{226}Ra standard solution was passed through the column. The HTO elutions showed that most of the HTO comes out after 10 mL of elution and therefore a total of 20 mL passing through the column was sufficient to know whether the radium would be eluted from the column. The results are shown in Figure 110 suggest that ^{226}Ra is not mobile under these conditions.

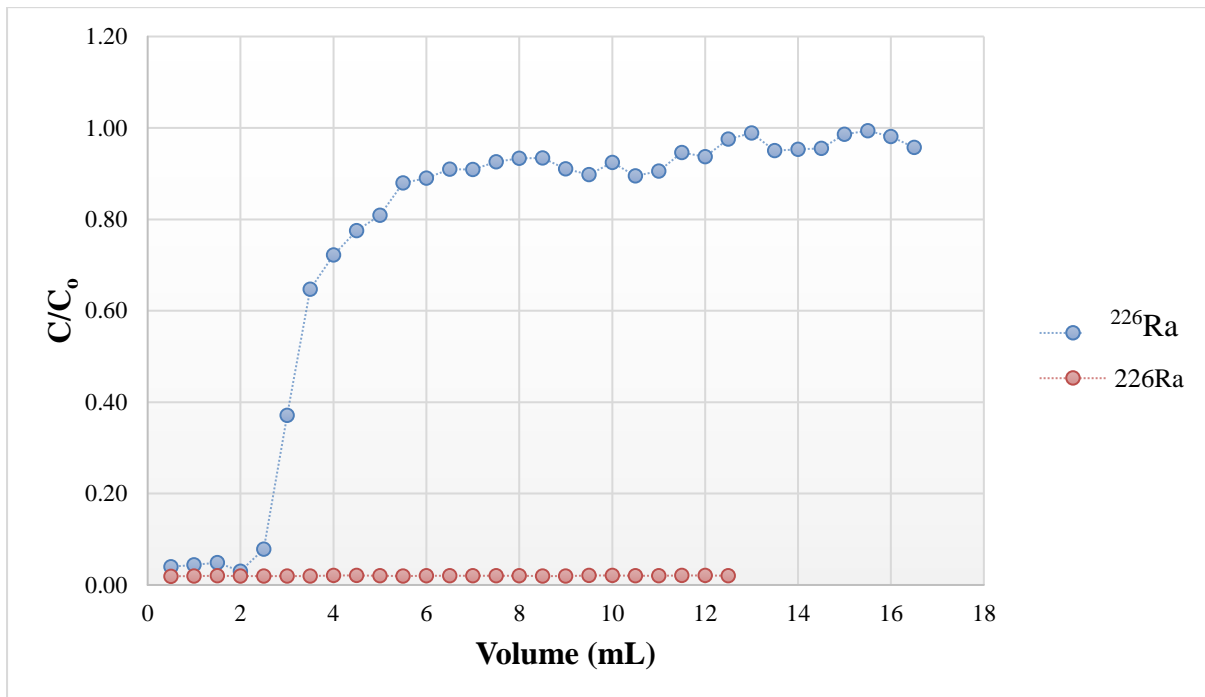


Figure 110. HTO and ^{226}Ra mobility through NE4T

To summarise, the gamma spectrometry measurements on the soil samples from Needle's Eye showed that equilibrium between ^{226}Ra and the two progenies (^{214}Bi and ^{214}Pb) was not reached, despite long collection times due to loss of radon gas from the experimental container. The UV - Vis analysis of samples generated by creating equilibrated water from the samples and altering the pH, suggests that the NOM that is present in the Needle's Eye soil samples is

predominantly in order of likelihood humin, fulvic and humic acid. The characterisation of topsoil from the organic rich location of the site showed significant activity concentration of radium ($\sim 30 \times 10^2 \text{ Bq kg}^{-1}$). Loss on ignition treatment (500 and 1000 °C) on the topsoil recorded mass loss of about 86 %, and further CHN analysis reported a strong presence of carbon ($\sim 41 \%$) suggesting that about half of the mass loss that recorded during loss on ignition is associated with carbon and the rest possibly with carbonate and the breakdown of hydrated minerals. The results of the sequential extractions showed that radium is not associated with a single fraction, and approximately a combined 80 % of radium is split between the carbonate, iron / manganese oxides and organic fractions. PXRD analysis successfully identified quartz, muscovite and chlorite phases in the bulk samples. PXRD for the samples after LoI at 500°C showed the presence of carbonate mineral phases, such as, calcite and sulfate containing anhydrite phases, whereas, PXRD analysis after heating the samples at 1000°C to indicated prominent phases are anhydrite, gehlenite, quartz and magnesioferrite. PXRD analysis supported by XRF elemental analysis, which showed elevated concentrations for calcium, suggesting also the presence of anhydrite, as well as calcite after the carbonate fraction of sequential extraction stage. The sorption experiments showed reported distribution ratios for radium to vary between 158.3- and 180.1-mL g^{-1} suggesting that radium is not mobile under these conditions. Finally, the column experiments in an effort to duplicate the environmental conditions of the Needle's Eye site showed that radium was not detected passing through the column and therefore it was concluded that is not mobile under these conditions.

Chapter 4. Conclusions

Chapter 4. Conclusions

Initial work was carried out at Needle's Eye natural analogue site in September 2014 in order to determine physicochemical and radiochemical imprint of the site and produce an initial characterisation of the site. The presence of ^{226}Ra has been shown to concentrate in the region close to the uraninite vein where the land is organic rich and saturated with water due to tidal flooding. Activity concentrations for ^{226}Ra at Needle's Eye site exceed the average reported levels of ^{226}Ra worldwide in the literature. The soil samples were characterised as silt type soils according to their measured particle size. That suggested that mainly clay minerals should be reported for Needle's Eye site by XRD analyses. The Needle's Eye site can be undoubtedly characterised as a highly - disturbed site by the human activity (arbitrary intense sampling) and therefore a second visit on the site was necessary in order to improve the quality of the samples and the sampling techniques in order to make conclusions about the research area.

The analysis of both bulk and different soil fraction samples from the second and third visit showed that the activity concentration of ^{226}Ra was higher compared to the activity concentration of ^{226}Ra in the samples (disturbed samples) from the first visit. The activity ratio of ^{226}Ra and ^{238}U showed that no correlation between ^{226}Ra and ^{238}U was found and therefore the two radionuclides are not in equilibrium. The results suggest that ^{238}U and ^{226}Ra fractionate in a different way due to the weathering of the metalliferous vein and the presence of materials which partition the species differently. ^{238}U is soluble (as reported in the literature) and the higher concentrations of ^{238}U were found in the samples located in and by the stream, whereas the behaviour of ^{226}Ra was found to be exactly the opposite.

Initially, the LoI (1000 °C) analysis showed that there is potentially a correlation between ^{226}Ra and NOM. This association of ^{226}Ra with NOM suggests that the NOM might be the reason for disturbing ^{226}Ra mobility. The UV-Visible analysis suggests that the soluble organic matter that is present in the Needle's Eye soil samples is predominantly humin, and secondary fulvic and humic acid.

The PXRD analysis supported the soil texture analysis that was conducted for the soil samples from the first visit on the site, which characterised the soil type as clay, as the mineral phases that were identified in the soil samples from the second and third visit on the site are: quartz

(SiO₂), muscovite (KAl₂(AlSi₃O₁₀)(F,OH)₂) and chlorite (Mg,Al)₆(Si,Al)₄O₁₀(OH)₈, as well as poorly crystalline feldspar phases as inorganic components of the soil samples taken from Needle's Eye due to the large proportion of organic matter in the soil. The presence of aluminosilicate mineral phases in the soil samples was supported as well by the elemental content that was carried out using ICP – OES analysis for aluminium and silica.

Investigation of topsoil was conducted in order to determine the potential mobility of ²²⁶Ra for the Needle's Eye site, as well as, to determine the mineral phases in which ²²⁶Ra appears to be sorbed. LoI treatment at 500 and 1000 °C treatment on the topsoil (NE4_T) showed that natural organic is more than 86 %, further CHN analysis reported a strong presence of carbon (~ 40.0 %) suggesting that the remaining 46 % may be associated with carbonate and the breakdown of hydrated minerals.

Sequential extractions were carried out on topsoil (NE4_T) and deeper soil (NE4-b1) to examine the potential association of ²²⁶Ra with exchangeable, carbonate, Fe/Mn Oxides, organic, and insoluble fractions. The results obtained from the sequential extractions suggest that ²²⁶Ra is mainly distributed and associated with the carbonate, Fe/Mn Oxides, organic material, and silicates and sulfates. This hypothesis was well supported by the geology of the site, as described in the literature, and the PXRD analysis, for both bulk topsoil and deeper soil samples (and the sequential extraction residual products), which identified the mineral phases of quartz, sodium chloride, anhydrite, calcite, and poorly crystalline mixed minerals of carbonate metals.

Sorption experiments onto topsoil (NE4_T) were investigated with binary experiments in three different systems (²²⁶Ra spiked equilibrated water (eqH₂O) - NE4_T, 2) ²²⁶Ra spiked demineralised water (dH₂O) - NE4_T, and 3) ²²⁶Ra spiked demineralised water (dH₂O) – prewashed NE4_T). The distribution ratio values varied from 158.3 to 180.1 cm³ g⁻¹ which is significantly lower than the values reported in the literature and suggest that ²²⁶Ra is not mobile in the Needle's Eye site.

Static batch experiments have been used to investigate further the potential mobility of ²²⁶Ra onto topsoil from the Needle's Eye site. In addition, column experiments were designed to duplicate, as much as possible, the environmental conditions of the site. The results from the column experiment confirmed that ²²⁶Ra is not mobile in these conditions, as no detectable concentration was detected in the effluent fractions that were eluted from the column.

Chapter 5. Further Work

Chapter 5. Further Work

5.1 $^{238}\text{U}/^{226}\text{Ra}$ Equilibrium – Disequilibrium

^{226}Ra is a progeny of ^{238}U which is at the head of the ^{238}U decay chain. Of interest is to determine whether uranium and radium have similar mobilities through the surface soils at Needle's Eye. If they have similar mobilities then uranium should be in equilibrium with radium in the soil but, if not, they should be in disequilibrium. Gamma ray spectrometry showed that ^{226}Ra activity was found to be 30.8 Bq (average value of 1 gram of NE4_T) and XRF showed ^{238}U to be equal to 0.25422 percent in NE4_T. Calculation of the activity of ^{238}U in 1 gram of NE4_T gives an activity of 31.42 Bq which is similar to that of ^{226}Ra . These measurements and calculations suggest that both isotopes are in equilibrium in this soil. Additional measurements are required to determine whether ^{238}U and ^{226}Ra are in equilibrium in different soil samples taken from different locations in the Needle's Eye site,

5.2 Binary – Ternary systems

The mobility of radium through surface environments is heavily dependent on the interaction of aqueous radium with materials which make up the surface environment. Transport models require quantitative data on these interactions so in order to gain these data, sorption from radium in solution on clay or on organic material (defined as a binary system) and the sorption of radium in solution on clay in the presence of organic material (defined as a ternary system) should be studied and radium sorption measurements taken.

Bibliography

1. Basham, I. ., Milodowski, A. ., Hyslop, E. . & Pearce, J. The location of uranium in source rocks and sites of secondary deposition at the Needle's Eye natural analogue site, Dumfries and Galloway. BGS Technical Report WE/89/56, 54 p (1989).
2. International Atomic Energy Agency (IAEA). The environmental behaviour of radium: revised edition. Tech. Reports Ser. No. 476 44–51 (2014). doi:10.1016/0883-2927(92)90073-C
3. C.M. Lederer; J.M. Hollander; I. Perlman (1968). Table of Isotopes (6th ed.). New York: John Wiley & Sons.
4. National Nuclear Data Center. at <<http://www.nndc.bnl.gov/>> (date accessed 06/10/1983).
5. Tomar, B. S. et al. Gamma Ray Spectroscopy. Dict. Gems Gemol. 98, 179 (2002).
6. Gilmore, G. Practical Gamma-ray Spectroscopy. Wiley. ISBN: 978-0-470-86196-7 (2011).
7. Turnbull R. Granite and Grit: A Walker's Guide to the Geology of British Mountains. Scottish Journal of Geology, 48, 147-151, 2 November 2012, <https://doi.org/10.1144/sjg2012-459>.
8. Miller, J.M., Taylor, K. (1966) Uranium mineralization near Dalbeattie, Kirkcudbrightshire. Bull. Geol. Surv. Gr. Brit. 25:1–18
9. Nenadović, S., Nenadović M., Kljajević L., Vukanac I., Poznanović M., Mihajlović-Radosavljević A., Pavlović V. Vertical distribution of natural radionuclides in soil: Assessment of external exposure of population in cultivated and undisturbed areas. Sci. Total Environ. 429, 309–316 (2012).
10. UNSCEAR. Sources and Effects of Ionizing Radiation. United Nations Scientific Committee on the Effects of Atomic Radiation (1993). at <<http://www.unscear.org/unscear/en/publications/1993.html>>
11. UNSCEAR. Sources and Effects of Ionizing Radiation, United Nations Scientific Committee on the Effects of Atomic Radiation UNSCEAR 2000 Report to the General Assembly, with Scientific Annexes. UNSCEAR 2000 Report I, (2000).
12. Pérez-Moreno, S. M., Gázquez, M. J., Pérez-López, R. & Bolivar, J. P. Validation of the BCR sequential extraction procedure for natural radionuclides. Chemosphere 198, 397–408 (2018).
13. Ames, L. L., Mcgarrah, J. E. & Battelle, B. A. W. Sorption of trace constituents from

- aqueous solutions onto secondary minerals. i. uranium. *Clays and Clay Miner* 31, (1983).
14. Zagorodni, A. *Ion exchange materials: Properties and applications*. Elsevier, Amsterdam (2006).
 15. Kaolinite, I. I., Benes, M. P., Borovec, Z. & Strejc, P. Interaction of radium with freshwater sediments and their mineral components. *J. Radioanal. Nucl. Chem.* 89, (1985).
 16. Benes, P., Strejc, P. & Lukavec, Z. Interaction of radium with freshwater sediments and their mineral components. i. ferric hydroxide and quartz. *J. Radioanal. Nucl. Chem.* 82, (1984).
 17. Drits, V. A., Zviagina, B. B., Mccarty, D. K. & Salyn, A. L. Factors responsible for crystal-chemical variations in the solid solutions from illite to aluminoceladonite and from glauconite to celadonite. *Am. Mineral.* 95, 348–361 (2010).
 18. Early, J.W., Osthaus, B. B., and Milne, I. H. Purification and properties of montmorillonite. *Am. Mineral.* 38, 707-724 (1953).
 19. S.K. Haldar, Josip Tišljarić, Chapter 2 - Basic Mineralogy, Editor(s): S.K. Haldar, Josip Tišljarić, *Introduction to Mineralogy and Petrology*, Elsevier, 2014, pp 39-79, ISBN 9780124081338, doi.org/10.1016/B978-0-12-408133-8.00002-X.
 20. Beyer C. *Applied numerical modeling of saturated / unsaturated flow and reactive contaminant transport: evaluation of site investigation strategies and assessment of environmental impact*. PhD Thesis, GeoHydrology and HydroInformatics, Center for Applied Geosciences, Tuebingen University (2007).
 21. A. Viani, A. F. Gualtieri, A. G. A. The nature of disorder in montmorillonite by simulation of X-ray powder patterns. *Am. Mineral.* 87, 966–975 (2002).
 22. Malmström, M. & Banwart, S. Biotite dissolution at 25°C: The pH dependence of dissolution rate and stoichiometry. *Geochim. Cosmochim. Acta* 61, 2779–2799 (1997).
 23. Carmichael, I. S. E., Turner, F. J. & Verhoogen, J. *Igneous petrology*. McGraw-Hill. (1974).
 24. Piggot C.S. Radium in rocks, V; the radium content of the four groups of pre-Cambrian granites of Finland. *Am. J. Sci.* 35-A: 227-229. (1938).
 25. Brigatti, M. F. & Davoli, P. Crystal-structure refinements of IM plutonic biotites. *Am. Mineral.* 75, 305–313 (1990).
 26. Blatt, H., Tracy, R. J. & Ehlers, E. G. *Petrology: igneous, sedimentary, and metamorphic*. W.H. Freeman (1996).

27. Radoslovich E.W. Feldspar Minerals. In: Giesecking J.E. (eds) Soil Components. Springer, Berlin, Heidelberg (1975).
28. Anderson, R. S. & Anderson, S. P. Geomorphology: The Mechanics and Chemistry of Landscapes. Cambridge University Press (2010).
29. Velde, Bruce B., Meunier, Alain. The Origin of Clay Minerals in Soils and Weathered Rocks. Springer (2008). ISBN 978-3-540-75634-7.
30. Henlow, E. The anorthoclase structures: the effects of temperature and composition. *Am. Mineral.* 67, 975-996, (1982).
31. Paige, C. R., Kornicker, W. A., Hileman, O. E. & Snodgrass, W. J. Kinetics of desorption of ions from quartz and mica surfaces. *J. Radioanal. Nucl. Chem.* 159 (1992).
32. Anderson, R. S. & Anderson, S. P. Geomorphology: The Mechanics and Chemistry of Landscapes. Cambridge University Press (2010).
33. Levien, L., Prewir, C. T. & Weidner, D. J. Structure and elastic properties of quartz at pressure. *Am. Mineral.* 65, (1980).
34. Hoehler, T. M. & Jørgensen, B. B. Microbial life under extreme energy limitation. *Nat. Rev. Microbiol.* 11, 83–94 (2013).
35. Usman, A. R. A., Kuzyakov, Y. & Stahr, K. Dynamics of organic C mineralization and the mobile fraction of heavy metals in a calcareous soil incubated with organic wastes. *Water, Air, Soil Pollut.* 158, 401–418 (2004).
36. Kuzyakov, Y. Priming effects: Interactions between living and dead organic matter. *Soil Biol. Biochem.* 42, 1363–1371 (2010).
37. Nathwani J. S & Phillips C. R. Adsorption of ^{226}Ra by soils in the presence of Ca^{2+} ions. Specific adsorption (II), *Chemosphere*, Volume 8, Issue 5, pp 293-299, ISSN 0045-6535, doi.org/10.1016/0045-6535(79)90112-7 (1979).
38. Edsfeldt, C. The radium distribution in some swedish soils and its effect on radon emanation. Doctoral thesis. KTH, Superseded Departments, Civil and Environmental Engineering. ISBN: 91-7283-150-2 (2001).
39. Gomes de Melo, A. B., Lopes-Motta, F., Andrade-Santana, M. A. Humic acids: Structural properties and multiple functionalities for novel technological developments, *Materials Science and Engineering: C*, Volume 62. pp 967-974. ISSN 0928-4931. doi.org/10.1016/j.msec.2015.12.001 (2016).
40. Doerner H. A., & Hoskins Wm., M. Co-precipitation of radium and barium sulfates. *J. Am. Chem. Soc.* 1925 47 (3), 662-675. DOI: 10.1021/ja01680a010.
41. Klinkenberg, M., Brandt, F., Breuer, U. & Bosbach, D. Uptake of radium during the

- recrystallization of barite: A microscopic and time of flight-secondary ion mass spectrometry study. *Environ. Sci. Technol.* 48, 6620–6627 (2014).
42. Langmuir, D. & Melchior, D. The geochemistry of Ca, Sr, Ba and Ra sulfates in some deep brines from the Palo Duro Basin, Texas. *Geochim. Cosmochim. Acta* 49, 2423–2432 (1985).
 43. Yoshida, Y., Nakazawa, T., Yoshikawa, H. & Nakanishi, T. Partition coefficient of radium in gypsum. *J. Radioanal. Nucl. Chem.* 280, 541–545 (2009).
 44. Andrews, J. N., Davis, S. N., Fabryka-Martin, J., Fontes, J-Ch., Lehmann, B. E., Loosli, Michelot, H.H., Moser, J-L., Smith, H., Wolf, M. The in situ production of radioisotopes in rock matrices with particular reference to the Stripa granite. *Geochim. Cosmochim. Acta* 53, 1803–1815 (1989).
 45. Witherspoon, P. A., Nelson, P., Doe, T., Thorpe, R., Paulsson, B., Gale, J., Forster, C. Rock characterization for storage of nuclear waste in granite. *IEEE Transactions on Nuclear Science*, vol. 27, no. 4, pp. 1280-1290, Aug. 1980. doi: 10.1109/TNS.1980.4331008 .
 46. British Geological Survey (BGS) <<https://www.bgs.ac.uk/>>
 47. Schmidt, S. & Cochran, J. K. Radium and radium-daughter nuclides in carbonates: A brief overview of strategies for determining chronologies. *J. Environ. Radioact.* 101, 530–537 (2010).
 48. Jones, M. J., Butchins, L. J., Charnock, J. M., Patrick, R. A. D., Small, J. S., Vaughan, D. J., Wincott, P. L., Livens, F. R. Reactions of radium and barium with the surfaces of carbonate minerals. *Appl. Geochem.* 2011; Vol. 26, No. 7. pp. 1231-1238.
 49. Landa, E. R. Uranium mill tailings: nuclear waste and natural laboratory for geochemical and radioecological investigations. *J. Environ. Radioact.* 77, 1–27 (2004).
 50. Anderson, H.L., Arthur, S.E., Brady, P.V., Cygan, R.T., Nagy, K.L., & Westrich, H.R. Irreversible Sorption of Contaminants During Ferrihydrite Transformation (SAND--99-1275C). United States (1999).
 51. Beneš, P. Physico-chemical forms and migration in continental waters of radium from uranium mining and milling. *Environ. Migr. long-lived radionuclides Proc. an Int. Symp. Migr. Terr. Environ. long-lived radionuclides from Nucl. fuel cycle* 3–23 (1982).
 52. Tomita, J., Zhang, J. & Yamamoto, M. Radium isotopes (^{226}Ra and ^{228}Ra) in Na-Cl type groundwaters from Tohoku District (Aomori, Akita and Yamagata Prefectures) in Japan. *J. Environ. Radioact.* 137, 204–212 (2014).
 53. Kreitler, C. W. et al. Patterns and variability of groundwater flow and radium activity at

- the coast: A case study from Waquoit Bay, Massachusetts. *J. Environ. Radioact.* 156, 49–61 (2012).
54. Ryon, A. D., Hurst, F. J., and Seeley, F. G. Nitric acid leaching of radium and other significant radionuclides from uranium ores and tailings. United States: N. p., 1977. doi:10.2172/7219223.
 55. Chen, M. A. & Kocar, B. D. Radium Sorption to iron hydroxides, pyrite, and montmorillonite: Implications for mobility. (2018). doi:10.1021/acs.est.7b05443.
 56. Bassot, S., Mallet, C. & Stammose, D. Experimental Study and Modeling of the Radium Sorption onto Goethite. *MRS Proc.* 663, 1081 (2000).
 57. Bassot, S., Stammose, D., Mallet, C., Lefebvre, C., & Ferreux, J.-M. Study of the radium sorption/desorption on goethite. *IRPA-10 Proceedings of the 10th international congress of the International Radiation Protection Association on harmonization of radiation, human life and the ecosystem*, (p. 1v). Japan: Japan Health Physics Society (2000).
 58. Mott, H. V., Singh, S. & Kondapally, V. R. Factors affecting radium removal using mixed iron-manganese oxides. *J. Am. Water Works Assoc.* 85, 114–121 (1993).
 59. Landa, E. R., Phillips, E. J. P. & Lovley, D. R. Release of ²²⁶Ra from uranium mill tailings by microbial Fe(III) reduction. *Appl. Geochem.* 6, 647–652 (1991).
 60. Mular, A. L., Barratt, D. J., Halbe, D. N. *Mineral Processing Plant Design, Practice, and Control (2 Volume Set) 1st Ed. Edition.* Society of mining, metallurgy and exploration, Inc, (SME) (2002).
 61. Laughlin, R. B. *In Situ Leach (ISL) Mining of Uranium.* World nuclear association. (2010).
 62. Enhanced, T. & Radioactive, N. O. Technologically Enhanced Naturally Occurring Radioactive Materials in the Southwestern Copper Belt of Arizona. *Environ. Prot.* (1999).
 63. *Environmental Remediation of Uranium Production Facilities A Joint Report by the OECD Nuclear Energy Agency and the International Atomic Energy Agency.* (2002).
 64. Jackson, M. L. *Soil Chemical Analysis*, Prentice-Hall, Inc. (1956).
 65. Shahul Hameed, P., Shaheed, K., Somasundaram, S. S. N. & Iyengar, M. A. R. Radium-226 levels in the Cauvery river ecosystem, India. *J. Biosci.* 225-231, (1997).
 66. Hylland K., Eriksen, D, O. Naturally occurring radioactive material (NORM) in North Sea produced water: environmental consequences. *Norsk Olje og Gass* (2013).
 67. Tsai, C. M. & Weng, P. S. Radium-226 concentrations in Taiwan hot spring and river waters. *Health Phys.* 24, 429–430 (1973).

68. Ali, K. K. & Ajina, A. R. Use of radium in studying water resources in Shanafiya-Samawa areas south Iraq. *Iraqi Journal of Science*, 2015, Vol 56, No.2C, pp: 1719-1727.
69. Kahn B1, Rosson R, Cantrell J. Analysis of ^{228}Ra and ^{226}Ra in public water supplies by a gamma-ray spectrometer. *Health Phys.* 1990 Jul;59(1):125-31.
70. Sheppard, S. C. Review of “Handbook of Parameter Values for the Prediction of Radionuclide Transfer in Terrestrial and Freshwater Environments”. *J. Environ. Radioact.* 102, 217 (2011).
71. Vasconcellos, L. M. H., Amaral, E. C. S., Vianna, M. E. & Penna Franca, E. Uptake of ^{226}Ra and ^{210}Pb by food crops cultivated in a region of high natural radioactivity in Brazil. *J. Environ. Radioact.* 5, (1987).
72. Urbina, I. Regulation Lax as Gas Wells’ Tainted Water Hits Rivers - The New York Times. *New York Times* (2011).
73. Michalik B., Chałupnik S, Skowronek J., Lebecka J., Guidelines for treatment of solid wastes with enhanced natural radioactivity in Polish coal industry 1995 Symposium on Radiation Protection Neighboring Counties in Central Europe, Slovenia, Portoro 1995, s. 145 - 149.
74. Moore, R. & Moore, W. S. Using the radium quartet for evaluating groundwater input and water exchange in salt marshes. *Geochim. Cosmochim. Acta* 60, 4645–4652 (1996).
75. Beck, A. J., Rapaglia, J. P., Cochran, J. K., Bokuniewicz, H. J. & Yang, S. Submarine groundwater discharge to Great South Bay, NY, estimated using Ra isotopes. (2007). doi:10.1016/j.marchem.2007.07.011
76. Moore, W. S., Blanton, J. O. & Joye, S. B. Estimates of flushing times, submarine groundwater discharge, and nutrient fluxes to Okatee Estuary, South Carolina. *J. Geophys. Res* 111, 9006 (2006).
77. Swarzenski, P. W., Reich, C., Kroeger, K. D. & Baskaran, M. Ra and Rn isotopes as natural tracers of submarine groundwater discharge in Tampa Bay, Florida. *Mar. Chem.* 104, 69–84 (2007).
78. Swarzenski, P. W., Orem, W. H., Mcpherson, B. F., Baskaran, M. & Wan, Y. Biogeochemical transport in the Loxahatchee River estuary, Florida: The role of submarine groundwater discharge. *Mar. Chem.* 101, 248–265 (2006).
79. Beck, A. J., Rapaglia, J. P., Cochran, J. K. & Bokuniewicz, H. J. Radium mass-balance in Jamaica Bay, NY: Evidence for a substantial flux of submarine groundwater. (2007). doi:10.1016/j.marchem.2007.03.008
80. Breier, J. A., Nidzieko, N., Monismith, S., Moore, W. & Paytan, A. Breier, J. A., N. et

- al. Tidally regulated chemical fluxes across the sediment-water interface in Elkhorn Slough, California: Evidence from a coupled geochemical and hydrodynamic approach. *Limnol. Oceanogr.*, 54(6), 2009, 1964–1980. *Limnol. Ocean.* 54, 1964–1980 (2009).
81. Young, M. B., Gonnee, M. E., Derek, F., Moore, W. S., Silveira, J. H., Paytan, A. Characterizing sources of groundwater to a tropical coastal lagoon in a karstic area using radium isotopes and water chemistry. (2007). doi:10.1016/j.marchem.2007.07.010
 82. Garcia-Solsona, E., Masque, R., Garcia-Orellana, J., Rapaglia, J., Beck, A., Cochran, J. K., Bokuniewicz, H., Zaggia, L., Collavini, F. Estimating submarine groundwater discharge around Isola La Cura, northern Venice Lagoon (Italy), by using the radium quartet. *Mar. Chem.* 109, 292–306 (2008).
 83. Hsieh, Y. T. et al. Using the radium quartet (Ra-228, Ra-226, Ra-224, and Ra-223) to estimate water mixing and radium inputs in Loch Etive, Scotland. 58, (2017).
 84. Technical reports series no 419. Extent of Environmental Contamination by Naturally Occurring Radioactive Material (NORM) and Technological Options for Mitigation. International Atomic Energy Agency (IAEA). Vienna, 2003.
 85. Dickson, B.L.. Radium in groundwater. The Environmental Behaviour of Radium, Vol. 1, Technical Reports Series No. Technical Reports Series No. 310, IAEA, Vienna (1990) 335–372
 86. Baraniak, L., Thieme, M., Bernhard, G. & Nitsche, H. Sorption behavior of radium on sandy and clayey sediments of the upper Saxon Elbe river valley. *J. Radioanal. Nucl. Chem.* 241, (1999).
 87. Martin, P. & Akber, R. A. Radium isotopes as indicators of adsorption-desorption interactions and barite formation in groundwater. *J. Environ. Radioact.* 46, 271–286 (1999).
 88. Pardue, J. H. & Guo, T. Z. Biogeochemistry of ²²⁶Ra in Contaminated Bottom Sediments and Oilfield Waste Pits. *J. Environ. Radioact.* 39, 239–253 (1998).
 89. Landa, E. R. & Gray, J. R. US Geological Survey research on the environmental fate of uranium mining and milling wastes. *Environ. Geol.* 26, 19–31 (1995).
 90. Beneg, P. & Strejc, P. Interaction of radium with freshwater sediments and their mineral components iv. waste water and riverbed sediments. *J. Radioanal. Nucl. Chem. Artic.* 99, 407–422 (1986).
 91. Understanding variation in partition coefficient, K_d , values Volume III: Review of geochemistry and available K_d values for americium, arsenic, curium, iodine, neptunium, radium, and technetium. (2004). United States Office of Air and Radiation

- EPA 402-R-04-002C Environmental Protection Agency (EPA).
92. Magil, J. & Galy, J. *Radioactivity Radionuclides Radiation*. Springer-Verlag (2005). doi:10.1007/b138236.
 93. Choppin, G., Liljenzin, J., Rydberg, J. & Ekberg, C. *Radiochemistry and Nuclear Chemistry*. Elsevier (2013).
 94. Jamet, P., Hooker, P. J., Schmitt, J. M., Ledoux, E. & Escalier Des Orres, P. Hydrogeochemical modelling of an active system of uranium fixation by organic soils and sediments (Needle's Eye, Scotland). *Miner. Depos.* 28, 66–76 (1993).
 95. Larsen, L. H., Prinz, M., Manson V. *Igneous and Metamorphic Geology*. Geological Society of America. ISBN: 9780813711157. <https://doi.org/10.1130/MEM115> (1969).
 96. Haq, B. U. & Schutter, S. R. A chronology of Paleozoic sea-level changes. *Science* 322, 64–8 (2008).
 97. Edryd Stephens, W., E. Whitley, J., F. Thirlwall, M. & Halliday, A. The Criffell zoned pluton: correlated behaviour of rare earth element abundances with isotopic systems. *Contributions to Mineralogy and Petrology* 89, (1985).
 98. Courrioux, G. Oblique diapirism: the criffell granodiorite/granite zoned pluton (southwest Scotland). *J. Struct. Geol.* 9, 313–330 (1987).
 99. Soil Survey Staff: *Soil Taxonomy: A Basic System of Soil Classification for Making and Interpreting Soil Surveys*, Agric. Handb. 436, 2nd Edn., US Dep. of Agric., Washington, DC, USA, 869 pp., (1999).
 100. Aslan, A., Karlstrom, K.E., Crossey, L.J., Kelley, S., Cole, R., Lazear, G., and Darling, A., 2010, Late Cenozoic evolution of the Colorado Rockies: Evidence for Neogene uplift and drainage integration, in Morgan, L.A., and Quane, S.L., eds., *Through the Generations: Geologic and Anthropogenic Field Excursions in the Rocky Mountains from Modern to Ancient: Geological Society of America Field Guide 18*, p. 21–54, doi:10.1130/2010.0018(02).
 101. Bucher, B. & Grapes, R. *Petrogenesis of Metamorphic Rocks*. Springer (2011). doi:10.1007/978-3-540-74169-5.
 102. Sahney, S. & Benton, M. J. Recovery from the most profound mass extinction of all time. *Proc. R. Soc. B.* 275, 759–65 (2008).
 103. Munnecke, A., Calner, M., Harper, D. A. T. & Servais, T. Ordovician and Silurian sea–water chemistry, sea level, and climate: A synopsis. *Palaeogeogr. Palaeoclimatol. Palaeoecol.* 296, 389–413 (2010).
 104. Read, D. et al. The migration of uranium into peat-rich soils at Broubster, Caithness,

- Scotland, U.K. *J. Contam. Hydrol.* 13, 291–308 (1993).
105. <https://e-rocks.com/item/raf220610/guilleminite-rutherfordine-cuprosklodowskite-pitchblende-digenite> (date accessed: 21/04/2018).
 106. Lockwood, J. G. & van Zinderen Bakker, E. M. The Antarctic Ice-Sheet: Regulator of Global Climates?: Review. *Geogr. J.* 145, 469 (1979).
 107. Augustin, L. et al. Eight glacial cycles from an Antarctic ice core. *Nature* 429, 623–8 (2004).
 108. Price, D. G. & De Freitas, M. H. *Engineering geology : principles and practice*. Springer (2008).
 109. Lisle, R. J. *Geological structures and maps*. Elsevier Butterworth-Heinemann Linacre House. ISBN: 0750657804 (2004).
 110. Parnell, J. The Mineralogy of Red Bed Uranium-Vanadium Mineralization in the Permo-Triassic of. Source: *Ir. J. Earth Sci.* 119-124., 9 (1988).
 111. Eakin, P. A. Isotopic and petrographic studies of uraniferous hydrocarbons from around the Irish Sea Basin. *J. Geol. Soc. London.* 146, 663–673 (1989).
 112. Fettes, D. J, Desmons, J., & Árkai, P. *Metamorphic rocks : a classification and glossary of terms : recommendations of the International Union of Geological Sciences Subcommittee on the Systematics of Metamorphic Rocks*. Cambridge: Cambridge University Press (2007).
 113. Kane, J. S. Reference samples for use in analytical geochemistry: their availability, preparation, and appropriate use. *J. Geochem. Explor.* Volume 44., Issues 1-3., pp. 37-63 (1992).
 114. Krasińska, M. & Krasiński, Z. A. in *European Bison*. Springer Berlin Heidelberg (2013). doi:10.1007/978-3-642-36555-3_14.
 115. Hendershot, W.H., Lalonde, H and Duquette, M. Ion Exchange and Exchangeable Exchangeable Cations. *Soil Sampling and Methods of Analysis*. CSSS. doi:10.1201/978142000 (2006).
 116. <https://earth.google.com/web/> (date accessed: 02/16/2018).
 117. Gardner, W.H. Water content. In *Methods of Soil Analysis, Part 1: Physical and Mineralogical Methods*, 2nd edn, Klute A (ed.). American Society of Agronomy, Soil Science Society of America: Madison, WI, USA; 493–544 (1986).
 118. Dann, S. E. *Reactions and Characterization of Solids*. Royal Society of Chemistry (2000).
 119. Moore, D. M. & Reynolds, R. C. *X-ray diffraction and the identification and analysis of*

- clay minerals. Oxford University Press (1997).
120. Hill, S. J. Inductively coupled plasma spectrometry and its applications. Blackwell Publishing. ISBN: 978-1-405-13594-8 (2006).
 121. Thomas, R. Practical Guide to ICP-MS. Marcel Dekker, Inc. ISBN: 0-8247-5319-4 (2004).
 122. Jarvis, K. E., A. L. Gray, and R. S. Houk. Handbook of Inductively Coupled Plasma Mass Spectrometry. Glasgow: Blackie, 1992.
 123. <http://community.asdlib.org/imageandvideoexchange/forum/2013/07/30/inductively-coupled-plasma-torch/> (date accessed: 26/10/2018).
 124. EPA. Method 3052. ReVision 1–20 (1996).
 125. Shackley, M. S. in X-Ray Fluorescence Spectrometry (XRF) in Geoarchaeology 1–6. Springer New York (2011). doi:10.1007/978-1-4419-6886-9_1
 126. <https://www.bruker.com/products/x-ray-diffraction-and-elemental-analysis/handheld-xrf/how-xrf-works.html> (date accessed: 15/08/2018).
 127. Gillings, H. Surface-modified minerals for radionuclide sequestration Surface Modified Minerals for Radionuclide Sequestration. A doctoral thesis submitted in partial fulfilment of the requirements for the award of Doctor of Philosophy Loughborough University Resear (2018).
 128. Walter E. Dean, Jr., W. E. Determination of Carbonate and Organic Matter in Calcareous Sediments and Sedimentary Rocks by Loss on Ignition: Comparison With Other Methods. *J. Sediment. Res.* Vol. 44, 242–248 (1974).
 129. Heiri, O., Lotter, A. F. & Lemcke, G. Loss on ignition as a method for estimating organic and carbonate content in sediments: reproducibility and comparability of results. *J. Paleolimnol.* 25, 101–110 (2001).
 130. Santisteban, J. I., Mediavilla, E., López-Pamo, C. J., Dabrio, M. B. R., Zapata, M. J. G., García, S., Castaño, P. E., Martínez-Alfaro. Loss on ignition: a qualitative or quantitative method for organic matter and carbonate mineral content in sediments? *J. Paleolimnol.*, 32 (3) (2004), pp. 287-299.
 131. P. Gillman, G., F. Sinclair, D. & A. Beech, T. Recovery of organic-carbon by the Walkley and Black procedure in highly weathered soil. *Commun. Soil Sci. Plant Anal.* 17, (1986).
 132. Mendez de Souza, D., Augusto de Oliveira Morais, P., Matsushige, I. & Alves Rosa, L. Development of Alternative Methods for Determining Soil Organic Matter. *Rev. Bras. Cienc. Solo.* (2016). doi:10.1590/18069657rbcs20150150.

133. Ritchey, E. L., Mcgrath, J. M., Gehring, D. Natural Resource Conservation Services. Determining Soil Texture by Feel. Agric. Nat. Resour. Fam. Consum. Sci. 4-H Youth Dev. Community Econ. Dev. I (2015).
134. Beretta, A. N. et al. Soil texture analyses using a hydrometer: modification of the Bouyoucos method. *Cienc. e Investig. Agrar.* 41, 25–26 (2014).
135. <https://www.nrcs.usda.gov/wps/portal/nrcs/main/soils/survey/class/> (date accessed: 03/06/2018).
136. Blanco Rodríguez, P., Vera Tomé, F., Lozano, J. C. & Pérez-Fernández, M. A. Influence of soil texture on the distribution and availability of ^{238}U , ^{230}Th , and ^{226}Ra in soils. *J. Environ. Radioact.* 99, 1247–1254 (2008).
137. Davies, K. S. & Shaw, G. Fixation of ^{137}Cs by soils and sediments in the Esk Estuary, Cumbria, UK. *Sci. Total Environ.* 132, 71–92 (1993).
138. G.E. Amidon, P.J. Meyer, D.M. Mudie. Chapter 10 - Particle, Powder, and Compact Characterization, Editor(s): Yihong Qiu, Yisheng Chen, Geoff G.Z. Zhang, Lawrence Yu, Rao V. Mantri, *Developing Solid Oral Dosage Forms (Second Edition)*, Academic Press, 2017, pp 271-293, ISBN 9780128024478, doi.org/10.1016/B978-0-12-802447-8.00010-8.
139. Marshall, J. L. in *Solder Joint Reliability* 173–224. Springer US (1991). doi:10.1007/978-1-4615-3910-0_6.
140. Betancourt T, Brannon-Peppas L. Micro- and nanofabrication methods in nanotechnological medical and pharmaceutical devices. *Int J Nanomedicine.* 2006 Dec;1(4):483-95. Epub 2006 Dec. PubMed PMID: 17722281; PubMed Central PMCID: PMC2676643.
141. Longworth, G., Carpenter, B. *Radiochemical manual.* AEA Technology (1998).
142. Malcolm-Lawes, D. J. *Introduction to radiochemistry.* Wiley (1979).
143. Niese, S. The First Paper About Exciting of Fluorescence of Liquid Biphenyl and Phenanthren by Fast Electrons by Lieselott Herforth and Hartmut Kallmann. *Radiocarbon* 43, 125–126 (2001).
144. Thermo Spectronic. *Basic UV-Vis Theory, Concepts and Applications.* (2013). doi:10.1021/bc049951i
145. Beckett, R., Jue, Z. & Gliddings, J. C. Determination of Molecular Weight Distributions of Fulvic and Humic Acids Using Flow Field-Flow Fractionation. *Environ. Sci. Technol.* 21, 289–295 (1987).
146. Tessier, A., Campbell, P. G. C. & Bisson, M. Sequential Extraction Procedure for the

- Speciation of Particulate Trace Metals. *Anal. Chem.* 51, 844–851 (1979).
147. Blanco, P., Vera Tomé, F. & Lozano, J. C. Sequential extraction for radionuclide fractionation in soil samples: A comparative study. *Appl. Radiat. Isot.* 61, 345–350 (2004).
 148. Lozano, J. C., Tomé, F. V., Rodríguez, P. B. & Prieto, C. A sequential method for the determination of ^{210}Pb , ^{226}Ra , and uranium and thorium radioisotopes by LSC and alpha-spectrometry. *Appl. Radiat. Isot.* 68, 828–831 (2010).
 149. Vandenhove, H., Vanhoudt, N., Duquène, L., Antunes, K. & Wannijn, J. Comparison of two sequential extraction procedures for uranium fractionation in contaminated soils. *J. Environ. Radioact.* 137, 1–9 (2014).
 150. Weil, R. R. & Brady, N. C. *The nature and properties of soils.* (Pearson Education Limited, 2017).
 151. Robert T., A. & Lovley, D. R. Chapter 7 Microbial redox interactions with uranium: an environmental perspective. *Radioact. Environ.* 2, 205–223 (2002).
 152. Gallego-Sala, A. V et al. Bioclimatic envelope model of climate change impacts on blanket peatland distribution in Great Britain. *Clim. Res.* (2010). doi:10.3354/cr00911
 153. Jones, J. A., Proctor, M. E. & Hollis, J. M. Extraction of NSI data for ALC Data Extraction from the National Soils Inventory for Agricultural Land Classification. (2010).
 154. Szarłowicz, K., Reczynski, W., Misiak, R. & Kubica, B. Radionuclides and heavy metal concentrations as complementary tools for studying the impact of industrialization on the environment. *J. Radioanal. Nucl. Chem.* 298, 1323–1333 (2013).
 155. Choppin, G. R., Liljenzin, J.-O., Rydberg, J. & Choppin, G. R. *Radiochem. Nucl. Chem.* (Butterworth-Heinemann, 1995).
 156. Geological disposal. NDA Report no. NDA/RWM/120 (2010).
 157. Kordel, W., Dassenakis, M., Lintemann, J. & Padberg, S. The importance of natural organic material for environmental processes in waters and soils. *Pure & Appl. Chem.* 69, IUPAC (1997).
 158. Kummert, R., & Stumm, W. The surface complexation of organic acids on hydrous $\gamma\text{-Al}_2\text{O}_3$. *J. Colloid Interface Sci.*, 75, 373-385. [https://doi.org/10.1016/0021-9797\(80\)90462-2](https://doi.org/10.1016/0021-9797(80)90462-2) (2010).
 159. Van Ommen, R. Sedimentation Particle Settling Velocity. *AIChE J.* 52(2):838–842 (2010).
 160. R. S. W. Braithwaite and J. R. Knight (1990) *Rare Minerals, Including Several New to*

- Britain, in *Supergene Alteration of U-Cu-As-Bi-Co Mineralisation Near Dalbeattie, South Scotland*. *Mineral. Mag.* 54:129-131.
161. Langmuir, D. *Aqueous Environmental Geochemistry*, Prentice Hall, Upper Saddle River, NJ (1997).
 162. Sheppard, S.C., Sheppard, M.I., Ilin, M., Tait, J., Sanipelli, B., Primordial radionuclides in Canadian background sites: secular equilibrium and isotopic differences, *J. Environ. Radioact.* 99 (2008) 933–946.
 163. Sheppard, M.I., Thibault, D.H., Default soil solid/liquid partition coefficients, K_{ds} for four major soil types: a compendium, *Health Phys.* 59 4 (1990) 471–482.
 164. Vandenhove, H., Gil-Garcia, C., Rigol, A. Vidal, M., New best estimates for radionuclide solid–liquid distribution coefficients in soils. Part 2: Naturally occurring radionuclides, *J. Environ. Radioact.* 100 (2009) 697–703
 165. Ames, L.L., McGarrah, J.E., Walker, B.A., Sorption of uranium and radium by biotite, muscovite, and phlogopite, *Clays Clay Miner.* 31 (1983) 343–351.
 166. Tachi, Y., Shibutani, T., Sato, H., Yui, M., Experimental and modeling studies on sorption and diffusion of radium in bentonite, *J. Contam. Hydrol.* 47 (2001) 171–186.
 167. Ames, L.L., McGarrah, J.E., Walker, B.A., Sorption of trace constituents from aqueous solutions onto secondary minerals; II, Radium, *Clays Clay Miner.* 31 (1983) 335–342.
 168. Ames, L.L., McGarrah, J.E., Walker, B.A., Salter, P.F., Uranium and radium sorption on amorphous ferric oxyhydroxide, *Chem. Geol.* 40 (1983) 135–148.
 170. Haji-Djafari, S., Antommaria, P.E., Crouse, H.L., “Attenuation of radionuclides and toxic elements by in situ soils at a uranium tailings pond in central Wyoming”, *Permeability and Groundwater Contamination Transport*, (Symp. ASTM Committee D-18 on Soil and Rock for Engineering Purposes, Philadelphia, PA, 1979), (Zimmie, T.F., Riggs, C.O., Eds.) ASTM Special Publication 746, ASTM, Philadelphia, USA (1981) 221–242.
 171. Giles, J.R., TAN TSF-07 Pond Ra-226 Concentrations and Corrections, INEEL/EXT-9800505, June 1998.